

**Elucidating the Role of Fluorine on Gas Transport Through Fluorinated
Polymer Membranes**

by

Albert Xiuyuan Wu

B.Ch.E., University of Minnesota – Twin Cities (2016)

M.S. Chemical Engineering Practice, Massachusetts Institute of Technology (2018)

Submitted to the Department of Chemical Engineering in
partial fulfillment of the requirements for the degree of

Doctor of Philosophy in Chemical Engineering

at the

MASSACHUSETTS INSTITUTE OF TECHNOLOGY

June 2021

© Massachusetts Institute of Technology 2021. All rights reserved.

Author

Department of Chemical Engineering
May 21, 2021

Certified by

Zachary P. Smith
Joseph R. Mares Career Development Professor of Chemical Engineering
Thesis Supervisor

Accepted by

Patrick S. Doyle
Robert T. Haslam (1911) Professor of Chemical Engineering
Chairman, Committee for Graduate Students

**Elucidating the Role of Fluorine on Gas Transport Through
Fluorinated Polymer Membranes**

by

Albert Xiuyuan Wu

Submitted to the Department of Chemical Engineering
on May 21, 2021, in partial fulfillment of the
requirements for the degree of
Doctor of Philosophy in Chemical Engineering

Abstract

Fully fluorinated polymers (*i.e.*, perfluoropolymers) are a unique class of materials that have shown exceptional separation performance due to their anomalous thermodynamic partitioning compared to typical hydrocarbon polymers. The goal of this work is to elucidate the role of fluorine on gas permeability, diffusion, and sorption through the systematic synthesis and characterization of hydrocarbon, partially fluorinated, and fully fluorinated polymer structures, with a particular focus on the development of structure–property relationships and connecting the behavior of hydrocarbon and fully fluorinated polymers. The effect of the higher sorption selectivity displayed by perfluoropolymers on separation performance was demonstrated through a refinement of upper bound theory. Inclusion of aliphatic fluorine groups resulted in higher diffusion due to increased interchain spacing caused by the larger size of fluorine, while inclusion of aromatic fluorine groups resulted in significantly higher diffusion but also lower diffusion selectivity due to weakened interchain interactions as well as increased interchain spacing. Through the lens of the dual-mode sorption model, increased polymer fluorination affected only the Henry sorption mode through increased amounts of unfavorable equilibrium mixing interactions while the sorption in the

Langmuir mode was relatively unchanged. Within the scope of the non-equilibrium lattice fluid model, increased fluorine content resulted in larger unfavorable deviations from ideal mixing, particularly for CH₄. Increased enthalpic selectivity with fluorine content was also observed, driving the increase in infinite dilution sorption selectivity. Additionally, an updated group contribution method for estimating fractional free volume in polymers was developed to streamline calculation for any polymer structure.

Thesis Supervisor:

Zachary P. Smith

Joseph R. Mares Career Development Professor of Chemical Engineering

Acknowledgments

When looking back on my Ph.D. journey, I realize how fortunate I have been for the experiences and friendships I have made during my (both incredibly short and infinitely long!) time at MIT.

To start, I would like to thank my advisor, Prof. Zachary Smith, for taking a chance and having me as one of his first students despite having effectively no experience in the field of polymers. It has been my absolute joy to see and help the lab grow and evolve from a small group of 5 stuck in temporary sub-basement lab space to the now-flourishing group of 20 with experiments running literally around the clock. Despite all of the difficulties and growing pains that come with starting up a lab (especially those darn sorption systems) and group, you were so patient and stuck with us every step of the way. Looking back, I would not have wanted it any other way and I am grateful to have worked with and learned so much from you. I would also like to thank my thesis committee, Prof. Gregory Rutledge and Prof. Jeremiah Johnson, for their helpful comments and providing fresh perspectives on my work throughout my entire thesis journey.

In keeping with the theme of lab, I would like to thank all lab mates past and present: Qihui, Sharon, Lucas, Francesco, Katherine, Patrick, Andy, Shiqi, Holden, Hyunhee, TJ, Moonjoo, Justin, Fatimah, Shaofei, Robin, Aristotle, Wan-Ni, and Kayla. The lab culture we made together made going in everyday a joy even during rough times. From our spontaneous lunch outings for hot pot to candlepin bowling to backyard barbeques, I enjoyed every moment with you all. To the new lab members who joined post-pandemic, Stephen, Eleonora, Eric, Pablo, and Jing Ying, I regret I was not able to get to know you all as well but I hope that you will be able to enjoy and thrive during your time as part of the group.

In particular, I would like to acknowledge Qihui, Sharon, and Lucas, for our times and struggles with building up the lab. The period when our group was only us was a particularly special time to me, full of learning and struggles and fun. I would also like to thank my undergrad researcher, James Drayton, for their incredible work back when I was focused on synthesis. I would not have been able to make the polymers in these studies without your help. To my collaborators within the lab, Qihui, Sharon, Katherine, Francesco, Holden, TJ, Aristotle, and Kayla, thank you all for your invaluable help with regards to synthesis, sorption analysis, and data collection. I would also like to thank Dr. Xinyi Ren and Prof. Jiwoong Lee at Copenhagen University for taking me in as a visiting student for two weeks and teaching organic synthesis to a person with extremely limited chemistry lab experience.

I am also grateful for the friendships made within the department. Especially to the Masters students, Steven, Robbie, Ben, Tyler, and Kate, thank you for letting me infiltrate your group even as a Ph.D. student. As someone who came to Boston not knowing anyone in the area, I am extremely grateful for the laughter you all brought during our difficult first semester as well as the lasting friendships we made. Out of everyone in our cohort who made that first year bearable, I would in particular like to thank Nik for perfectly assimilating with us at Corning for Practice School, the entire crew of students at EGA, as well as Cynthia, Webster, and Nathan for embracing my love for ultimate frisbee and becoming my teammates on the field.

To the ultimate frisbee community at MIT, I had the time of my life playing with you all. Especially to my MIT teammates on Grim and the Woodmunchers over the past 5 years, thank you for accepting this old man graduate student and letting me feel young when playing and competing with the team. Our brand of frisbee is truly one-of-a-kind and I will truly miss it all. As Coach Axis says at the beginning of every year, "I often hear from graduating students that joining the

MIT frisbee team was the best decision of their college career.” For myself, I would have to say that joining the MIT frisbee team was only the second-best decision I made during my graduate career...

The best decision being marrying my lovely wife, Stephanie. We’ve been through so much together, especially this past year with both of us working from home in our Boston-sized studio apartment. We’ve often said we wanted another honeymoon and we were given that, in a strange sense. You’ve always been so supportive and understanding of my irregular work schedule and the various demands of graduate life. I can only hope to have supported you as much as you have supported me. Most importantly, you’ve made me a better person in every way. To both sets of parents and siblings, Weibao, Ailian, Mary, Jintu, Julia, and Shelley, thank you for always supporting us as we start our lives together. Stephanie, thank you for moving out here to be with me and thank you for being willing to move again. You’re the best and I am excited to start our next chapter together.

Table of Contents

Chapter 1: Introduction	11
1.1. Dissertation Goals	11
1.2. Dissertation Outline.....	13
1.3. References	15
Chapter 2: Background	17
2.1. The Need for Energy-Efficient Gas Separations.....	17
2.2. Existing and Emerging Technologies for Gas Separations	18
2.3. Current Status of Membrane-based Gas Separations	23
2.3.1. Applications of Membranes for Gas Separations	26
2.3.2. Challenges Associated with Polymer Membranes	28
2.3.2.1. Permeability-Selectivity Tradeoff.....	29
2.3.2.2. Membrane Stability.....	31
2.4. References	34
Chapter 3: Materials and Experimental Methods	40
3.1. Monomer and Polymer Synthesis	40
3.1.1. 6FDA-6HpDA, 6FDA-6FpDA, 6FDA-OHB, and 6FDA-OFB Polyimide Synthesis	40
3.1.2. 10FEDA Monomer Synthesis.....	41
3.1.3. 10HEDA-MPD, 10HEDA-TFMPD, 10FEDA-MPD, and 10FEDA-TFMPD Poly(Ether Imide) Synthesis.....	45
3.2. Film Casting	45
3.3. Characterization Methods	46
3.3.1. Pure-gas Permeation Measurements.....	46
3.3.2. Pure-gas Sorption Measurements	48
3.3.3. Physical and Chemical Characterization	49
3.4. References	49
Chapter 4: The Perfluoropolymer Upper Bound	51
4.1. Introduction	52
4.2. Theory & Background.....	53
4.3. Analysis Procedure.....	58
4.3.1. Modifications from Previous Analysis	58
4.3.2. Necessity of Non-perfluoropolymer Upper Bounds.....	60
4.3.3. Selection of Molecular Diameters	61
4.3.4. Calculation of Individual f values for each Gas Pair.....	62

4.3.5. Adjustment in Solubility Correlation	62
4.4. Results	63
4.4.1. The Perfluoropolymer Upper Bound.....	63
4.4.2. Comparison of Diffusivity and Solubility Selectivity Effects on Shifting the Upper Bound.....	67
4.4.3. Prediction of Upper Bound Fronts from Penetrant Properties	72
4.4.4. Promising Future Gas Separation Applications for Perfluoropolymers.....	76
4.5. Conclusions	77
4.6. References	78
Chapter 5: Influence of Aliphatic and Aromatic Fluorine Groups on Gas Permeability and Morphology of Fluorinated Polyimide Films	83
5.1. Introduction	84
5.2. Theory	85
5.3. Results	86
5.3.1. Polymer Synthesis and Structure Confirmation	86
5.3.2. Effect of Fluorination on Pure-gas Permeation, Diffusion, Sorption, and Energetics	88
5.3.3. Effect of Fluorination on Solid-state Morphology	95
5.4. Conclusions	102
5.5. References	103
Chapter 6: Elucidating the Role of Fluorine Content on Gas Sorption Properties of Fluorinated Polyimides.....	107
6.1. Introduction	108
6.2. Theory	111
6.3. Results	114
6.3.1. Gas Sorption Isotherms and Dual-mode Model Parameter Fitting	114
6.3.2. Effect of Fluorination on Sorption and Dual-mode Parameters	120
6.3.3. Effect of Fluorine on LFERs	126
6.3.4. Effect of Fluorine on Sorption Energetics.....	128
6.4. Conclusions	135
6.5. References	136
Chapter 7: Non-Equilibrium Lattice Fluid Modeling of Gas Sorption for Fluorinated Poly(Ether Imide)s	142
7.1. Introduction	143
7.2. Theory	145
7.3. Results	151

7.3.1. Monomer Synthesis and Characterization	151
7.3.2. Polymer Synthesis and Characterization	152
7.3.3. Estimation of Lattice Fluid Parameters	155
7.3.4. NELF Gas Sorption Modeling and Effect of Fluorine on the Binary Interaction Parameter	159
7.3.5. Effect of Fluorine on Enthalpic and Entropic Contributions to Gas Sorption at Infinite Dilution	164
7.4. Conclusions	168
7.5. References	169
Chapter 8: Revisiting Group Contribution Theory for Estimating Fractional Free Volume of Microporous Polymer Membranes	174
8.1. Introduction	175
8.2. Methods	178
8.2.1. Changes from Bondi's Method	178
8.2.2. Procedure for Simulated V_W of Groups	181
8.3. Results	183
8.3.1. Simulated V_W Values for Previously Reported and New Structural Groups	183
8.3.2. Updated FFV Estimates for Literature Microporous Polymers	199
8.3.3. Impact of New FFV Values on Gas Transport Correlations for Microporous Polymers	202
8.3.3.1. Permeability Correlations with Respect to FFV	202
8.3.3.2. Revisiting Packing Factor Assumptions	204
8.4. Conclusions	206
8.5. References	207
Chapter 9: Conclusions and Future Directions	212
9.1. Conclusions	212
9.2. Recommendations for Future Work	216
9.2.1. Noble Gases Sorption in Fluorinated Polymers	216
9.2.2. Sorption of Hydrocarbon, Perfluorocarbon, and Partially Fluorinated Gases in Fluorinated Polymers	217
9.2.3. Development of Structure–Property Relationships Relating Fluorine Content to Plasticization and Physical Aging Resistance	218
9.3. References	218
Appendix A: Supplementary Information for Chapter 4	219
Appendix B: Supplementary Information for Chapter 5	226
Appendix C: Supplementary Information for Chapter 6	239

Appendix D: Supplementary Information for Chapter 7	256
Appendix E: Supplementary Information for Chapter 8.....	268

Chapter 1: Introduction

1.1. Dissertation Goals

Gas separations are essential to obtain high purity gases used for a variety of applications, such as pure oxygen used for medical procedures or pure hydrogen and nitrogen used for ammonia production, a crucial component of fertilizer.¹ Current processes for gas separations (*e.g.*, cryogenic distillation, pressure-swing adsorption, or amine absorption) are energy-intensive.² The development of polymer membranes as a more energy-efficient process for gas separations has attracted significant research effort due to their potential for significant energy savings and smaller carbon footprint compared to the current methods.² Since the first industrial implementation in 1977 for hydrogen recovery from ammonia plants,³ polymer membranes have been successfully implemented for a variety of applications, such as nitrogen production, natural gas treatment, and gasoline vapor recovery.^{4,5}

An industry that is rapidly becoming more prominent where polymer membranes could occupy a large market share is helium recovery.⁶ Pure helium is used in large quantities for applications such as magnetic resonance imaging and welding, among many others.⁷ Helium is a non-renewable resource and the only viable commercial source is natural gas streams, where it typically occupies up to 1 to 4 mol% of the stream.⁸ In the past 20 years, the price point for Grade-A helium (>99.997% pure) has grown fourfold due to market corrections related to policy changes for the United States Helium Reserve sell-off.^{7,9} The price point is projected to keep increasing in the future as the Reserve is depleted and demand from developing countries continues to increase. As such, there has been interest among research communities to develop membrane technologies that could produce Grade-A helium from natural gas streams containing less than 0.3 mol% to provide financial incentive for companies to harvest from those streams.¹⁰ However, current membrane

technologies do not reach this benchmark. For a membrane-based gas separation, the isolation of helium from the other gases present in a mixture is difficult because of competing diffusion and sorption selective effects inherent to the properties of the penetrants. For example, natural gas streams contain many components from which helium needs to be separated, primarily methane, nitrogen, carbon dioxide, and higher hydrocarbons.⁸ For this mixture, helium is smaller than all of the other components and is therefore favored in terms of diffusion selectivity but is also less condensable than all of the other components and is therefore disfavored in terms of sorption selectivity.¹¹

One class of polymer materials that has shown the best combinations of permeability and selectivity for all helium-based gas pairs is perfluoropolymers.¹² Perfluoropolymers are defined by the presence of C–F bonds and the absence of C–H bonds. It has been previously shown that perfluoropolymers display distinct thermodynamic partitioning compared to hydrocarbon polymers, thereby resulting in high sorption selectivity for certain gas pairs.¹³ Despite extensive theoretical and computational effort investigating the mixing of hydrocarbon and perfluorocarbon liquids, the anomalous solubility behavior remains unexplained at a molecular level.^{14–17} Additionally, due to synthetic difficulties and chemical safety issues, limited amounts of perfluorinated structures have been studied for gas separation, thereby limiting our understanding of specific structure–property relationships related to fluorine.¹⁸ While perfluoropolymers show potential for industrial implementation, their separation performance is currently not well-understood from a fundamental perspective.

The unifying theme of this dissertation is to investigate and understand the role of fluorine content on gas transport, with an emphasis on gas sorption. With the goal of providing deeper understanding of the effects of fluorine on gas separation performance to aid in the design of

industrially-relevant polymers, the aims of this dissertation are to quantify the effect of fluorination on gas separation performance, develop relevant structure–property relationships related to fluorine, and identify specific mechanisms by which fluorination affects gas sorption. Through the systematic synthesis of partially and fully fluorinated polymers, changes in separation performance and sorption behavior were analyzed in the context of various transport and sorption models, such as upper bound theory, the Brandt model, the dual-mode sorption model, and the non-equilibrium lattice fluid model. The final aim of this dissertation is to examine and update group contribution theory to accommodate modern polymer structures and provide an accessible procedural framework for consistent and accurate fractional free volume calculation.

1.2. Dissertation Outline

The various transport and sorption models mentioned above also serve as an outline for this dissertation. A brief introduction motivating the need for energy-efficient separations and discussing essential challenges that must be addressed for polymer membrane-based gas separation processes to surpass competing technologies is the focus of Chapter 2. Experimental methods for the results presented in this dissertation are provided in Chapter 3.

Chapter 4 presents our work towards reconciling the unexpectedly high performance of perfluoropolymers with classical upper bound theory.¹⁹ The original theory was refined to consider changes in sorption capacity and selectivity resulting from altered chemical functionality of the polymer backbone.¹⁹ The distinct thermodynamic partitioning behavior of perfluoropolymers compared to non-perfluoropolymers was applied to construct theoretical “perfluoropolymer upper bounds”, highlighting the effect of altered sorption selectivity on overall separation performance for all helium- and most methane-based gas pairs. Through this work, we are able to quantify the improvement in separation performance resulting from perfluoropolymer sorption behavior.

Chapter 5 develops structure–property relationships related to fluorine connectivity (*i.e.*, aliphatic versus aromatic fluorine) on gas permeation and diffusion. The synthesis of partially fluorinated, structurally-analogous polyimides is presented, including the synthesis and film casting of a highly fluorinated polyimide structure, a traditionally difficult task. The role of aliphatic versus aromatic fluorine on the structural analogues was investigated through changes in morphology and diffusion-related properties. Fluorination resulted in higher diffusion coefficients for both cases, but the corresponding decrease in diffusion selectivity was smaller for aliphatic fluorination than for aromatic fluorination. This difference was explained via structural and electronic changes brought about by aromatic fluorine groups resulted in lower activation energy of diffusion caused by weakened secondary interactions, such as π - π stacking.

Chapter 6 is a sibling study with Chapter 5, using the same set of partially fluorinated polyimide structures to elucidate the role of fluorine content on gas sorption behavior using the dual-mode model.¹¹ Changes in sorption selectivity was found to be primarily driven by changes in the Henry mode of sorption, as opposed to the Langmuir mode, drawing parallels to anomalous mixing behavior exhibited by hydrocarbon-perfluorocarbon solutions.¹³ An analysis of the enthalpy of sorption as a function of penetrant concentration revealed a slower transition from Langmuir to Henry sorption for the more fluorinated polymers, suggesting a greater enthalpic penalty related to penetrant-polymer mixing caused by increased bulk fluorine content.

Chapter 7 extends the analysis into the role of fluorine on gas sorption behavior through the non-equilibrium lattice fluid model. In addition to the four partially fluorinated polymers previously synthesized, the synthesis and characterization of a perfluorinated dianhydride and its polymerization is described, creating the basis for four new polymers and expanding the analysis set to include fully hydrocarbon and fully fluorinated polymers. An increase in unfavorable

deviation from ideal mixing was observed with increasing fluorine content, particularly for CH₄. Continuous trends for enthalpic selectivity, entropic selectivity, and infinite dilution sorption selectivity were observed, where the increase in enthalpic selectivity with fluorine content was found to be the driver for improved infinite dilution sorption selectivity.

Lastly, Chapter 8 examines and refines Bondi's group contribution theory, the most common method to calculate fractional free volume in polymer membranes.²⁰ Assumptions inherent to the original method were critically evaluated and four changes were implemented as part of a modernized, streamlined procedure for fractional free volume calculation. Fractional free volumes were calculated for a literature database of microporous polymers, showing an apparent increase compared to those originally reported. Standardization of the method for fractional free volume calculation allows for direct comparison of values across studies. Finally, conclusions and future directions are presented in Chapter 9. Supplementary information for Chapter 4 to 8 are included in the appendices.

1.3. References

- (1) Sanders, D. F.; Smith, Z. P.; Guo, R.; Robeson, L. M.; McGrath, J. E.; Paul, D. R.; Freeman, B. D. Energy-Efficient Polymeric Gas Separation Membranes for a Sustainable Future: A Review. *Polymer* **2013**, *54* (18), 4729–4761. <https://doi.org/10.1016/j.polymer.2013.05.075>.
- (2) Sholl, D. S.; Lively, R. P. Seven Chemical Separations to Change the World. *Nature* **2016**, *532*, 435–437. <https://doi.org/10.1038/532435a>.
- (3) Van Gelder, J. M. Hydrogen Recovery Made Simple. *Chem. Eng. News* **1979**, *57* (48), 26–27. <https://doi.org/10.1021/cen-v057n048.p026>.
- (4) Galizia, M.; Chi, W. S.; Smith, Z. P.; Merkel, T. C.; Baker, R. W.; Freeman, B. D. 50th Anniversary Perspective: Polymers and Mixed Matrix Membranes for Gas and Vapor Separation: A Review and Prospective Opportunities. *Macromolecules* **2017**, *50* (20), 7809–7843. <https://doi.org/10.1021/acs.macromol.7b01718>.
- (5) Qian, Q.; Asinger, P. A.; Lee, M. J.; Han, G.; Mizrahi Rodriguez, K.; Lin, S.; Benedetti, F. M.; Wu, A. X.; Chi, W. S.; Smith, Z. P. MOF-Based Membranes for Gas Separations. *Chem. Rev.* **2020**, *120* (16), 8161–8266. <https://doi.org/10.1021/acs.chemrev.0c00119>.

- (6) Sunarso, J.; Hashim, S. S.; Lin, Y. S.; Liu, S. M. Membranes for Helium Recovery: An Overview on the Context, Materials and Future Directions. *Sep. Purif. Technol.* **2017**, *176*, 335–383. <https://doi.org/10.1016/j.seppur.2016.12.020>.
- (7) Peterson, J. B. *Helium*; 2019. <https://doi.org/10.1017/CBO9781107415324.004>.
- (8) Scholes, C. A.; Ghosh, U. K. Review of Membranes for Helium Separation and Purification. *Membranes* **2017**, *7* (1), 1–13. <https://doi.org/10.3390/membranes7010009>.
- (9) Wheeler M. Sears. *Helium: The Disappearing Element*; 2015. <https://doi.org/10.5860/choice.191700>.
- (10) Bare, S. R.; Lilly, M.; Chermak, J.; Eggert, R.; Halperin, W.; Hannahs, S.; Hayes, S.; Hendrich, M.; Hurd, A.; Osofsky, M.; et al. *The U.S. Research Community's Liquid Helium Crisis*; 2016.
- (11) Matteucci, S.; Yampolskii, Y.; Freeman, B. D.; Pinnau, I. Transport of Gases and Vapors in Glassy and Rubbery Polymers. In *Materials Science of Membranes for Gas and Vapor Separation*; 2006; pp 1–47. <https://doi.org/10.1002/047002903X.ch1>.
- (12) Robeson, L. M. The Upper Bound Revisited. *J. Membr. Sci.* **2008**, *320* (1–2), 390–400. <https://doi.org/10.1016/j.memsci.2008.04.030>.
- (13) Merkel, T. C.; Pinnau, I.; Prabhakar, R. S.; Freeman, B. D. Gas and Vapor Transport Properties of Perfluoropolymers. In *Materials Science of Membranes for Gas and Vapor Separation*; 2006; pp 251–270.
- (14) Scott, R. L. The Anomalous Behavior of Fluorocarbon Solutions. *J. Phys. Chem.* **1958**, *62* (2), 136–145. <https://doi.org/10.1021/j150560a002>.
- (15) Scott, R. L. The Solubility of Fluorocarbons. *J. Am. Chem. Soc.* **1948**, *70* (12), 4090–4093. <https://doi.org/10.1021/ja01192a036>.
- (16) Hildebrand, J. H. The Entropy of Solution of Molecules of Different Size. *J. Chem. Phys.* **1947**, *15* (5), 225–228. <https://doi.org/10.1063/1.1746484>.
- (17) Song, W.; Rosky, P. J.; Maroncelli, M. Modeling Alkane+perfluoroalkane Interactions Using All-Atom Potentials: Failure of the Usual Combining Rules. *J. Chem. Phys.* **2003**, *119* (17), 9145–9162. <https://doi.org/10.1063/1.1610435>.
- (18) Yampolskii, Y.; Belov, N.; Alentiev, A. Perfluorinated Polymers as Materials of Membranes for Gas and Vapor Separation. *J. Membr. Sci.* **2020**, 117779. <https://doi.org/10.1016/j.memsci.2019.117779>.
- (19) Freeman, B. D. Basis of Permeability/Selectivity Tradeoff Relations in Polymeric Gas Separation Membranes. *Macromolecules* **1999**, *32* (2), 375–380. <https://doi.org/10.1021/ma9814548>.
- (20) Bondi, A. Van Der Waals Volumes and Radii. *J. Phys. Chem.* **1964**, *68* (3), 441–451. <https://doi.org/10.1021/j100785a001>.

Chapter 2: Background

This chapter has been adapted from: Qian, Q.; Asinger, P. A.; Lee, M. J.; Han, G.; Mizrahi Rodriguez, K.; Lin, S.; Benedetti, F. M.; Wu, A. X.; Chi, W. S.; Smith, Z. P. MOF-Based Membranes for Gas Separations. *Chem. Rev.* **2020**, *120* (16), 8161–8266.

2.1. The Need for Energy-Efficient Gas Separations

Gas separations are crucial in today's energy and chemical production industries, playing an important role in capturing fuels for combustion, purifying chemical building blocks for plastics, and isolating pure, non-combustible gases for inerting, all of which are ubiquitous in daily life.¹ Within the United States, the separations industry consumes 16 quadrillion BTU (Quads) of energy per year,^{2,3} on par with the total yearly primary energy production of Australia.⁴ Approximately 50% of all industrial energy consumption in the United States is a result of separations, nearly half of which comes from thermally driven separations, such as distillation, that rely on liquid-vapor phase changes.^{2,5} As such, the energy input associated with overcoming heats of vaporization can make these processes very energy-intensive. Therefore, distillation, the dominant method used to perform over 200 unique separations, is a key contributor to energy consumption across the globe.⁵ One of the largest gas-phase separations is the separation of alkenes from alkanes, also known as olefin/paraffin separation.⁶ In this process, ethylene and propylene (olefins) are separated from ethane and propane (paraffins), respectively, to be used as precursors in the synthesis of polyethylene, ethylene glycol, polyvinyl chloride, polypropylene, isopropyl alcohol, and epoxy resins, among others.^{7,8} Currently, olefin/paraffin separation is achieved via an energy-intensive distillation process that separates components based on differences in volatility. The small difference in volatility between olefins and paraffins, as gleaned from the similar boiling points of ethylene and ethane (170 K and 184 K, respectively) and propylene and propane (226 K and 231

K, respectively), necessitates the use of large towers between 200 to 300 feet tall and a high reflux ratio between 10 and 15 in order to produce 99.9% pure olefins (polymer-grade) streams required for further processing.^{1,9} Olefin/paraffin separation processes consume approximately 0.75 Quads/year in energy costs related to pressurizing and cooling the tower, comprising 0.3% of global energy use.^{5,9,10} Other large-scale separations such as vapor/vapor separations (*e.g.*, ethanol/water dehydration and ortho- and meta-xylenes from para-xylenes) and hydrocarbons from crude oil, both of which utilize distillation, consume approximately 1.5 Quads/year and 6.6 Quads/year, respectively.⁵ The end-goal would be to replace distillation columns with more energy-efficient methods, such as membrane-based technologies. Importantly, these membrane-based technologies work toward the electrification of industrial processes since their pumps are electrically powered. Such a transition towards non-thermal methods of separation in the petroleum, chemical, and paper manufacturing sectors is estimated to reduce energy costs by 90%, eliminate 100 million tons of CO₂ emissions, and save \$4 billion in energy costs per year in the United States alone.⁵

2.2. Existing and Emerging Technologies for Gas Separations

At the industrial scale, the choice of a separation process depends on a variety of factors including purity, recovery, flow rate, and capital cost. Currently, distillation, pressure swing adsorption (PSA) and temperature swing adsorption (TSA), and chemical absorption technologies are the dominant methods for commercial gas separations due to favorable economics at their respective process scales and their ability to isolate high-purity products.^{1,11} Alternative technologies for separations, such as membrane separations, are the subject of significant research efforts to reduce the carbon and energy footprints related to these traditional unit operations. Ideally, these alternative

technologies would produce at the same scale and purity as existing processes but with lower energy use.

Cryogenic distillation functions similarly to conventional distillation, but is run at low temperatures in order to achieve a separation based on the differences in boiling points of the molecular components.¹² For air separation, one of the most common separations performed via cryogenic distillation, nitrogen (boiling point of 77.4 K) is removed at the top of the column via the distillate stream, while the more condensable gases such as argon (87.3 K) and oxygen (90.2 K) exit via the bottoms stream and continue to a second column for further separation. The resulting outlet streams typically have greater than 99% purity.¹³ Cryogenic distillation is commonly deployed for continuous, high-volume applications, such as air and olefin/paraffin separations, thus taking advantage of its favorable cost-capacity scaling while achieving a high purity separation.^{11,13,14} As with conventional distillation, the flow rate and purity of the distillate and bottoms streams are a function of the feed flow rate and composition, number of stages, operating temperature range and pressure, reflux ratio, and the physical properties of the gaseous components to be separated. Consideration of all the variables requires complex equipment design and heat integration, incurring long start-up and shut-down periods and large capital costs.¹⁵ A large-scale separation train for 500 kt per year ethylene production from a catalytic cracker can amount to approximately \$800 million in total capital cost and \$9.2 million per year in operating costs, as estimated using the 2018 Chemical Engineering Plant Cost Index.¹⁶ The majority of the operating costs is associated with cooling and pressurizing the entire column to condense gases and is the primary mode of energy consumption in the process.^{1,16,17}

PSA and TSA are attractive technologies for separations where certain gaseous compounds in a mixture exhibit preferential and reversible adsorption at relevant temperatures and pressures.

Accordingly, developing improved adsorbent materials is an area of significant research efforts within the PSA and TSA communities.^{18,19} Traditionally, solid-state materials such as zeolites and activated carbons are used for PSA and TSA.²⁰ These materials are typically high-surface area and porous materials that preferentially adsorb gases based on either molecule size or affinity.^{20,21} In the case of adsorption processes, the weakly adsorbing gases more quickly break through an adsorbent bed, leaving the strongly adsorbing gases in the column. In PSA, a change in pressure is used to regenerate the column.²² TSA processes operate similarly, but use elevated temperatures to induce desorption.²³ When incorporating these technologies into overall flow diagrams, adequate time must be allowed for complete regeneration of the adsorbent. Therefore, both PSA and TSA processes are typically designed to have multiple chambers running in parallel to increase total throughput and allow for continuous separation.²⁴ The efficiency of the separation depends highly on the adsorbent and mixture composition, but for many applications, such as oxygen purification, nitrogen enrichment, and CO₂-based separations, product purities that exceed 98% are commonly reached.^{15,25} Because PSA and TSA are typically batch operations, and because throughput often scales linearly with the amount of adsorbent required, these processes are often economical for medium-scale processes with lower purity requirements than those achieved via distillation.²⁶ In many applications, PSA is preferred over TSA due to ease of operation and challenges associated with heating the adsorbent materials for proper regenerative cycling.²⁷ Thus, PSA is the primary processes for many hydrogen recovery applications, such as CO₂ removal from steam reforming of hydrocarbons and CO removal for syngas ratio adjustment, as well as high purity nitrogen generation.^{22,28}

Chemical absorption most directly competes with other technologies for CO₂ separation applications such as natural gas sweetening or carbon capture from flue gas emissions.^{29,30} The

absorbent typically is a liquid amine (*e.g.*, monoethanolamine (MEA), diethanolamine (DEA), or methyldiethanolamine (MDEA)) which reacts with CO₂ to form a nitrogen-substituted carbamic acid.³¹ The carbamic acid product is relatively unstable and decomposes at elevated temperatures, thus releasing the captured CO₂ and regenerating the amine. The non-volatile fraction of the amines are then recycled, allowing for nearly continuous operation to recover or remove high purity CO₂ from product streams.³² There are a few drawbacks to this technology. First, the carbamic acid product requires regeneration temperatures greater than 100°C, thus necessitating a significant thermal input for this aqueous system.³³ Second, the amines can form non-reversible salts in the presence of trace SO₂ and NO_x, thus requiring addition of more amines over time.³⁴ Additionally, the amines can undergo degradation in the presence of O₂, creating corrosive mixtures that can endanger operators and corrode the entire process if left unmonitored.^{1,29}

Compared to these other processes, membrane-based separations are an attractive option for energy-efficiency because they do not require thermally driven phase changes and they do not require solid or liquid sorbents that must be regenerated at some cost in energy. A rough estimate of the relative energy intensities for each of the discussed separation technologies, as well as for other unit operations, is summarized in Figure 2.1 below.³⁵ Distillation accounts for approximately 50% of the energy consumed by industrial separations, while non-phase change driven processes such as adsorption and membrane processes account for 7% and 4% of the total energy consumption, respectively.²

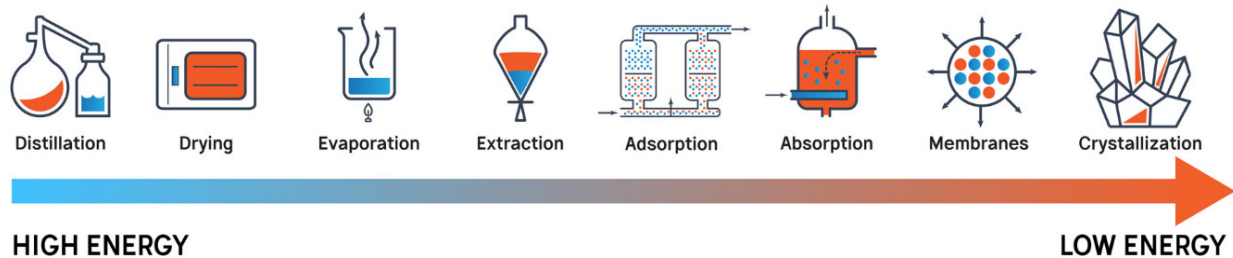


Figure 2.1. Comparison of relative energy required for separation unit operations, ranging from thermal processes (high energy) to non-thermal processes (low energy). Reprinted with permission from NASEM.³⁵

For membrane separations, gases are separated based on their differences in diffusion and sorption coefficients, which are molecular properties governed largely by properties of the membrane material.³⁶ In 1977, Monsanto launched the first successful industrial implementation of a membrane-based gas separation for hydrogen purge recovery for petrochemical and ammonia plants.³⁷ In the following 40 years, polymer membrane-based gas separations have developed into an economically competitive alternative to existing separation technologies. As shown in Figure 2.2 and Table 2.1, the market for gas separation membranes has found success in four primary applications and is projected to continue its steady growth through the near future.³⁸ Overall, membrane-based gas separations have emerged as a promising platform for energy-efficient gas separation, showing potential to provide savings in capital costs and energy-related operating costs as well as offering advantages related to ease of operation and compact footprint.^{1,5,29,30,36}

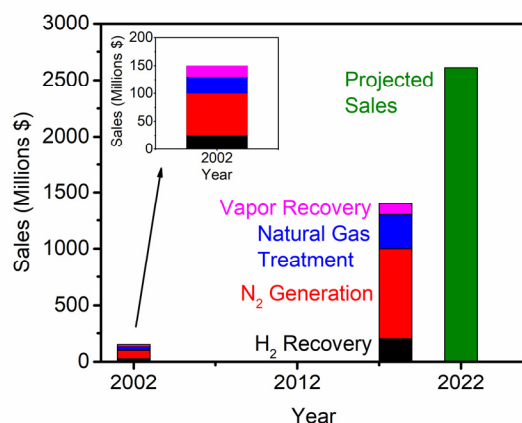


Figure 2.2. Approximate market size in millions of US dollars, divided by major application, of membrane-based gas separations in 2002 and 2018, and projected market size in 2022.^{30,38,39}

Table 2.1. Approximate market size in millions of US dollars, divided by major application, of membrane-based gas separations in 2002 and 2018, and projected market size in 2022.^{30,38,39}

Application	Approximate market size (Millions \$)		
	2002	2018	2022 (projected)
H ₂ Recovery	25	200	-
N ₂ Generation	75	800	-
Natural Gas Treatment	30	300	-
Vapor Recovery	20	100	-
Total	150	1,400	2,610

2.3. Current Status of Membrane-based Gas Separations

Today, most membranes used in industry are fabricated via a phase-inversion process first introduced by Loeb and Sourirajan.^{1,36} This process results in the formation of an asymmetric

membrane that comprises a thin selective layer (0.1-1.0 μm thickness) set on a porous support to provide mechanical strength.³⁶ Modern gas separation plants contain 1,000 m^2 to 500,000 m^2 of membrane film area, but this requirement directly correlates with the thickness of the selective layer.³⁶ Therefore, finding methods to make thinner membranes minimizes the required membrane area, thereby decreasing the capital cost of the entire separation system while maintaining the desired throughput.³⁶

There are two common membrane geometries used today: hollow fibers and spiral wound modules. These two configurations, depicted in Figure 2.3a, maximize the amount of membrane surface area that can fit in a given cylindrical volume. A higher surface-area-to-volume ratio reduces the size of pressure vessels required for these separations.⁴⁰ For hollow-fibers, single or dual-layer systems can be used to form membranes. Single-layer hollow fibers have one polymer component for both the selective layer and the porous support.⁴¹ Dual-layer hollow fibers contain one polymer for the selective layer and a second polymer for the porous support. By using different materials for the dual-layer design, more exotic and hence, more expensive, materials can be accommodated for membrane systems.^{42,43} Membranes fabricated in other configurations are relatively uncommon and are made primarily to satisfy specific process specifications and conditions. For example, plate-and-frame modules are being scaled for post-combustion carbon capture by Membrane Technology and Research (MTR) in order to achieve an acceptable pressure loss across the membrane module.⁴⁴

In the hollow fiber configuration, a thin selective layer is fabricated onto the surface of a cylindrical porous support; a cross-sectional view of a fiber is shown in Figure 2.3b. A typical hollow fiber module contains on the order of 10^5 tightly packed hollow fibers, which are sealed at the ends with thermosetting epoxy.⁴⁵ The feed gas can be introduced on either the shell or tube side of the fibers

and is typically run in a counter-current configuration to the permeate stream to maximize mass transfer rates.^{46,47} A typical spiral wound membrane consists of alternating layers of flat sheet asymmetric membranes separated by porous spacers, with the permeate and feed streams flowing through alternating layers.⁴⁸ Hollow fiber modules provide the benefit of higher surface-area-to-volume ratios, which enables the design of smaller membrane plants for certain separations, but they require a larger pressure drop compared to that of spiral wound membrane modules.^{48,49}

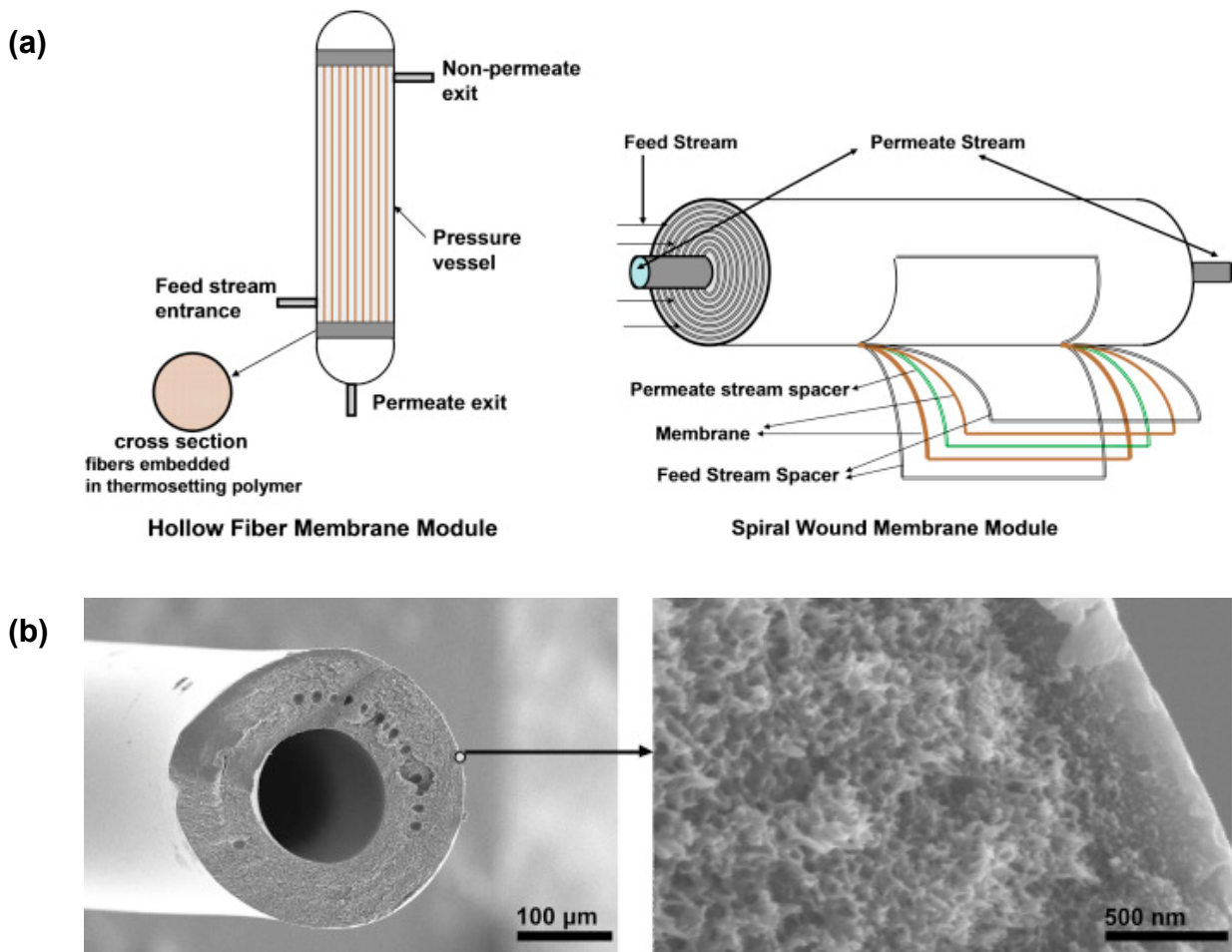


Figure 2.3. (a) Schematic of hollow fiber and spiral wound membrane modules as part of a membrane separation unit operation. Reprinted with permission of Elsevier.¹ (b) Cross-sectional view of a polysulfone single-layer hollow fiber with a thin selective layer on the outer surface. Reprinted with permission of Elsevier.¹

2.3.1. Applications of Membranes for Gas Separations

Membrane separations are often economically favorable in the gas separations market for smaller-scale operations due to their generally lower capital cost and linear cost-throughput scaling.^{50,51} A common challenge is the ability of membranes to achieve high purity separations, which, in the absence of pressure-ratio limitations, depends on the separation performance of the membrane material.⁴⁸ Thus, membranes generally provide sufficient product recovery in applications where high purity is not crucial (*e.g.*, 99% N₂ / 1% O₂ from air).^{29,39} Membranes are currently used in limited industrial capacity, with major successes in four applications that represent 80-90% of the current \$1.0-1.5 billion per year membrane market: nitrogen production (O₂/N₂), natural gas treatment (CO₂/CH₄, H₂S/CH₄, He/CH₄), hydrogen recovery (H₂/N₂, H₂/CH₄, H₂/CO), and vapor recovery (C₃H₆/N₂, C₂H₄/N₂, C₂H₄/Ar, C₃₊/CH₄, CH₄/N₂).^{30,36} The breakdown of the market by application is shown in Figure 2.2 and Table 2.1. While the commercial success of polymer membrane separations is promising, there is still significant room for market expansion within current applications and opportunities in emerging markets. For example, membranes currently occupy about 10% of the natural gas purification market, with the rest of the market occupied by chemical amine absorption, primarily as a result of relatively low permeability and selectivity to treat certain natural gas streams.²⁹ In this case, membranes with better performance would allow for expanded use. There are also many potential applications in which better membrane performance could allow for entry into new markets – promising separations on the verge of industrial relevance include olefin/paraffin separation and carbon capture from flue gas or syngas streams.³⁰

Ethylene and propylene are the two largest-volume organic chemical feedstocks because of their use in the synthesis of various vinyl polymers and monomers such as polyethylene and ethylene

oxide from ethylene and polypropylene and acrylonitrile from propylene, with total global production exceeding 250 million tons combined.^{5,10} It is estimated that approximately 290 Mt of the 380 Mt of polymer resins and fibers (~77%) produced globally in 2015 are formed from vinyl precursors.⁵² As current global demand for polymers is nearly \$500 billion per year,⁵³ the inexpensive supply of basic commodity vinyl monomers is a critical need for society. As mentioned previously, olefin/paraffin separations are among the most energy-intensive separation processes performed today and therefore has been a primary target market for membrane separations for many years. For propylene purge gas streams, membranes with a propylene permeance of 20-40 gas permeation units (GPU, 1 GPU = 10^{-6} cm³(STP) cm⁻² s⁻¹ cmHg⁻¹) and a stable selectivity of 6-10 can be used to selectively recycle 90% of propylene otherwise lost in the purge stream.³⁶ For more ambitious applications, such as replacing distillation columns for the direct separation of feeds from olefin crackers, a stable selectivity of at least 15-20 would be required.³⁶ An intermediate approach that has shown promise is forming distillation-membrane hybrid systems, which can be used to de-bottleneck distillation columns and increase capacity.^{36,54}

The field for carbon capture via membrane separations is vast, comprising applications ranging from CO₂ capture for sequestration from post-combustion flue gas (CO₂/N₂) to treatment of synthesis gas (syngas) streams (CO₂/H₂) generated during the pre-combustion process. Capture of CO₂ from flue gas has the very attractive end-goal of reducing the amount of anthropogenic CO₂ emissions to the atmosphere from power plants, while CO₂ capture of pre-combustion syngas produces a H₂-rich stream that could be used as a hydrogen source in a refinery or as fuel.^{1,30} The market for CO₂ separations is dominated by amine adsorption, but this technology is hamstrung by large plant sizes and the toxicity of the amines.²⁹ For flue gas feed streams, membranes with high CO₂ permeance of 1000-5000 GPU and a selectivity of 30-50 are required in order to be

economically competitive with amine adsorption.³⁰ This high standard for membrane performance is a result of the typical flue gas feed stream: a typical 550 MW power plant produces 2 MMscf of flue gas per minute, which is enough gas to fill the volume of the Goodyear blimp every 9 seconds at STP. These sources only contain 12-14 mol% of CO₂, necessitating an enormous CO₂ permeance relative to traditional polymer membrane systems while maintaining moderate selectivity in order to process the high feed flow rate.⁵⁵ For pre-combustion applications, membranes with a CO₂ permeance greater than 200 and a selectivity greater than 20 are desired to be competitive with typical PSA processes.³⁰ The largest hurdle for this application is the high operating temperature necessary for economical separation, as temperatures between 300-500 °C are required for high conversion towards CO₂/H₂ of the water-gas shift reaction.¹

2.3.2. Challenges Associated with Polymer Membranes

Despite the synthesis and characterization of thousands of newly reported materials, 90% of current commercial membranes are comprised of fewer than 10 polymers (*e.g.*, polysulfone, cellulose acetate, polyimides, polyphenylene oxide, substituted polycarbonates, polyaramides, and silicone rubber), most of which were developed and successfully implemented in or before the 1990s.³⁶ The stagnation in development for these “solved” membrane applications is a result of the minimal decrease in capital cost associated with the adoption of many new materials. While improved permeability would decrease the total membrane area required and improved selectivity would decrease the compressor size, these significant development efforts are estimated to provide a total capital savings of only 5-10% due to the comparatively high, fixed costs of other process components in the overall membrane skid (*e.g.*, pumps, compressors, steel vessels, pipes, valves, etc.).^{29,30} In order to truly promote the adoption of new materials, a step change in materials performance is required to enable a step change in reducing fixed component costs, such as

reducing compressor and pump sizes. For these “solved” applications, as well as for any new application, optimization of the process flow diagram to minimize energy and capital costs is required to determine if a membrane separation would be competitive with other current unit operations.^{56,57} Therefore, the primary focus for gas separation membrane researchers is to develop materials that can break through in new application areas, including but not limited to those mentioned above, by addressing challenges related to membrane performance and stability over time.

2.3.2.1. Permeability-Selectivity Tradeoff

Ideally, a membrane would provide high flux and high gas purity in order to maximize throughput and minimize costs. Permeability and selectivity are, fundamentally, properties resulting from the structure of the membrane material, logically prompting research into structure-property relationships. As the amount of data on membrane separations increased with time, it became apparent that a tradeoff relationship between gas permeability and ideal selectivity existed, first characterized for a large database of homogenous polymer membranes by the so-called Robeson upper bound in 1991 and revisited in 2008.^{58,59} These upper bounds first demonstrated this inverse relationship for common gas pairs (He, H₂, O₂, CO₂, N₂, and CH₄) and display the best combinations of permeability and selectivity at a given time, thereby setting a standard of comparison for performance metrics of newly developed materials. The majority of the polymers that defined the 2008 upper bound fronts were glassy, high-free volume polymers and perfluoropolymers.⁵⁹ Since 2008, there has been significant research effort and progress in polymers with intrinsic microporosity (PIMs), a class of high-free volume polymers. Researchers involved in the development of these high performing PIMs have defined more recent upper bounds for certain gas pairs based off of their works, such as Swaidan in 2015 for O₂/N₂, H₂/N₂,

and H₂/CH₄ and Comesaña-Gándara in 2019 for CO₂/N₂ and CO₂/CH₄.^{60,61} Figure 2.4 shows the Robeson and Comesaña-Gándara upper bounds for CO₂/CH₄, demonstrating the progress in separation performance over each time frame.^{60–62}

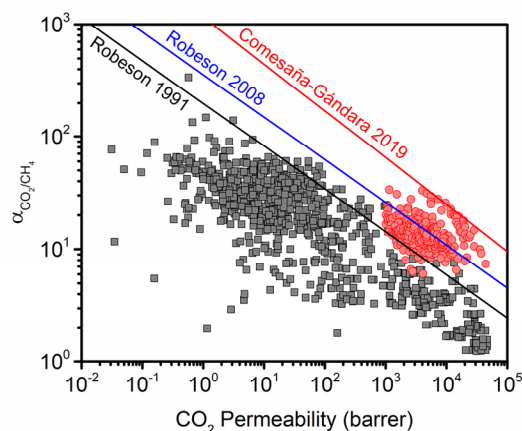


Figure 2.4. Upper bound plot for CO₂/CH₄, for homogenous, solution-processable polymeric materials, showing the separation performance for conventional polymers (gray squares) and PIMs (red circles). The upper bounds established by Robeson in 1991 and 2008 and by Comesaña-Gándara in 2019 are labeled accordingly.^{58,59,61}

It should be noted that surpassing the upper bound should not be considered the end-goal of materials developed for industrial use. The upper bound plots represent pure-gas permeation data under a narrow range of testing conditions (typically 35 °C and 1 atm). These ideal testing conditions are far from those relevant for industrial operating temperatures and pressures. Additionally, separation performance can be significantly different for gas mixtures compared to pure gases, especially those involving condensable gases, due to behaviors such as competitive sorption and swelling effects.³⁶ Finally, permeability is a material property, but permeance is far more adequate in representing properties for materials that can be formed into useful thin-film

geometries.³⁶ While it is encouraging to develop a material with performance that surpasses the upper bound, doing so is only a minor indication of identifying an industrially viable material.

2.3.2.2. Membrane Stability

Another important application consideration is membrane stability to the process conditions over time. An industrially relevant membrane would be able to last three to five years while providing predictable purity for outlet streams.³⁶ These stability issues relate primarily to three categories: plasticization, physical aging, and chemical stability. The first two considerations are essential for viscoelastic polymer-based membranes, and the final consideration is important for all materials.

Plasticization is a phenomenon that occurs when the increasing concentration of a highly sorbing gas (*e.g.*, CO₂, C₂H₄, C₃H₆, etc.) in a polymer matrix causes the polymer to swell, thereby resulting in an increase in diffusion coefficients of all gases present and a corresponding decrease in selectivity.^{63,64} For lab-scale tests, this process is commonly observed when determining permeabilities for incremental increases in pressure. For low pressures, permeability decreases with increasing pressure and eventually reaches a minimum known as the “plasticization pressure” point, followed by an increase in permeability at high penetrant pressures.⁶⁵ Figure 2.5a shows the general shape of a plasticization-pressure curve, indicating significant and measurable plasticization behavior has occurred as a result of a high penetrant concentration of CO₂ in the polymers. Plasticization pressures often occur over a range of gas-phase activities, and the origins of the onset of plasticization is still a matter of debate within the membrane community.^{66–68} Plasticization effects have shown a large effect in many separations of interest, such as CO₂/CH₄ and C₃H₆/C₃H₈, where mixed-gas tests have shown a 2.5 to 10-fold decrease in mixed-gas selectivities compared to their respective ideal selectivities.^{69,70} This effect is further exacerbated

for real gas mixtures; for example, natural gas consists not only of CO₂ and CH₄, but also can contain 5-15% of C₂-C₆ hydrocarbons and up to 500 ppm of benzene, toluene, ethylbenzene, and xylene (BTEX aromatics). At typical pressures for natural gas processing (20-60 bar), these additional contaminants sorb into the polymer and cause significant plasticization and a corresponding loss of selectivity.³⁶ While plasticization pressure tests are a useful first test in studying plasticization, synthetic and real gas mixtures must be tested to ultimately evaluate plasticization behavior.

Another parameter of interest for industrial applications is the rate of physical aging. Physical aging is a phenomenon that affects polymers in their glassy state. Within a solid-state polymer film, frustrated packing, which generally correlates with polymer backbone rigidity, results in a distribution of stochastically fluctuating unoccupied spaces that are known as non-equilibrium free volume elements.⁷¹ Over time, the chains slowly reorder to an equilibrium state, eliminating the excess free volume and thereby decreasing molecular diffusivity and increasing selectivity of permeating species.⁷² Because higher contributions of non-equilibrium free volume can increase diffusion rates, it is no coincidence that many of the polymers defining the recent 2015 and 2019 upper bounds are glassy and possess high fractional free volume.⁶³ In turn, because aging rates scale with excess free volume, many of these highest-performing polymers suffer higher rates of physical aging.⁷¹ This effect is shown in Figure 2.5b, comparing the relative O₂ permeability after 1000 hours (approximately 42 days) to that after 1 h for various glassy polymers. Following the dashed line to guide the eye, it can be seen that, in general, polymers with higher fractional free volume lose permeability much faster than polymers with lower fractional free volume. Perfluoropolymers appear to be a significant anomaly to this trend for unknown reasons,⁷³ but the

development of permanently porous materials is envisioned as an attractive means to form “ageless” membrane materials or to stabilize polymers susceptible to aging.^{74,75}

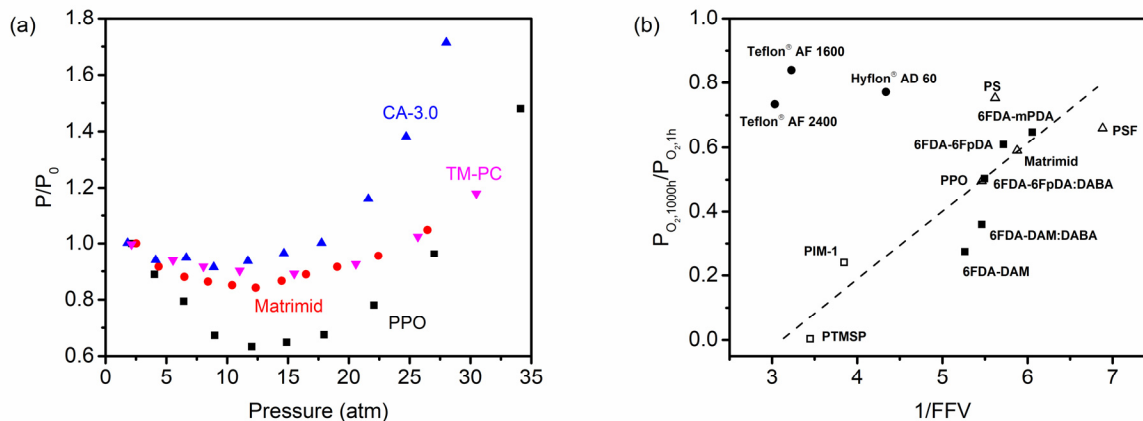


Figure 2.5. (a) Relative permeability (P), with respect to permeability at 1 bar (P_0), as a function of feed pressure of CO_2 for various glassy polymer films. CA-3.0 is cellulose triacetate, TM-PC is tetramethyl bisphenol A polycarbonate, and PPO is poly(2,6-dimethyl-1,4-phenylene oxide). The tests were run at approximately $25^\circ C$ with film thicknesses of approximately $18\text{-}45\ \mu m$.⁶⁶ Adapted from Sanders *et al.*¹ (b) Relative permeability of oxygen after 1000 h ($P_{O_2,1000h}$) with respect to permeability after 1 h ($P_{O_2,1h}$) from film formation for a variety of polymers: high free-volume polymers (\square), polyimides (\blacksquare), commercial polymers (\triangle), and perfluoropolymers (\bullet). The films are approximately 400 nm in thickness with the exception of PTMSP at 700 nm thickness. Adapted from Tiwari *et al.*⁷³

Finally, membranes must be chemically resistant towards potentially damaging process contaminants, such as H_2S in natural gas purification or SO_2 and NO_x in carbon capture applications from flue gas. In these cases, stability tests should be conducted to determine the lifetime of the membrane when exposed to corrosive and acidic gases.^{1,36}

2.4. References

- (1) Sanders, D. F.; Smith, Z. P.; Guo, R.; Robeson, L. M.; McGrath, J. E.; Paul, D. R.; Freeman, B. D. Energy-Efficient Polymeric Gas Separation Membranes for a Sustainable Future: A Review. *Polymer* **2013**, *54* (18), 4729–4761. <https://doi.org/10.1016/j.polymer.2013.05.075>.
- (2) U.S. Department of Energy. *Materials for Separation Technologies: Energy and Emission Reduction Opportunities*; 2005.
- (3) U.S. Energy Information Administration. *Energy Consumption by Sector*; 2019.
- (4) U.S. Energy Information Administration. *International Energy Statistics Database*; 2016.
- (5) Sholl, D. S.; Lively, R. P. Seven Chemical Separations to Change the World. *Nature* **2016**, *532*, 435–437. <https://doi.org/10.1038/532435a>.
- (6) McCoy, M.; Reisch, M. S.; Tullo, A. H.; Tremblay, J.-F.; Voith, M. Output Declines in U.S., Europe. *Chem. Eng. News* **2010**, *88* (27), 54–62.
- (7) Ceresana. *Ethylene Market Report*; 2014.
- (8) Ceresana. *Propylene Market Report*; 2014.
- (9) Wang, Y.; Peh, S. B.; Zhao, D. Alternatives to Cryogenic Distillation: Advanced Porous Materials in Adsorptive Light Olefin/Paraffin Separations. *Small* **2019**, *15* (25), 1–38. <https://doi.org/10.1002/smll.201900058>.
- (10) Campos, A. C. C.; Dos Reis, R. A.; Ortiz, A.; Gorri, D.; Ortiz, I. A Perspective of Solutions for Membrane Instabilities in Olefin/Paraffin Separations: A Review. *Ind. Eng. Chem. Res.* **2018**, *57* (31), 10071–10085. <https://doi.org/10.1021/acs.iecr.8b02013>.
- (11) Smith, Z. P. *Fundamentals of Gas Sorption and Transport in Thermally Rearranged Polyimides*, 2014.
- (12) Compressed Gas Association. *Handbook of Compressed Gases*, 4th ed.; Kluwer Academic Publishers: Norwell, MA, 1999.
- (13) Gunardson, H. *Industrial Gases in Petrochemical Processing: Chemical Industries*; Marcel Dekker, Inc.: New York, NY, 1998.
- (14) Katzenstein, P. *Distillation Resistance: A Quick Cost and Duty Estimation for a Simple Distillation Columns Train*, 2015.
- (15) Chuah, C. Y.; Goh, K.; Yang, Y.; Gong, H.; Li, W.; Karahan, H. E.; Guiver, M. D.; Wang, R.; Bae, T. H. Harnessing Filler Materials for Enhancing Biogas Separation Membranes. *Chem. Rev.* **2018**, *118* (18), 8655–8769. <https://doi.org/10.1021/acs.chemrev.8b00091>.
- (16) Motelica, A.; Bruinsma, O. S. L.; Kreiter, R.; Den Exter, M.; Vente, J. F. Membrane Retrofit Option for Paraffin/Olefin Separation—a Technoeconomic Evaluation. *Ind. Eng. Chem. Res.* **2012**, *51* (19), 6977–6986. <https://doi.org/10.1021/ie300587u>.
- (17) Eldridge, R. B. Olefin/Paraffin Separation Technology: A Review. *Ind. Eng. Chem. Res.* **1993**, *32* (10), 2208–2212. <https://doi.org/10.1021/ie00022a002>.

- (18) Zhu, X.; Li, S.; Shi, Y.; Cai, N. Recent Advances in Elevated-Temperature Pressure Swing Adsorption for Carbon Capture and Hydrogen Production. *Prog. Energy Combust. Sci.* **2019**, *75*. <https://doi.org/10.1016/j.peecs.2019.100784>.
- (19) Yu, J.; Xie, L. H.; Li, J. R.; Ma, Y.; Seminario, J. M.; Balbuena, P. B. CO₂ Capture and Separations Using MOFs: Computational and Experimental Studies. *Chem. Rev.* **2017**, *117* (14), 9674–9754. <https://doi.org/10.1021/acs.chemrev.6b00626>.
- (20) Lee, K. B.; Beaver, M. G.; Caram, H. S.; Sircar, S. Reversible Chemisorbents for Carbon Dioxide and Their Potential Applications. *Ind. Eng. Chem. Res.* **2008**, *47* (21), 8048–8062. <https://doi.org/10.1021/ie800795y>.
- (21) Li, Y.; Liang, F.; Bux, H.; Yang, W.; Caro, J. Zeolitic Imidazolate Framework ZIF-7 Based Molecular Sieve Membrane for Hydrogen Separation. *J. Membr. Sci.* **2010**, *354* (1–2), 48–54. <https://doi.org/10.1016/j.memsci.2010.02.074>.
- (22) Sircar, S. Pressure Swing Adsorption. *Ind. Eng. Chem. Res.* **2002**, *41* (6), 1389–1392. <https://doi.org/10.1021/ie0109758>.
- (23) Hedin, N.; Andersson, L.; Bergström, L.; Yan, J. Adsorbents for the Post-Combustion Capture of CO₂ Using Rapid Temperature Swing or Vacuum Swing Adsorption. *Appl. Energy* **2013**, *104*, 418–433. <https://doi.org/10.1016/j.apenergy.2012.11.034>.
- (24) Dąbrowski, A. Adsorption - From Theory to Practice. *Adv. Colloid Interface Sci.* **2001**, *93* (1–3), 135–224. [https://doi.org/10.1016/S0001-8686\(00\)00082-8](https://doi.org/10.1016/S0001-8686(00)00082-8).
- (25) Kikkinides, E. S.; Yang, R. T.; Cho, S. H. Concentration and Recovery of CO₂ from Flue Gas by Pressure Swing Adsorption. *Ind. Eng. Chem. Res.* **1993**, *32* (11), 2714–2720. <https://doi.org/10.1021/ie00023a038>.
- (26) Prasad, R.; Notaro, F.; Thompson, D. R. Evolution of Membranes in Commercial Air Separation. *J. Membr. Sci.* **1994**, *94*, 225–248.
- (27) Riemer, P. W. F.; Webster, I. C.; Ormerod, W. G.; Audus, H. Results and Full Fuel Cycle Study Plans from the IEA Greenhouse Gas Research and Development Programme. *Fuel* **1994**, *73* (7), 1151–1158. [https://doi.org/10.1016/0016-2361\(94\)90252-6](https://doi.org/10.1016/0016-2361(94)90252-6).
- (28) Barelli, L.; Bidini, G.; Gallorini, F.; Servili, S. Hydrogen Production through Sorption-Enhanced Steam Methane Reforming and Membrane Technology: A Review. *Energy* **2008**, *33* (4), 554–570. <https://doi.org/10.1016/j.energy.2007.10.018>.
- (29) Baker, R. W.; Lokhandwala, K. Natural Gas Processing with Membranes: An Overview. *Ind. Eng. Chem. Res.* **2008**, *47* (7), 2109–2121. <https://doi.org/10.1021/ie071083w>.
- (30) Galizia, M.; Chi, W. S.; Smith, Z. P.; Merkel, T. C.; Baker, R. W.; Freeman, B. D. 50th Anniversary Perspective: Polymers and Mixed Matrix Membranes for Gas and Vapor Separation: A Review and Prospective Opportunities. *Macromolecules* **2017**, *50* (20), 7809–7843. <https://doi.org/10.1021/acs.macromol.7b01718>.
- (31) Hampe, E. M.; Rudkevich, D. M. Exploring Reversible Reactions between CO₂ and Amines. *Tetrahedron* **2003**, *59* (48), 9619–9625. <https://doi.org/10.1016/j.tet.2003.09.096>.

- (32) Bottoms, R. R. Process for Separating Acidic Gases. US Patent 1,834,016, 1931.
- (33) Yu, C. H.; Huang, C. H.; Tan, C. S. A Review of CO₂ Capture by Absorption and Adsorption. *Aerosol Air Qual. Res.* **2012**, *12* (5), 745–769. <https://doi.org/10.4209/aaqr.2012.05.0132>.
- (34) Olajire, A. A. CO₂ Capture and Separation Technologies for End-of-Pipe Applications - A Review. *Energy* **2010**, *35* (6), 2610–2628. <https://doi.org/10.1016/j.energy.2010.02.030>.
- (35) National Academies of Sciences, Engineering, and Medicine. *A Research Agenda for Transforming Separation Science*; The National Academies Press: Washington, DC, 2019. <https://doi.org/10.17226/25421>.
- (36) Baker, R. W.; Low, B. T. Gas Separation Membrane Materials: A Perspective. *Macromolecules* **2014**, *47* (20), 6999–7013. <https://doi.org/10.1021/ma501488s>.
- (37) Van Gelder, J. M. Hydrogen Recovery Made Simple. *Chem. Eng. News* **1979**, *57* (48), 26–27. <https://doi.org/10.1021/cen-v057n048.p026>.
- (38) MarketsandMarkets. *Gas Separation Membranes Market by Material (Polyimide & Polyaramide, Polysulfone, Cellulose Acetate), Application (Nitrogen Generation & Oxygen Enrichment, Hydrogen Recovery, Carbon Dioxide Removal), and Region - Global Forecast to 2022*; 2017.
- (39) Baker, R. W. Future Directions of Membrane Gas Separation Technology. *Ind. Eng. Chem. Res.* **2002**, *41* (6), 1393–1411. <https://doi.org/10.1021/ie0108088>.
- (40) Robeson, L. M. Polymer Membranes. In *Polymer Science: A Comprehensive Reference, 10 Volume Set*; Elsevier B.V., 2012; Vol. 8, pp 325–347. <https://doi.org/10.1016/B978-0-444-53349-4.00211-9>.
- (41) Strathmann, H.; Kock, K.; Amar, P.; Baker, R. W. The Formation Mechanism of Asymmetric Membranes. *Desalination* **1975**, *16* (2), 179–203. [https://doi.org/10.1016/S0011-9164\(00\)82092-5](https://doi.org/10.1016/S0011-9164(00)82092-5).
- (42) Jiang, L.; Chung, T. S.; Li, D. F.; Cao, C.; Kulprathipanja, S. Fabrication of Matrimid/Polyethersulfone Dual-Layer Hollow Fiber Membranes for Gas Separation. *J. Membr. Sci.* **2004**, *240* (1–2), 91–103. <https://doi.org/10.1016/j.memsci.2004.04.015>.
- (43) Li, D. F.; Chung, T. S.; Wang, R.; Liu, Y. Fabrication of Fluoropolyimide/Polyethersulfone (PES) Dual-Layer Asymmetric Hollow Fiber Membranes for Gas Separation. *J. Membr. Sci.* **2002**, *198* (2), 211–223. [https://doi.org/10.1016/S0376-7388\(01\)00658-5](https://doi.org/10.1016/S0376-7388(01)00658-5).
- (44) Merkel, T. C. *Integrated Testing of a Membrane CO₂ Capture Process with a Coal-Fired Boiler*; 2018.
- (45) Coker, D. T.; Freeman, B. D.; Fleming, G. K. Modeling Multicomponent Gas Separation Using Hollow-Fiber Membrane Contactors. *AIChE J.* **1998**, *44* (6), 1289–1302. <https://doi.org/10.1002/aic.690440607>.
- (46) Geankoplis, C. J. *Transport Processes and Separation Process Principles*, 4th ed.; Prentice Hall, 2003.

- (47) Lemanski, J.; Lipscomb, G. G. Effect of Shell-Side Flows on Hollow-Fiber Membrane Device Performance. *AIChE J.* **1995**, *41* (10), 2322–2326. <https://doi.org/10.1017/CBO9781107415324.004>.
- (48) Baker, R. W. *Membrane Technology and Applications*; 2004. <https://doi.org/10.1002/0470020393>.
- (49) Henis, J. M. S. Commercial and Practical Aspects of Gas Separation Membranes. In *Polymeric Gas Separation Membranes*; CRC Press: Boca Raton, FL, 1994.
- (50) Paul, D. R.; Yampolskii, Y. P. *Polymeric Gas Separation Membranes*; CRC Press: Boca Raton, FL, 1994.
- (51) Drioli, E.; Giorno, L. *Membrane Operations: Innovative Separations and Transformations*; Wiley-VCH: Weinheim, 2009.
- (52) Geyer, R.; Jambeck, J. R.; Law, K. L. Production, Use, and Fate of All Plastics Ever Made. *Sci. Adv.* **2017**, *3* (7), 25–29. <https://doi.org/10.1126/sciadv.1700782>.
- (53) Lodge, T. P. Celebrating 50 Years of Macromolecules. *Macromolecules* **2017**, *50* (24), 9525–9527. <https://doi.org/10.1021/acs.macromol.7b02507>.
- (54) Ma, X.; Kumar, P.; Mittal, N.; Khlyustova, A.; Daoutidis, P.; Andre Mkhoyan, K.; Tsapatsis, M. Zeolitic Imidazolate Framework Membranes Made by Ligand-Induced Permselectivation. *Science* **2018**, *361* (6406), 1008–1011. <https://doi.org/10.1126/science.aat4123>.
- (55) US Department of Energy Basic Energy Sciences Workshop for Carbon Capture. *Basic Research Needs for Carbon Capture: Beyond 2020*; 2010.
- (56) Merkel, T. C.; Lin, H.; Wei, X.; Baker, R. Power Plant Post-Combustion Carbon Dioxide Capture: An Opportunity for Membranes. *J. Membr. Sci.* **2010**, *359* (1–2), 126–139. <https://doi.org/10.1016/j.memsci.2009.10.041>.
- (57) Alcheikhhamdon, Y.; Pinnau, I.; Chen, B.; Hoorfar, M. Propylene - Propane Separation Using Zeolitic-Imidazolate Framework (ZIF-8) Membranes: Process Techno-Commercial Evaluation. *J. Membr. Sci.* **2019**. <https://doi.org/10.1016/j.memsci.2019.117252>.
- (58) Robeson, L. M. Correlation of Separation Factor versus Permeability for Polymeric Membranes. *J. Membr. Sci.* **1991**, *62* (2), 165–185. [https://doi.org/10.1016/0376-7388\(91\)80060-J](https://doi.org/10.1016/0376-7388(91)80060-J).
- (59) Robeson, L. M. The Upper Bound Revisited. *J. Membr. Sci.* **2008**, *320* (1–2), 390–400. <https://doi.org/10.1016/j.memsci.2008.04.030>.
- (60) Swaidan, R.; Ghanem, B.; Pinnau, I. Fine-Tuned Intrinsically Ultramicroporous Polymers Redefine the Permeability/Selectivity Upper Bounds of Membrane-Based Air and Hydrogen Separations. *ACS Macro Lett.* **2015**, *4* (9), 947–951. <https://doi.org/10.1021/acsmacrolett.5b00512>.
- (61) Comesaña-Gándara, B.; Chen, J.; Bezzu, C. G.; Carta, M.; Rose, I.; Ferrari, M. C.; Esposito, E.; Fuoco, A.; Jansen, J. C.; McKeown, N. B. Redefining the Robeson Upper Bounds for

- CO₂/CH₄ and CO₂/N₂ Separations Using a Series of Ultraparpermeable Benzotriptycene-Based Polymers of Intrinsic Microporosity. *Energy Environ. Sci.* **2019**, *12* (9), 2733–2740. <https://doi.org/10.1039/c9ee01384a>.
- (62) Robeson, L. M.; Dose, M. E.; Freeman, B. D.; Paul, D. R. Analysis of the Transport Properties of Thermally Rearranged (TR) Polymers and Polymers of Intrinsic Microporosity (PIM) Relative to Upper Bound Performance. *J. Membr. Sci.* **2017**, *525*, 18–24. <https://doi.org/10.1016/j.memsci.2016.11.085>.
- (63) Pixton, M. R.; Paul, D. R. Relationships between Structure and Transport Properties for Polymers with Aromatic Backbones. In *Polymeric Gas Separation Membranes*; CRC Press: Boca Raton, FL, 1994; pp 83–154.
- (64) Petropoulos, J. H. Mechanisms and Theories for Sorption and Diffusion of Gases in Polymers. In *Polymeric Gas Separation Membranes*; CRC Press: Boca Raton, FL, 1994; pp 17–82.
- (65) Horn, N. R.; Paul, D. R. Carbon Dioxide Plasticization and Conditioning Effects in Thick vs. Thin Glassy Polymer Films. *Polymer* **2011**, *52* (7), 1619–1627. <https://doi.org/10.1016/j.polymer.2011.02.007>.
- (66) Wessling, M.; Strathmann, H.; Bos, A.; Pu, I. G. M. CO₂ -Induced Plasticization Phenomena in Glassy Polymers. **1999**, *155*, 67–78.
- (67) Swaidan, R.; Ghanem, B.; Litwiller, E.; Pinnau, I. Physical Aging, Plasticization and Their Effects on Gas Permeation in “Rigid” Polymers of Intrinsic Microporosity. *Macromolecules* **2015**, *48* (18), 6553–6561. <https://doi.org/10.1021/acs.macromol.5b01581>.
- (68) He, Y.; Benedetti, F. M.; Lin, S.; Liu, C.; Zhao, Y.; Ye, H.-Z.; Voorhis, T. Van; Angelis, M. G. De; Swager, T. M.; Smith, Z. P. Polymers with Side Chain Porosity for Ultraparpermeable and Plasticization Resistant Materials for Gas Separations. *Adv. Mater.* **2019**. <https://doi.org/10.1002/adma.201807871>.
- (69) Donohue, M. D.; Minhas, B. S.; Lee, S. Y. Permeation Behavior of Carbon Dioxide-Methane Mixtures in Cellulose Acetate Membranes. *J. Membr. Sci.* **1989**, *42* (3), 197–214. [https://doi.org/10.1016/S0376-7388\(00\)82376-5](https://doi.org/10.1016/S0376-7388(00)82376-5).
- (70) Merkel, T. C.; Pinnau, I.; Prabhakar, R. S.; Freeman, B. D. Gas and Vapor Transport Properties of Perfluoropolymers. In *Materials Science of Membranes for Gas and Vapor Separation*; 2006; pp 251–270.
- (71) Struik, L. C. E. Physical Aging in Polymers and Other Amorphous Materials. **1978**, *17* (3).
- (72) Rowe, B. W.; Freeman, B. D.; Paul, D. R. Physical Aging of Ultrathin Glassy Polymer Films Tracked by Gas Permeability. *Polymer* **2009**, *50* (23), 5565–5575. <https://doi.org/10.1016/j.polymer.2009.09.037>.
- (73) Tiwari, R. R.; Smith, Z. P.; Lin, H.; Freeman, B. D.; Paul, D. R. Gas Permeation in Thin Films of “High Free-Volume” Glassy Perfluoropolymers: Part I. Physical Aging. *Polymer* **2014**, *55* (22), 5788–5800. <https://doi.org/10.1016/j.polymer.2014.09.022>.
- (74) Lau, C. H.; Konstas, K.; Doherty, C. M.; Kanehashi, S.; Ozcelik, B.; Kentish, S. E.; Hill, A.

- J.; Hill, M. R. Tailoring Physical Aging in Super Glassy Polymers with Functionalized Porous Aromatic Frameworks for CO₂ Capture. *Chem. Mater.* **2015**, *27* (13), 4756–4762. <https://doi.org/10.1021/acs.chemmater.5b01537>.
- (75) Lau, C. H.; Konstas, K.; Thornton, A. W.; Liu, A. C. Y.; Mudie, S.; Kennedy, D. F.; Howard, S. C.; Hill, A. J.; Hill, M. R. Gas-Separation Membranes Loaded with Porous Aromatic Frameworks That Improve with Age. *Angew. Chemie Int. Ed.* **2015**, *54* (9), 2669–2673. <https://doi.org/10.1002/anie.201410684>.

Chapter 3: Materials and Experimental Methods

This chapter has been adapted from sections of: (1) Wu, A. X.; Drayton, J. A.; Rodriguez, K. M.; Qian, Q.; Lin, S.; Smith, Z. P. Influence of Aliphatic and Aromatic Fluorine Groups on Gas Permeability and Morphology of Fluorinated Polyimide Films. *Macromolecules* **2020**, *53* (13), 5085–5095.; (2) Wu, A. X.; Drayton, J. A.; Mizrahi Rodriguez, K.; Benedetti, F. M.; Qian, Q.; Lin, S.; Smith, Z. P. Elucidating the Role of Fluorine Content on Gas Sorption Properties of Fluorinated Polyimides. *Macromolecules* **2021**, *54* (1), 22–34.; (3) Wu, A. X.; Drayton, J. A.; Ren, X.; Mizrahi Rodriguez, K.; Grosz, A. F.; Lee, J. -W.; Smith, Z. P. Non-Equilibrium Lattice Fluid Modeling of Gas Sorption for a Series of Fluorinated Poly(Ether Imide) Membranes. *Submitted*.

3.1. Monomer and Polymer Synthesis

3.1.1. 6FDA-6HpDA, 6FDA-6FpDA, 6FDA-OHB, and 6FDA-OFB Polyimide Synthesis

The dianhydride monomer, 2,2'-bis(3,4-dicarboxyphenyl) hexafluoropropane dianhydride (6FDA, Chem-Impex International, Wood Dale, IL), was purified via vacuum sublimation at 235 °C. Two of the diamines, 2,2-bis(4-aminophenyl)propane (6HpDA, Matrix Scientific, Columbia, SC) and 2,2-bis(4-aminophenyl)hexafluoropropane (6FpDA, TCI America, Portland, OR), were purified via vacuum sublimation at 115 °C and 185 °C, respectively. The hydrocarbon-based diamine, 4,4'-diaminobiphenyl (OHB, MilliporeSigma, St. Louis, MO), was purified via recrystallization (dissolved at 1 g / 100 mL H₂O at 100 °C then cooled to room temperature), and its fluorinated structural analogue, 4,4'-diaminooctafluorobiphenyl (OFB, TCI America, Portland, OR), was used as received. Anhydrous 1-methyl-2-pyrrolidinone (NMP, MilliporeSigma, St. Louis, MO) was used as received.

The polyimides were synthesized through a two-stage procedure shown in Figure 3.1. The first stage is synthesizing a poly(amic acid) and the second stage is forming a polyimide. For the first stage, a mechanical stirrer was attached to a 250 mL round-bottom three-neck flask, and the flask was purged with flowing N₂. The diamine (6 mmol) and NMP (10 mL) were added to the flask and stirred vigorously to dissolution. An equimolar amount of dianhydride (6 mmol) and additional anhydrous NMP (11 mL) were then added, resulting in a 20% w/v solution. The reaction solution was then stirred at 150 rpm and, for all samples except 6FDA-OFB, held at room temperature for 24 h to form the poly(amic acid). In the case of 6FDA-OFB, the three-neck flask was placed in a silicone oil bath and the reaction was run at 180 °C for 5 h, following a procedure outlined by Hougham *et al.*¹ During the course of the 6FDA-6HpDA and 6FDA-OHB polymerizations, an additional 10 and 15 mL of NMP were added to the reaction solution, respectively, to reduce solution viscosity.

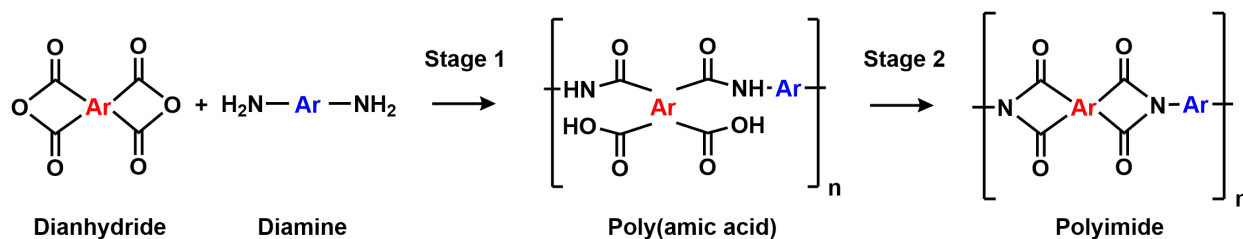


Figure 3.1. General two-stage synthesis procedure for forming polyimide films. For these polymers, the dianhydride is always 6FDA, and the diamine was varied. **Ar** represents aromatic units.

3.1.2. 10FEDA Monomer Synthesis

The perfluorinated dianhydride monomer, 1,4-bis(3,4-dicarboxytrifluorophenoxy)tetrafluorobenzene (10FEDA), was synthesized using the procedure described below. Tetrafluorohydroquinone (TFHQ, TCI America, Portland, OR, USA) was

purified via vacuum sublimation at 160 °C and tetrafluorophthalonitrile (TFPN, TCI America, Portland, OR, USA) was used as received. The hydrogen dianhydride monomer, 1,4-bis(3,4-dicarboxyphenoxy)benzene dianhydride (10HEDA), was purchased from Marshallton Research Laboratories Inc. (King, NC, USA) and used as received. The hydrogen diamine, m-phenylenediamine (MPD, MilliporeSigma, St. Louis, MO, USA) was purified via recrystallization (2 g / 4 mL H₂O at 25 °C) and the fluorinated diamine, 2,3,5,6-tetrafluoro-1,4-phenylenediamine (TFMPD, TCI America, Portland, OR, USA), was purified via vacuum sublimation at 130 °C. Dimethylformamide (DMF, MilliporeSigma, St. Louis, MO, USA), triethylamine (Et₃N, MilliporeSigma, St. Louis, MO, USA), 2.0 M hydrochloric acid (HCl, MilliporeSigma, St. Louis, MO, USA), toluene (MilliporeSigma, St. Louis, MO, USA), sulfuric acid (H₂SO₄, 99.99%, MilliporeSigma, St. Louis, MO, USA), xylenes (MilliporeSigma, St. Louis, MO, USA), acetic anhydride (AcAn, MilliporeSigma, St. Louis, MO, USA), petroleum ether (MilliporeSigma, St. Louis, MO, USA), and dimethylacetamide (DMAc, MilliporeSigma, St. Louis, MO, USA) were used as received.

The 10FEDA monomer synthesis consists of three steps adapted from Ando *et al.*²⁻⁴, summarized in Figure 3.2 below. The bisphthalonitrile precursor (10FEDP) is first formed by the aromatic nucleophilic substitution of TFHQ and TFPN in base. Next, 10FEDP is hydrolyzed to form a tetracarboxylate in step 2, which is finally dehydrated into the 10FEDA dianhydride in step 3.

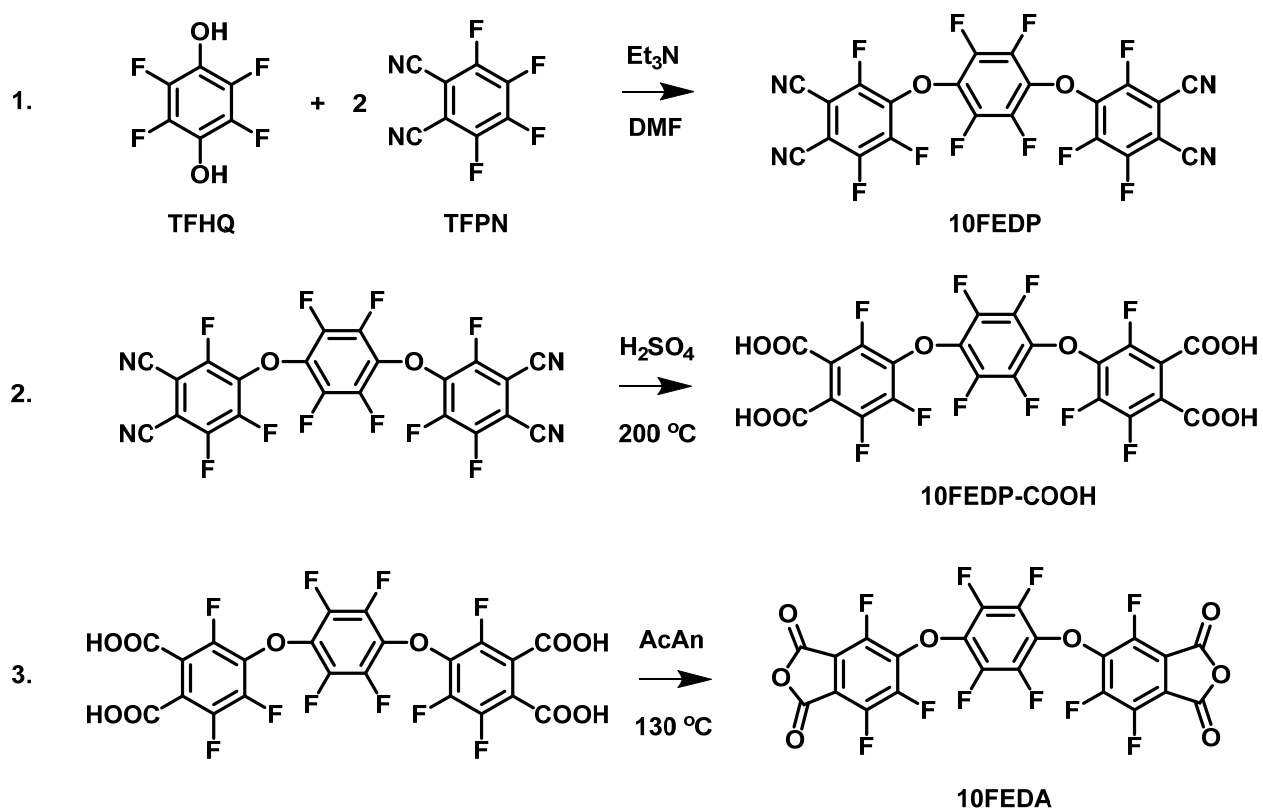


Figure 3.2. Synthetic pathway to synthesize 10FEDA from TFHQ and TFPN.

10FEDP Synthesis. 1.82 g of TFHQ (10 mmol), 8.0 g of TFPN (40 mmol), and 40 mL of DMF were added into a 100 mL round bottom flask with a magnetic stir bar. The mixture was stirred until all solids were dissolved and the flask was immersed in an ice bath. The ice bath was found to improve yield. A syringe pump was set up to add 2.8 mL of Et₃N (20 mmol) dropwise into the solution over 20 minutes (0.14 mL/min). The reaction solution was then stirred for 10 more minutes on ice (30 minutes total), after which the ice bath was removed and the reaction was stirred at room temperature for an additional 1.5 hours. The solution was poured into a 0.4 M HCl solution (200 mL) in an Erlenmeyer flask, resulting in a cloudy, white solution and an oily precipitate. The white solution was decanted and the oily precipitate was washed twice with deionized water. The precipitate was left to dry in the flask overnight at 60 °C, resulting in off-white crystals. As-

synthesized 10FEDP was purified in the same flask via recrystallization in toluene by heating to 110 °C and cooling to room temperature. The resulting 2.26 g (4.2 mmol, 42% yield) of white powder was collected via vacuum filtration and dried in the oven overnight at 60 °C.

10FEDP Hydrolysis to 10FEDP-COOH. 2.26 g of 10FEDP and 40 mL of 60%/40% H₂SO₄/deionized water was added into a 100 mL round bottom flask with a magnetic stir bar. The flask was connected to a water condenser, placed in an oil bath and heated to 200 °C. An initial stir rate of approximately 900 rpm was required to initiate good mixing of the solids in the liquid, then the stirring rate was reduced to 300 rpm. After 4 hours, the mixture was cooled to room temperature and deionized water was slowly added into the reaction solution to induce precipitation of the product. A gray-white product (2.11 g, 3.4 mmol, 82% yield) was collected via vacuum filtration using glass microfiber fiber paper (Cytiva Whatman GF/C, Marlborough, MA), washed with deionized water, and dried in the oven overnight at 60 °C.

Dehydration of 10FEDP-COOH to 10FEDA. 2.11 g of 10FEDP-COOH, 20 mL of xylenes, and 3.2 mL of AcAn (34 mmol) were added with a magnetic stir bar to a 50 mL round bottom flask. The flask was connected to a water condenser, placed in an oil bath, heated at 130 °C and stirred at 300 rpm for 2 hours, and then cooled to room temperature. Petroleum ether was slowly added to the reaction solution to induce precipitation of the final product. The white powder product (1.82 g, 3.1 mmol, 92% yield) was collected via vacuum filtration, dried under full vacuum at 60 °C, and stored under vacuum. The overall yield of 10FEDA was 31% with respect to the starting reagents.

3.1.3. 10HEDA-MPD, 10HEDA-TFMPD, 10FEDA-MPD, and 10FEDA-TFMPD Poly(Ether Imide) Synthesis

The poly(ether imide)s were synthesized through the same general two-step procedure shown in Figure 3.1. In the first step to create the poly(amic acid), the center joint of a 100 mL three-neck round bottom flask was attached to a Schlenk line. A magnetic stir bar was put inside and the joints were sealed using rubber septa. The flask was evacuated to full vacuum and filled with flowing N₂, cycled three more times, and left under flowing N₂ for the remainder of the synthesis. For the two 10FEDA-based polymers, equimolar amounts of dianhydride (3 mmol) and diamine (3 mmol) were separately dissolved in 5.5 mL of DMAc each. The diamine solution was injected into the flask through the rubber septum, followed by the dianhydride solution to make a 20% w/v solution (11 mL total volume). The flask was then covered with aluminum foil to prevent potential MPD monomer decomposition and left to stir for 3 days at room temperature. For the two 10HEDA-based polymers, 3 mmol of 10HEDA was dissolved in 15 mL of DMAc by stirring at 80 °C overnight. An equimolar amount of diamine (3 mmol) was separately dissolved in 4 mL DMAc. The two solutions were mixed following the same procedure as above, resulting in a 9.3% w/v solution. The 10HEDA-TFMPD polymerization was performed at 80 °C to encourage higher molecular weight. All other syntheses were performed at room temperature.

3.2. Film Casting

A procedure first reported by Hougham *et al.* was followed for imidization and film formation.¹ For the 6FDA-based polyimides, ~0.1 g of polymer from the poly(amic acid) solution was mixed with NMP to form a 2% w/v dilute solution. The casting solution was filtered through a 5.0 µm Whatman PTFE syringe filter (GE Life Sciences, Pittsburgh, PA) into a 5 cm diameter glass Petri dish (DWK Life Sciences, Germany) and placed inside a vacuum oven. Vacuum was applied (25

inHg) to the solution for 30 min at room temperature to remove dissolved gases, and then the oven was set to 60 °C for 16 h to facilitate slow removal of solvent. A light, constant dynamic vacuum was applied throughout the course of solvent evaporation to remove solvent from the headspace of the vacuum oven. The poly(amic acid) film was then transferred to a tube furnace (Carbolite Gero HST 12/900, Newtown, PA), and heated under a N₂ atmosphere at 1 °C/min to 350 °C, held for 1 h, and then slowly cooled to room temperature. The resultant polyimide films of ~30 μm thickness were then detached from the Petri dish with the assistance of deionized water.

For the 10HEDA- and 10FEDA-based poly(ether imide)s, the above procedure was modified to use DMAc as the casting solvent. After placing the petri dish inside the vacuum oven, a 16 h dynamic vacuum was applied (25 inHg) to the casting solution for slow removal of solvent at room temperature. The same tube furnace curing procedure was used to imidize the film, resulting in poly(ether imide) films of approximately 30 μm thickness.

3.3. Characterization Methods

3.3.1. Pure-gas Permeation Measurements

Helium, hydrogen, oxygen, nitrogen, methane, and carbon dioxide gases (UHP grade, Airgas, Radnor, PA) were used as received. Pure-gas permeation tests at 15 psi for He, H₂, O₂, N₂, CH₄, and CO₂ at temperatures ranging from 35 to 65 °C were performed in an automated constant-volume, variable-pressure system designed by Maxwell Robotics. A small portion (~1 cm²) was cut from the film and its thickness measured by using a Mitutoyo Series 293 micrometer (Mitutoyo America Corporation, Aurora, IL). Next, the film was placed over the hole in a brass washer and attached to the washer using Loctite EA E-214HP epoxy (Henkel, Rocky Hill, CT, USA). To cure the epoxy, the prepared sample was heated in a convection oven at 150 °C for 2 h. The sample was

then sealed inside a stainless steel permeation cell. The cell and the entire permeation testing chamber were submerged in a constant-temperature water bath controlled by an immersion circulator (Thermo Fischer SC150 L). All samples were held under vacuum for at least 8 h in the cell prior to testing to remove dissolved atmospheric gases, and a downstream volume of 40.0 cm³ was used for all tests. When changing between gases, a 1 bar helium flush followed by dynamic vacuum was applied to clear out residual gas inside the system. The duration of dynamic vacuum applied upstream and downstream of the membrane was greater than six time lag equivalents for all gas–polymer pairs. The permeability was calculated as shown in Equation 3.1 below:

$$P = 10^{-10} \frac{Vl}{p_2ART} \left[\left(\frac{dp}{dt} \right)_{ss} - \left(\frac{dp}{dt} \right)_{leak} \right] \quad (3.1)$$

where P is the permeability (barrer), V is the downstream volume (cm³), l is the membrane thickness (cm), p_2 is the upstream feed pressure (cmHg), A is the film area available for permeation (cm²), R is the gas constant (0.278 cmHg cm³ cm⁻³(STP) K⁻¹), T is the temperature (K), $(dp/dt)_{ss}$ (cmHg s⁻¹) is the steady-state change in pressure in the downstream volume during the experiment, and $(dp/dt)_{leak}$ (cmHg s⁻¹) is the leak rate under vacuum.⁵

Diffusion coefficients were estimated through a time-lag analysis of the permeation data, as shown in Equation 3.2 below:

$$D = \frac{l^2}{6\theta} \quad (3.2)$$

where D is the diffusion coefficient (cm² s⁻¹), l is the film thickness (cm), and θ is the time lag. Through the sorption–diffusion model, the sorption coefficient can then be estimated as the quotient of permeability and the diffusion coefficient.⁵

3.3.2. Pure-gas Sorption Measurements

Pure-gas sorption tests were performed for He, H₂, O₂, N₂, CH₄, and CO₂ at temperatures ranging from 35 °C to 65 °C using an automated dual-volume, dual-transducer pressure decay system purchased from Maxwell Robotics. The high-pressure and low-pressure charge volumes were 8.40 and 8.32 cm³, respectively, with a sample volume of 2.849 cm³, calibrated by volume expansion from an external volume measured by a Brunauer-Emmett-Teller machine. For O₂, N₂, CH₄, and CO₂, isotherms were measured up to 40 atm, and for He and H₂, isotherms were measured up to 3 atm due to suspected permeation through polytetrafluoroethylene (PTFE) valve stem tips that could occur in our system at higher pressures, which would result in artificially high measured sorption. Approximately 0.2 g to 0.5 g of polymer film, averaging 30 μm in thickness, was cut into approximately 0.75 cm by 1.5 cm rectangles, loaded into the sample chamber and sealed tightly using VCR gaskets. Prior to testing, all samples were held under vacuum for at least 8 hours inside the sample chamber to remove any dissolved atmospheric gases. The system used a constant-temperature water bath controlled by an immersion circulator (Thermo Fischer SC150 L). Sorption isotherms were determined by calculating the moles of sorbed gas at each equilibrium pressure by applying a mass balance between the initial pressure of gas charged and the equilibrium pressure after a designated hold time at each step. The second virial coefficient equation of state was used to correct for non-ideal gas behavior.^{5,6} Equilibration hold times varied for each gas and polymer, ranging from 0.5 h for He and H₂ to 8 h for CH₄. After measuring the sorption isotherm of one gas, the sample was held under vacuum for a hold time equal to that used for the prior gas before starting the next gas. In the case of CO₂, the sample was replaced after each isotherm to avoid conditioning effects.

3.3.3. Physical and Chemical Characterization

The materials were characterized through a variety of techniques. A Thermo Fisher FTIR6700 Fourier-transform infrared (FTIR) spectrometer in attenuated total reflection (ATR) mode, scanning from 400 to 4000 cm^{-1} , was used for functional group characterization. A SAXSLAB instrument containing a Rigaku 002 microfocus X-ray source and a DECTRIS PILATUS3 R 300K detector was used to perform wide-angle X-ray scattering (WAXS) tests to determine the average *d*-spacing of the polymers. The glass transition temperature (T_g) was determined by using a TA Instruments DSC 250 differential scanning calorimeter (DSC), cycling from 25 °C to 400 °C at 10 °C/min, and evaluating the third scan. The molecular weights of the poly(amic acid)s were evaluated relative to a polystyrene standard by using a gel permeation chromatography (GPC) system from Waters with a mobile phase of dimethylformamide (DMF) with 0.01 M lithium bromide. The samples for GPC were prepared at a concentration of 5 mg/mL polymer to DMF. The density of the films was determined from Archimedes' principle with water as the buoyant liquid using a density measurement kit from Mettler Toledo (ME-DNY-4). ^{19}F nuclear magnetic resonance (NMR) in DMSO- d_6 (Cambridge Isotope Laboratories, Tewksbury, MA, USA) on a 400 MHz Bruker instrument was used to verify the chemical structure of 10FEDA and its intermediates.

3.4. References

- (1) Hougham, G.; Tesoro, G.; Shaw, J. Synthesis and Properties of Highly Fluorinated Polyimides. *Macromolecules* **1994**, *27* (13), 3642–3649. <https://doi.org/10.1021/ma00091a028>.
- (2) Ando, S.; Matsuura, T.; Sasaki, S. Synthesis and Properties of Perfluorinated Polyimides. In *Fluoropolymers 2: Properties*; Plenum Press: New York, 1999; pp 277–303.
- (3) Ando, S.; Matsuura, T.; Sasaki, S.; Yamamoto, F. Method for Preparing Aromatic Compounds. US Patent 6,048,986, 2000.

- (4) Ando, S.; Matsuura, T.; Sasaki, S. Perfluorinated Polyimide Synthesis. *Macromolecules* **1992**, *25* (21), 5858–5860. <https://doi.org/10.1021/ma00047a045>.
- (5) Lin, H.; Freeman, B. D. Permeation and Diffusion. In *Springer-Handbook of Materials Measurement Methods*; 2006.
- (6) Dymond, J. H.; Marsh, K. N.; Wilhoit, R. C.; Wong, K. C. *The Virial Coefficients of Pure Gases and Mixtures: Subvolume A*; 2001.

Chapter 4: The Perfluoropolymer Upper Bound

Abstract

Perfluoropolymers have fundamentally distinct thermodynamic partitioning properties compared to their hydrocarbon counterparts. However, current upper bound theory assumes hydrocarbon solubility behavior for all polymers. Herein, the fundamental presupposition of invariance in solubility behavior to upper bound performance is critically assessed for perfluoropolymers and hydrocarbon polymers. By modifying solubility relationships, theoretical perfluoropolymer upper bounds are established, showing a positive shift of the upper bound front as a result of beneficial solubility selectivities for certain gas pairs, including N_2/CH_4 , He/H_2 , He/N_2 , He/CH_4 , and He/CO_2 . Within the framework of the solution-diffusion model, an analysis is presented to compare two independent approaches often pursued in efforts to surpass the polymer upper bound: (1) achieving solubility selectivity via perfluoropolymers and (2) improving diffusion selectivity via rigid hydrocarbon polymers. This analysis demonstrates the significant benefit that can be achieved by considering both the chemical composition and morphology of solid-state macromolecules when designing membrane materials.

This chapter has been adapted from: Wu, A. X.; Drayton, J. A.; Smith, Z. P. The Perfluoropolymer Upper Bound. *AIChE J.* **2019**, *65* (12), e16700.

4.1. Introduction

A major challenge preventing membranes from wider industrial deployment is a general tradeoff between gas permeability and selectivity, which is described empirically by the so-called Robeson upper bound.¹ First established in 1991 and revisited in 2008, the upper bound showed this general inverse relationship for many common gas pairs and described the best performing materials at the time, thereby setting a standard of comparison for newly developed materials.^{1,2} A theoretical analysis by Freeman revealed two pathways to surpass current limitations in membrane performance; namely, improving diffusion selectivity and/or improving sorption selectivity.³ Since then, researchers have focused predominantly on creating novel materials to improve diffusion selectivity,⁴⁻⁷ whereas far fewer efforts have been expended on sorption selectivity.^{8,9}

Perfluoropolymers are an unusual class of polymeric materials with performance characteristics that define the upper bound front for several gas pairs. These polymers have C-F bonds instead of the more typical C-H bonds, a distinct chemical feature that influences polymer-penetrant interactions. Within the solution-diffusion framework, these modifications to polymer-penetrant interactions alter sorption selectivities, and hence, permselectivities, thereby shifting upper bound performance for certain separations.¹⁰ Readers are directed to a book chapter by Merkel that expounds on the unique solubility characteristics of perfluoropolymers and recounts a brief history of research efforts in this area.¹¹ In the time span between the publication of the first upper bound database in 1991 and the revisited database in 2008, a variety of new perfluoropolymers had been tested. Robeson noted that perfluoropolymers showed the highest combinations of permeability and selectivity for all He- and many CH₄-based separations, and suggested that the unique solubility behavior of perfluoropolymers was responsible for these findings.²

The majority of publications on novel membrane materials development in the past 30 years have focused on improving performance via diffusion selectivity by simultaneously creating stiffer polymer backbones and increasing interchain spacing, thus following the materials design strategy originally proposed by Freeman.³ Although still profitable for the development of fundamental science, practically, improvements in diffusion selectivity often result in reduced mechanical integrity and increased physical aging rates.^{12,13} Therefore, this work aims to highlight potential improvements in transport properties by considering solubility selectivity as a primary consideration. Results suggest that this approach offers the ability to surpass current limitations in materials performance while simultaneously circumventing some of the key challenges associated with diffusion-selective polymers mentioned above. To this end, the permeability and selectivity of hydrocarbon polymers, partially fluorinated polymers, and perfluoropolymers were collected from literature sources. Upper bounds for non-perfluoropolymers (*i.e.*, hydrocarbon and partially fluorinated species) are established and shifted according to the theoretical framework developed by Freeman but now allowing the underlying assumption of fixed hydrocarbon solubility selectivity to be relaxed.

4.2. Theory & Background

Membrane separation performance is typically evaluated by determining the permeability and selectivity of certain gases in a polymer. Permeability is defined as the flux of gas through the membrane normalized by the pressure differential across the membrane and the thickness of the membrane:

$$P = \frac{Nl}{\Delta p} \quad (4.1)$$

where P is the permeability of a gas, N is the molar flux through the membrane, l is the membrane thickness, and Δp is the pressure differential.¹⁴

Permeability is commonly expressed in units of barrer:

$$1 \text{ barrer} = 10^{-10} \frac{\text{cm}^3(\text{STP}) \cdot \text{cm}}{\text{cm}^2 \cdot \text{s} \cdot \text{cmHg}} = 3.35 \times 10^{-16} \frac{\text{mol} \cdot \text{m}}{\text{m}^2 \cdot \text{s} \cdot \text{Pa}} \quad (4.2)$$

Gas transport through polymeric membranes is commonly described via the solution-diffusion model. Within this theoretical framework, gases sorb into the upstream face of the membrane, diffuse across the membrane along a chemical potential gradient, and then desorb from the downstream face of the membrane. From this model, permeability can be represented as the product of an effective diffusion coefficient, D , and the equilibrium sorption or solubility coefficient, S .¹⁰

$$P = D \times S \quad (4.3)$$

The units for D and S are traditionally $\text{cm}^2 \text{ s}^{-1}$ and $\text{cm}^3(\text{STP}) \text{ cm}^{-3} \text{ cmHg}^{-1}$ respectively.

The ideal selectivity for a gas pair is defined as the permeability ratio of the faster permeating gas, A, to that of the slower permeating gas, B. Using the solution-diffusion model, the ideal selectivity, α , can be written as the product of diffusion selectivity and solubility selectivity:

$$\alpha_{A/B} = \frac{P_A}{P_B} = \frac{D_A S_A}{D_B S_B} \quad (4.4)$$

As mentioned previously, a major challenge in membrane separations is the inverse relationship between permeability and selectivity, which is clearly apparent from the Robeson upper bound.^{1,2}

As exemplified for He/H₂ separation in Figure 4.1, an upper bound plot is a log-log plot of permeability and selectivity that is populated with experimental performance data for a variety of

polymers. Describing the best-performing materials at the time, Robeson established empirical upper bounds for common gas pairs involving He, H₂, O₂, N₂, CO₂, and CH₄ using the following mathematical form:

$$P_A = k\alpha_{A/B}^n \quad (4.5.1)$$

where n and k are the slope and front factor, respectively. Robeson identified a linear relationship between n and the difference in the kinetic diameters of each gas pair.¹

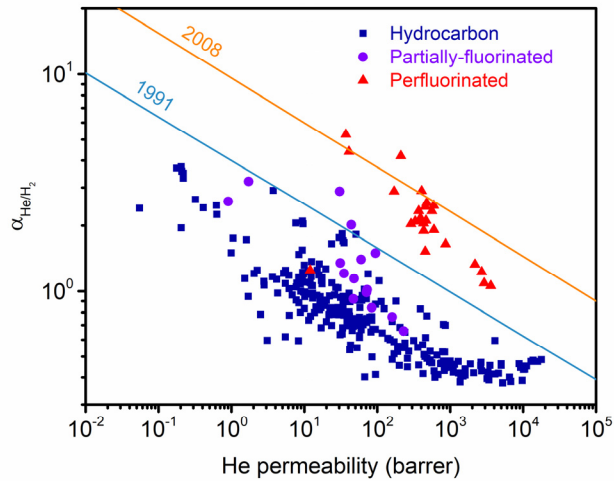


Figure 4.1. Example upper bound plot for He/H₂ separation. The 1991 and 2008 upper bound lines illustrate the trade-off between permeability and selectivity.^{1,2}

In 1999, Freeman derived a theoretical expression for the upper bound that matched the empirical mathematical expression originally proposed by Robeson.³ Freeman's approach was based on the solution-diffusion model and activated diffusion theory,^{15,16} defining the slope and front factor in terms of penetrant and polymer properties.³ Freeman used an equivalent form of the upper bound relationship:

$$\alpha_{A/B} = \frac{\beta_{A/B}}{P_A^{\lambda_{A/B}}} \quad (4.5.2)$$

where $\lambda_{A/B}$ and $\beta_{A/B}$ are altered forms for the slope and front factor, respectively.

The slope was derived to be:

$$\lambda_{A/B} = -\frac{1}{n} = \left(\frac{d_B}{d_A}\right)^2 - 1 = \left(\frac{d_B + d_A}{d_A^2}\right)(d_B - d_A) \quad (4.6)$$

where d_A and d_B are the gas kinetic diameters, suggesting that the upper bound slope is exclusively dependent on the gas pair and not on any characteristics intrinsic to the polymer. This result is consistent with the aforementioned observation originally described by Robeson.¹

The front factor was derived to be:

$$\beta_{A/B} = k^{-\frac{1}{n}} = \frac{S_A}{S_B} S_A^{\lambda_{A/B}} \exp\left(-\lambda_{A/B} \left(b - f \frac{1-a}{RT}\right)\right) \quad (4.7)$$

where S_A and S_B are the solubility coefficients for gases A and B, and a , b , and f are parameters resulting from the application of activated diffusion theory.

To estimate the solubility and solubility selectivity (S_A/S_B) of gas in the polymer, penetrant partitioning is viewed as a two-step process, consisting of a condensation-like step of the gas adsorbing onto the polymer followed by mixing of the penetrant into the polymer matrix.^{10,17} These effects can be generalized by correlating the sorption of penetrants with some thermodynamic potential, such as the Lennard-Jones well depth of a penetrant, ε_A/k :¹⁴

$$\ln(S_A) = M + N \frac{\varepsilon_A}{k} \quad (4.8)$$

where M and N are parameters fit from experimental data on solubility for various penetrants. Freeman used values of $M = -9.84$ and $N = 0.023$ for all polymers, in units of $\text{cm}^3(\text{STP}) \text{cm}^{-3} \text{cmHg}^{-1}$, based on established correlations for hydrocarbon species.

The other parameters, a , b , and f , are a result of the application of activated diffusion theory, using Arrhenius behavior to describe the diffusion coefficient based on the activation energy of diffusion, E_D , an Arrhenius prefactor, D_0 , the ideal gas constant, R , and absolute temperature, T :¹⁵

$$D_A = D_{0,A} \exp\left(-\frac{E_{D,A}}{RT}\right) \quad (4.9)$$

The parameters a and b originate from the linear free energy relationship proposed by Barrer¹⁸:

$$\ln(D_{0,A}) = a \frac{E_{D,A}}{RT} - b \quad (4.10)$$

Freeman used values of $a = 0.64$ for all polymers and $b = 9.2$ or 11.5 for rubbery or glassy polymers, respectively, in units of $\text{cm}^2 \text{s}^{-1}$ for the diffusion coefficient.

The f parameter originates from the Brandt model relating the diffusion activation energy to the gas kinetic diameter, which describes the energy required to open a transient gap for a molecular jump to occur between free volume elements:¹⁹

$$E_{D,A} = cd_A^2 - f \quad (4.11)$$

where c and f are constants that relate to the size-sieving ability of the polymer. The c parameter is related to backbone stiffness and acts as an energy scaling factor with respect to the penetrant diameter squared, and the f parameter is related to interchain spacing. The quantity $\sqrt{f/c}$ can be interpreted as a rough estimate of the average chain spacing. Freeman calculated a best-fit f value of 52.7 kJ mol^{-1} for the 1991 upper bounds from a least squares regression of theoretical and experimental $\beta_{A/B}$ values across all gas pairs considered.³

Freeman's definitions for $\lambda_{A/B}$ and $\beta_{A/B}$ allow for theoretical predictions of the slopes of the upper bounds with no adjustable parameters and front factors with two adjustable parameters: f , relating

to the interchain spacing, and S_A/S_B , relating to the solubility selectivity of the gases in the polymer. Since $\lambda_{A/B}$ theoretically is not affected by polymer materials characteristics, these parameters represent the two major pathways towards increasing the value of the front factor and therefore improving the separation performance for polymeric membranes.

4.3. Analysis Procedure

This analysis focuses on the theoretical shifts to the upper bound fronts through the modification of the solubility terms in Equation 4.14. Non-perfluoropolymer upper bound fronts were refit from an updated Robeson's database excluding perfluoropolymer data points to establish a clear baseline for this analysis.²⁰ The solubility correlation parameters were adjusted for perfluoropolymers while retaining the fitted f values from the non-perfluoropolymer upper bounds. By doing so, this procedure illustrates the potential improvements to using perfluoropolymers under the key assumption that fluorine functionality has no other effect on transport performance other than adjusting gas-polymer molecular partitioning. It should be noted that some recent data on new diffusion-selective polymers have been reported with property sets that surpass certain upper bounds.^{21,22} There are a limited number of these polymers, and they show beneficial upper bound performance for O₂/N₂, CO₂/CH₄, H₂/N₂, and H₂/CH₄ separations, which are not the primary consideration for this work. Therefore, we have chosen not to include these polymers in our analysis, thereby allowing us to use a widely accepted and published database of separation property sets.

4.3.1. Modifications from Previous Analysis

The analysis originally considered by Freeman was derived using a form of the linear free energy relationship proposed by Barrer.¹⁸ However, an alternative mathematical form has also been

proposed by van Amerongen.²³ In 2005, Prabhakar considered the linear free energy relationships proposed by van Amerongen (Equation 4.12.1) and Barrer (Equation 4.13.1) respectively:²⁴

$$\ln(D_0) = a \frac{E_D}{R} - b \quad (4.12.1)$$

$$\ln(D_0) = a' \frac{E_D}{RT} - b' \quad (4.13.1)$$

When substituting these expressions into the Arrhenius diffusion relationship, we arrive at the following distinct definitions for diffusion coefficients:

$$D = \exp\left(a \frac{E_D}{R} - b\right) \exp\left(-\frac{E_D}{RT}\right) \quad (4.12.2)$$

$$D = \exp(-b') \exp\left(\frac{(a' - 1)E_D}{RT}\right) \quad (4.13.2)$$

Prabhakar argued against the use of the Barrer form of the linear free energy relationship because it would require a fixed intercept of b' when plotting $\ln(D)$ vs. $1/T$, regardless of the polymer-penetrant system, while conversely, the van Amerongen form would allow for an intercept that depended on the polymer-penetrant system. The null hypothesis of a fixed intercept regardless of the polymer-penetrant system was tested through a two-factor analysis of variance (ANOVA) without replication using van Amerongen's data (see Appendix A, Section A.2).²³ The variance in the intercept was found to be statistically significant when considering both polymer composition and gas selection for a separation based off both critical F - and p -values, thus suggesting the van Amerongen form of the linear free energy relationship should be used for this analysis. Prabhakar reported values of $a = 0.00203$ and $b = 8.3$ for rubbery polymers and van Krevelen reported $b =$

11.5 for glassy polymers.^{24,25} This aforementioned modification leads to a slightly modified form of $\beta_{A/B}$:

$$\beta_{A/B} = \frac{S_A}{S_B} S_A^{\lambda_{A/B}} \exp\left(-\lambda_{A/B} \left(b - f \frac{1 - aT}{RT}\right)\right) \quad (4.14)$$

4.3.2. Necessity of Non-perfluoropolymer Upper Bounds

New non-perfluoropolymer upper bounds were determined by eye for this analysis, following a similar procedure to that used by Robeson in estimating the original 1991 and 2008 upper bounds.^{1,2} An example highlighting the need for the creation of distinct upper bounds based off chemical structure is shown in Figure 4.2a, where there is a significant difference in the location of the upper bound front depending on whether or not perfluorinated polymers are considered. A particular distinction is made for this work in describing the new upper bounds as “non-perfluoropolymer” instead of “hydrocarbon”. This terminology is chosen because many partially fluorinated polymers (*e.g.*, 4,4'-(hexafluoroisopropylidene)diphthalic anhydride (6FDA) based polyimides) have shown sorption behavior more similar to that of hydrocarbon polymers than perfluoropolymers.²⁶ An exception to this distinction is made for Viton[®] E60 and Viton[®] GF, both highly fluorinated elastomers (65 wt% F and 75 wt% F respectively), since they display sorption behavior consistent with perfluoropolymers.²⁷ A remarkable example of how transport properties for partially fluorinated Viton[®] polymers more closely align to those of perfluoropolymers is noted for the He/H₂ upper bound presented in Figure 4.3a. In this example, Viton[®] polymers are the only non-perfluorinated polymers exceeding the non-perfluoropolymer upper bound.

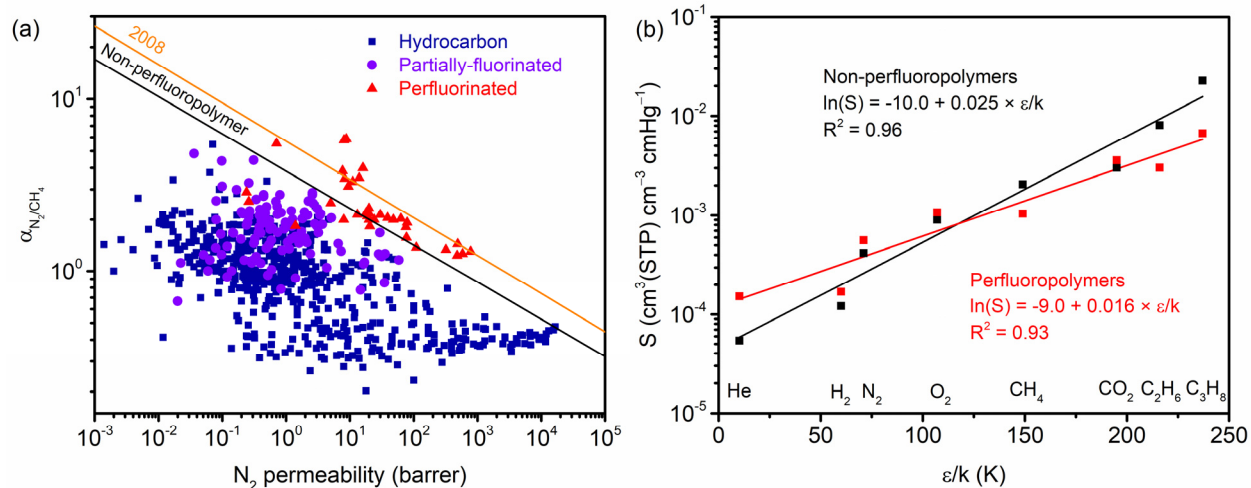


Figure 4.2. (a) A representative upper bound plot with data points identified as hydrocarbon, partially-fluorinated, and perfluorinated. Non-perfluoropolymer upper bounds are established for this work because the upper bound database includes a large amount of perfluoropolymer data. (b) Best-fit solubility correlation parameters when comparing non-perfluorinated and perfluorinated polymers at 35 °C and 1 atm.

4.3.3. Selection of Molecular Diameters

It has been previously noted that theoretical upper bounds calculated from Freeman’s approach match poorly with Robeson’s experimental upper bound plots, primarily as a result of the use of kinetic diameters for the analysis.²⁸ This inconsistency has prompted studies into using new sets of diameter definitions suitable for describing diffusion through polymeric media such as the “Dal-Cin” and the “permeability correlation” diameters.^{28,29} For this study, the so-called “diffusion” diameters were employed.²⁰ These diameters are calculated from a least-squares minimization approach that optimizes a fit for molecular diameters based on correlations from a large database of gas diffusion coefficients in polymer membranes.²⁰ This diameter set assumes a fixed CH₄ diameter of 3.817 Å (1 Å = 10⁻¹⁰ m) as a basis for the least-squares minimization because CH₄ is

nearly spherical and there is little variation in literature-reported diameters.²⁹ For this analysis, diffusion diameters resulted in the lowest sum-of-squared residuals when comparing between predicted and non-perfluoropolymer $\lambda_{A/B}$ values for all gas pairs considered in this analysis. Other diameter sets considered included the kinetic, Dal-Cin, Teplyakov-Meares, Lennard-Jones, permeability correlation, Lennard-Jones collision, and effective diameters.²⁸⁻³⁵

4.3.4. Calculation of Individual f values for each Gas Pair

With the non-perfluoropolymer upper bounds and the diameter sets established, f values were calculated for each gas pair to exactly match the upper bound fit to the empirical non-perfluoropolymer upper bounds. Fitting a singular best-fit f value across all gas pairs resulted in significant variability to upper bound fits, suggesting that this simplification would severely limit the predictive applicability of the theory developed in this study. Therefore, f values are defined for each gas pair.

4.3.5. Adjustment in Solubility Correlation

The non-perfluoropolymer upper bounds were shifted by adjusting the S_A and S_B values in Equation 4.14 according to observed changes in M and N between non-perfluoropolymers and perfluoropolymers. The changes in correlation parameters were determined from a collection of published non-perfluorocarbon and perfluorocarbon sorption coefficients at or near standard testing conditions of 35 °C and 1 atm (see Table A.4), as shown in Figure 4.2b. The parameters for the non-perfluorocarbons were $M = -10.0 \pm 0.3$ and $N = 0.025 \pm 0.002$ and the parameters for the perfluorocarbons were $M = -9.0 \pm 0.3$ and $N = 0.016 \pm 0.002$. These parameters were determined by performing linear regression on the natural log of the sorption coefficient with respect to the Lennard-Jones temperature for a variety of common gases. The natural log of the

gas solubility coefficient is commonly correlated, to good accuracy, with respect to other thermodynamic properties of gases such as critical temperature or boiling temperature (see Equation 4.8).³⁶ The Lennard-Jones temperature was chosen as the correlation variable because it originates from Lennard-Jones potential energy well depth, while other measures of condensability such as critical and boiling temperature can be influenced by the strength of the intermolecular forces between individual gas molecules. The noted change in gas solubility and solubility selectivity between non-perfluoropolymers and perfluoropolymers is hypothesized to be the basis for the observed improvement in separation performance shown by perfluoropolymers for certain gas pairs.

4.4. Results

4.4.1. The Perfluoropolymer Upper Bound

The above analysis procedure was implemented on gas pairs (He/H₂, He/CO₂, He/N₂, He/CH₄, and N₂/CH₄) where perfluoropolymer performance was particularly notable. Figure 4.3 presents upper bound plots for these gas pairs. Included on each plot are permeabilities and selectivities for hydrocarbon, partially fluorinated, and perfluorinated polymers, and two distinct upper bounds are shown to represent the non-perfluoropolymer and perfluoropolymer upper bounds. The slope and front factor for each upper bound are listed in Table 4.1. The front factors for the perfluoropolymer upper bounds are significantly increased when solubility selectivities are made in accordance with empirical trends reported in the literature while retaining the non-perfluoropolymer f value.¹¹

Table 4.1. Tabulation of n (slopes) and k (front factors) for the gas pairs analyzed.

Gas pair	n , non-perfluoropolymer and perfluoropolymer	k , non-perfluoropolymer (barrer)	k , perfluoropolymer (barrer)
He/H ₂	-4.6	786	18,700
He/CO ₂	-1.6	5,100	79,500
He/N ₂	-1.0	19,900	85,800
He/CH ₄	-0.8	11,100	67,600
N ₂ /CH ₄	-4.6	508	19,900

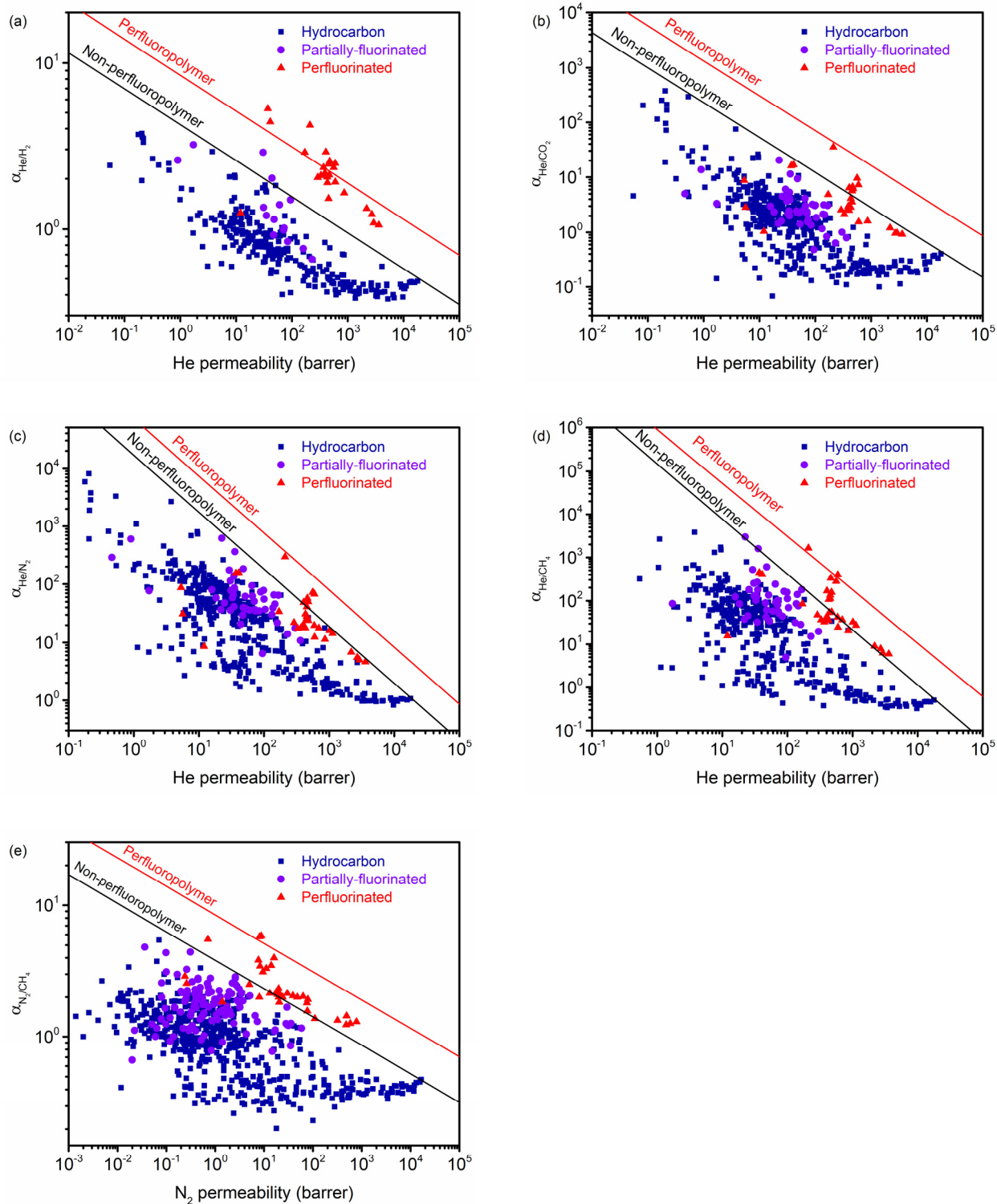


Figure 4.3. Upper bound plots showing the non-perfluoropolymer and perfluoropolymer upper bounds: (a) He/H₂ (b) He/CO₂ (c) He/N₂ (d) He/CH₄ (e) N₂/CH₄

When comparing experimental perfluoropolymer data points with the perfluoropolymer upper bounds, there are cases where the perfluoropolymer upper bound approximately matches data for the best observed performance of known perfluoropolymers (He/CO₂, He/N₂, He/CH₄) and cases where experimental data surpasses the shifted upper bound (He/H₂, N₂/CH₄). In the most general sense, the perfluoropolymer upper bound represents the potential separation performance of the best performing non-perfluorinated polymers if they were to theoretically retain their backbone stiffness and interchain spacing (c and f values from Equation 4.11) while improving their sorption selectivities to those of perfluoropolymers. This interpretation implies that perfluoropolymers with property sets below the shifted upper bound would have a hypothetical hydrocarbon counterpart that exhibits separation performance below that of the non-perfluoropolymer upper bound. Conversely, perfluoropolymers at or surpassing the shifted upper bound are able to take advantage of perfluoropolymer solubility selectivity while simultaneously possessing size-sieving properties greater than or equal to that of the best non-perfluoropolymers for these gas pairs.

There are two subclasses of perfluoropolymers that either define or surpass the perfluoropolymer upper bound for the gas pairs considered in Figure 4.3: various Nafion[®] block copolymers and glassy dioxolane-based perfluoropolymers. Nafion[®] polymers are well-known for their unique packing structure due to their amphiphilic side chains. After wetting and drying of the polymer, the hydrophilic sulfonated side chains are believed to form ionic clusters within the matrix, causing the hydrophobic portion of the perfluoropolymer to pack irregularly about the clusters.³⁷ The notable glassy dioxolane-based perfluoropolymers are recently developed polymers of perfluoro-2-methylene-1,3-dioxolane (poly(PFMD)) and perfluoro-2-methylene-4-methyl-1,3-dioxolane (poly(PFMMD)), as well as PFMD-PFMMD block copolymers with varying block lengths.^{8,9}

These dioxolane-based polymers possess cyclic structures in their backbones that frustrate packing and demonstrate glass transition temperatures ranging from 123 °C to 135 °C.^{8,9} Therefore, the resulting packing structure of these two subclasses of perfluoropolymers leads to good diffusion selectivity performance.³⁷ Such a finding reveals that it is possible to develop materials that have solubility selectivities and size-sieving behavior that is both complementary and beneficial in surpassing property sets of conventional hydrocarbon polymers.

4.4.2. Comparison of Diffusivity and Solubility Selectivity Effects on Shifting the Upper Bound

A helpful exercise is to consider improvements that have been made in separation performance since the publication of the 1991 upper bounds for perfluorinated and non-perfluorinated polymer structures. These performance improvements can be quantified by comparing the f values for the 1991 upper bounds with the newly fitted f values for the non-perfluoropolymer upper bounds and the “effective f ” values for the perfluoropolymer upper bounds. In this study, the “effective f ” values are defined as the calculated f values necessary to replicate the perfluoropolymer upper bound front while retaining non-perfluoropolymer solubility selectivity. In other words, the effective f for a gas pair is the f value required to shift the non-perfluoropolymer front to match that of the perfluoropolymer upper bound. Table 4.2 shows the newly fitted f values and the effective f values for the five gas pairs considered to match the non-perfluoropolymer and perfluoropolymer upper bounds, respectively, as previously shown in Figure 4.3. The effective f values are between 15 and 29% greater than the non-perfluoropolymer f values, depending on the gas pair, with an average increase of 20%.

A similar procedure as described previously was used to calculate f values for the 1991 upper bounds. By doing so, a qualitative measure of the improvement in gas separation performance between 1991 and the current non-perfluoropolymer upper bounds could be established. The 1991 upper bounds were chosen as a baseline comparison, as opposed to the 2008 upper bounds, because the only perfluoropolymer data point at the time (Nafion[®] 117) was considered to be an outlier and was not included in the upper bound analysis.¹

Table 4.2 presents the percentage increase in calculated f values from 1991 to the current non-perfluoropolymer upper bounds for the analyzed gas pairs. For these separations (*e.g.*, He/H₂, He/CO₂, He/N₂, He/CH₄, N₂/CH₄), f values shift between -1.7% and 19%. Note that the -1.7% shift for He/H₂ separation results from our decision to group Viton[®] elastomers with perfluoropolymers. Viton[®] was originally included in the 1991 upper bound, and to date, there have been no reported property sets for non-perfluorinated polymers that have surpassed the He/H₂ separation performance of Viton[®].²⁷ As for the other gas pairs, this analysis reveals that mild improvements to separation performance have been made using synthetic design strategies that do not include perfluorinated polymers.

Conversely, Table 4.2 also presents a comparison of the increase in f values for the newly fitted non-perfluoropolymer upper bounds and the effective f values. In this case, significant shifts in f values between 14.9% and 28.8% are observed for the gas pairs analyzed. This remarkable finding quantitatively demonstrates the benefit to using perfluoropolymers for the five primary separations analyzed in this work. Despite nearly three decades of membrane research since the publication of the 1991 upper bound, there have been no successful design strategies for non-perfluorinated polymers capable of achieving the same performance improvements as those obtained through the use of perfluoropolymers.

Table 4.2. Actual and effective f values and relative increases from baseline comparisons. There was no N₂/CH₄ upper bound reported by Robeson in 1991.¹

Gas pair	f value		Increase in f value	
	f for non-perfluoropolymer upper bound (kJ mol ⁻¹)	Effective f for perfluoropolymer upper bound (kJ mol ⁻¹)	Increase in f , 1991 f to non-perfluoropolymer f	Increase in f , non-perfluoropolymer f to effective f
He/H ₂	79.9	102	-1.7%	27.1%
He/CO ₂	84.1	103	19%	22.3%
He/N ₂	67.2	77.2	5.0%	14.9%
He/CH ₄	70.3	82.6	8.4%	17.6%
N ₂ /CH ₄	87.0	112	-	28.8%

A full list of f values for the 1991 upper bounds and the newly fitted non-perfluoropolymer upper bounds are compiled in Table A.5 along with the corresponding percent change in f values. The newly fitted non-perfluoropolymer f values shift between -1.7% and 106% compared to the 1991 f values, depending on the gas pair, with an average increase of 27% . Of note, the two separations with the greatest improvements in non-perfluorinated property sets are CO₂/CH₄ and O₂/N₂ separations. Unlike all other separations tabulated, these separations benefit from both diffusion and solubility selectivities. For example, in the case of CO₂/CH₄ separation, CO₂ is both smaller than CH₄ and more soluble than CH₄ in polymers, thereby resulting in favorable diffusion selectivities and solubility selectivities, and hence, permselectivities. Conversely, for all of the separations enhanced through the use of perfluoropolymers, solubility selectivity is intrinsically

unfavorable. For example, in the case of He/H₂ separation, He is less soluble than H₂ in polymers, thereby resulting in unfavorable solubility selectivities.^{26,38} Therefore, from the standpoint of the solution-diffusion model, perfluoropolymers are attractive for separations that benefit from weak solubility selectivities (*i.e.*, solubility selectivities closer to unity). Heuristically, Table A.5 highlights the importance of considering both molecular size and polymer-penetrant interactions when choosing a polymer for a given separation.

Figure 4.4 present upper bound plots for He/CH₄, H₂/CH₄, and CO₂/CH₄. The line labeled “1991” is the upper bound front originally described by Robeson. Accompanying values of f , M , and N required to obtain this fit are provided as a reference. The non-perfluoropolymer upper bound, which maintains an identical M and N value to that of the 1991 upper bound but a modified value of f is labeled as “Non-perfluoropolymer”. This change in f corresponds to the shift in state-of-the-art performance for non-perfluoropolymers, as described previously. The final line, labeled “1991 Shifted”, presents f values characteristic of upper bound non-perfluoropolymers in 1991, but with the solubility relationship coefficients, M and N , shifted to hypothetically account for solubility behavior that is expected for perfluoropolymers according to the solubility terms in Equation 4.14. For He/CH₄, modifying the 1991 upper bound by only changing the analysis to consider perfluoropolymer solubility characteristics results in a greater shift to the upper bound front than that observed for the present non-perfluoropolymer upper bound. The same qualitative findings are observed for He/H₂, He/CO₂, He/CH₄, and N₂/CH₄ as well. For H₂/CH₄, which is shown in Figure 4.4b, the adjustment to perfluoropolymer solubility coefficients resulted in an improvement surpassing the 1991 baseline but did not reach the current performance limit of the non-perfluoropolymer upper bound. Lastly, there are general cases in which the use of the perfluoropolymer solubility correlation negatively impacts performance. One commonly studied

gas separation that does not benefit from the sorption behavior of perfluoropolymers is CO₂/CH₄. An illustration of this behavior is shown in Figure 4.4c. In this case, the more strongly-sorbing penetrant (*i.e.*, CO₂) is also faster permeating compared to the other component (*i.e.*, CH₄), resulting in a lowered upper bound front. This penetrant size/solubility argument can be used to predict the effects of solubility changes on the upper bound position for all other gas pairs.

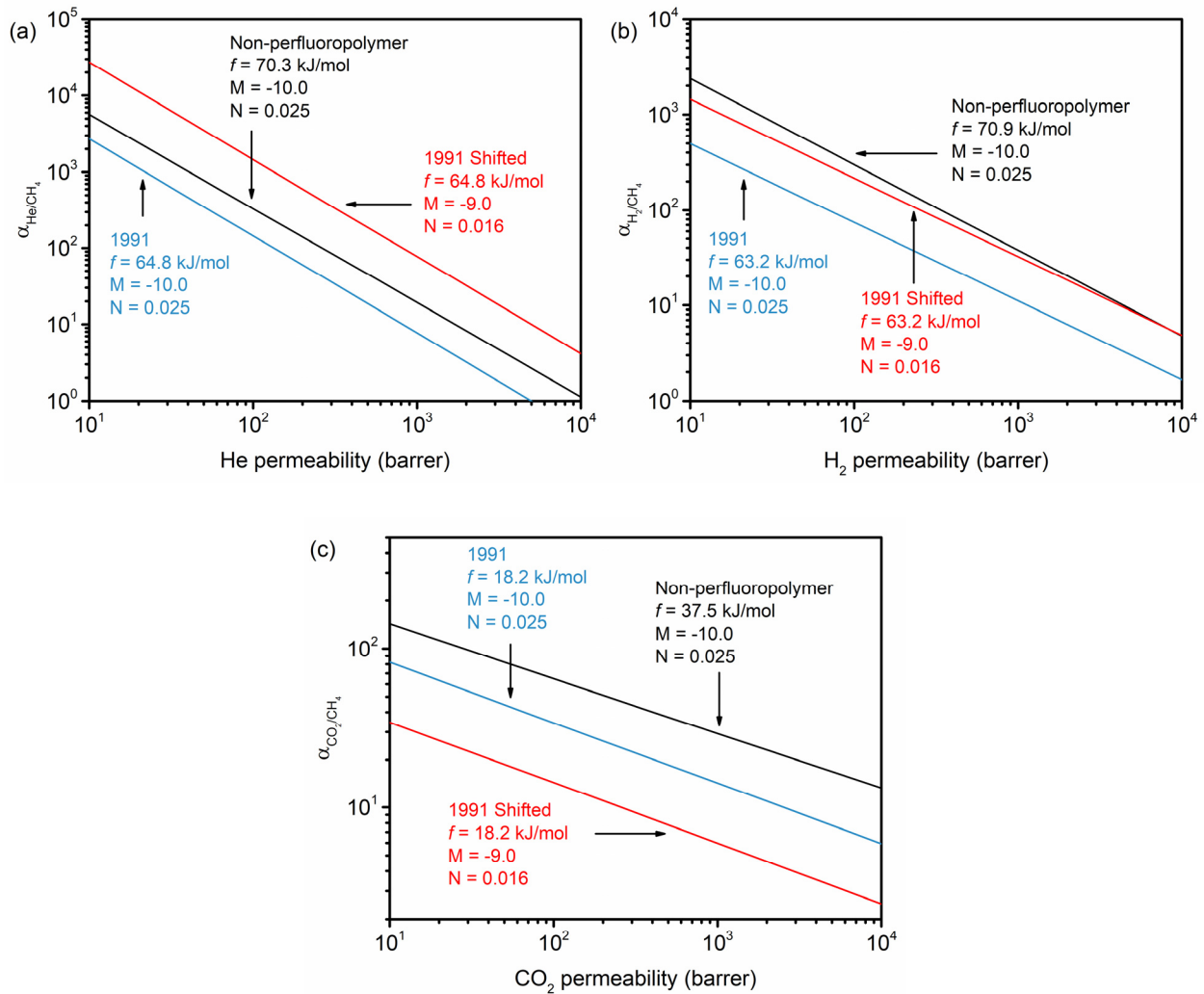


Figure 4.4. Comparison in the shifts of the upper bound plots from 1991 by changing either f or the characteristic solubility correlations for non-perfluoropolymers and perfluoropolymers. Results are shown for: (a) He/CH₄ (b) H₂/CH₄ (c) CO₂/CH₄

4.4.3. Prediction of Upper Bound Fronts from Penetrant Properties

A key challenge in the membrane field is the ability to predict performance limits for separations where little to no experimental data exists. Such limitations often preclude the use of process modeling to incorporate membranes into the design of separations processes. On the contrary, however, many thermally-driven separations, such as distillation, have abundant accessible datasets and tested models to ensure good predictive capabilities when designing new chemical plants. An interesting consequence of our work is the ability to leverage theory to predict membrane separation performance for less well-studied separations. Of particular importance is a correlation that can be gleaned from the compilation of f values for individual gas pairs, as shown in Figure 4.5a for the non-perfluoropolymer upper bounds. When plotting $\ln(f)$ versus $\lambda_{A/B} \times S_A/S_B$ for each gas pair, there is a resulting linear correlation with a R^2 value of 0.655 and a Pearson correlation coefficient of -0.809 . A F -test of overall significance was performed with the null hypothesis stating that the fit matches the reduced model containing parameters for the intercept only. The calculated F -value for this fit was 20.9 and the critical F -value, with degrees of freedom corresponding to a 2 parameter fit and 13 observations, was equal to 4.84 for $p = 0.05$. Since the calculated F -value is larger than the critical F -value, the null hypothesis was rejected in favor of the full model containing parameters for one independent variable and the intercept, suggesting some physical meaning for this trend.³⁹

A potential interpretation is that $\lambda_{A/B}$ and the predicted value of S_A/S_B serve as proxies for diffusion and actual solubility selectivities based exclusively on correlations with well-known penetrant properties. Therefore, a larger product of the two terms represents, in general, a more efficient separation with higher selectivities because the separation is aided by properties intrinsic to the penetrants (*i.e.*, He/CO₂ is the least efficient, while CO₂/CH₄ is the most efficient). However,

our interpretation of a unique f value for every gas pair is contrary to the Brandt model (see Equation 4.11) where a polymer possesses a singular f value, which is seen as an intrinsic property related to the interchain spacing of the polymer.¹⁹ Therefore, we chose to carefully apply these predictions with the knowledge that additional theory must still be developed to fully understand the fundamental origins underlying our approach.

The obvious application of this correlation is to predict present day f values for gas pairs of interest that were not considered in this work. In doing so, new upper bounds can be predicted. Ethylene/ethane (C_2H_4/C_2H_6) and propylene/propane (C_3H_6/C_3H_8) upper bound limits have been previously established, albeit using the Lennard-Jones and Lennard-Jones collision diameters respectively.^{32,33,40,41} When our analysis was repeated using the respective diameter sets for each separation, the predicted f values are 72.1 kJ mol^{-1} for ethylene/ethane and 66.0 kJ mol^{-1} for propylene/propane. The original and current predicted non-perfluoropolymer upper bound fronts with the original data sets are shown in Figures 4.5b-c, where a modest shift in the upper bound front is predicted. It should be noted that the trend shown in Figure 4.5a reflects the current progress in polymer membrane performance and should be updated as upper bound front factors increase over time with the development of new materials. Predicted perfluoropolymer upper bounds, based off of the predicted non-perfluoropolymer upper bounds, were calculated using the f values following the procedure outlined in Section 4.3 and are shown in Figures 4.5b-c, predicting essentially no shift for C_2H_4/C_2H_6 and a negative shift for C_3H_6/C_3H_8 . Examining Equation 4.14 and Figure 4.2b, this outcome can be attributed to a decrease in $S_A^{\lambda_{A/B}}$ when switching from hydrocarbon to perfluoropolymer solubility for these gas pairs. In the case of C_2H_4/C_2H_6 , there is no shift in the front factor because the decrease in $S_A^{\lambda_{A/B}}$ is approximately equal to the increase in S_A/S_B , while in the case of C_3H_6/C_3H_8 , the negative shift is due to the

predominant decrease in $S_A^{\lambda_{A/B}}$ over the increase in S_A/S_B . This effect scales primarily with the condensability of gas A, revealing limiting cases where perfluoropolymers would not improve performance even for certain gas pairs that do follow the size/solubility argument presented in Section 4.4.2.

Figure 4.5d shows the predicted non-perfluoropolymer and perfluoropolymer upper bounds for H₂/C₃H₆, an industrially important separation for olefin recovery, again using the Lennard-Jones collision diameter for this analysis.^{42,43} From the predicted upper bound fronts, it is expected that hydrogen separation from olefin streams could greatly benefit from the use of perfluoropolymers. The ability to predict upper bound fronts for gas pairs with no data points allows for a rough estimate of performance and suggests pathways for improvement. However, this approach must be used with caution, as limited data is currently available to test the key assumptions outlined in this work.

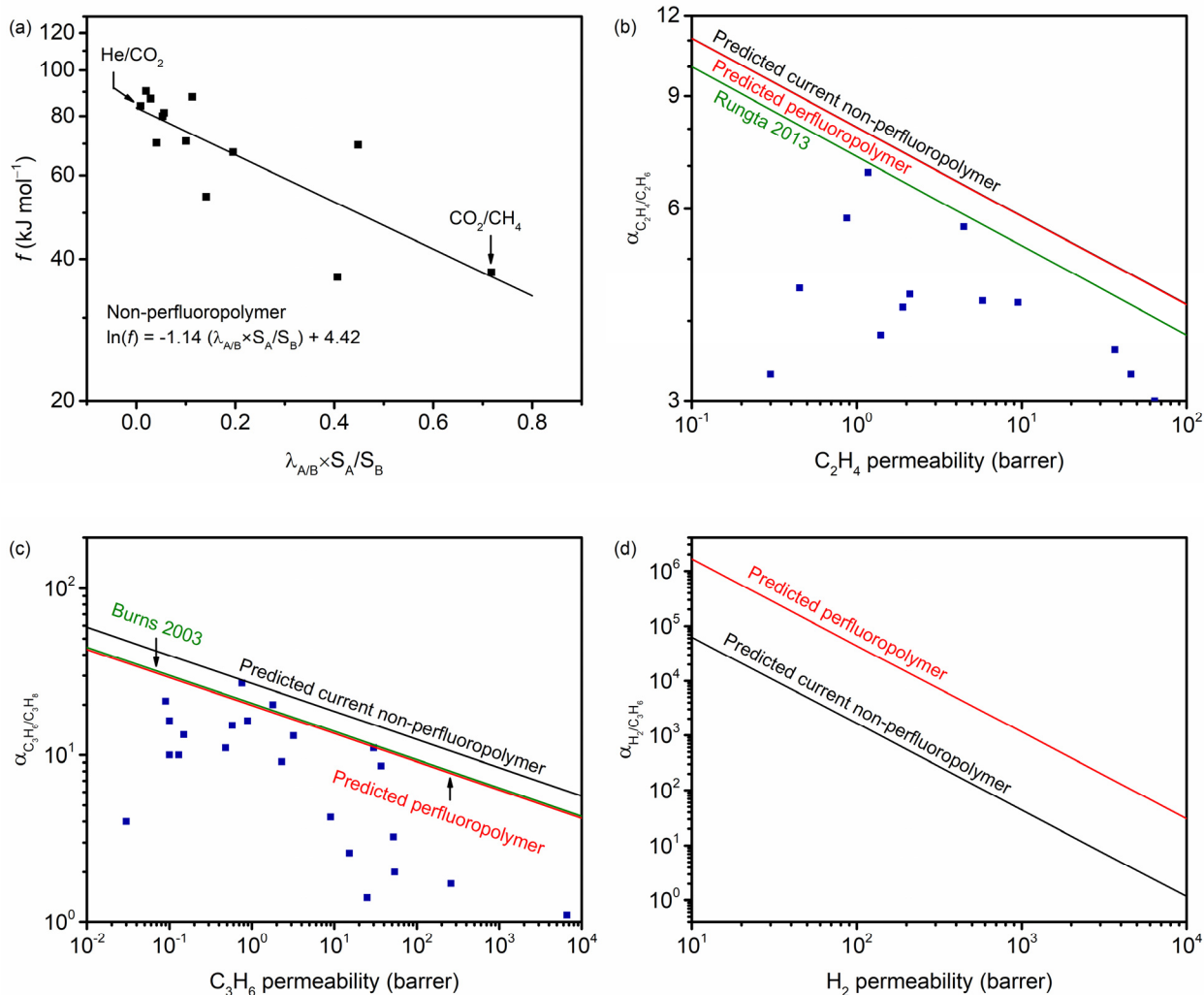


Figure 4.5. (a) Semi-log plot showing the correlation between $\lambda_{A/B} \times S_A/S_B$ and non-perfluoropolymer upper bound f values. (b) The previous upper bound, predicted current non-perfluoropolymer upper bound, and predicted perfluoropolymer upper bound for C₂H₄/C₂H₆ separation.⁴⁰ The two predicted upper bounds are essentially overlapping. (c) The previous upper bound, predicted current non-perfluoropolymer upper bound, and predicted perfluoropolymer upper bound for C₃H₆/C₃H₈ separation.⁴¹ (d) Predicted current non-perfluoropolymer upper bound and perfluoropolymer upper bound for H₂/C₃H₆ separation.

4.4.4. Promising Future Gas Separation Applications for Perfluoropolymers

Although the five gas pairs analyzed were selected because of the known performance improvements that result from using perfluoropolymers, there are other separations where modifications to solubility selectivity present a benefit. In particular, He/O₂ and H₂/CH₄ have similar intrinsic advantageous metrics of relative molecular sizes and solubilities for their respective gas pairs that could benefit from the use of perfluoropolymers. Following the analysis procedure outlined in Section 4.3, Figure 4.6 demonstrate the predicted shift in upper bound performance that can be achieved using perfluoropolymers for these separations. Interestingly, in contrast to our predictions, currently available data indicates that perfluoropolymers exhibit nearly the same performance as that of the best performing non-perfluoropolymers. In the case for He/O₂ separation, it has been experimentally shown that perfluorocarbon liquids have anomalously high sorption capacity for O₂, which would lower the solubility selectivity and result in depressed separation performance.⁴⁴ In the case of H₂/CH₄, it is possible that similarities in the chemical composition between H₂ and CH₄ result in H₂ having anomalous interactions with fluorocarbons, similar to that of CH₄ with C-F bonds, again resulting in lower solubility selectivity and separation performance than predicted by our solubility correlations.^{45,46} Note that in Figure 4.2b, H₂ and CH₄ are the two gases that deviate the most significantly from our solubility correlation. Currently, H₂/CH₄ separation represents an important challenge in refinery off-gas purification, and while He/O₂ separation is currently not practiced in industry, it could become useful in the future as helium-containing natural gas resources continue to diminish.^{14,47} Perfluoropolymers also show promise in improving H₂/C₃H₆ separations for olefin recovery from thermal cracking or off-gas streams, as shown in Figure 4.5d.^{42,43} Additionally, perfluoropolymers, which possess a nano-confined packing structure with unique electronic interactions stemming from their highly

polarized C-F bonds,^{48,49} could also be of interest for a variety of valuable isotope separations such as H₂/D₂ separation for the production of “heavy drugs” associated with decreased pharmacokinetics and fewer side effects, or for ³He/⁴He separation for medical applications related to imaging of the human lungs.^{50,51}

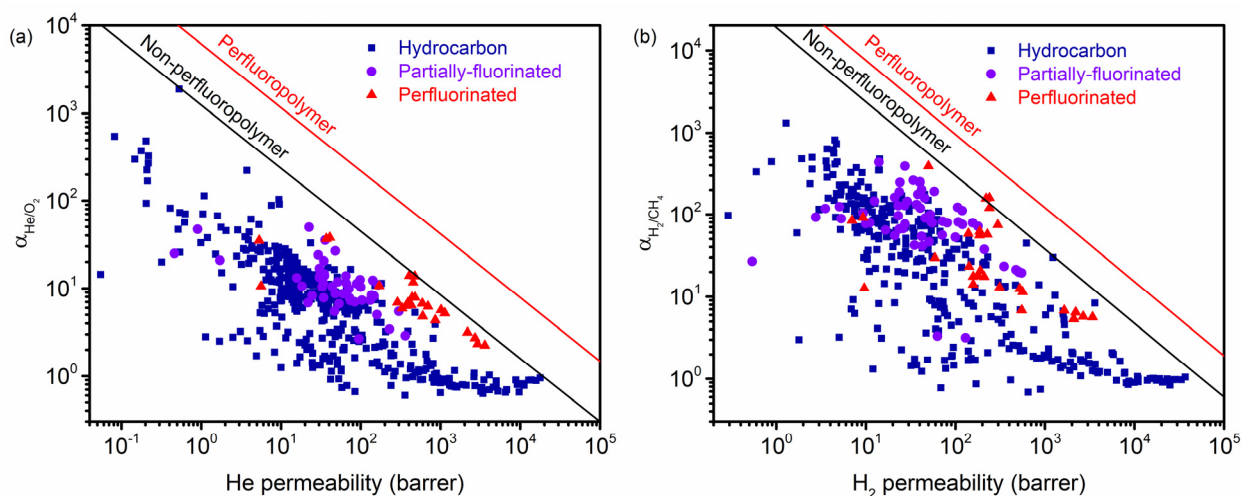


Figure 4.6. Upper bound plots showing gas pairs where perfluorinated polymers display performance similar to the best non-perfluorinated polymers: (a) He/O₂ (b) H₂/CH₄

4.5. Conclusions

The solubility behavior of gases in perfluoropolymers is not considered in the current theoretical framework used to define the Robeson upper bound. This analysis addresses this key limitation by considering distinct theoretical trends in solubility for non-perfluorocarbons and perfluorocarbons. By doing so, new non-perfluoropolymer and perfluoropolymer upper bounds are established and compared to current data. For the five gas pairs examined, it was found that perfluoropolymer data either matched or surpassed the theoretical perfluoropolymer upper bounds established in this work, indicating that the best-performing perfluoropolymers exhibit size-sieving ability equal to or greater than that of the best performing non-perfluoropolymers. Of note, polymers such as

Nafion[®] block copolymers, poly(PFMD), poly(PFMMD), and PFMD-PFMMD block copolymers demonstrate the separation performance that can be accessed through improvements in both the diffusivity and solubility terms originally revealed in Freeman's analysis. Additionally, a new trend based on penetrant size and solubility selectivity is presented as a predictive method to estimate non-perfluoropolymer f values, which can then be used to predict both the non-perfluoropolymer and perfluoropolymer upper bound fronts for separations not explicitly considered in this work.

4.6. References

- (1) Robeson, L. M. Correlation of Separation Factor versus Permeability for Polymeric Membranes. *J. Membr. Sci.* **1991**, *62* (2), 165–185. [https://doi.org/10.1016/0376-7388\(91\)80060-J](https://doi.org/10.1016/0376-7388(91)80060-J).
- (2) Robeson, L. M. The Upper Bound Revisited. *J. Membr. Sci.* **2008**, *320* (1–2), 390–400. <https://doi.org/10.1016/j.memsci.2008.04.030>.
- (3) Freeman, B. D. Basis of Permeability/Selectivity Tradeoff Relations in Polymeric Gas Separation Membranes. *Macromolecules* **1999**, *32* (2), 375–380. <https://doi.org/10.1021/ma9814548>.
- (4) Park, H. B.; Jung, C. H.; Lee, Y. M.; Hill, A. J.; Pas, S. J. Polymers with Cavities Tuned for Fast Selective Transport of Small Molecules and Ions. *Science* **2007**, *318* (October), 254–259. <https://doi.org/10.1126/science.1146744>.
- (5) Ma, X.; Pinnau, I. A Novel Intrinsically Microporous Ladder Polymer and Copolymers Derived from 1,1',2,2'-Tetrahydroxy-Tetraphenylethylene for Membrane-Based Gas Separation. *Polym. Chem.* **2016**, *7* (6), 1244–1248. <https://doi.org/10.1039/c5py01796c>.
- (6) Carta, M.; Croad, M.; Malpass-Evans, R.; Jansen, J. C.; Bernardo, P.; Clarizia, G.; Friess, K.; Lanč, M.; McKeown, N. B. Triptycene Induced Enhancement of Membrane Gas Selectivity for Microporous Tröger's Base Polymers. *Adv. Mater.* **2014**, *26* (21), 3526–3531. <https://doi.org/10.1002/adma.201305783>.
- (7) Rose, I.; Bezzu, C. G.; Carta, M.; Comesanã-Gándara, B.; Lasseuguette, E.; Ferrari, M. C.; Bernardo, P.; Clarizia, G.; Fuoco, A.; Jansen, J. C.; et al. Polymer Ultrapermeability from the Inefficient Packing of 2D Chains. *Nat. Mater.* **2017**, *16* (9), 932–937. <https://doi.org/10.1038/nmat4939>.
- (8) Yavari, M.; Fang, M.; Nguyen, H.; Merkel, T. C.; Lin, H.; Okamoto, Y. Dioxolane-Based Perfluoropolymers with Superior Membrane Gas Separation Properties. *Macromolecules* **2018**, *51* (7), 2489–2497. <https://doi.org/10.1021/acs.macromol.8b00273>.

- (9) Fang, M.; He, Z.; Merkel, T. C.; Okamoto, Y. High-Performance Perfluorodioxolane Copolymer Membranes for Gas Separation with Tailored Selectivity Enhancement. *J. Mater. Chem. A* **2018**, *6* (2), 652–658. <https://doi.org/10.1039/c7ta09047a>.
- (10) Wijmans, J. G.; Baker, R. W. The Solution-Diffusion Model: A Review. *J. Membr. Sci.* **1995**, *107* (1–2), 1–21. [https://doi.org/10.1016/0376-7388\(95\)00102-I](https://doi.org/10.1016/0376-7388(95)00102-I).
- (11) Merkel, T. C.; Pinnau, I.; Prabhakar, R. S.; Freeman, B. D. Gas and Vapor Transport Properties of Perfluoropolymers. In *Materials Science of Membranes for Gas and Vapor Separation*; 2006; pp 251–270.
- (12) Bernardo, P.; Bazzarelli, F.; Tasselli, F.; Clarizia, G.; Mason, C. R.; Maynard-Atem, L.; Budd, P. M.; Lanč, M.; Pilnáček, K.; Vopička, O.; et al. Effect of Physical Aging on the Gas Transport and Sorption in PIM-1 Membranes. *Polymer* **2017**, *113*, 283–294. <https://doi.org/10.1016/j.polymer.2016.10.040>.
- (13) Tiwari, R. R.; Jin, J.; Freeman, B. D.; Paul, D. R. Physical Aging, CO₂ Sorption and Plasticization in Thin Films of Polymer with Intrinsic Microporosity (PIM-1). *J. Membr. Sci.* **2017**, *537* (January), 362–371. <https://doi.org/10.1016/j.memsci.2017.04.069>.
- (14) Sanders, D. F.; Smith, Z. P.; Guo, R.; Robeson, L. M.; McGrath, J. E.; Paul, D. R.; Freeman, B. D. Energy-Efficient Polymeric Gas Separation Membranes for a Sustainable Future: A Review. *Polymer* **2013**, *54* (18), 4729–4761. <https://doi.org/10.1016/j.polymer.2013.05.075>.
- (15) Barrer, R. M. Activated Diffusion in Membranes. *Trans. Faraday Soc.* **1939**, *35*, 644–656. <https://doi.org/10.1039/tf9393500644>.
- (16) Cohen, M. H.; Turnbull, D. Molecular Transport in Liquids and Glasses. *J. Chem. Phys.* **1959**, *31* (5), 1164–1169. <https://doi.org/10.1063/1.1730566>.
- (17) Van der Vegt, N. F. A. A Molecular Dynamics Simulation Study of Solvation Thermodynamical Quantities of Gases in Polymeric Solvents. *J. Membr. Sci.* **2002**, *205* (1–2), 125–139. [https://doi.org/10.1016/S0376-7388\(02\)00071-6](https://doi.org/10.1016/S0376-7388(02)00071-6).
- (18) Barrer, R. M.; Skirrow, G. Transport and Equilibrium Phenomena in Gas-Elastomer Systems. I. Kinetic Phenomena. *J. Polym. Sci.* **1948**, *3* (4), 549–563. <https://doi.org/10.5254/1.3542972>.
- (19) Brandt, W. W. Model Calculation of the Temperature Dependence of Small Molecule Diffusion in High Polymers. *J. Phys. Chem.* **1959**, *63* (7), 1080–1084. <https://doi.org/10.1021/j150577a012>.
- (20) Robeson, L. M.; Smith, Z. P.; Freeman, B. D.; Paul, D. R. Contributions of Diffusion and Solubility Selectivity to the Upper Bound Analysis for Glassy Gas Separation Membranes. *J. Membr. Sci.* **2014**, *453*, 71–83. <https://doi.org/10.1016/j.memsci.2013.10.066>.
- (21) Swaidan, R.; Ghanem, B.; Pinnau, I. Fine-Tuned Intrinsically Ultramicroporous Polymers Redefine the Permeability/Selectivity Upper Bounds of Membrane-Based Air and Hydrogen Separations. *ACS Macro Lett.* **2015**, *4* (9), 947–951. <https://doi.org/10.1021/acsmacrolett.5b00512>.
- (22) He, Y.; Benedetti, F. M.; Lin, S.; Liu, C.; Zhao, Y.; Ye, H.-Z.; Voorhis, T. Van; Angelis,

- M. G. De; Swager, T. M.; Smith, Z. P. Polymers with Side Chain Porosity for Ultrapermearable and Plasticization Resistant Materials for Gas Separations. *Adv. Mater.* **2019**. <https://doi.org/10.1002/adma.201807871>.
- (23) Van Amerongen, G. J. The Permeability of Different Rubbers to Gases and Its Relation to Diffusivity and Solubility. *J. Appl. Phys.* **1946**, *17* (11), 972–985. <https://doi.org/10.1063/1.1707667>.
- (24) Prabhakar, R. S.; Raharjo, R.; Toy, L. G.; Lin, H.; Freeman, B. D. Self-Consistent Model of Concentration and Temperature Dependence of Permeability in Rubbery Polymers. *Ind. Eng. Chem. Res.* **2005**, *44* (5), 1547–1556. <https://doi.org/10.1021/ie0492909>.
- (25) van Krevelen, D. W.; te Nijenhuis, K. *Properties of Polymers*, 4th ed.; Elsevier: Oxford, 2009. <https://doi.org/10.1017/cbo9780511623097.008>.
- (26) Smith, Z. P.; Tiwari, R. R.; Dose, M. E.; Gleason, K. L.; Murphy, T. M.; Sanders, D. F.; Gunawan, G.; Robeson, L. M.; Paul, D. R.; Freeman, B. D. Influence of Diffusivity and Sorption on Helium and Hydrogen Separations in Hydrocarbon, Silicon, and Fluorocarbon-Based Polymers. *Macromolecules* **2014**, *47* (9), 3170–3184. <https://doi.org/10.1021/ma402521h>.
- (27) Fitch, M. W.; Koros, W. J.; Nolen, R. L.; Carnes, J. R. Permeation of Several Gases through Elastomers, with Emphasis on the Deuterium/Hydrogen Pair. *J. Appl. Polym. Sci.* **1993**, *47* (6), 1033–1046. <https://doi.org/10.1002/app.1993.070470610>.
- (28) Dal-Cin, M. M.; Kumar, A.; Layton, L. Revisiting the Experimental and Theoretical Upper Bounds of Light Pure Gas Selectivity-Permeability for Polymeric Membranes. *J. Membr. Sci.* **2008**, *323* (2), 299–308. <https://doi.org/10.1016/j.memsci.2008.06.027>.
- (29) Robeson, L. M.; Freeman, B. D.; Paul, D. R.; Rowe, B. W. An Empirical Correlation of Gas Permeability and Permselectivity in Polymers and Its Theoretical Basis. *J. Membr. Sci.* **2009**, *341* (1–2), 178–185. <https://doi.org/10.1016/j.memsci.2009.06.005>.
- (30) Breck, D. W. *Zeolite Molecular Sieves: Structure, Chemistry, and Use*; John Wiley & Sons Ltd.: New York, 1974.
- (31) Teplyakov, V.; Meares, P. Correlation Aspects of the Selective Gas Permeabilities of Polymeric Materials and Membranes. *Gas Sep. Purif.* **1990**, *4* (2), 66–74. [https://doi.org/10.1016/0950-4214\(90\)80030-O](https://doi.org/10.1016/0950-4214(90)80030-O).
- (32) Reid, R. C.; Prausnitz, J. M.; Sherwood, T. K. *The Properties of Gases and Liquids*; McGraw Hill Book Co.: New York, NY, 1977.
- (33) Bird, R. B.; Stewart, W. E.; Lightfoot, E. N. *Transport Phenomena*, 2nd ed.; John Wiley & Sons Ltd.: New York, NY, 1961.
- (34) Shieh, J. J.; Chung, T. S. Gas Permeability, Diffusivity, and Solubility of Poly(4-Vinylpyridine) Film. *J. Polym. Sci. Part B Polym. Phys.* **1999**, *37* (20), 2851–2861. [https://doi.org/10.1002/\(SICI\)1099-0488\(19991015\)37:20<2851::AID-POLB5>3.0.CO;2-U](https://doi.org/10.1002/(SICI)1099-0488(19991015)37:20<2851::AID-POLB5>3.0.CO;2-U).
- (35) Robeson, L. M.; Dose, M. E.; Freeman, B. D.; Paul, D. R. Analysis of the Transport

- Properties of Thermally Rearranged (TR) Polymers and Polymers of Intrinsic Microporosity (PIM) Relative to Upper Bound Performance. *J. Membr. Sci.* **2017**, *525* (December 2016), 18–24. <https://doi.org/10.1016/j.memsci.2016.11.085>.
- (36) Matteucci, S.; Yampolskii, Y.; Freeman, B. D.; Pinnau, I. Transport of Gases and Vapors in Glassy and Rubbery Polymers. In *Materials Science of Membranes for Gas and Vapor Separation*; 2006; pp 1–47. <https://doi.org/10.1002/047002903X.ch1>.
- (37) Mukaddam, M.; Litwiller, E.; Pinnau, I. Gas Sorption, Diffusion, and Permeation in Nafion. *Macromolecules* **2016**, *49* (1), 280–286. <https://doi.org/10.1021/acs.macromol.5b02578>.
- (38) Galizia, M.; Smith, Z. P.; Sarti, G. C.; Freeman, B. D.; Paul, D. R. Predictive Calculation of Hydrogen and Helium Solubility in Glassy and Rubbery Polymers. *J. Membr. Sci.* **2015**, *475*, 110–121. <https://doi.org/10.1016/j.memsci.2014.10.009>.
- (39) Bevington, P. R.; Robinson, D. K. *Data Reduction and Error Analysis for the Physical Sciences*, 3rd ed.; McGraw-Hill: New York, 2003. <https://doi.org/10.1063/1.4823194>.
- (40) Rungta, M.; Zhang, C.; Koros, W. J. Membrane-Based Ethylene/Ethane Separation: The Upper Bound and Beyond. *AIChE J.* **2013**, *59* (9), 3475–3489. <https://doi.org/10.1002/aic>.
- (41) Burns, R. L.; Koros, W. J. Defining the Challenges for C₃H₆/C₃H₈ Separation Using Polymeric Membranes. *J. Membr. Sci.* **2003**, *211* (2), 299–309. [https://doi.org/10.1016/S0376-7388\(02\)00430-1](https://doi.org/10.1016/S0376-7388(02)00430-1).
- (42) Baker, R. W.; Lokhandwala, K. A.; He, Z.; Pinnau, I. Process, Including PSA and Membrane Separation, for Separating Hydrogen from Hydrocarbons. US Patent 6,183,628 B1, 2001.
- (43) Howard, L. J.; Howard, C. R. Olefin Recovery from Olefin-Hydrogen Mixtures. US Patent 5,634,354, 1997.
- (44) Clark Jr., L. C.; Gollan, F. Survival of Mammals Breathing Organic Liquids Equilibrated with Oxygen at Atmospheric Pressure. *Science* **1966**, *152* (3730), 1755–1756.
- (45) Merkel, T. C.; Bondar, V.; Nagai, K.; Freeman, B. D.; Yampolskii, Y. P. Gas Sorption, Diffusion, and Permeation in Poly(2,2-Bis(Trifluoromethyl)-4,5-Difluoro-1,3-Dioxole-Co-Tetrafluoroethylene). *Macromolecules* **1999**, *32* (25), 8427–8440. <https://doi.org/10.1021/ma990685r>.
- (46) Alentiev, A. Y.; Shantarovich, V. P.; Merkel, T. C.; Bondar, V. I.; Freeman, B. D.; Yampolskii, Y. P. Gas and Vapor Sorption, Permeation, and Diffusion in Glassy Amorphous Teflon AF1600. *Macromolecules* **2002**, *35* (25), 9513–9522. <https://doi.org/10.1021/ma020494f>.
- (47) Scholes, C. A.; Stevens, G. W.; Kentish, S. E. Membrane Gas Separation Applications in Natural Gas Processing. *Fuel* **2012**, *96*, 15–28. <https://doi.org/10.1016/j.fuel.2011.12.074>.
- (48) Miyake, H.; Matsuyama, M.; Ashida, K.; Watanabe, K. Permeation, Diffusion, and Solution of Hydrogen Isotopes, Methane, and Inert Gases in/through Tetrafluoroethylene and Polyethylene. *J. Vac. Sci. Technol. A Vacuum, Surfaces, Film.* **1983**, *1* (3), 1447–1451. <https://doi.org/10.1116/1.572038>.

- (49) Agrinier, P.; Roizard, D.; Ruiz-lopez, M. F.; Favre, E. Permeation Selectivity of Gaseous Isotopes through Dense Polymers: Peculiar Behavior of the Hydrogen Isotopes. *J. Membr. Sci.* **2008**, *318* (1–2), 373–378. <https://doi.org/10.1016/j.memsci.2008.03.011>.
- (50) Leawoods, J. C.; Yablonskiy, D. A.; Gierada, D. S.; Conradi, M. S.; Saam, B. Production and MR Imaging of the Lung. *Concepts Magn. Reson.* **2001**, *13* (5), 277–293.
- (51) Sanderson, K. Big Interest in Heavy Drugs. *Nature* **2009**, *458* (7236), 269.

Chapter 5: Influence of Aliphatic and Aromatic Fluorine Groups on Gas Permeability and Morphology of Fluorinated Polyimide Films

Abstract

Partially fluorinated polymers often exhibit exceptional membrane-based separation performance for a variety of gas pairs. While many gas transport studies focus on the incorporation of aliphatic fluorine groups (*e.g.*, $-\text{CF}_3$) on the polymer backbone, few studies have systematically investigated structure–property relationships for aromatic fluorine groups. Here, the effect of aliphatic and aromatic fluorine groups on solid-state morphology and gas transport is compared for structural analogues of 6FDA-based polyimides that contain either hydrogen or fluorine functional groups on the diamine monomer. Both fluorinated analogues displayed higher gas diffusivity compared to their hydrocarbon-based counterparts. However, the aromatic fluorinated analogue displayed a larger decrease in diffusivity selectivity due to weakened secondary interchain forces and a larger increase in interchain spacing, suggesting a greater extent of packing disruption resulting from increased steric hindrance associated with aromatic fluorine groups. This study establishes guiding principles for how carbon–fluorine bonds affect macromolecular packing structure and gas separation performance.

This chapter has been adapted from: Wu, A. X.; Drayton, J. A.; Rodriguez, K. M.; Qian, Q.; Lin, S.; Smith, Z. P. Influence of Aliphatic and Aromatic Fluorine Groups on Gas Permeability and Morphology of Fluorinated Polyimide Films. *Macromolecules* **2020**, 53 (13), 5085–5095.

5.1. Introduction

Fluorination typically affects the sorption behavior of gases in the polymer, resulting in higher sorption selectivities than those displayed by conventional hydrocarbon-based polymers for certain separations.¹⁻³ Despite displaying the best combinations of permeability and selectivity for all helium-based and most methane-based gas pairs (*e.g.*, H₂/CH₄ and N₂/CH₄),⁴ perfluoropolymers, and more broadly the effect of fluorine groups on gas transport as a whole, are not well-understood in part because of the limited number of perfluoropolymer structures available for testing due to challenging and oftentimes dangerous synthetic conditions.^{5,6} Additionally, all current commercial perfluoropolymers possess only aliphatic fluorine connectivity,¹ leaving the effects of aromatic fluorine groups on gas transport performance still to be investigated. Fluorine atoms, due to their electron withdrawing nature, are expected to interact differently when connected to electron-dense aromatic groups compared to aliphatic groups, which could lead to interesting changes in solid-state morphology and corresponding transport properties.

This study compares two structural analogues of polyimides that contain varying amounts of fluorine, as shown in Figure 5.1, to investigate the effects of aliphatic and aromatic fluorine connectivity on transport properties. The synthesis and characterization of highly fluorinated polyimides are described, and their permeability, diffusivity, and sorption, as well as their respective energetics, are reported. Transport results are rationalized by several means, including materials characterization to probe solid-state morphology, application of transport theory using the Brandt model for activated diffusion, and conformational energy modeling. It should be noted that this study aims to establish fundamental structure–property relationships related to transport performance to aid in the future design of high-performance materials and thus does not attempt to address questions related to plasticization resistance or physical aging of these polymers. Of

course, these types of additional experiments would be highly valuable in the future to better understand the role of fluorine on polyimides for applying these materials to industrial applications.

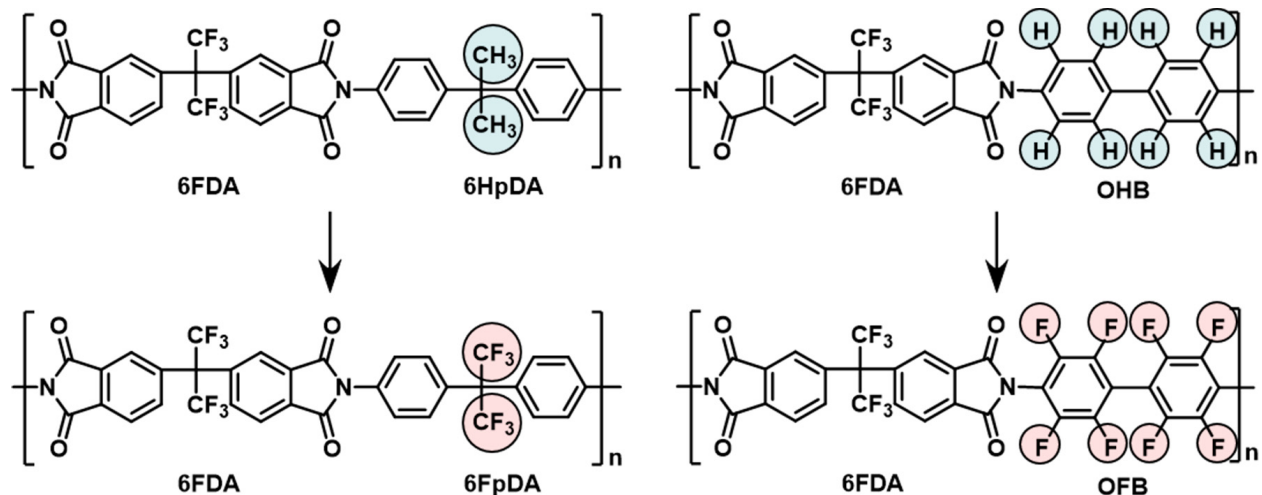


Figure 5.1. Repeat unit structures for the four partially fluorinated polyimides considered in this study. The structural analogue pairs are 6FDA-6HpDA/6FDA-6FpDA and 6FDA-OHB/6FDA-OFB, where the base backbone structure is retained but the diamine is changed to a fluorinated analogue. Functional changes are highlighted for clarity.

5.2. Theory

The effect of temperature on permeability, diffusion, and sorption is described through Arrhenius or Van't Hoff dependencies:⁷

$$P = P_0 \exp\left(-\frac{E_P}{RT}\right) \quad (5.1)$$

$$D = D_0 \exp\left(-\frac{E_D}{RT}\right) \quad (5.2)$$

$$S = S_0 \exp\left(-\frac{\Delta H_S}{RT}\right) \quad (5.3)$$

where P_0 , D_0 , and S_0 are the pre-exponential coefficients, E_p and E_D are the activation energies of permeation and diffusion (kJ mol^{-1}), respectively, and ΔH_S is the enthalpy of sorption (kJ mol^{-1}). Diffusion is considered to be an activated process and therefore has a positive activation energy, while sorption is generally considered to be an exothermic process with a negative enthalpy of sorption. Through the sorption–diffusion model, the energetics can be related:⁷

$$E_p = E_D + \Delta H_S \quad (5.4)$$

The activation energy for diffusion can be related to the penetrant size through the Brandt model for glassy polymers:^{8–10}

$$E_D = cd^2 - f \quad (5.5)$$

where c ($\text{kJ } \text{Å}^{-2} \text{ mol}^{-1}$) and f (kJ mol^{-1}) are constants describing the polymer and d is the kinetic diameter (Å). The c term is the energy scaling factor, and $\sqrt{f/c}$ is a length scale corresponding to an activation energy of zero. Theoretically, $\sqrt{f/c}$ describes the largest size penetrant that could freely diffuse through the interchain polymer spacing without requiring additional energy to widen the channel spacing.¹⁰ From this perspective, the c and f terms describe properties of the polymer backbone in terms of energy required to promote diffusion through the polymer matrix.

5.3. Results

5.3.1. Polymer Synthesis and Structure Confirmation

After the first stage of the reaction shown in Figure 3.1, the resultant poly(amic acid) solutions for 6FDA-6HpDA, 6FDA-6FpDA, and 6FDA-OHB became qualitatively viscous, while the solution for 6FDA-OFB had a viscosity that was similar to that of the monomeric solution, suggesting limited reactivity for the OFB-containing sample. Therefore, the molecular weight of the 6FDA-

OFB poly(amic acid) was evaluated by using GPC, which revealed a predominance of monomeric species, along with some detectable concentration of dimers and trimers of the repeating unit, as presented in Table B.1. The abundance of highly electronegative fluorine atoms on the OFB aromatic ring strongly deactivate diamine nucleophilicity because fluorine is a strong electron-withdrawing group, thus leading to low reaction rates and a correspondingly low molecular weight.^{11,12} To increase molecular weight sufficiently to form a film from the low molecular weight poly(amic acid) solution, the casting procedure outlined in Section 3.2 was followed. In short, Hougham *et al.* proposed that a solid-state chain extension reaction can occur during a high temperature cure for poly(amic acid)s.¹² During this cure, end-to-end chain extension reactions are believed to increase molecular weight while simultaneously imidizing the poly(amic acid), resulting in a continuous polyimide film.¹² The increase in molecular weight for 6FDA-OFB before and after the high temperature cure, as well as the molecular weights for the other polymers, is shown in Table B.1. To retain consistency in thermal history, all polymers were imidized and cast using the same high temperature curing method. The resulting films are shown in Figure 5.2.

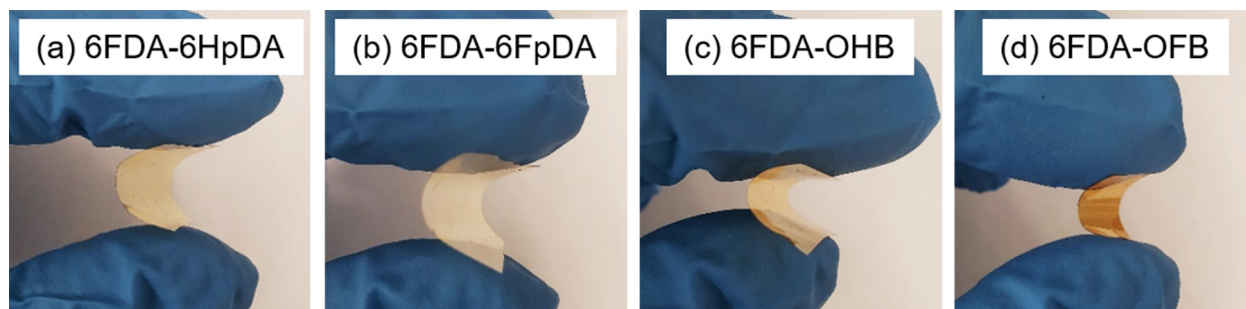


Figure 5.2. Continuous films were formed for (a) 6FDA-6HpDA, (b) 6FDA-6FpDA, (c) 6FDA-OHB, and (d) 6FDA-OFB. All films are transparent and easy to handle.

Synthesis of the expected polyimide structures was verified via FTIR. The FTIR spectra from 400 to 2000 cm^{-1} for all polymers are shown in Figure 5.3, and the full spectra can be found in Figure

B.1. In particular, the presence of characteristic imide peaks at 1780, 1720, and 1380 cm^{-1} show that the high-temperature cure resulted in imidization of the film.^{12,13} In the case of 6FDA-OFB, characteristic aromatic fluorine peaks in the range of 1000–1500 cm^{-1} were present, matching the FTIR spectra of the OFB diamine and indicating retention of the aromatic C–F functionality after the high-temperature cure.¹⁴ Additionally, amide or carboxylic acid peaks associated with the poly(amic acid) structure were not observed, indicating full conversion to the imide structure within the resolution of this technique.¹⁵

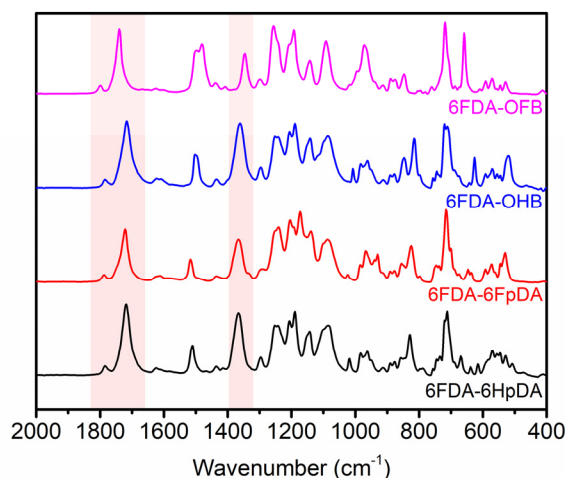


Figure 5.3. FTIR spectra for the four polymers synthesized in this study. The characteristic imide peaks are highlighted in the light red areas. The peaks at 1780 and 1720 cm^{-1} are associated with imide stretching and the peak at 1380 cm^{-1} is associated with C–N imide stretching.

5.3.2. Effect of Fluorination on Pure-gas Permeation, Diffusion, Sorption, and Energetics

The permeabilities of six light gases (He, H₂, O₂, N₂, CH₄, and CO₂) were determined at 15 psi and 35, 45, 55, and 65 °C. Diffusion coefficients for each gas were found via the time-lag method using Equation 3.2, except for He and H₂ because their fast transient behavior could not be captured within the time-scale resolution of the system. Sorption coefficients were then back-calculated via

Equation 4.3. The permeation and diffusion results at 35 °C are shown as a function of effective diameter and effective diameter squared of the penetrant gas molecules in Figure 5.4a and 5.4b, respectively, and the sorption coefficients at 35 °C are shown as a function of penetrant Lennard-Jones temperature in Figure 5.4c.^{7,16} The results for all temperatures are tabulated in Tables B.2 to B.5. Uncertainties were estimated via propagation of error analysis.¹⁷

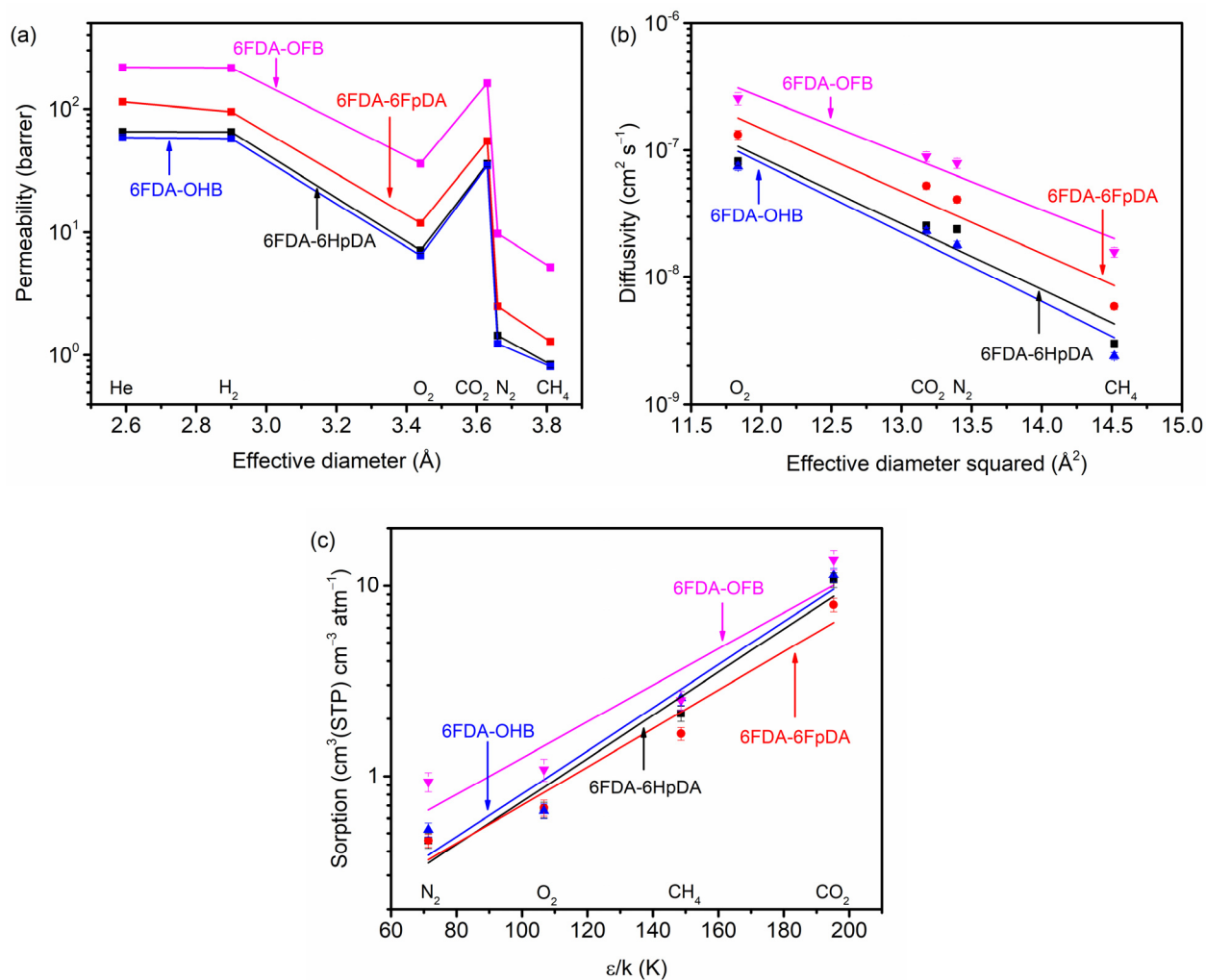


Figure 5.4. (a) Permeability, (b) diffusion, and (c) sorption at 35 °C and 15 psi for all four polymers as a function of correlating variables. Lines in (a) are connected to each data point to guide the eye, and linearized fits are included in (b) and (c).

All polymers followed expected trends for diffusivity and sorption with respect to the size and molecular interaction of the penetrant molecules, respectively.⁷ Permeability versus effective diameter follows trends similar to those of diffusivity with the notable exception of CO₂, which has significantly higher sorption coefficients than other gases of similar size.¹⁸ When comparing permeability across polymers, it is apparent that the more highly fluorinated structural analogues (*i.e.*, 6FDA-6FpDA and 6FDA-OFB) are more permeable than their less fluorinated counterparts. A similar trend was observed for the diffusion coefficients for all polymers, where the more highly fluorinated polymers displayed higher diffusivity values for all gases. On the other hand, the trend for sorption was not immediately as clear. Notably, there was no difference between the degree of fluorination of the polymers and the total sorption of gases. When considering the primary mechanism behind the increase in gas permeability for the more highly fluorinated analogues, it appears that the addition of fluorine has a larger impact on diffusion-related processes compared to sorption-related processes.

In addition to permeability, the effect of fluorine on selectivity was also considered. Table 5.1a presents the permselectivity of relevant gas pairs at 35 °C. When comparing across structural analogues, a modest increase in permselectivity was observed for most gas pairs when comparing 6FDA-6HpDA to 6FDA-6FpDA. Conversely, a significant decrease in permselectivity was observed for most gas pairs when comparing 6FDA-OHB to 6FDA-OFB with the notable exception of N₂/CH₄. Because the more highly fluorinated polymers had higher permeabilities for all gases considered, corresponding increases in selectivity demonstrate trends that are counter to the expected trade-off between permeability and permselectivity as expounded by Robeson, thus indicating some underlying competing effects between diffusion and sorption selectivity.^{4,19}

The slopes of the best-fit lines for the diffusivity and sorption trends in Figures 5.4b and c qualitatively represent a measure of diffusion and sorption selectivity, respectively. These slopes are tabulated in Table 5.1b.^{2,20} When comparing across structural analogues, the diffusion slope became less negative for the fluorinated analogues, indicating a lower diffusion selectivity under the condition where the faster permeating gas is also the smaller gas. Similarly, the sorption slope became smaller for the fluorinated analogues, indicating a higher sorption selectivity under the condition where the faster permeating gas has the weaker polymer–penetrant interaction. The diffusion and sorption selectivities for the N₂/CH₄ gas pair are also presented in Table 5.1b as representative examples of this behavior. Because N₂ is smaller and less polarizable than CH₄, competing effects of diffusion and sorption selectivity are observed; namely, the addition of fluorine results in a simultaneous decrease in diffusion selectivity and increase in sorption selectivity. Moreover, the relative change in each of these terms manifests itself in the overall change in permselectivity.

Following this same type of analysis, the relative effects of aliphatic versus aromatic fluorine groups on diffusion and sorption selectivity can be described by considering the permselectivities of He-based gas pairs. For 6FDA-6HpDA/6FDA-6FpDA, the addition of aliphatic fluorine groups caused a modest decrease in diffusion selectivity that was balanced by the corresponding increase in sorption selectivity, overall resulting in higher permeability while retaining permselectivity. Notably, similar permeability and permselectivity trends have been reported in the literature when comparing separation performance between polymers containing –CF₃ moieties versus other substitutions.^{21–23} In contrast, for 6FDA-OHB/6FDA-OFB, the addition of aromatic fluorine groups resulted in a large decrease in diffusion selectivity that outweighed the increase in sorption

selectivity, resulting in an overall decrease in permselectivity that was more pronounced for gas pairs with larger size differences (*e.g.*, He/CH₄).

Table 5.1. (a) Pure-gas permselectivities for gas pairs of interest and (b) parameters related to overall and specific diffusion and sorption selectivity for all polymers at 35 °C and 15 psi.

(a)	Polymer	$P_{\text{He}}/P_{\text{H}_2}$	$P_{\text{He}}/P_{\text{CO}_2}$	$P_{\text{He}}/P_{\text{N}_2}$	$P_{\text{He}}/P_{\text{CH}_4}$	$P_{\text{N}_2}/P_{\text{CH}_4}$
	6FDA-6HpDA	1.00 ± 0.08	1.8 ± 0.2	45 ± 4	78 ± 7	1.7 ± 0.1
	6FDA-6FpDA	1.20 ± 0.08	2.1 ± 0.2	46 ± 3	89 ± 6	1.9 ± 0.1
	6FDA-OHB	1.02 ± 0.08	1.7 ± 0.1	48 ± 4	73 ± 6	1.5 ± 0.1
	6FDA-OFB	1.01 ± 0.1	1.3 ± 0.1	22 ± 2	42 ± 4	1.9 ± 0.2
(b)	Polymer	Slope of $\ln(D)$ vs D_{eff}^2	Slope of $\ln(S)$ vs ε/k	$D_{\text{N}_2}/D_{\text{CH}_4}$	$S_{\text{N}_2}/S_{\text{CH}_4}$	
	6FDA-6HpDA	-1.2	0.026	8.0 ± 0.8	0.21 ± 0.03	
	6FDA-6FpDA	-1.1	0.023	7.0 ± 0.6	0.27 ± 0.03	
	6FDA-OHB	-1.3	0.026	7.5 ± 0.7	0.20 ± 0.02	
	6FDA-OFB	-1.0	0.022	5.0 ± 0.6	0.37 ± 0.06	

The effect of temperature on permeability is shown in Figure 5.5 for 6FDA-OFB and in Figure B.2 for the other three polyimides. The E_p terms were calculated by fitting these data to Equation 5.1. To calculate E_D , ΔH_S at 15 psi was first calculated from Equation 5.3 over an identical temperature range through direct sorption experiments (see Chapter 6). Next, the value of E_D was calculated from Equation 5.4.²⁴ Calculation of E_D through this method allows for reasonable estimates of E_D for He and H₂, which cannot be obtained with good accuracy through Equation

5.2 for those gases.²⁵ The permeation and diffusion energetics are summarized in Table 5.2. Almost all gas–polymer pairs show a positive value of E_P , indicating that E_D is larger in magnitude than ΔH_S (*i.e.*, $E_D > |\Delta H_S|$), except in the case of CO₂ for 6FDA-OFB where the opposite is the case (*i.e.*, $E_D < |\Delta H_S|$). Thus, permeability increases with increasing temperature except for CO₂ through 6FDA-OFB.²⁴ These findings are common for polymers that are analyzed within the framework of the sorption–diffusion model,^{26–28} although in rare circumstances, negative activation energies of permeation, such as those observed for CO₂ through 6FDA-OFB, can suggest the presence of alternative modes of transport for this gas–polymer pair, such as surface diffusion.²⁹

For most cases, E_D decreased with increasing fluorination across structural analogues, indicating that the more highly fluorinated structures possessed lower barriers to activated diffusion. These trends corresponded with the observed decrease in diffusion selectivity shown in Figure 5.4b, and thus, the origin of the larger decrease in E_D for aromatic fluorine groups compared to that for aliphatic fluorine groups results from an altered packing structure for the more highly fluorinated samples. Structure–property relationships with respect to diffusion energetics, as well as changes in diffusion and diffusion selectivity discussed above, are explored in depth in the following section.

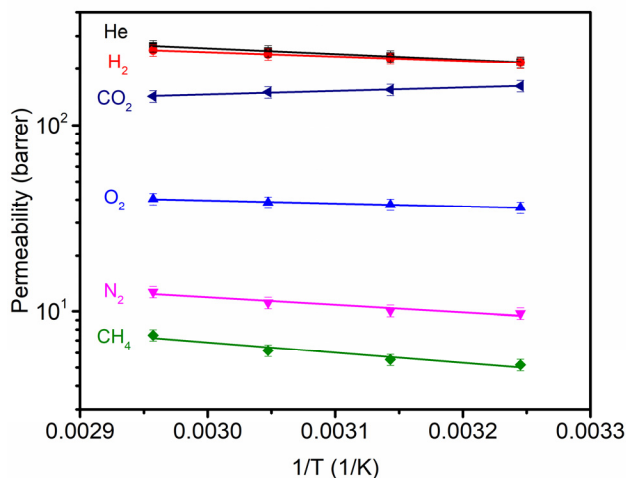


Figure 5.5. Arrhenius plots showing the effect of temperature on gas permeability for 6FDA-OFB measured at 35, 45, 55, and 65 °C and 15 psi. Increasing permeability with temperature was observed for all gases except for CO₂.

Table 5.2. Activation energy of permeation and diffusion for all four polymers. Activation energy of diffusion was calculated via $E_D = E_P - \Delta H_S$ at 15 psi.

Activation energy of permeation (kJ mol ⁻¹)						
Polymer	He	H ₂	O ₂	N ₂	CH ₄	CO ₂
6FDA-6HpDA	9.83 ± 0.02	9.20 ± 0.05	10.9 ± 0.3	20 ± 2	24 ± 1	3.2 ± 0.1
6FDA-6FpDA	8.91 ± 0.03	8.99 ± 0.07	9.2 ± 0.3	17.2 ± 0.7	23 ± 1	2.48 ± 0.08
6FDA-OHB	10.22 ± 0.03	9.9 ± 0.1	12.1 ± 0.4	24 ± 1	25.6 ± 0.3	4.6 ± 0.3
6FDA-OFB	5.74 ± 0.05	4.50 ± 0.01	3.0 ± 0.1	7.6 ± 0.7	10.4 ± 0.9	-3.5 ± 0.1

Activation energy of diffusion (kJ mol ⁻¹)						
Polymer	He	H ₂	O ₂	N ₂	CH ₄	CO ₂
6FDA-6HpDA	14 ± 7	20 ± 1	26.3 ± 0.4	36 ± 2	42 ± 1	21.8 ± 0.9
6FDA-6FpDA	12 ± 7	19 ± 2	21.0 ± 0.8	32.5 ± 0.9	40 ± 1	23.7 ± 0.8
6FDA-OHB	14 ± 5	21 ± 1	27.9 ± 0.7	41 ± 1	45.1 ± 0.4	25.1 ± 0.7
6FDA-OFB	9 ± 5	13 ± 2	18.3 ± 0.8	23.7 ± 0.9	30 ± 2	17.9 ± 0.5

5.3.3. Effect of Fluorination on Solid-state Morphology

The polymers were further characterized to elucidate the effect of aliphatic and aromatic fluorine groups on their solid-state packing structure and morphology. When considering the solid-state packing structure of dense polymer films, the two primary factors with regard to diffusion-related processes are chain mobility and interchain spacing.^{30,31} As such, the polyimide films were characterized via DSC, WAXS, and density measurements, as summarized in Table 5.3. Relevant scans from DSC and WAXS are presented in Figures B.3 and B.4, respectively. The fractional free volume (FFV) was calculated for each polymer via Equation 5.6:

$$FFV = \frac{V - V_{oc}}{V} \quad (5.6)$$

where V is the specific volume of the polymer (cm³ g⁻¹), obtained from the inverse of the experimental density, and V_{oc} is the volume occupied by the polymer chains (cm³ g⁻¹), estimated through Bondi's group contribution method.³²

Table 5.3. Summary of physical characterization data of films related to solid-state morphology.

Polymer	T _g (°C)	<i>d</i> -spacing (Å)	Density (g cm ⁻³)	FFV	<i>c</i> (kJ Å ⁻² mol ⁻¹)	$\sqrt{f/c}$ (Å)
6FDA-6HpDA	314	5.8; 3.5	1.353 ± 0.009	0.163	3.4 ± 0.3	1.8 ± 0.3
6FDA-6FpDA	320	5.9; 3.5	1.448 ± 0.003	0.195	3.2 ± 0.3	1.8 ± 0.3
6FDA-OHB	361	5.6; 3.5	1.456 ± 0.007	0.133	3.9 ± 0.3	1.9 ± 0.2
6FDA-OFB	343	6.5; 3.7	1.559 ± 0.003	0.203	2.5 ± 0.1	1.9 ± 0.2

Changes in the measured T_g, an indicator of chain mobility, can be attributed to a variety of competing sources, most notably secondary interchain forces, steric effects, and backbone rigidity.³³ Steric hindrance effects are sometimes observed when rigid and bulky functional groups are added to the backbone because the larger groups make chain rearrangement more difficult, resulting in decreased chain mobility and a higher T_g.³⁴ For example, the replacement of the three pendant methyl hydrogens with fluorine on polypropylene is estimated to increase T_g from -1 to 21 °C.^{33,35} By comparison, the increase in T_g from 6FDA-6HpDA to 6FDA-6FpDA was a mere 6°C despite the incorporation of two pendant trifluoromethyl groups. This finding suggests that the glassy nature and concomitant backbone rigidity of these polyimide analogues likely diminish the influence that slight changes to aliphatic side groups have on polymer chain cooperativity.

Conversely, an 18 °C decrease in T_g was observed from 6FDA-OHB to 6FDA-OFB, indicating a more significant reduction in steric hindrance effects on polymer chain cooperativity for the aromatic case. Factors that can reduce T_g include either a decrease in the rigidity of the polymer backbone or an increase in chain mobility due to weakened interchain secondary forces.³⁴

Characterization of the d -spacing of the polymers suggests the latter is the primary mechanism behind our observed results. From WAXS analysis in Figure B.4, a secondary peak shift from 3.5 Å for 6FDA-OHB to 3.7 Å for 6FDA-OFB was observed. Packing structures in this length scale are attributed to molecular-level packing structures such as π - π stacking.³⁶ A decrease in the strength of this attractive secondary interaction, as suggested by the increase in d -spacing, could be a consequence of the electronegativity of fluorine. Fluorine acts as a strong electron withdrawing group when attached to aromatic rings.³⁷ In this sense, withdrawing delocalized electrons from the ring that otherwise participate in π - π stacking would decrease backbone interaction strength, increase chain mobility, and lower T_g , which supports the finding we have seen here. Increased chain mobility is commonly associated with lower E_D and higher diffusion coefficients, both of which were observed for 6FDA-OFB.⁹

Evaluation of d -spacing can also be used to describe differences in interchain spacing.⁷ 6FDA-6HpDA had a slightly smaller d -spacing value compared to 6FDA-6FpDA, whereas 6FDA-OHB had a significantly lower d -spacing value than that of 6FDA-OFB. For both structural analogues, such changes can be attributed to the larger size of fluorine compared to hydrogen,³⁸ resulting in less efficient packing and thus larger void spaces. Additionally, the larger impact for the aromatic analogues compared to aliphatic analogues could be attributed to electronic effects. More specifically, aromatic fluorines can withdraw delocalized electrons from the aromatic ring, resulting in higher relative electron densities than those of aliphatic fluorines, which can cause increased interchain spacing. The d -spacing results correspond with trends estimated by FFV, as larger interchain spacing suggests higher free volume for a given sample. Larger d -spacing and FFV are often correlated to larger diffusion coefficients and lower diffusion selectivity, which is true of the structural analogues considered here.⁷ This general trend has been previously observed

for various polymer structures, including other 6FDA-based polyimides and copolymers.^{7,39} Many aromatic polyimides occupy a range of d -spacing between 4.9–6.5 Å and FFV between 0.12–0.20, resulting in CO₂ diffusion coefficients ranging from 5.7×10^{-10} to 10×10^{-8} cm² s⁻¹.^{40–43} Of the four polyimides considered here, 6FDA-OFB and 6FDA-6FpDA show d -spacing, FFV, and CO₂ diffusion coefficients all near the upper limit of this respective range, while 6FDA-OHB and 6FDA-6HpDA reside near the lower limit.

Additional information related to polymer morphology can be obtained from E_D data through the Brandt model (see Equation 5.5).^{8,9} Figure 5.6 shows the relationship between E_D and the kinetic diameter of the gases squared. The resultant c and $\sqrt{f/c}$ terms are tabulated in Table 5.3. The kinetic diameter set, representing the smallest channel inside a zeolite through which the penetrant can fit, is most commonly chosen for the model.^{10,29,44} Within the scope of the model, the kinetic diameter, as opposed to other diameter sets, describes the minimum activation energy to promote diffusion and, in general, provides the best correlations with respect to E_D .^{10,38} Therefore, we use kinetic diameters in this part of our analysis, whereas we previously considered effective diameters.

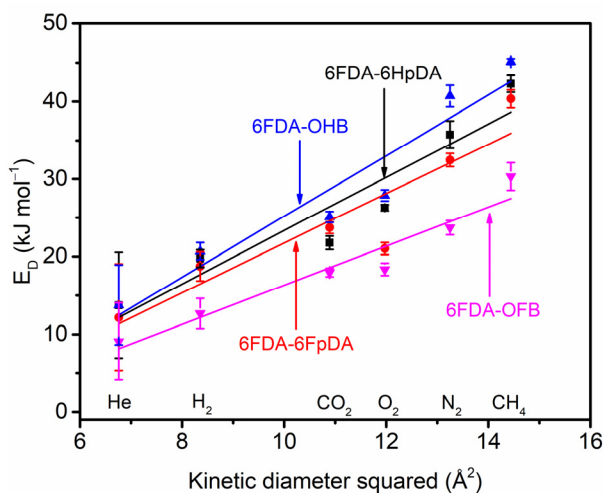


Figure 5.7. Scaling of E_D with penetrant kinetic diameter squared according to the Brandt model.

The slope of the best-fit line, c , or the energy scaling factor, describes how the activation energy scales with penetrant size. In other words, this factor represents the energy required for polymer chains to move sufficiently to reveal an unobstructed surface in the polymer matrix through which gas molecules can diffuse. Therefore, the magnitude of c is closely related to chain mobility. When comparing across structural analogues, it can be seen that the more fluorinated structures have lower c values compared to their counterparts, albeit with the 6FDA-6HpDA/6FDA-6FpDA pair displaying a decrease that is within error. Broadly, chain mobility is comprised of two effects: interchain interactions and intrachain rigidity.⁴⁵ Changes in interchain interactions resulting from fluorination were observed through the WAXS and DSC analysis. However, changes in intrachain rigidity may also contribute towards changes in c and chain mobility.

To investigate effects related to changes in intrachain rigidity, Figures 5.7 show simulated conformational energy diagrams for residues of structural units contained within the diamine portion of each polyimide, where the dihedral angle is the primary rotational bond (see Appendix B for procedure). The plots are normalized such that the global minimum for each diamine is set equal to 0 to allow for straightforward comparison of rotational energy barriers. Here, rotation about bonds is only considered in the diamine portion of the polyimide structure because the dianhydride is the same across all polymers. Of note, this analysis was performed for small segments of structure that are unconnected to neighboring structural units and do not contain characteristic imide linkages. Therefore, this analysis provides a helpful benchmark for assessing rotational energy barriers, but it does not fully consider longer range intramolecular neighboring functionality or intermolecular interactions from adjacent polymer chains.

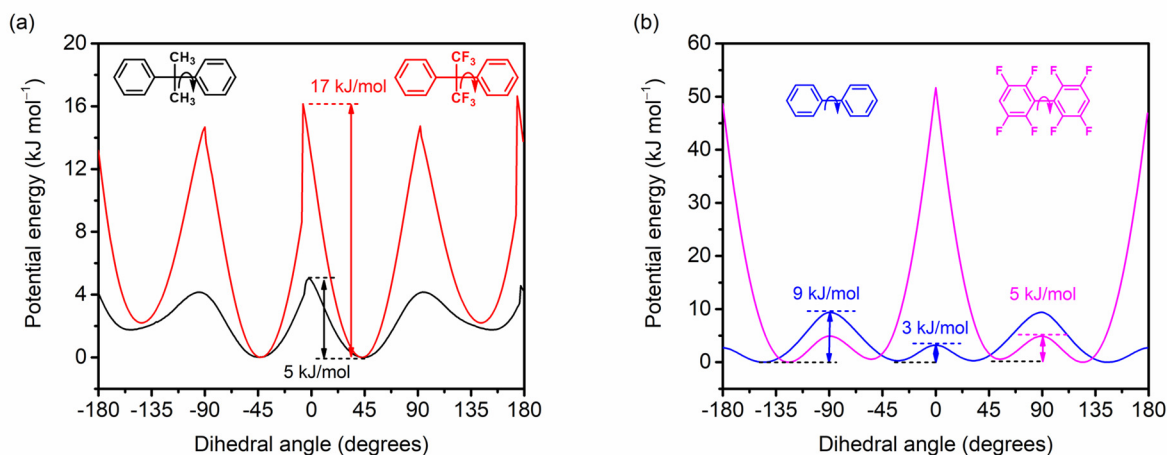


Figure 5.7. Conformational energy diagrams for (a) 6HpDA (black) and 6FpDA (red) and (b) OHB (blue) and OFB (magenta) diamine residues rotated about the indicated bond, simulated using Materials Studio 2019 by BIOVIA.

The energy diagrams for 6HpDA versus 6FpDA are very similar with four preferred conformations (two unique conformations when accounting for symmetry) and similarly sized barriers towards rotation due to the isopropylidene/hexafluoroisopropylidene bridging unit.³³ The difference in activation energy for rotation is likely due to the larger size of $-\text{CF}_3$ versus $-\text{CH}_3$ that causes conformational strain,³² indicating that these two polymers have similar intrachain rigidity. Since little change in the interchain interactions was observed previously, the two polymers therefore possess similar c and E_D values.

On the other hand, the energy diagrams for OHB versus OFB are very different due to changes in structure. OHB has four preferred conformations (two unique conformations when accounting for symmetry) at approximately $\pm 34^\circ$, with two unique barriers to rotation of 3 kJ mol^{-1} and 9 kJ mol^{-1} across the coplanar and orthogonal conformations, respectively. The conformational energy diagram for biphenyl structures has been the focus of researchers in the past, where the effect of steric repulsion between the *ortho*-H atoms, preferring a nonplanar conformation, competes

against effect of delocalized, conjugated π electron density, preferring a coplanar conformation.⁴⁶ It has also been suggested that an attractive H–H bonding interaction is present for biphenyl in its coplanar conformation, acting to stabilize the coplanar transition state and lower the energy barrier for rotation.⁴⁷ In the case of OHB, it appears that the impact of *ortho*-H steric hindrance is small compared to that of delocalized π electrons due to the relatively small size of the H atoms. Therefore, the barrier to rotation across the coplanar conformation is smaller.

Meanwhile, OFB also shows four preferred conformations (two unique conformations when accounting for symmetry) at approximately $\pm 56^\circ$. However, the energy barrier for rotation across the coplanar conformer is prohibitively large, so the only viable barrier towards rotation is across the orthogonal conformation at 5 kJ mol^{-1} . The differences between the OHB and OFB diagrams can largely be explained through steric and electronic arguments stemming from the larger size and electron-withdrawing nature of F atoms. The *ortho*-F atoms, which are larger than *ortho*-H atoms in OHB, would provide greater steric repulsion and result in the large barrier for rotation across the co-planar conformation. Additionally, OFB would have less delocalized π electron density than OHB due to the electron-withdrawing nature of fluorine atoms, resulting in a smaller barrier for rotation across the orthogonal conformation compared to OHB. Additionally, this preferred offset of rings in the fluorinated biphenyl structure suggests less efficient packing for 6FDA-OFB compared to 6FDA-OHB. The less coplanar arrangement of OFB could also inhibit the aforementioned π – π stacking effects. Preferred π – π stacking arrangements, such as off-center parallel stacking and edge-to-face interactions, are spatially more difficult to achieve for more orthogonal arrangements (*i.e.*, OFB) than for more coplanar arrangements (*i.e.*, OHB).⁴⁸ Such an interpretation is supported by WAXS data in Figure B.4. However, the overall differences in rotational energy barriers between OHB and OFB are fairly minimal, thereby suggesting minimal

changes in intrachain rigidity. Therefore, the effects related to decreased interchain interactions are largely responsible for the observed decrease in c and E_D for 6FDA-OFB compared to 6FDA-OHB.

The $\sqrt{f/c}$ term shows change within error when comparing across analogues and so we prefer to avoid an in-depth evaluation of any specific trends. In general, within the Brandt model, this term represents a measure of free volume connectivity. For example, high free volume polymers such as polymers of intrinsic microporosity (PIMs) and their derivatives display $\sqrt{f/c}$ values of 2.4 Å to 2.7 Å.²⁹ Future investigations into correlations between free volume connectivity and $\sqrt{f/c}$ would be very useful to further understand the nature of diffusion in highly glassy polymers, such as those considered in this study.

5.4. Conclusions

The effect of aliphatic and aromatic fluorine substitution on pure-gas permeability, diffusion, sorption, and energetics of transport was elucidated through the comparison of two sets of partially fluorinated 6FDA-based polyimide structural analogues. The pure-gas permeability increased with fluorination primarily as a result of increased diffusion coefficients for both aliphatic and aromatic fluorine substitutions. Permselectivity remained the same for the aliphatic case, whereby the decrease in diffusion selectivity was balanced by an increase in sorption selectivity. In contrast, significantly lower permselectivity was observed in general for the aromatic case because the decrease in diffusion selectivity was larger than the increase in sorption selectivity. The larger decrease in diffusion selectivity for the aromatic fluorine case was consistent with lower activation energies of diffusion. The variations in diffusion coefficients, selectivities, and activation energies were explained by changes in the solid-state polymer morphology. It was found that aliphatic

fluorine substitutions had minimal effect on chain mobility but caused larger inter-chain spacing due to the large size of fluorine, thereby resulting in increased diffusivity and slightly lowered diffusivity selectivity. Aromatic fluorine substitutions showed an increase in chain mobility through a weakening in π - π stacking interactions as well as larger interchain spacing, resulting in much larger diffusivity but significantly decreased diffusion selectivity. These findings enable the development of clear structure-property trends in gas transport for the under-investigated materials space of highly fluorinated polyimides.

5.5. References

- (1) Merkel, T. C.; Pinnau, I.; Prabhakar, R. S.; Freeman, B. D. Gas and Vapor Transport Properties of Perfluoropolymers. In *Materials Science of Membranes for Gas and Vapor Separation*; 2006; pp 251–270.
- (2) Smith, Z. P.; Tiwari, R. R.; Dose, M. E.; Gleason, K. L.; Murphy, T. M.; Sanders, D. F.; Gunawan, G.; Robeson, L. M.; Paul, D. R.; Freeman, B. D. Influence of Diffusivity and Sorption on Helium and Hydrogen Separations in Hydrocarbon, Silicon, and Fluorocarbon-Based Polymers. *Macromolecules* **2014**, *47* (9), 3170–3184. <https://doi.org/10.1021/ma402521h>.
- (3) Wu, A. X.; Drayton, J. A.; Smith, Z. P. The Perfluoropolymer Upper Bound. *AIChE J.* **2019**, *65* (12), e16700. <https://doi.org/10.1002/aic.16700>.
- (4) Robeson, L. M. The Upper Bound Revisited. *J. Membr. Sci.* **2008**, *320* (1–2), 390–400. <https://doi.org/10.1016/j.memsci.2008.04.030>.
- (5) Scott, R. L. The Anomalous Behavior of Fluorocarbon Solutions. *J. Phys. Chem.* **1958**, *62* (2), 136–145. <https://doi.org/10.1021/j150560a002>.
- (6) Song, W.; Rosky, P. J.; Maroncelli, M. Modeling Alkane+perfluoroalkane Interactions Using All-Atom Potentials: Failure of the Usual Combining Rules. *J. Chem. Phys.* **2003**, *119* (17), 9145–9162. <https://doi.org/10.1063/1.1610435>.
- (7) Matteucci, S.; Yampolskii, Y.; Freeman, B. D.; Pinnau, I. Transport of Gases and Vapors in Glassy and Rubbery Polymers. In *Materials Science of Membranes for Gas and Vapor Separation*; 2006; pp 1–47. <https://doi.org/10.1002/047002903X.ch1>.
- (8) Brandt, W. W. Model Calculation of the Temperature Dependence of Small Molecule Diffusion in High Polymers. *J. Phys. Chem.* **1959**, *63* (7), 1080–1084. <https://doi.org/10.1021/j150577a012>.
- (9) Brandt, W. W.; Anysas, G. A. Diffusion of Gases in Fluorocarbon Polymers. *J. Appl. Polym. Sci.* **1963**, *7* (5), 1919–1931. <https://doi.org/10.1002/app.1963.070070527>.

- (10) Freeman, B. D. Basis of Permeability/Selectivity Tradeoff Relations in Polymeric Gas Separation Membranes. *Macromolecules* **1999**, *32* (2), 375–380. <https://doi.org/10.1021/ma9814548>.
- (11) Ghosh, M. *Polyimides: Fundamentals and Applications*; CRC Press, 1996.
- (12) Hougham, G.; Tesoro, G.; Shaw, J. Synthesis and Properties of Highly Fluorinated Polyimides. *Macromolecules* **1994**, *27* (13), 3642–3649. <https://doi.org/10.1021/ma00091a028>.
- (13) Smith, Z. P.; Sanders, D. F.; Ribeiro, C. P.; Guo, R.; Freeman, B. D.; Paul, D. R.; McGrath, J. E.; Swinnea, S. Gas Sorption and Characterization of Thermally Rearranged Polyimides Based on 3,3'-Dihydroxy-4,4'-Diamino-Biphenyl (HAB) and 2,2'-Bis-(3,4-Dicarboxyphenyl) Hexafluoropropane Dianhydride (6FDA). *J. Membr. Sci.* **2012**, *415–416*, 558–567. <https://doi.org/10.1016/j.memsci.2012.05.050>.
- (14) [1,1'-Biphenyl]-4,4'-Diamine, 2,2',3,3',5,5',6,6'-Octafluoro- IR Spectrum. *NIST Chemistry WebBook*.
- (15) Liu, Y.; Wang, R.; Chung, T. S. Chemical Cross-Linking Modification of Polyimide Membranes for Gas Separation. *J. Membr. Sci.* **2001**, *189* (2), 231–239. [https://doi.org/10.1016/S0376-7388\(01\)00415-X](https://doi.org/10.1016/S0376-7388(01)00415-X).
- (16) Shieh, J.; Chung, T. S. Gas Permeability, Diffusivity, and Solubility of Poly(4-Vinylpyridine) Film. *J. Polym. Sci. Part B Polym. Phys.* **1999**, *37*, 2851–2861. [https://doi.org/10.1016/0095-8956\(85\)90059-0](https://doi.org/10.1016/0095-8956(85)90059-0).
- (17) Bevington, P. R.; Robinson, D. K. *Data Reduction and Error Analysis for the Physical Sciences*, 3rd ed.; McGraw-Hill: New York, 2003. <https://doi.org/10.1063/1.4823194>.
- (18) Baker, R. W.; Low, B. T. Gas Separation Membrane Materials: A Perspective. *Macromolecules* **2014**, *47* (20), 6999–7013. <https://doi.org/10.1021/ma501488s>.
- (19) Robeson, L. M. Correlation of Separation Factor versus Permeability for Polymeric Membranes. *J. Membr. Sci.* **1991**, *62* (2), 165–185. [https://doi.org/10.1016/0376-7388\(91\)80060-J](https://doi.org/10.1016/0376-7388(91)80060-J).
- (20) Robeson, L. M.; Smith, Z. P.; Freeman, B. D.; Paul, D. R. Contributions of Diffusion and Solubility Selectivity to the Upper Bound Analysis for Glassy Gas Separation Membranes. *J. Membr. Sci.* **2014**, *453*, 71–83. <https://doi.org/10.1016/j.memsci.2013.10.066>.
- (21) He, Y.; Benedetti, F. M.; Lin, S.; Liu, C.; Zhao, Y.; Ye, H.-Z.; Voorhis, T. Van; Angelis, M. G. De; Swager, T. M.; Smith, Z. P. Polymers with Side Chain Porosity for Ultrapermearable and Plasticization Resistant Materials for Gas Separations. *Adv. Mater.* **2019**. <https://doi.org/10.1002/adma.201807871>.
- (22) Tanaka, K.; Kita, H.; Okano, M.; Okamoto, K. Permeability and Permselectivity of Gases in Fluorinated Polyimides. *Polymer* **1992**, *33* (3), 585–592. https://doi.org/10.2115/fiber.46.12_541.
- (23) Finkelshtein, E. S.; Bermeshev, M. V; Gringolts, M. L.; Starannikova, L. E.; Yampolskii, Y. P. Substituted Polynorbornenes as Promising Materials for Gas Separation Membranes.

- Russ. Chem. Rev.* **2011**, *80* (4), 341–361. <https://doi.org/10.1070/rc2011v080n04abeh004203>.
- (24) Merkel, T. C.; Bondar, V.; Nagai, K.; Freeman, B. D.; Yampolskii, P. Y. Gas Sorption, Diffusion, and Permeation in Poly(2,2-Bis(Trifluoromethyl)-4,5-Difluoro-1,3-Dioxole-Co-Tetrafluoroethylene). *Macromolecules* **1999**, *32* (25), 8427–8440. <https://doi.org/10.1021/ma990685r>.
- (25) Lin, H.; Freeman, B. D. Permeation and Diffusion. In *Springer-Handbook of Materials Measurement Methods*; 2006.
- (26) Aguilar-Vega, M.; Paul, D. R. Gas Transport Properties of Polycarbonates and Polysulfones with Aromatic Substitutions on the Bisphenol Connector Group. *J. Polym. Sci. Part B Polym. Phys.* **1993**, *31* (11), 1599–1610. <https://doi.org/10.1002/polb.1993.090311116>.
- (27) Lin, W. H.; Chung, T. S. Gas Permeability, Diffusivity, Solubility, and Aging Characteristics of 6FDA-Durene Polyimide Membranes. *J. Membr. Sci.* **2001**, *186* (2), 183–193. [https://doi.org/10.1016/S0376-7388\(01\)00333-7](https://doi.org/10.1016/S0376-7388(01)00333-7).
- (28) Costello, L. M.; Koros, W. J. Thermally Stable Polyimide Isomers for Membrane-based Gas Separations at Elevated Temperatures. *J. Polym. Sci. Part B Polym. Phys.* **1995**, *33* (1), 135–146. <https://doi.org/10.1002/polb.1995.090330114>.
- (29) Lai, H. W. H.; Benedetti, F. M.; Jin, Z.; Teo, Y. C.; Wu, A. X.; Angelis, M. G. De; Smith, Z. P.; Xia, Y. Tuning the Molecular Weights, Chain Packing, and Gas-Transport Properties of CANAL Ladder Polymers by Short Alkyl Substitutions. *Macromolecules* **2019**, *52* (16), 6294–6302. <https://doi.org/10.1021/acs.macromol.9b01155>.
- (30) Barrer, R. M. Activated Diffusion in Membranes. *Trans. Faraday Soc.* **1939**, *35*, 644–656. <https://doi.org/10.1039/tf9393500644>.
- (31) Barrer, R. M.; Skirrow, G. Transport and Equilibrium Phenomena in Gas-Elastomer Systems. I. Kinetic Phenomena. *J. Polym. Sci.* **1948**, *3* (4), 549–563. <https://doi.org/10.5254/1.3542972>.
- (32) Park, J. Y.; Paul, D. R. Correlation and Prediction of Gas Permeability in Glassy Polymer Membrane Materials via a Modified Free Volume Based Group Contribution Method. *J. Membr. Sci.* **1997**, *125* (1), 23–39. [https://doi.org/10.1016/S0376-7388\(96\)00061-0](https://doi.org/10.1016/S0376-7388(96)00061-0).
- (33) Odian, G. *Principles of Polymerization*, 4th ed.; John Wiley & Sons Ltd., 2004.
- (34) Hiemenz, P. C.; Lodge, T. P. *Polymer Chemistry*, 2nd ed.; CRC Press, 2007.
- (35) Brown, D. W.; Wall, L. A. Glass Transition Temperature of Several Fluorine-Containing Polymers. *J. Polym. Sci. Part A-2* **1969**, *7*, 601–608. <https://doi.org/10.1021/ba-1965-0048.ch002>.
- (36) Chen, W.; Wu, K.; Qu, Z.; Lu, M. Intrinsic High Thermal Conductive Co-Polyester Based on Offset π - π Stacking. *Eur. Polym. J.* **2019**, *121* (August), 109275. <https://doi.org/10.1016/j.eurpolymj.2019.109275>.
- (37) Holmes, S. A.; Thomas, T. D. Electron Distribution in Trifluoromethylbenzenes. *Electron*

- Donation by the Trifluoromethyl Group. *J. Am. Chem. Soc.* **1975**, *97* (9), 2337–2341. <https://doi.org/10.1021/ja00842a004>.
- (38) van Krevelen, D. W.; te Nijenhuis, K. *Properties of Polymers*, 4th ed.; Elsevier: Oxford, 2009. <https://doi.org/10.1017/cbo9780511623097.008>.
- (39) Sanders, D. F.; Smith, Z. P.; Guo, R.; Robeson, L. M.; McGrath, J. E.; Paul, D. R.; Freeman, B. D. Energy-Efficient Polymeric Gas Separation Membranes for a Sustainable Future: A Review. *Polymer* **2013**, *54* (18), 4729–4761. <https://doi.org/10.1016/j.polymer.2013.05.075>.
- (40) Coleman, M. R.; Koros, W. J. Isomeric Polyimides Based on Fluorinated Dianhydrides and Diamines for Gas Separation Applications. *J. Membr. Sci.* **1990**, *50* (3), 285–297. [https://doi.org/10.1016/S0376-7388\(00\)80626-2](https://doi.org/10.1016/S0376-7388(00)80626-2).
- (41) Chung, T.; Lin, W.; Vora, R. H. Gas Transport Properties of 6FDA-Durene/1,3-Phenylenediamine (MPDA) Copolyimides. *J. Appl. Polym. Sci.* **2001**, *81* (14), 3552–3564.
- (42) Hirayama, Y.; Yoshinaga, T.; Kusuki, Y.; Ninomiya, K.; Sakakibara, T.; Tamari, T. Relation of Gas Permeability with Structure of Aromatic Polyimides I. *J. Membr. Sci.* **1996**, *111* (2), 183–192. [https://doi.org/10.1016/0376-7388\(95\)00173-5](https://doi.org/10.1016/0376-7388(95)00173-5).
- (43) Wang, Y. C.; Huang, S. H.; Hu, C. C.; Li, C. L.; Lee, K. R.; Liaw, D. J.; Lai, J. Y. Sorption and Transport Properties of Gases in Aromatic Polyimide Membranes. *J. Membr. Sci.* **2005**, *248* (1–2), 15–25. <https://doi.org/10.1016/j.memsci.2004.09.015>.
- (44) Breck, D. W. *Zeolite Molecular Sieves: Structure, Chemistry, and Use*; John Wiley & Sons Ltd.: New York, 1974.
- (45) Swaidan, R.; Ghanem, B.; Al-Saedi, M.; Litwiller, E.; Pinnau, I. Role of Intrachain Rigidity in the Plasticization of Intrinsically Microporous Triptycene-Based Polyimide Membranes in Mixed-Gas CO₂/CH₄ Separations. *Macromolecules* **2014**, *47* (21), 7453–7462. <https://doi.org/10.1021/ma501798v>.
- (46) Grein, F. Twist Angles and Rotational Energy Barriers of Biphenyl and Substituted Biphenyls. *J. Phys. Chem. A* **2002**, *106* (15), 3823–3827. <https://doi.org/10.1021/jp0122124>.
- (47) Hernández-Trujillo, J.; Matta, C. F. Hydrogen-Hydrogen Bonding in Biphenyl Revisited. *Struct. Chem.* **2007**, *18* (6), 849–857. <https://doi.org/10.1007/s11224-007-9231-5>.
- (48) Martinez, C. R.; Iverson, B. L. Rethinking the Term “Pi-Stacking.” *Chem. Sci.* **2012**, *3* (7), 2191–2201. <https://doi.org/10.1039/c2sc20045g>.

Chapter 6: Elucidating the Role of Fluorine Content on Gas Sorption Properties of Fluorinated Polyimides

Abstract

Hydrocarbon and perfluorinated polymers display distinct thermodynamic partitioning characteristics. These differences enable perfluoropolymers to outperform hydrocarbon polymers for many membrane-based gas separations, but the mechanism by which fluorine affects gas sorption and sorption selectivity in polymers is still not well-understood. To bridge the existing gap in our fundamental understanding of sorption in hydrocarbon and perfluorinated polymers, this study investigates gas sorption across a range of temperatures, pressures, and gas species for four polyimides containing varying fluorine content. Observed improvements in sorption selectivity for the highly fluorinated polymers were analyzed through the dual-mode model and were found to result primarily from increased Henry sorption selectivity. Additionally, analysis of the energetics of sorption revealed a greater enthalpic penalty for Henry sorption in highly fluorinated polymers. Finally, consistent with the anomalous solubility behavior observed for hydrocarbon–perfluorocarbon liquid mixtures, our results indicate that fluorination appears to affect bulk penetrant–polymer mixing through unfavorable mixing interactions.

This chapter has been adapted from: Wu, A. X.; Drayton, J. A.; Mizrahi Rodriguez, K.; Benedetti, F. M.; Qian, Q.; Lin, S.; Smith, Z. P. Elucidating the Role of Fluorine Content on Gas Sorption Properties of Fluorinated Polyimides. *Macromolecules* **2021**, *54* (1), 22–34.

6.1. Introduction

The unique thermodynamic partitioning of hydrocarbons and perfluorocarbons remains unexplained at a molecular level and cannot be described within the theoretical framework of regular solution theory despite extensive research efforts in the 1950s–1960s as well as more recent computational studies on the topic.^{1–5} The anomalous mixing behavior displayed by perfluorocarbon liquids can be extended to gas–perfluoropolymer systems, where perfluoropolymers show altered sorption trends.^{6–8} In Chapter 4, the exceptional performance of perfluoropolymers on Robeson upper bound plots was reconciled through consideration of distinct hydrocarbon and perfluoropolymer sorption trends within the scope of upper bound theory.⁹ However, the mechanism by which fluorine affects gas sorption and sorption selectivity in polymers is not well-understood. Thus, this study aims to investigate partially fluorinated polyimides to help bridge the gap in understanding between the sorption behavior of hydrocarbon and perfluorinated polymers. Here, the sorption behavior of the four partially fluorinated polyimides studied in Chapter 5 was characterized as a function of pressure and temperature, allowing for analysis of the role of fluorine content on gas sorption in structural analogues. The sorption results were further interpreted through the dual-mode sorption model to determine changes in the Henry and Langmuir sorption modes and their associated energetics with respect to fluorination.

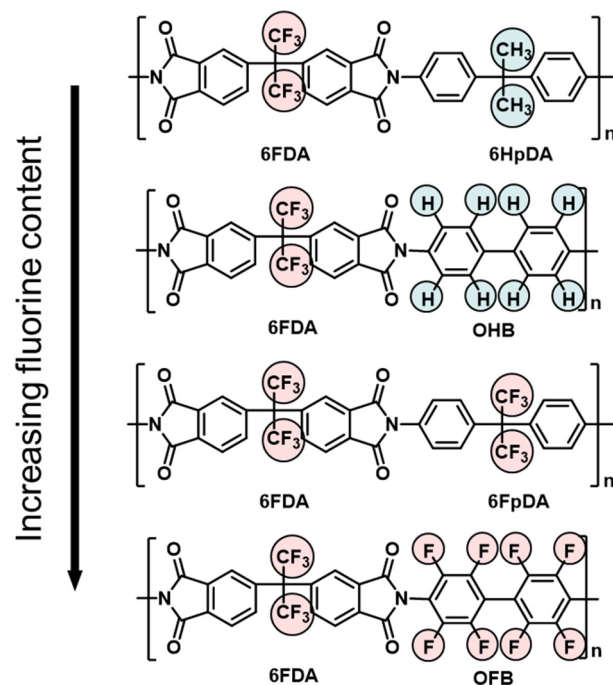


Figure 6.1. The four partially fluorinated polyimides, 6FDA-6HpDA, 6FDA-OHB, 6FDA-6FpDA, and 6FDA-OFB, considered in this work. 6FDA-6HpDA and 6FDA-OHB are considered to be “lightly fluorinated” and 6FDA-6FpDA and 6FDA-OFB are considered to be “highly fluorinated”. The blue and red circles highlight hydrogen and fluorine substitution, respectively. The order of total mole percent of fluorine content, from lowest to highest, is 6FDA-6HpDA < 6FDA-OHB < 6FDA-6FpDA < 6FDA-OFB. The structural analogue pairs are 6FDA-6HpDA/6FDA-6FpDA and 6FDA-OHB/6FDA-OFB.

The dual-mode sorption model was chosen for sorption analysis in this study due to its widespread use in the current membrane literature, representing what we found to be the best compromise between scientific rigor and ease of communication. More specifically, the three model parameters possess a pedagogically compelling connection to physical meaning within the scope of model allowing for the development of structure–property relationships, such as relating changes in structure (*e.g.*, addition of polar groups) to changes in the parameters.^{10–22} It should be noted that

the usefulness of the dual-mode model in describing the physical behavior of gas sorption in polymers has come into question, primarily due to its origin being a simple additive model between Henry and Langmuir sorption models.²³ Additionally, the generation of inconsistent best-fit parameters resulting from nonlinear fitting has also been a concern of several researchers.^{24,25} We address this concern here by reporting a novel method towards the non-linear fitting and achieving reproducible dual-mode model parameters. More recently, models based on the non-equilibrium thermodynamics for glassy polymers (NET-GP) framework have been extensively developed to describe gas sorption in glassy polymers starting from a thermodynamic basis, with the most well-known being the non-equilibrium lattice fluid (NELF) model.^{23,26} The NELF model, based on an assumption of a pseudo-equilibrium state in glassy polymers, has been successfully used in the fitting and prediction of gas sorption in glassy polymers given their respective lattice fluid parameters.²⁷⁻³¹ Interestingly, both the dual-mode sorption and NELF frameworks have shown reliable mixed-gas permeation and sorption predictions when compared to experimental results.^{12,20,25,31-34} Both models capture the physical nature of competitive phenomena. In particular, it has been observed that when dual-mode sorption parameters are retrieved from data sets at multiple temperatures,^{25,35} as done in this work, the prediction of multicomponent sorption is much more in line with that of more sophisticated models.³⁴

Regardless, the mathematical and thermodynamic deficiencies of the dual-mode model were taken into consideration in our analysis and are highlighted here. Additionally, any conclusions made using the dual-mode model are emphasized as such and are kept separate from analyses and conclusions that are not constrained by the model, such as those related to infinite dilution sorption and its energetics. In analyzing the change in gas sorption behavior through the dual-mode model, we aim to provide a preliminary platform toward understanding the role of fluorine on gas sorption

behavior through an approachable and widely-used model while recognizing its deficiencies. Analysis of the role of fluorine using other models, such as NELF, would provide additional insight into the anomalous sorption behavior displayed by these materials and is the subject of Chapter 7. By analyzing sorption data through the lens of multiple sorption models, a more comprehensive understanding of gas sorption in fluorinated materials can be achieved.

6.2. Theory

The sorption coefficient can be determined through direct sorption experiments, in which the concentration of gases sorbed is measured as a function of equilibrium pressure at a fixed temperature to create a sorption isotherm.³⁶ The behavior of gas sorption in glassy polymers is most commonly described using the dual-mode sorption model, which is a simple additive model of Henry and Langmuir sorption:³⁷

$$C = k_D p + \frac{C'_H b p}{1 + b p} \quad (6.1)$$

where C is the concentration of gas sorbed in the polymer ($\text{cm}^3(\text{STP}) \text{cm}^{-3}$), k_D is the Henry's constant ($\text{cm}^3(\text{STP}) \text{cm}^{-3} \text{atm}^{-1}$), p is the equilibrium pressure (atm), C'_H is the Langmuir sorption capacity ($\text{cm}^3(\text{STP}) \text{cm}^{-3}$), and b is the Langmuir affinity constant (atm^{-1}).³⁷ In particular, k_D represents an equilibrium constant of a penetrant in the gaseous state versus in the dissolved state, and b represents an equilibrium constant describing the relative rates of surface adsorption to desorption to the Langmuir mode.³⁸

The sorption coefficient for a gas can be calculated as:³⁷

$$S = \frac{C}{p} = k_D + \frac{C'_H b}{1 + b p} \quad (6.2)$$

In the limit of zero pressure, the infinite dilution sorption coefficient can be calculated, describing the sorption behavior of the first penetrant in the polymer matrix. This term is analogous to the infinite dilution limit of a solute in a solvent considered in solution thermodynamics.³⁹

$$\lim_{p \rightarrow 0} S = S_{\infty} = k_D + C'_H b \quad (6.3)$$

Infinite dilution sorption is an equilibrium process and can thus be described in terms of Gibbs free energy:⁴⁰

$$S_{\infty} = \exp\left(-\frac{\Delta G_{S_{\infty}}}{RT}\right) \quad (6.4)$$

The Gibbs free energy term can be split into its corresponding entropic and enthalpic terms, $\Delta S_{S_{\infty}}$ and $\Delta H_{S_{\infty}}$, respectively, to arrive at the following equation:

$$S_{\infty} = \exp\left(\frac{\Delta S_{S_{\infty}}}{R}\right) \exp\left(-\frac{\Delta H_{S_{\infty}}}{RT}\right) = S_{\infty,0} \exp\left(-\frac{\Delta H_{S_{\infty}}}{RT}\right) \quad (6.5)$$

where $S_{\infty,0}$ is the pre-exponential factor ($\text{cm}^3(\text{STP}) \text{ cm}^{-3} \text{ atm}^{-1}$) and $\Delta H_{S_{\infty}}$ is the infinite dilution heat of sorption (kJ mol^{-1}). As both k_D and b describe equilibrium constants, they are subject to the same analysis and Van't Hoff temperature dependency:³⁸

$$k_D = k_{D,0} \exp\left(-\frac{\Delta H_D}{RT}\right) \quad (6.6)$$

$$b = b_0 \exp\left(-\frac{\Delta H_b}{RT}\right) \quad (6.7)$$

where $k_{D,0}$ and b_0 are pre-exponential factors ($\text{cm}^3(\text{STP}) \text{ cm}^{-3} \text{ atm}^{-1}$ and atm^{-1} , respectively), ΔH_D is the enthalpy of Henry sorption (kJ mol^{-1}), and ΔH_b is the enthalpy of Langmuir sorption

(kJ mol⁻¹).^{37,38} The C'_H parameter has been shown to decrease with increasing temperature, but there exists some debate as to the specific functional form (*e.g.*, linear or Van't Hoff).^{38,41}

The enthalpy of sorption of a gas into a polymer matrix is considered to be a function of two processes: condensation from the gas to sorbed phase and mixing:

$$\Delta H_S = \Delta H_{cond} + \Delta H_{mix} \quad (6.8)$$

where ΔH_{cond} is an exothermic process describing the energy difference between a penetrant in its gaseous state and its sorbed state and ΔH_{mix} is the energy penalty associated with full integration of the penetrant into the polymer matrix.³⁹ Example mixing processes include the energy penalty related to opening a gap in the polymer matrix to accommodate the penetrant and/or energy required to overcome unfavorable chemical interactions with the polymer matrix.³⁹ For many penetrants, ΔH_{cond} is mildly exothermic while ΔH_{mix} is very weakly endothermic, thereby resulting in ΔH_S being exothermic and overall a thermodynamically favorable process.³⁹

The dependence of enthalpy of sorption on penetrant concentration sorbed is described through the isosteric heat of sorption:

$$\left(\frac{d \ln p}{d 1/T}\right)_C = \frac{\Delta H_I}{zR} \quad (6.9)$$

where z is the compressibility factor calculated via an equation of state, and ΔH_I is the enthalpy of sorption at concentration C .³⁸ As such, the shape of the curve for linearized isosteric heat plots describes the behavior of ΔH_S and can be used to deconvolute Langmuir and Henry mode sorption as a function of penetrant concentration.^{35,38,39}

6.3. Results

6.3.1. Gas Sorption Isotherms and Dual-mode Model Parameter Fitting

He, H₂, N₂, O₂, CH₄, and CO₂ high-pressure gas sorption isotherms were measured for the four polyimides at 35, 45, 55, and 65 °C. In all cases, the pressure was corrected for non-ideal behavior using the virial equation of state with second virial coefficients to obtain fugacity.⁴² CH₄ sorption isotherms for the four polyimides at four temperatures are shown in Figure 6.2, along with their dual-mode model fits. The fitting method used is described in detail below. Analogous plots displaying the effect of temperature on the sorption of other gas–polymer pairs are shown in Figures C.1–C.5.

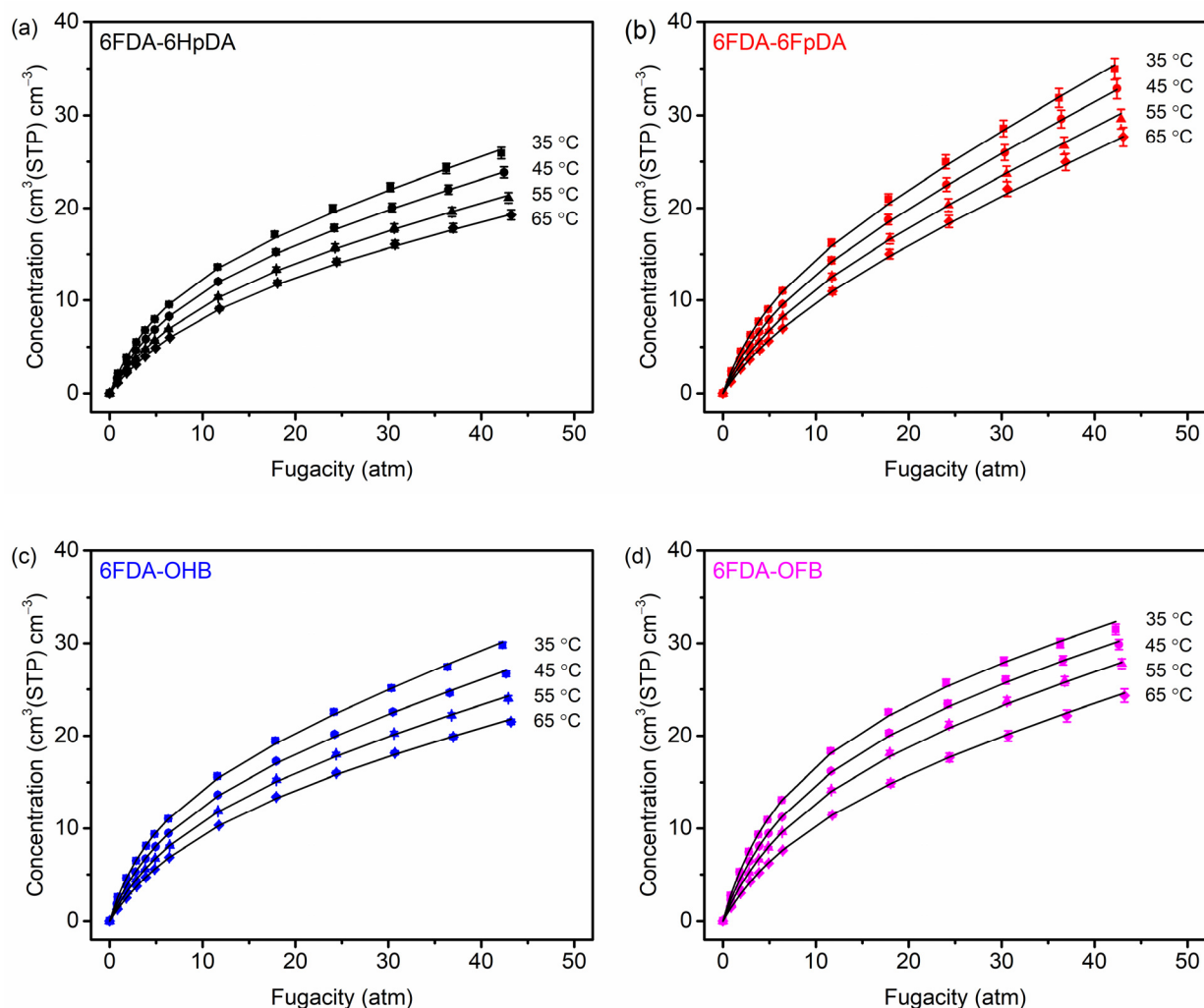


Figure 6.2. Sorption isotherms as a function of CH_4 pressure at 35 °C (squares), 45 °C (circles), 55 °C (triangles), and 65 °C (diamonds) for (a) 6FDA-6HpDA, (b) 6FDA-6FpDA, (c) 6FDA-OHB, and (d) 6FDA-OFB. Individual points indicate experimental data and lines indicate the dual-mode model fits.

The sorption isotherms follow expected behavior with respect to curvature, temperature, and penetrant, *i.e.*, displaying characteristic dual-mode isotherm shapes, decreasing sorption with increasing temperature, and increasing sorption with increasing penetrant condensability.³⁷ When comparing across structural analogues for all gases, the highly fluorinated analogues displayed

higher sorption than that of the lightly fluorinated analogues. As noted in Chapter 5, the substitution of fluorine in both the aliphatic and aromatic cases resulted in higher excess free volume, which is expected to correlate with increased Langmuir sorption capacity.⁴³ Additionally, the slope of the isotherm at high pressures is significantly different across polymers, indicating differences in Henry sorption behavior. The effect of fluorine on the two sorption modes can be decoupled and explored further through comparison of dual-mode model parameters.

To allow for the deconvolution of Henry and Langmuir sorption modes, dual-mode model parameters (*i.e.*, k_D , b , and C'_H) need to be fit through nonlinear optimization. However, it is well known that the model parameters are interdependent (*i.e.*, two unique sets of k_D , b , and C'_H values could give equally optimized fits), leading to imprecise parameter sets that may not be physically meaningful within the context of the model.^{25,35} Therefore, a variety of constraints have been applied to instill more physical meaning to the fitted parameters, most notably by fixing the slope of k_D and/or b versus T_C to match the total sorption versus T_C at a specified pressure and/or by enforcing Van't Hoff constraints for k_D and b if temperature-dependent sorption data is available.^{25,35,44,45} Here, precise best-fit dual-mode parameters were obtained via nonlinear optimization by introducing additional constraints identified through a cross-correlation analysis. The resulting functional form bears similarity to linear free energy relationships (LFERs) for k_D and b , relating the entropic and enthalpic components of Equations 6.6 and 6.7:

$$\Delta H_D = \alpha_D \ln(k_{D,0}) + \beta_D \quad (6.10)$$

$$\Delta H_b = \alpha_b \ln(b_0) + \beta_b \quad (6.11)$$

where α_D , β_D , α_b , and β_b are fitted parameters relating the log of the pre-exponential factor ($\text{cm}^3(\text{STP}) \text{ cm}^{-3} \text{ atm}^{-1}$ for $k_{D,0}$ and atm^{-1} for b_0) to its corresponding enthalpy for k_D and b (kJ

mol⁻¹), respectively.⁴⁶ Additionally, an inequality constraint was applied to the C'_H values such that the value strictly decreased with increasing temperature for a gas–polymer pair, but no particular functional form was enforced.⁴¹

The nonlinear optimization was run in MATLAB using the χ^2 parameter as the objective function, constrained by the Van't Hoff relationship and the LFER for both k_D and b . The uncertainties used for the χ^2 parameter were estimated via propagation of error analysis.⁴⁷ The optimization for each gas–polymer pair considered all temperatures tested, but each unique gas–polymer pair was optimized independently to allow for comparison across both gases and polymers. The error in the best-fit parameters was estimated using a single-parameter approach about a quadratic estimation of the χ^2 surface with respect to that specific parameter.⁴⁷ The optimization conditions are summarized in Table 6.1 below.

Table 6.1. Summary of the constraints and objective function used in the nonlinear optimization to find best-fit dual-mode model parameters for a single gas–polymer pair.

Description	Equation
k_D Van't Hoff	$k_D = k_{D,0} \exp\left(-\frac{\Delta H_D}{RT}\right)$
k_D LFER	$\Delta H_D = \alpha_D \ln(k_{D,0}) + \beta_D$
b Van't Hoff	$b = b_0 \exp\left(-\frac{\Delta H_b}{RT}\right)$
b LFER	$\Delta H_b = \alpha_b \ln(b_0) + \beta_b$
C'_H	$C'_{H,35^\circ\text{C}} > C'_{H,45^\circ\text{C}} > C'_{H,55^\circ\text{C}} > C'_{H,65^\circ\text{C}}$
Objective function	$\chi^2 = \sum_T \sum_i \frac{(C_{model,i} - C_{exp,i})^2}{\sigma_i^2}$

The LFER parameters (α_D , β_D , α_b , and β_b) for each gas–polymer pair (*e.g.*, CH₄ for 6FDA-6HpDA) were determined by running 1000 optimizations constrained *only* by Van’t Hoff relationships for a total of 8 parameters with randomly distributed initial guesses that adhered to realistic physical expectations (*e.g.*, C'_H cannot be negative, etc.), which are summarized in Table C.1. Best-fit parameters that were identified as extreme outliers (*i.e.*, greater than three median absolute deviations from the mean) were removed from the final set, as these originated from optimization runs where the maximum number of 100,000 optimization steps was reached. If LFER constraints were not applied, optimizations using only the Van’t Hoff relationships resulted in significant variability in parameters with multiple unique parameter sets having the same minimized χ^2 value as mentioned above. Example resultant $\ln(k_{D,0})$ versus ΔH_D and $\ln(b_0)$ versus ΔH_b plots are shown in Figure 6.3a with their best-fit line and parameters. All LFER parameters are tabulated in Table C.2.

With the LFER parameters for all gas–polymer pairs, the LFER constraints were introduced to the optimization to determine precise best-fit dual-mode model parameters. Histograms comparing the variation in results for 1000 runs for the best-fit ΔH_D with and without the LFER constraints are shown in Figure 6.3b. Introduction of the LFER constraint eliminated two optimization variables and greatly improved the precision of the parameters, essentially allowing the optimization to output a single set of best-fit parameters independent of the initial guess. The best-fit parameters are fully tabulated in Table C.3 and the resultant dual-mode model parameters are tabulated in Tables C.4–C.7.

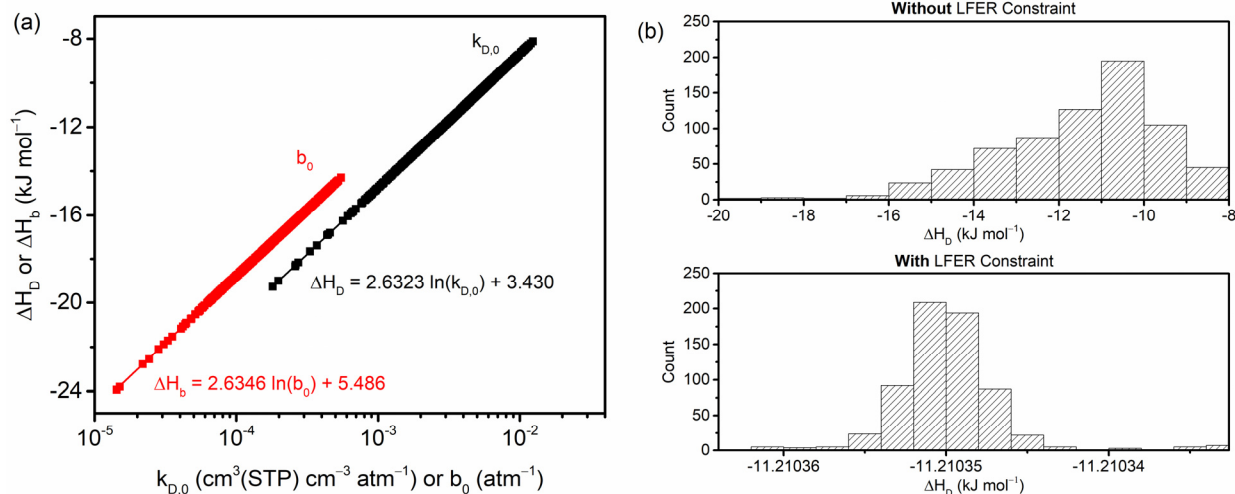


Figure 6.3. (a) Resultant LFERs observed through a cross-correlation analysis of 1000 initial guesses for CH₄ in 6FDA-6HpDA using only the Van't Hoff constraints. The best-fit line showing the LFER parameters is shown for both k_D and b . (b) Histogram showing the change in precision of the output ΔH_D parameter with and without the LFER constraint for the 1000 initial guesses. All other parameters experienced a similar narrowed distribution.

It should be noted that dual-mode model fits are not feasible for the He and H₂ isotherms obtained due to their linearity at the pressures and temperatures tested, consistent with other literature observations.^{7,39,40,44} Here, a careful distinction must be made regarding the sorption of He and H₂. It has been observed that H₂ isotherms at low temperatures and high pressures show curvature,⁴⁰ indicating separate Henry and Langmuir sorption modes as dictated by the dual-mode model. Expecting similar behavior for He, the curvature indicates that Langmuir sorption occurs at low pressures, thereby suggesting that the isotherms observed in Figures C.4 and C.5 only appear linear due to the low pressure range tested and is not indicative of sorption in the Henry mode. Therefore, linear fits were performed using only the two linear isotherm-related constraints (*i.e.*, k_D Van't Hoff and k_D LFER from Table 6.1). The constrained linear optimization of the He and H₂ isotherms produced slopes that were used for S_∞ and ΔH_{S_∞} related analyses only.

6.3.2. Effect of Fluorination on Sorption and Dual-mode Parameters

It is a well-documented phenomenon that perfluoropolymers display high sorption selectivity for certain gas pairs.^{6-9,48} This behavior is best visualized when considering sorption trends with respect to metrics of condensability, such as Lennard-Jones parameters, ε/k :

$$\ln(S) = M \times \varepsilon/k + N \quad (6.12)$$

where M and N are the best-fit slope and intercept, respectively.³⁷ It has been previously shown that hydrocarbon and perfluorocarbon polymers show distinct sorption trends when applying Equation 6.12 for various gases; that is, perfluoropolymers show a decreased slope and an increased intercept relative to their hydrocarbon counterparts, resulting in higher sorption for lighter gases and lower sorption for heavier gases.^{6,9} To elucidate the role of fluorine content on sorption for samples considered in this study, trends related to the infinite dilution sorption coefficient were investigated. Using the infinite dilution sorption coefficient removes the role of pressure on sorption as a variable, and thus, sorption is represented solely as the interactions between the penetrant and polymer being considered.

The S_∞ parameter is a function of three independent variables: testing temperature, penetrant properties (*e.g.*, condensability, size, etc.), and polymer-related properties (*e.g.*, fluorine content, etc.). Analogous to Equation 6.12, the sorption at infinite dilution (*i.e.*, in the limit as pressure approaches zero) follows a trend with respect to metrics of condensability, plotted in Figure C.6a for the four polyimides:

$$\ln(S_\infty) = A \times \varepsilon/k + B \quad (6.13)$$

where A and B are parameters derived from the best-fit line for each polymer. Other measures of condensability, such as critical temperature (T_C), are commonly used for these trends as well.⁷ The

best-fit parameters describe the general behavior of S_∞ with respect to penetrant properties, and thus represent properties of the polymer. Of particular interest in this study is the role of fluorine content on gas sorption, which can be represented in a convenient and straightforward way by calculating the van der Waals volume fraction of fluorine, ϕ_F , within a repeat unit via Bondi's group contribution method.⁴⁹ Volume fraction of fluorine was chosen as the measure of fluorine content because of its prevalence in site-based mixing models for both regular and polymer solution theories.^{50,51}

Here, A and B represent polymer properties that can then be correlated with respect to ϕ_F to quantify how changes in polymer composition affect sorption behavior. The effect of fluorine content on the slope of Equation 6.13 is shown in Figure 9.4 for each polymer, demonstrating a monotonic decreasing linear trend. The slope is of particular interest for gas separation applications because it dictates the sorption selectivity and thus affects the energy efficiency of the process. Trends for k_D and b are discussed further below. The existence of a continuous trend for the slope suggests that the distinct sorption trends for hydrocarbon and perfluorocarbon polymers could be unified by an additive model based on fluorine content. Thus, investigating the sorption of gases in partially fluorinated materials could provide deeper insight into sorption behavior that is currently viewed as anomalous.⁵² Additionally, there are other relevant material properties to gas separations that are viewed as anomalous for perfluoropolymers, such as physical aging and plasticization.^{6,53,54} Because these materials properties correlate with second derivatives of fundamental relations in thermodynamics,⁵⁵ such as coefficients of thermal expansion, the continuous nature of the trends in Figure 9.4 suggests that studying partially fluorinated polymers may provide insights into phenomena other than gas sorption that are also not well-understood today. Of course, such interpretations must be bound carefully within the framework of non-

equilibrium thermodynamics,^{26,27} since the aforementioned properties of physical aging and potentially plasticization would need to be applied to non-equilibrium glassy polymers.

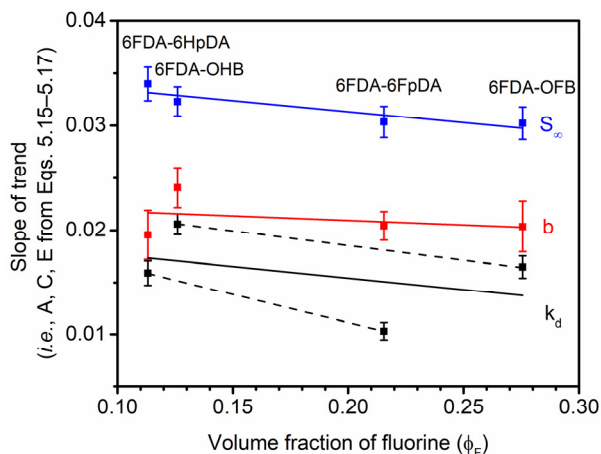


Figure 9.4. The slope for the S_∞ , k_D , and b sorption correlations for each polymer with respect to ε/k , plotted as a function of fluorine volume fraction, ϕ_F . The black dashed lines highlight the change in C across structural analogues.

The analysis procedure for S_∞ can be replicated for any macroscopic parameter of interest. Here, we select the k_D and b parameters from the dual-mode model to deconvolute the effects of Henry and Langmuir sorption modes on overall sorption capacity. The k_D and b parameters can be correlated with ε/k in a similar way to S_∞ , as shown in plots in Figure C.6b and C.6c for the four polyimides, and shown by the following equations:

$$\ln(k_D) = C \times \varepsilon/k + D \quad (6.14)$$

$$\ln(b) = E \times \varepsilon/k + F \quad (6.15)$$

where C , D , E , and F are best-fit parameters representing polymer properties.³⁷ The effect of fluorine content on the slopes of Equations 6.14 and 6.15 is shown in Figure 6.4 for each polymer, allowing for comparison of the relative effects of Henry and Langmuir sorption on total sorption.

When comparing across structural analogues, a lower slope was observed for Henry sorption for both of the highly fluorinated structures, while the slope was relatively invariant for Langmuir sorption, suggesting that changes in Henry sorption selectivity are the primary driver behind changes in S_{∞} with respect to fluorine content. Henry sorption in polymers is typically described as “equilibrium sorption”, where the penetrant (solute) is envisioned as being fully dissolved into the equilibrium free volume of the polymer matrix (solvent); as such, k_D for individual gases is a function of bulk penetrant–polymer mixing interactions and is analogous to mixing processes considered in regular solution theory.^{38,39} Thus, within the context of the dual-mode model, it appears that fluorine affects the equilibrium mixing process and causes changes in sorption selectivity. This result is consistent with previous hydrocarbon–perfluorocarbon liquid miscibility studies, where hydrocarbon–perfluorocarbon alkane analogues (*e.g.*, n-hexane and n-perfluorohexane) were found to be immiscible despite possessing similar Hildebrand solubility parameters.⁶ The anomalous Henry sorption behavior of perfluorocarbon liquids seems to extend to partially fluorinated polymers when viewed through the dual-mode model.

The existence of two separate trends for Henry sorption, instead of one unified trend relating the change in C to ϕ_F , could be attributed to the difference in structural groups on polymer properties. From an energetics perspective, Henry sorption imposes enthalpic penalties related to mixing, namely energy to open a gap in the polymer matrix large enough to accommodate the penetrant and energy to overcome unfavorable mixing interactions with the bulk matrix.^{38,39} The energy to open a gap in the polymer matrix can be related to backbone stiffness (*i.e.*, glass transition temperature (T_g)), where a lower stiffness would expect to result in a smaller enthalpic penalty and lower selectivity (*i.e.*, higher C). In Chapter 5,⁴³ it was found that there was negligible change in T_g from 314 °C to 320 °C for the 6FDA-6HpDA/6FDA-6FpDA pair and a moderate decrease in

T_g from 361 °C to 343 °C for the 6FDA-OHB/6FDA-OFB pair. For the 6FDA-6HpDA/6FDA-6FpDA pair, this interpretation suggests that the decrease in C is effectively a result of only increased unfavorable mixing interactions caused by fluorination. Meanwhile, for the 6FDA-OHB/6FDA-OFB pair, a decrease in C is observed even with the decrease in T_g . The competing effects between backbone stiffness and unfavorable mixing interactions could explain the smaller decrease in C observed for 6FDA-OHB/6FDA-OFB compared to that for 6FDA-6HpDA/6FDA-6FpDA despite the larger increase in fluorination for the former pair. While C appears to be a function of polymer properties other than fluorine content, for these cases, an increase in Henry sorption selectivity was observed with increasing fluorination and is responsible for increased sorption selectivity.

On the other hand, changes in Langmuir sorption are insignificant. As mentioned in Section 6.2, the total Langmuir contribution consists of b and C'_H terms. Here, only changes in b are considered because it is more closely associated with the thermodynamics of polymer–penetrant interactions. In contrast, C'_H values are closely correlated with excess free volume, which has a larger impact on diffusion-related properties.^{41,43} Strictly, b represents the relative surface adsorption to desorption rates of the penetrant onto the excess free volume surfaces inside the polymer matrix.³⁸ While it is expected that the presence of fluorine groups would have an effect on surface–penetrant interactions, such an effect was not observed for the dense polymers considered here.

In order to provide a broader context for the observed changes in sorption trends, the change in A and B (see Equation 6.13) with respect to polymer properties was compared against other S_∞ data reported in the literature. Note that to enable more robust conclusions, this section only includes literature data that also reports helium and hydrogen infinite dilution sorption data, which limits the total amount of viable data sets. Polymers considered in this analysis include hydrocarbon

polymers (*e.g.*, PIM-1)⁵⁶, other partially fluorinated polyimides (*e.g.*, 6FDA-HAB)^{7,35,44}, and perfluorinated polymers (*e.g.*, Teflon[®] AF 2400)^{39,57}. In this case, a weak linear correlation was observed when considering the change in A with respect to ϕ_F , as shown in Figure 6.5a. A moderate amount of vertical variation off of the best-fit line was observed as well, indicating that other functional groups present on the polymer backbone (*e.g.*, carbonyl, nitrile, dioxolane groups) likely have a moderate effect on the slope, and therefore sorption selectivity, but the magnitude of the change is comparatively less than that of fluorination. Another correlation was observed when considering the change in B with respect to inverse fractional free volume ($1/\text{FFV}$), as shown in Figure 6.5b. As discussed in Chapter 5,⁴³ the large size of fluorine generally results in more frustrated packing and therefore higher FFV. Using $1/\text{FFV}$ in place of ϕ_F as the correlating variable allows for the inclusion of high-free volume polymers in the correlation, indicating that the intercept of the trend relates only to FFV. In short, comparison of S_∞ trends (see Equation 6.13) across a variety of polymers suggests that the slope is a function of ϕ_F and the intercept is inversely related to FFV, thus fully describing the parameters in this trend in terms of polymer properties. It should be noted that these correlations are not meant to be predictive but instead demonstrate interesting trends. Larger data sets and sorption testing of partially fluorinated polymers in the 0.3 to 0.5 fluorine volume fraction range could enable more robust and predictive conclusions.

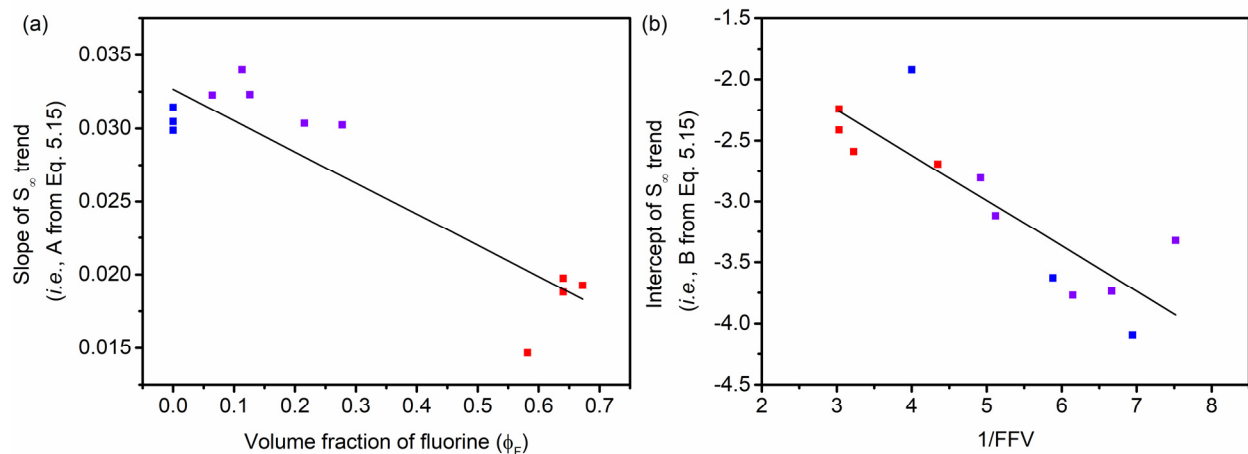


Figure 6.5. The (a) slope and (b) intercept of the S_{∞} correlation reported in the literature with respect to ε/k , plotted as a function of ϕ_F and $1/FFV$, respectively. The blue points represent fully hydrocarbon polymers (PIM-1,⁵⁶ Matrimid,^{7,58} and polysulfone^{7,59}), the purple points represent partially fluorinated polymers (6FDA-HAB^{7,35,44} and the four polymers investigated here), and the red points represent perfluorinated polymers (Hyflon[®] AD 80,⁶ Teflon[®] AF 1600,⁶⁰ and Teflon[®] AF 2400^{39,57}).

6.3.3. Effect of Fluorine on LFERs

As discussed in Section 6.2, S_{∞} is a fundamental thermodynamic parameter analogous to infinite dilution solubility. Therefore, within the framework of classical thermodynamics, we sought to carefully investigate the role of fluorination on S_{∞} to provide clearer insight into the mechanism of sorption. Similar to Equations 6.10 and 6.11, an LFER can be used to relate the entropic pre-exponential factor of a Van't Hoff relationship to its corresponding enthalpy for each polymer from Equation 6.5:

$$\Delta H_{S_{\infty}} = \alpha_{S_{\infty}} \times \ln(S_{\infty,0}) + \beta_{S_{\infty}} \quad (6.16)$$

An LFER was constructed for each polymer by first determining its infinite dilution sorption enthalpy and pre-exponential factor for each gas and then fitting these data to obtain the coefficients, α_{S_∞} and β_{S_∞} . The concept of LFERs, also termed as entropy–enthalpy compensation (EEC), is a common occurrence in the physical sciences. For example, within catalysis, it has been widely observed that the entropic and enthalpic terms of a reaction are linearly related.^{61–63} Nevertheless, despite being frequently reported, the molecular origin of this relationship is still heavily debated today.^{64,65} The most common forms of LFERs are Hammett plots, which show a linear relationship between the reaction rate and equilibrium constant for reactions with similar mechanisms; for example, the original Hammett plot is centered on the mechanism of benzoic acid deprotonation and describes the effect of various meta- and para- substituents on the reaction rate and equilibrium constant.⁶¹

Within the membrane field, the concept of EEC has been generalized to apply for physical processes, such as activated diffusion, to excellent agreement.^{66–68} Based on the Hammett plot interpretation, polymers with similar α_{S_∞} and β_{S_∞} coefficients have similar mechanisms for infinite dilution sorption.⁴⁶ Therefore, to investigate if the anomalous sorption behavior of fluorinated polymers was additively linked to LFERs, this relationship was plotted in Figure C.7 for the four polyimides and the resulting slope and intercept are plotted in Figure 6.6. These findings reveal an exponential relationship with respect to fluorine content and a good fit for both α_{S_∞} and β_{S_∞} , suggesting a continuous change in the mechanism for infinite dilution sorption with increasing fluorine content. The exponential nature also suggests that a small amount of fluorine has a large effect on the LFER coefficients and could therefore show relatively significant impact on the observed sorption selectivity even at small volume fractions. While these results are intriguing, one must be careful of drawing significant mechanistic conclusions from this analysis.

Additional studies of the application of EEC for sorption processes on a broader set of samples would be required to provide deeper insight into changes in mechanism with respect to fluorine content.

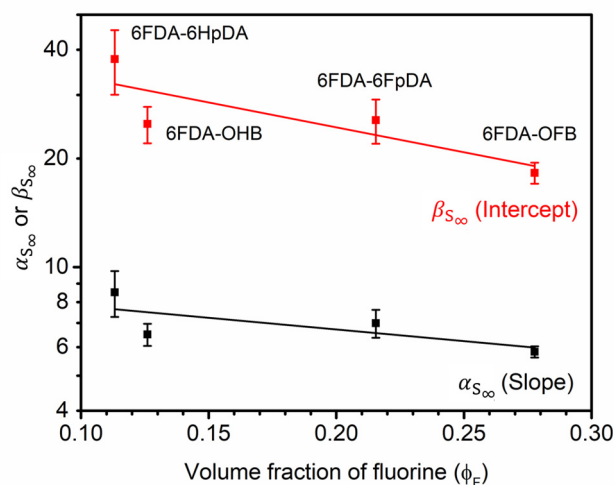


Figure 6.6. The slope and intercept of the experimental S_∞ LFER trend for each polymer plotted as a function of ϕ_F . The exponential relationship shown suggests a change in sorption mechanism with respect to degree of fluorination.

6.3.4. Effect of Fluorine on Sorption Energetics

To further investigate changes in sorption behavior with respect to fluorine content, sorption energetics for infinite dilution sorption and dual-mode parameters were evaluated. The enthalpy of sorption at infinite dilution can be determined via Equation 6.5. Figure 6.7a displays the calculated ΔH_{S_∞} values for each gas–polymer pair, as well as reported ΔH_{S_∞} values for the subset of the hydrocarbon, partially fluorinated, and perfluorinated polymers considered in Figure 6.5. The ΔH_{S_∞} values can be roughly divided into two regimes where (1) hydrocarbon-based polymers and partially fluorinated polymers show ΔH_{S_∞} values ranging from -8 kJ mol^{-1} for H_2 to -28 kJ mol^{-1} for CO_2 and (2) perfluoropolymers span a smaller range of ΔH_{S_∞} values from -8 kJ mol^{-1}

for H₂ to -16 kJ mol^{-1} for CO₂.^{39,60} To the best of our knowledge, there are no sorption energetics points for He in perfluoropolymers reported in the literature. Interestingly, the ΔH_{S_∞} values in regime 1 show relative independence with respect to fluorine content. Comparing differences in ΔH_{S_∞} values across regimes 1 and 2, it is apparent that a larger endothermic penalty is observed for perfluoropolymers with the magnitude of the penalty being larger for the most condensable penetrants. Stated another way, when comparing regime 2 to regime 1, ΔH_{S_∞} is increasingly more negative in the follow order: H₂ > N₂ > O₂ > CH₄ > CO₂.

Two hypotheses could explain this observed behavior of ΔH_{S_∞} . The first hypothesis is that ΔH_{S_∞} has an exponential dependence with respect to ϕ_F such that increases in ΔH_{S_∞} do not appear significant until high ϕ_F values are approached. This hypothesis could be empirically fit and validated with access to more sorption experiments for intermediate values of ϕ_F between 0.3 and 0.6. The second hypothesis is that there are differences in sorption site availability of non-perfluorinated and perfluorinated polymers. Since ΔH_{S_∞} describes the enthalpy for the first penetrant in the system, it is expected that the first penetrant will preferentially sorb into its most favorable domain. Hydrocarbon and partially fluorinated polymers share identical backbone moieties, such as C–H bonds, such that the most favorable site for the first penetrant could be equivalent irrespective of fluorine content. On the other hand, perfluoropolymers possess chemistry that is fundamentally different from that of non-perfluorinated polymers, thereby forcing sorption into relatively less favorable domains containing C–F bonds. This second hypothesis could be tested by comparing ΔH_{S_∞} values for partially fluorinated or perfluorinated polymers with equivalent ϕ_F values or by comparing ΔH_S values at high pressures where the preferential sites are hypothesized to be saturated. The latter consideration is described in detail later.

As mentioned in Section 6.2, the k_D and b dual-mode parameters both follow Van't Hoff relationships with respect to temperature (see Equations 6.6 and 6.7). Individually, each enthalpy describes the difference in energy between a penetrant in the gaseous state, H_g , and a penetrant sorbed through its respective mode, such that their difference describes the relative energy difference between the two states:³⁸

$$\Delta H_D = H_D - H_g \quad (6.17)$$

$$\Delta H_b = H_b - H_g \quad (6.18)$$

$$\Delta H_D - \Delta H_b = H_D - H_b \quad (6.19)$$

In a typical case, ΔH_b is more negative than ΔH_D , indicating that sorption into Langmuir modes is more favorable than sorption into Henry modes. This feature is attributed to differences in ΔH_{mix} for the two processes – Langmuir sorption has very little mixing penalty while Henry sorption has additional associated endothermic processes such as moving chains to open a gap in the matrix and overcoming unfavorable chemical interactions.^{38,39} Typical values of $\Delta H_D - \Delta H_b$ are in the range of 5–8 kJ mol⁻¹, with variation depending on the penetrant and polymer system tested.^{38,69,70}

The enthalpies of the individual modes of sorption within the dual-mode model were fitted through the optimization procedure described above. The difference in energetics between Henry and Langmuir sorption for each gas as a function of ϕ_F is shown in Figure 6.7b. In general, each gas shows a monotonic increase in $\Delta H_D - \Delta H_b$ across polymers, indicating an increasingly larger difference in energy between the two modes of sorption. Recalling Equation 6.8, the enthalpy of sorption can be decoupled into ΔH_{mix} and ΔH_{cond} . As ΔH_{cond} is determined by the penetrant identity,⁷¹ $\Delta H_D - \Delta H_b$ showcases differences in ΔH_{mix} across the two sorption modes. Since changes in $\Delta H_D - \Delta H_b$ are largely driven by changes in ΔH_D (see Table C.3), the observed

increase in $\Delta H_D - \Delta H_b$ could then be attributed to an increasingly endothermic ΔH_{mix} for the Henry sorption mode with respect to fluorine content, while that for the Langmuir mode is relatively unchanging. As mentioned in Chapter 5,⁴³ it was found that for these polymers, the change in the glass transition temperature was negligible when comparing 6FDA-6HpDA/6FDA-6FpDA and was slightly lower for the fluorinated analogue when comparing 6FDA-OHB/6FDA-OFB. Thus, this trend in the energy difference between the sorption modes suggests that the energy involved in gap opening is small compared to the energy involved in overcoming the increasing amount of unfavorable C–F interactions. Within the context of the dual-mode model, this finding suggests that the mixing process of Henry sorption is affected by fluorine content, again drawing parallels to the anomalous immiscibility observed by hydrocarbon and perfluorocarbon liquids.⁶

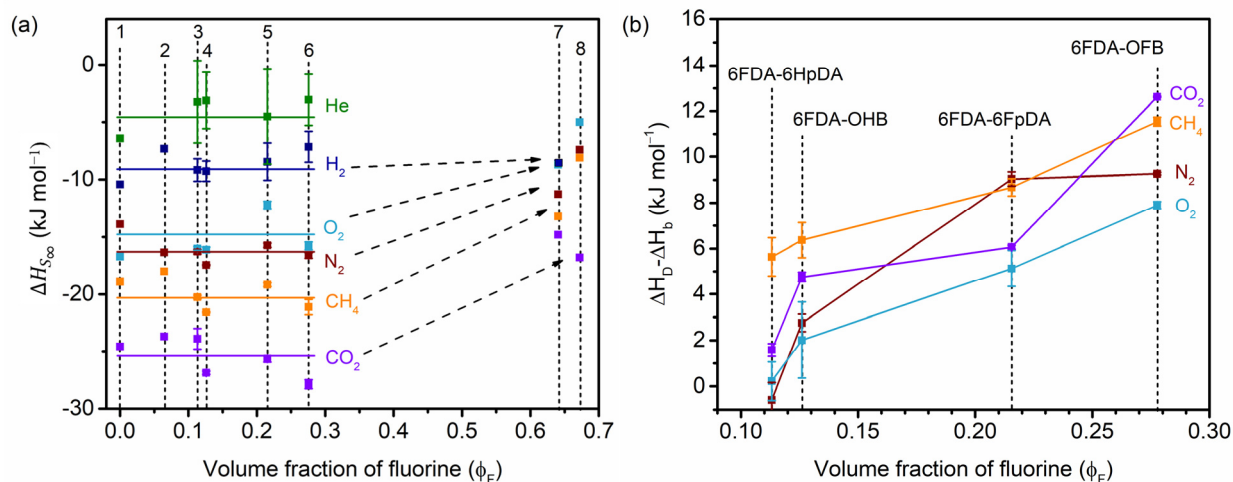


Figure 6.7. (a) Calculated ΔH_{S_∞} values for the four polymers, along with representative literature data, plotted as a function of ϕ_F . The polymers are labeled numerically in the following order: PIM-1,^{72,73} 6FDA-HAB,³⁵ 6FDA-6HpDA, 6FDA-OHB, 6FDA-6FpDA, 6FDA-OFB, Teflon[®] AF 2400,³⁹ and Teflon[®] AF 1600.⁶⁰ The horizontal lines are to guide the eye. (b) The difference in $\Delta H_D - \Delta H_b$ for the four polymers, representing the energy difference between the two modes of sorption, plotted as a function of ϕ_F .

The effect of fluorine on ΔH_I was also evaluated. The isosteric heat of sorption describes ΔH_S as a function of penetrant concentration and, for glassy polymers examined using the dual-mode model, shows the transition from sorption into Langmuir modes at low concentration to Henry sorption at higher concentrations.³⁹ The isosteric heats for all gases and polymers are shown in Figure C.8, calculated using the dual-mode model results for interpolation and plotted up to the maximum sorbed concentration for each gas–polymer pair. The curves for He and H₂ are flat, as expected for the low pressure range considered for these gases. The curves for N₂ and O₂ show some curvature but the variation is within the calculated error, making it difficult to draw conclusions; thus, the CH₄ and CO₂ isosteric heats are the focus of this analysis.

Within the context of the dual-mode model, only two modes of sorption are available. Thus, using a linear combination of their respective enthalpies of sorption, the number fraction of each mode can be calculated:

$$\Delta H_I = \Delta H_{S_\infty} \times \phi_{Langmuir} + \Delta H_D \times (1 - \phi_{Langmuir}) \quad (6.20)$$

where $\phi_{Langmuir}$ is the estimated occupied number fraction of Langmuir sites compared to the total number of both Henry and Langmuir sites occupied, defined mathematically as:

$$\phi_{Langmuir} = \frac{n_{Occupied\ Langmuir\ Sites}}{n_{Occupied\ Langmuir\ Sites} + n_{Occupied\ Henry\ Sites}} \quad (6.21)$$

There are several considerations contained in this simple linear model that must be addressed. First, this model suggests that the first penetrant at infinite dilution will undergo Langmuir sorption and distributes subsequent penetrants into each mode using their relative energies as weighting coefficients. When considering the formulation for S_∞ (see Equation 6.3), both Henry and Langmuir contributions are present. The relative contribution of the Langmuir to Henry mode at

infinite dilution can be determined via their coefficients (*e.g.*, $C'_H b/k_D$). For the gases examined below, CH₄ and CO₂, the $C'_H b/k_D$ value ranges from 4.5 to 21.2 depending on the polymer–gas pair, indicating a significant preference for the Langmuir mode at infinite dilution. Additionally, it was shown in Figure 6.7b that ΔH_b is more exothermic than ΔH_D for these polymer–gas pairs, indicating that sorption in the Langmuir mode is also thermodynamically preferred. Together, these two metrics estimating the relative Langmuir to Henry contributions suggest a strong preference for Langmuir sorption at infinite dilution. Thus, the model approximates that the first penetrant sorbs in the Langmuir mode, resulting in $\phi_{Langmuir} = 1$ as C approaches 0. It should also be noted that Equation 6.20 uses ΔH_{S_∞} , as opposed to ΔH_b , as the base case for the first penetrant. It has been previously reported, and observed here, that ΔH_b is not as exothermic as ΔH_{S_∞} .^{69,70} The reason behind this phenomenon is not well-understood and may indicate a deficiency in the dual-mode model, which lacks a rigorous thermodynamic basis.³⁸ For this reason, ΔH_{S_∞} is used as it represents a fundamental thermodynamic quantity as well as describes ΔH_I as C approaches 0. Lastly, an additional aspect of the isosteric heat curve that is not accounted for through this simple linear combination model is the initial decrease and minima observed for some gas–polymer pairs. This initial drop has been qualitatively attributed to the initial penetrants that may alter the surface of the polymer to make subsequent penetrants sorb more favorably in a “like-dissolves-like” fashion, with the subsequent increase in ΔH_I representing the transition from Langmuir to Henry sorption.³⁹ The minima can be predicted using the dual-mode model under the key assumption of an apparent Van’t Hoff relationship for C'_H ; however, the physical meaning of such a relationship for C'_H is unclear and unresolved.³⁸ For the simple linear model proposed here, the minima in the isosteric heat curve results in unphysical cases where $\phi_{Langmuir} > 1$. Therefore, the derivative of the $\phi_{Langmuir}$ curves with respect to penetrant concentration, representing the

rate of change from Langmuir to Henry sorption modes, is the primary consideration for this analysis. As a whole, introduction of this simple additive model revealed thermodynamic inconsistencies in the framework of the dual-mode model, for which further investigation into sorption energetics and isosteric heats of sorption is encouraged to reconcile these issues.

The derivative curves of $\phi_{Langmuir}$ with respect to CH₄ concentration are highlighted in Figure 6.8. The $\phi_{Langmuir}$ results for CH₄ and CO₂, as well as the derivative of each curve, are shown in Figures C.9a and C.9b, respectively. For the CH₄ set of derivative curves, it can be seen that the two less-fluorinated analogues are essentially identical in maximum rate of Langmuir to Henry transition of approximately $-0.05 \text{ cm}^3 \text{ cm}^{-3}(\text{STP})$. On the other hand, the two more fluorinated analogues show a distinctly lower rate of transition of approximately $-0.035 \text{ cm}^3 \text{ cm}^{-3}(\text{STP})$, indicating more resistance toward Henry sorption modes with increasing fluorine content. Interestingly, the concentrations of sorbed gas corresponding to the minima of each curve in Figure 6.8 align exactly with the respective C'_H values for each polymer (15, 17, 17, and 24 $\text{cm}^3(\text{STP}) \text{ cm}^{-3}$ for 6FDA-6FpDA, 6FDA-6HpDA, 6FDA-OHB, and 6FDA-OFB, respectively), representing the saturation of Langmuir sites for each case. Similar conclusions were drawn when applying this analysis to CO₂. There is a clear distinction between the two sets of structural analogues, where the maximum rate for 6FDA-6FpDA is less than that of 6FDA-6HpDA, and the same is true for 6FDA-OFB and 6FDA-OHB. In both cases, the more heavily fluorinated analogue shows a slower transition toward Henry sorption. For CO₂, the concentration at which the maximum rate occurs again follows the order of the respective C'_H values for each polymer (30, 33, 37, and 45 $\text{cm}^3(\text{STP}) \text{ cm}^{-3}$ for 6FDA-6HpDA, 6FDA-OHB, 6FDA-6FpDA, and 6FDA-OFB, respectively). The analysis of isosteric heats using the dual-mode model reveals that the more heavily fluorinated materials

undergo slower rates of sorption mode transition, suggesting an additional enthalpic penalty related to the mixing process in Henry sorption for fluorine-containing polymers.

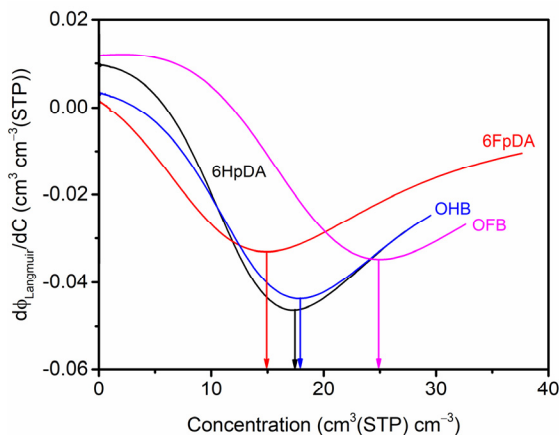


Figure 6.8: The derivatives of the $\phi_{Langmuir}$ curve estimated from the calculated isosteric heat of sorption values using Equation 6.20 for CH₄ for all polymers considered.

6.4. Conclusions

The anomalous sorption behavior displayed by perfluoropolymers was examined through sorption characterization of four lightly to highly fluorinated polyimides. Pure-gas sorption isotherms at 35, 45, 55, and 65 °C were collected for six common gases. A new approach toward dual-mode model parameter fitting involving an LFER-inspired constraint allowed for calculation of precise and optimized dual-mode model parameters for each polymer. The resulting k_D , b , and S_∞ parameters were plotted as a function of penetrant condensability. The slope for the k_D trend was lower for the highly fluorinated structures while the slope for the b trend remained invariant, suggesting that fluorination primarily affects the Henry sorption mode and its selectivity. A larger enthalpic difference between ΔH_D and ΔH_b was found for the more fluorinated polymers, suggesting a greater enthalpic penalty required to overcome unfavorable chemical interactions related to the mixing process of Henry sorption. This result was supported through a dual-mode model analysis

of the isosteric heat of sorption, where a slower transition from Langmuir to Henry sorption for CH₄ and CO₂ was observed for the fluorinated analogues. These findings give insight into changes in gas sorption mechanisms caused by fluorination and provide a platform toward understanding the exceptional gas separation performance of highly fluorinated and perfluorinated polymers.

6.5. References

- (1) Scott, R. L. The Solubility of Fluorocarbons. *J. Am. Chem. Soc.* **1948**, *70* (12), 4090–4093. <https://doi.org/10.1021/ja01192a036>.
- (2) Hildebrand, J. H. The Entropy of Solution of Molecules of Different Size. *J. Chem. Phys.* **1947**, *15* (5), 225–228. <https://doi.org/10.1063/1.1746484>.
- (3) Scott, R. L. The Anomalous Behavior of Fluorocarbon Solutions. *J. Phys. Chem.* **1958**, *62* (2), 136–145. <https://doi.org/10.1021/j150560a002>.
- (4) Scott, R. L.; Fenby, D. V. Solutions of Nonelectrolytes. *Annu. Rev. Phys. Chem.* **1969**, *20*, 111–138.
- (5) Song, W.; Rosicky, P. J.; Maroncelli, M. Modeling Alkane+perfluoroalkane Interactions Using All-Atom Potentials: Failure of the Usual Combining Rules. *J. Chem. Phys.* **2003**, *119* (17), 9145–9162. <https://doi.org/10.1063/1.1610435>.
- (6) Merkel, T. C.; Pinnau, I.; Prabhakar, R. S.; Freeman, B. D. Gas and Vapor Transport Properties of Perfluoropolymers. In *Materials Science of Membranes for Gas and Vapor Separation*; 2006; pp 251–270.
- (7) Smith, Z. P.; Tiwari, R. R.; Dose, M. E.; Gleason, K. L.; Murphy, T. M.; Sanders, D. F.; Gunawan, G.; Robeson, L. M.; Paul, D. R.; Freeman, B. D. Influence of Diffusivity and Sorption on Helium and Hydrogen Separations in Hydrocarbon, Silicon, and Fluorocarbon-Based Polymers. *Macromolecules* **2014**, *47* (9), 3170–3184. <https://doi.org/10.1021/ma402521h>.
- (8) Yampolskii, Y.; Belov, N.; Alentiev, A. Perfluorinated Polymers as Materials of Membranes for Gas and Vapor Separation. *J. Membr. Sci.* **2020**, 117779. <https://doi.org/10.1016/j.memsci.2019.117779>.
- (9) Wu, A. X.; Drayton, J. A.; Smith, Z. P. The Perfluoropolymer Upper Bound. *AIChE J.* **2019**, *65* (12), e16700. <https://doi.org/10.1002/aic.16700>.
- (10) Ogieglo, W.; Genduso, G.; Rubner, J.; Hofmann-Préveraud de Vaumas, J.; Wessling, M.; Pinnau, I. CO₂/CH₄ Pure- and Mixed-Gas Diffusion and Sorption in Thin (~500 nm) and Ultrathin (~50 nm) Polymers of Intrinsic Microporosity. *Macromolecules* **2020**, [acs.macromol.0c01163](https://doi.org/10.1021/acs.macromol.0c01163). <https://doi.org/10.1021/acs.macromol.0c01163>.
- (11) Maroon, C. R.; Townsend, J.; Gmernicki, K. R.; Harrigan, D. J.; Sundell, B. J.; Lawrence, J. A.; Mahurin, S. M.; Vogiatzis, K. D.; Long, B. K. Elimination of CO₂/N₂ Langmuir

- Sorption and Promotion of “N₂-Phobicity” within High-Tg Glassy Membranes. *Macromolecules* **2019**, *52* (4), 1589–1600. <https://doi.org/10.1021/acs.macromol.8b02497>.
- (12) Genduso, G.; Ghanem, B. S.; Pinnau, I. Experimental Mixed-Gas Permeability, Sorption and Diffusion of CO₂-CH₄ Mixtures in 6FDA-MPDA Polyimide Membrane: Unveiling the Effect of Competitive Sorption on Permeability Selectivity. *Membranes* **2019**, *9* (1). <https://doi.org/10.3390/membranes9010010>.
- (13) Fuoco, A.; Satilmis, B.; Uyar, T.; Monteleone, M.; Esposito, E.; Muzzi, C.; Tocci, E.; Longo, M.; De Santo, M. P.; Lanč, M.; et al. Comparison of Pure and Mixed Gas Permeation of the Highly Fluorinated Polymer of Intrinsic Microporosity PIM-2 under Dry and Humid Conditions: Experiment and Modelling. *J. Membr. Sci.* **2020**, *594* (August 2019), 117460. <https://doi.org/10.1016/j.memsci.2019.117460>.
- (14) Scholes, C. A. Blended Perfluoropolymer Membranes for Carbon Dioxide Separation by Miscible and Immiscible Morphologies. *J. Membr. Sci.* **2021**, *618* (January 2021), 118675. <https://doi.org/10.1016/j.memsci.2020.118675>.
- (15) Moon, J. D.; Galizia, M.; Borjigin, H.; Liu, R.; Riffle, J. S.; Freeman, B. D.; Paul, D. R. Water Vapor Sorption, Diffusion, and Dilation in Polybenzimidazoles. *Macromolecules* **2018**, *51* (18), 7197–7208. <https://doi.org/10.1021/acs.macromol.8b01659>.
- (16) Yavari, M.; Fang, M.; Nguyen, H.; Merkel, T. C.; Lin, H.; Okamoto, Y. Dioxolane-Based Perfluoropolymers with Superior Membrane Gas Separation Properties. *Macromolecules* **2018**, *51* (7), 2489–2497. <https://doi.org/10.1021/acs.macromol.8b00273>.
- (17) Zekriar dehani, S.; Joshi, A. S.; Jabarin, S. A.; Gidley, D. W.; Coleman, M. R. Effect of Dimethyl Terephthalate and Dimethyl Isophthalate on the Free Volume and Barrier Properties of Poly(Ethylene Terephthalate) (PET): Amorphous PET. *Macromolecules* **2018**, *51* (2), 456–467. <https://doi.org/10.1021/acs.macromol.7b02230>.
- (18) Noorani, N.; Mehrdad, A. Modification of PVC with 1-Vinylimidazole for CO₂/CH₄ Separation: Sorption, Permeation and DFT Studies. *Phys. Chem. Reserach* **2020**, *8* (4), 689–703. <https://doi.org/10.22036/pcr.2020.227164.1757>.
- (19) Loianno, V.; Bye, K.; Galizia, M.; Musto, P. Plasticization Mechanism in Polybenzimidazole Membranes for Organic Solvent Nanofiltration: Molecular Insights from in Situ FTIR Spectroscopy. *J. Polym. Sci.* **2020**, No. March, 2547–2560. <https://doi.org/10.1002/pol.20200151>.
- (20) Genduso, G.; Pinnau, I. Quantification of Sorption, Diffusion, and Plasticization Properties of Cellulose Triacetate Films under Mixed-Gas CO₂/CH₄ Environment. *J. Membr. Sci.* **2020**, *610*, 118269. <https://doi.org/10.1016/j.memsci.2020.118269>.
- (21) Liu, Y.; Liu, Z.; Liu, G.; Qiu, W.; Bhuwania, N.; Chinn, D.; Koros, W. J. Surprising Plasticization Benefits in Natural Gas Upgrading Using Polyimide Membranes. *J. Membr. Sci.* **2020**, *593*, 117430. <https://doi.org/10.1016/j.memsci.2019.117430>.
- (22) Sanyal, O.; Hays, S. S.; León, N. E.; Guta, Y. A.; Itta, A. K.; Lively, R. P.; Koros, W. J. A Self-Consistent Model for Sorption and Transport in Polyimide-Derived Carbon Molecular Sieve Gas Separation Membranes. *Angew. Chemie Int. Ed.* **2020**, anie.202006521.

<https://doi.org/10.1002/anie.202006521>.

- (23) Minelli, M.; Sarti, G. C. 110th Anniversary: Gas and Vapor Sorption in Glassy Polymeric Membranes - Critical Review of Different Physical and Mathematical Models. *Ind. Eng. Chem. Res.* **2020**, *59* (1), 341–365. <https://doi.org/10.1021/acs.iecr.9b05453>.
- (24) Bondar, V. I.; Kamiya, Y.; Yampolskii, Y. P. On Pressure Dependence of the Parameters of the Dual-Mode Sorption Model. *J. Polym. Sci. Part B Polym. Phys.* **1996**, *34* (2), 369–378. [https://doi.org/10.1002/\(SICI\)1099-0488\(19960130\)34:2<369::AID-POLB18>3.0.CO;2-H](https://doi.org/10.1002/(SICI)1099-0488(19960130)34:2<369::AID-POLB18>3.0.CO;2-H).
- (25) Ricci, E.; De Angelis, M. G. Modelling Mixed-Gas Sorption in Glassy Polymers for CO₂ Removal: A Sensitivity Analysis of the Dual Mode Sorption Model. *Membranes* **2019**, *9* (1), 1–26. <https://doi.org/10.3390/membranes9010008>.
- (26) Doghieri, F.; Sarti, G. C. Nonequilibrium Lattice Fluids: A Predictive Model for the Solubility in Glassy Polymers. *Macromolecules* **1996**, *29* (24), 7885–7896. <https://doi.org/10.1021/ma951366c>.
- (27) Baschetti, M. G.; Doghieri, F.; Sarti, G. C. Solubility in Glassy Polymers: Correlations through the Nonequilibrium Lattice Fluid Model. *Ind. Eng. Chem. Res.* **2001**, *40* (14), 3027–3037. <https://doi.org/10.1021/ie000834q>.
- (28) Galizia, M.; Stevens, K. A.; Smith, Z. P.; Paul, D. R.; Freeman, B. D. Nonequilibrium Lattice Fluid Modeling of Gas Solubility in HAB-6FDA Polyimide and Its Thermally Rearranged Analogues. *Macromolecules* **2016**, *49* (22), 8768–8779. <https://doi.org/10.1021/acs.macromol.6b01479>.
- (29) Minelli, M.; Doghieri, F. Predictive Model for Gas and Vapor Sorption and Swelling in Glassy Polymers: II. Effect of Sample Previous History. *Fluid Phase Equilib.* **2017**, *444*, 47–55. <https://doi.org/10.1016/j.fluid.2017.04.012>.
- (30) Loianno, V.; Zhang, Q.; Luo, S.; Guo, R.; Galizia, M. Modeling Gas and Vapor Sorption and Swelling in Triptycene-Based Polybenzoxazole: Evidence for Entropy-Driven Sorption Behavior. *Macromolecules* **2019**, *52* (11), 4385–4395. <https://doi.org/10.1021/acs.macromol.9b00577>.
- (31) Ricci, E.; Gameda, A. E.; Du, N.; Li, N.; De Angelis, M. G.; Guiver, M. D.; Sarti, G. C. Sorption of CO₂/CH₄ Mixtures in TZ-PIM, PIM-1 and PTMSP: Experimental Data and NELF-Model Analysis of Competitive Sorption and Selectivity in Mixed Gases. *J. Membr. Sci.* **2019**, *585* (May), 136–149. <https://doi.org/10.1016/j.memsci.2019.05.026>.
- (32) Minelli, M.; Campagnoli, S.; De Angelis, M. G.; Doghieri, F.; Sarti, G. C. Predictive Model for the Solubility of Fluid Mixtures in Glassy Polymers. *Macromolecules* **2011**, *44* (12), 4852–4862. <https://doi.org/10.1021/ma200602d>.
- (33) Gleason, K. L.; Smith, Z. P.; Liu, Q.; Paul, D. R.; Freeman, B. D. Pure- and Mixed-Gas Permeation of CO₂ and CH₄ in Thermally Rearranged Polymers Based on 3,3'-Dihydroxy-4,4'-Diamino-Biphenyl (HAB) and 2,2'-Bis-(3,4-Dicarboxyphenyl) Hexafluoropropane Dianhydride (6FDA). *J. Membr. Sci.* **2015**, *475*, 204–214. <https://doi.org/10.1016/j.memsci.2014.10.014>.

- (34) Ricci, E.; Benedetti, F. M.; Dose, M. E.; De Angelis, M. G.; Freeman, B. D.; Paul, D. R. Competitive Sorption in CO₂/CH₄ Separations: The Case of HAB-6FDA Polyimide and Its TR Derivative and a General Analysis of Its Impact on the Selectivity of Glassy Polymers at Multicomponent Conditions. *J. Membr. Sci.* **2020**, *612*, 118374. <https://doi.org/10.1016/j.memsci.2020.118374>.
- (35) Stevens, K. A.; Smith, Z. P.; Gleason, K. L.; Galizia, M.; Paul, D. R.; Freeman, B. D. Influence of Temperature on Gas Solubility in Thermally Rearranged (TR) Polymers. *J. Membr. Sci.* **2017**, *533* (March), 75–83. <https://doi.org/10.1016/j.memsci.2017.03.005>.
- (36) Lin, H.; Freeman, B. D. Permeation and Diffusion. In *Springer-Handbook of Materials Measurement Methods*; 2006.
- (37) Matteucci, S.; Yampolskii, Y.; Freeman, B. D.; Pinnau, I. Transport of Gases and Vapors in Glassy and Rubbery Polymers. In *Materials Science of Membranes for Gas and Vapor Separation*; 2006; pp 1–47. <https://doi.org/10.1002/047002903X.ch1>.
- (38) Koros, W. J.; Paul, D. R.; Huvard, G. S. Energetics of Gas Sorption in Glassy Polymers. *Polymer* **1979**, *20*, 956–960. [https://doi.org/10.1016/0032-3861\(79\)90192-7](https://doi.org/10.1016/0032-3861(79)90192-7).
- (39) Merkel, T. C.; Bondar, V.; Nagai, K.; Freeman, B. D.; Yampolskii, P. Y. Gas Sorption, Diffusion, and Permeation in Poly(2,2-Bis(Trifluoromethyl)-4,5-Difluoro-1,3-Dioxole-Co-Tetrafluoroethylene). *Macromolecules* **1999**, *32* (25), 8427–8440. <https://doi.org/10.1021/ma990685r>.
- (40) Smith, Z. P.; Tiwari, R. R.; Murphy, T. M.; Sanders, D. F.; Gleason, K. L.; Paul, D. R.; Freeman, B. D. Hydrogen Sorption in Polymers for Membrane Applications. *Polymer* **2013**, *54* (12), 3026–3037. <https://doi.org/10.1016/j.polymer.2013.04.006>.
- (41) Koros, W. J.; Paul, D. R. CO₂ Sorption in Poly(Ethylene Terephthalate) above and below the Glass Transition. *J. Polym. Sci. Polym. Phys. Ed.* **1978**, *16*, 1947–1963. <https://doi.org/10.1002/pol.1978.180161105>.
- (42) Dymond, J. H.; Marsh, K. N.; Wilhoit, R. C.; Wong, K. C. *The Virial Coefficients of Pure Gases and Mixtures: Subvolume A*; 2001.
- (43) Wu, A. X.; Drayton, J. A.; Rodriguez, K. M.; Qian, Q.; Lin, S.; Smith, Z. P. Influence of Aliphatic and Aromatic Fluorine Groups on Gas Permeability and Morphology of Fluorinated Polyimide Films. *Macromolecules* **2020**, *53* (13), 5085–5095. <https://doi.org/10.1021/acs.macromol.0c01024>.
- (44) Smith, Z. P.; Sanders, D. F.; Ribeiro, C. P.; Guo, R.; Freeman, B. D.; Paul, D. R.; McGrath, J. E.; Swinnea, S. Gas Sorption and Characterization of Thermally Rearranged Polyimides Based on 3,3'-Dihydroxy-4,4'-Diamino-Biphenyl (HAB) and 2,2'-Bis-(3,4-Dicarboxyphenyl) Hexafluoropropane Dianhydride (6FDA). *J. Membr. Sci.* **2012**, *415–416*, 558–567. <https://doi.org/10.1016/j.memsci.2012.05.050>.
- (45) Lai, H. W. H.; Benedetti, F. M.; Jin, Z.; Teo, Y. C.; Wu, A. X.; Angelis, M. G. De; Smith, Z. P.; Xia, Y. Tuning the Molecular Weights, Chain Packing, and Gas-Transport Properties of CANAL Ladder Polymers by Short Alkyl Substitutions. *Macromolecules* **2019**, *52* (16), 6294–6302. <https://doi.org/10.1021/acs.macromol.9b01155>.

- (46) Freeman, B. D. Basis of Permeability/Selectivity Tradeoff Relations in Polymeric Gas Separation Membranes. *Macromolecules* **1999**, *32* (2), 375–380. <https://doi.org/10.1021/ma9814548>.
- (47) Bevington, P. R.; Robinson, D. K. *Data Reduction and Error Analysis for the Physical Sciences*, 3rd ed.; McGraw-Hill: New York, 2003. <https://doi.org/10.1063/1.4823194>.
- (48) Robeson, L. M. The Upper Bound Revisited. *J. Membr. Sci.* **2008**, *320* (1–2), 390–400. <https://doi.org/10.1016/j.memsci.2008.04.030>.
- (49) Park, J. Y.; Paul, D. R. Correlation and Prediction of Gas Permeability in Glassy Polymer Membrane Materials via a Modified Free Volume Based Group Contribution Method. *J. Membr. Sci.* **1997**, *125* (1), 23–39. [https://doi.org/10.1016/S0376-7388\(96\)00061-0](https://doi.org/10.1016/S0376-7388(96)00061-0).
- (50) Flory, P. J. Thermodynamics of High Polymer Solutions. *J. Chem. Phys.* **1942**, *10*, 51. <https://doi.org/10.1007/s12045-017-0481-2>.
- (51) Kiszka, M. B.; Meilchen, M. A.; McHugh, M. A. Modeling High-Pressure Gas-Polymer Mixtures Using the Sanchez-Lacombe Equation of State. *J. Appl. Polym. Sci.* **1988**, *36* (3), 583–597. <https://doi.org/10.1002/app.1988.070360311>.
- (52) Yavari, M.; Okamoto, Y.; Lin, H. The Role of Halogens in Polychlorotrifluoroethylene (PCTFE) in Membrane Gas Separations. *J. Membr. Sci.* **2018**, *548* (October 2017), 380–389. <https://doi.org/10.1016/j.memsci.2017.11.043>.
- (53) Tiwari, R. R.; Smith, Z. P.; Lin, H.; Freeman, B. D.; Paul, D. R. Gas Permeation in Thin Films of “High Free-Volume” Glassy Perfluoropolymers: Part I. Physical Aging. *Polymer* **2014**, *55* (22), 5788–5800. <https://doi.org/10.1016/j.polymer.2014.09.022>.
- (54) Tiwari, R. R.; Smith, Z. P.; Lin, H.; Freeman, B. D.; Paul, D. R. Gas Permeation in Thin Films of “High Free-Volume” Glassy Perfluoropolymers: Part II. CO₂ Plasticization and Sorption. *Polymer* **2015**, *61*, 1–14. <https://doi.org/10.1016/j.polymer.2014.12.008>.
- (55) Callen, H. B. *Thermodynamics and an Introduction to Thermostatistics*, 2nd ed.; Wiley, 1985.
- (56) Li, P.; Chung, T. S.; Paul, D. R. Gas Sorption and Permeation in PIM-1. *J. Membr. Sci.* **2013**, *432*, 50–57. <https://doi.org/10.1016/j.memsci.2013.01.009>.
- (57) Bondar, V. I.; Freeman, B. D.; Yampolskii, Y. P. Sorption of Gases and Vapors in an Amorphous Glassy Perfluorodioxole Copolymer. *Macromolecules* **1999**, *32* (19), 6163–6171. <https://doi.org/10.1021/ma9817222>.
- (58) Moore, T. T.; Koros, W. J. Gas Sorption in Polymers, Molecular Sieves, and Mixed Matrix Membranes. *J. Appl. Polym. Sci.* **2007**, *104*, 4053–4059. <https://doi.org/10.1002/app.25653>.
- (59) Ghosal, K.; Chern, R. T.; Freeman, B. D.; Daly, W. H.; Negulescu, I. I. Effect of Basic Substituents on Gas Sorption and Permeation in Polysulfone. *Macromolecules* **1996**, *29* (12), 4360–4369. <https://doi.org/10.1021/ma951310i>.
- (60) Alentiev, A. Y.; Shantarovich, V. P.; Merkel, T. C.; Bondar, V. I.; Freeman, B. D.; Yampolskii, Y. P. Gas and Vapor Sorption, Permeation, and Diffusion in Glassy

- Amorphous Teflon AF1600. *Macromolecules* **2002**, *35* (25), 9513–9522. <https://doi.org/10.1021/ma020494f>.
- (61) Anslyn, E. V.; Dougherty, D. A. *Modern Physical Organic Chemistry*; University Science Books, 2006; Vol. 24. <https://doi.org/10.1002/poc.1909>.
- (62) Starikov, E. B.; Nordén, B. Entropy-Enthalpy Compensation as a Fundamental Concept and Analysis Tool for Systematical Experimental Data. *Chem. Phys. Lett.* **2012**, *538*, 118–120. <https://doi.org/10.1016/j.cplett.2012.04.028>.
- (63) Pan, A.; Biswas, T.; Rakshit, A. K.; Moulik, S. P. Enthalpy-Entropy Compensation (EEC) Effect: A Revisit. *J. Phys. Chem. B* **2015**, *119* (52), 15876–15884. <https://doi.org/10.1021/acs.jpcc.5b09925>.
- (64) Sharp, K. Entropy – Enthalpy Compensation: Fact or Artifact? *Protein Sci.* **2001**, *10*, 661–667. <https://doi.org/10.1110/ps.37801.Cp>.
- (65) Cornish-Bowden, A. Enthalpy-Entropy Compensation: A Phantom Phenomenon. *J. Biosci.* **2002**, *27* (2), 121–126. <https://doi.org/10.1007/BF02703768>.
- (66) Barrer, R. M. Permeability in Relation to Viscosity and Structure of Rubber. *Trans. Faraday Soc.* **1942**, *38*, 322–330. <https://doi.org/10.1039/TF9423800322>.
- (67) Van Amerongen, G. J. The Permeability of Different Rubbers to Gases and Its Relation to Diffusivity and Solubility. *J. Appl. Phys.* **1946**, *17* (11), 972–985. <https://doi.org/10.1063/1.1707667>.
- (68) van Krevelen, D. W.; te Nijenhuis, K. *Properties of Polymers*, 4th ed.; Elsevier: Oxford, 2009. <https://doi.org/10.1017/cbo9780511623097.008>.
- (69) Yang, D. K.; Koros, W. J.; Hopfenberg, H. B.; Stannett, V. T. Sorption and Transport Studies of Water in Kapton Polyimide. I. *J. Appl. Polym. Sci.* **1985**, *30* (3), 1035–1047. <https://doi.org/10.1002/app.1985.070300313>.
- (70) Ranade, G.; Stannett, V.; Koros, W. J. Temperature Dependence and Energetics of the Equilibrium Sorption of Water Vapor in Glassy Polyacrylonitrile. *J. Appl. Polym. Sci.* **1980**, *25* (10), 2179–2186. <https://doi.org/10.1002/app.1980.070251004>.
- (71) Raharjo, R. D.; Freeman, B. D.; Sanders, E. S. Pure and Mixed Gas CH₄ and n-C₄H₁₀ Sorption and Dilution in Poly(Dimethylsiloxane). *J. Membr. Sci.* **2007**, *292* (1–2), 45–61. <https://doi.org/10.1016/j.memsci.2007.01.012>.
- (72) Li, P.; Chung, T. S.; Paul, D. R. Temperature Dependence of Gas Sorption and Permeation in PIM-1. *J. Membr. Sci.* **2014**, *450*, 380–388. <https://doi.org/10.1016/j.memsci.2013.09.030>.
- (73) Thomas, S.; Pinnau, I.; Du, N.; Guiver, M. D. Pure- and Mixed-Gas Permeation Properties of a Microporous Spirobisindane-Based Ladder Polymer (PIM-1). *J. Membr. Sci.* **2009**, *333*, 125–131. <https://doi.org/10.1016/j.memsci.2009.02.003>.

Chapter 7: Non-Equilibrium Lattice Fluid Modeling of Gas Sorption for Fluorinated Poly(Ether Imide)s

Abstract

Perfluoropolymers are a unique class of materials that display anomalous thermodynamic partitioning compared to hydrocarbon polymers and show exceptional separation performance for certain gas pairs. However, the molecular origin by which fluorine affects gas sorption is not well-understood, and the sorption behavior of partially fluorinated polymer analogues is rarely quantified. Here, we synthesized and characterized a series of structurally analogous poly(ether imide)s spanning from fully hydrocarbon to perfluorinated, which involved the synthesis of a perfluorinated dianhydride monomer. Sorption isotherms for multiple temperatures and gases were analyzed using the non-equilibrium lattice fluid model. The lattice fluid parameters were estimated from infinite dilution sorption data. The binary interaction parameter increased with polymer fluorine content for all gases, with CH₄ showing the largest increase in unfavorable deviation from ideal mixing. Continuous trends for the enthalpic, entropic, and infinite dilution sorption selectivity with fluorine content were observed, wherein the increase in enthalpic selectivity was greater than the decrease in entropic selectivity, resulting in overall increased sorption selectivity. Our findings connect the sorption behavior of hydrocarbon polymers and perfluoropolymers and provide mechanistic insight into the role of fluorine on gas sorption.

This chapter has been adapted from: Wu, A. X.; Drayton, J. A.; Ren, X.; Mizrahi Rodriguez, K.; Grosz, A. F.; Lee, J. -W.; Smith, Z. P. Non-Equilibrium Lattice Fluid Modeling of Gas Sorption for a Series of Fluorinated Poly(Ether Imide) Membranes. *Submitted*.

7.1. Introduction

To probe the mechanism by which fluorination affects gas sorption and sorption selectivity, it is of interest to study changes in sorption behavior of polymers with systematic addition of fluorine using well-established sorption models. The most common sorption model for glassy polymers is the dual-mode model, where the sorption isotherm is described as the sum of the Henry and Langmuir sorption modes.¹ Chapter 6 investigated changes in the various dual-mode model parameters as a function of fluorine content for a set of 6FDA-based polyimides, wherein fluorination was found to primarily affect the Henry sorption mode.² While the dual-mode model is widely accessible and can be used to understand and develop structure–property relationships, it is inherently a phenomenological model,³ thereby compelling researchers to develop more thermodynamically rigorous models to describe gas sorption in glassy polymers. In recent years, non-equilibrium thermodynamics models have been developed to successfully model sorption isotherms in glassy polymers with the most well-known being the non-equilibrium lattice fluid (NELF) model.^{4,5} The NELF model represents an evolution of lattice site-based theories through the relaxation of various assumptions present in previous models (*i.e.*, the Flory-Huggins⁶ and Sanchez-Lacombe⁷⁻⁹) to allow for the description of light gas sorption in glassy polymers.¹⁰⁻¹⁴ In particular, an assumption of a pseudo-equilibrium state for glassy polymers (*i.e.*, change of density over time is approximately equal to zero) is required and differentiates the NELF model from its predecessors.⁴ Details related to NELF formulation and the incorporation of density as an order parameter are described in depth elsewhere.^{4,15}

Additionally, the synthesis of perfluoropolymers remains a key challenge precluding the development of fundamental structure–property relationships related to the role of fluorine on gas transport and sorption.¹⁶ The most well-known and benchmark perfluoropolymers in the field are

Teflon[®] AF^{17,18} and Hyflon[®] AD¹⁹, a series of amorphous polymers that were commercially developed and produced in the 1990s and thoroughly investigated in the early 2000s.^{20–24} Since then, there have been few new amorphous perfluoropolymers developed for gas separations, due in part to synthetic difficulties and hazards related to fluorinated solvents as well as increased interest in other emerging materials for separations, such as microporous hydrocarbon-based polymers²⁵ and other composite materials²⁶. Recently, the synthesis and transport characterization of poly(PFMD) and poly(PFMMD) was reported, showing record separation performance for certain gas pairs and marking a major milestone in the development of perfluoropolymers for gas separations.²⁷

In this study, we report the synthesis and gas sorption characterization of a series of structurally analogous, amorphous poly(ether imides) shown in Figure 7.1. These polymers span the range from fully hydrocarbon (10HEDA-MPD) to fully fluorinated (10FEDA-TFMPD) and include partially fluorinated intermediates (10HEDA-TFMPD and 10FEDA-MPD). Therefore, this study aims to bridge the gap in understanding the sorption behavior of hydrocarbon polymers and perfluoropolymers. High pressure sorption isotherms for four light gases were collected at multiple temperatures for all polymers. The sorption data was analyzed using the NELF model to identify trends in the model parameters and to establish fundamental structure–property relationships, particularly in the limit of infinite dilution with respect to fluorine content.

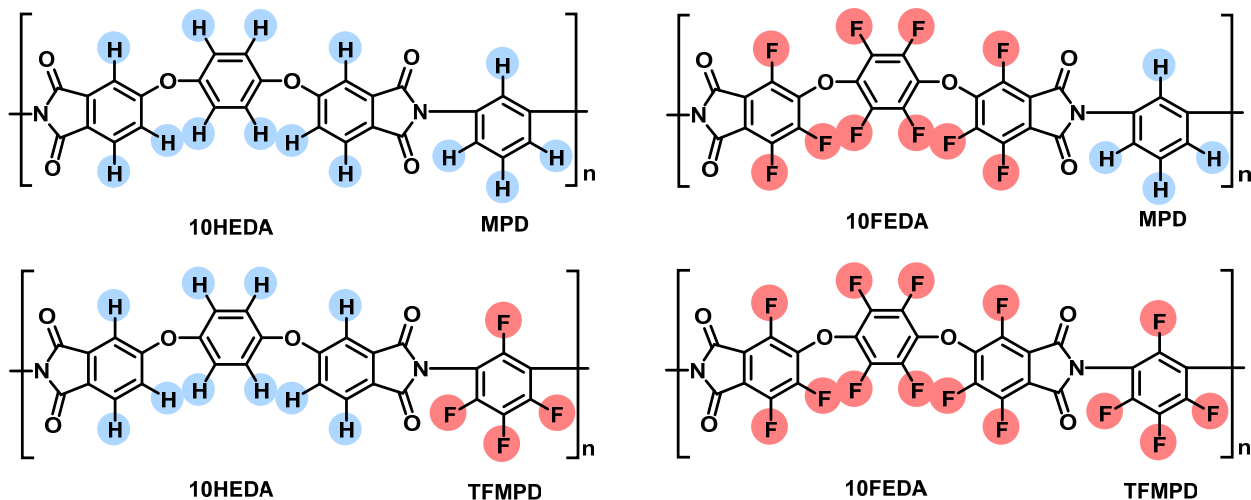


Figure 7.1. The four poly(ether imides) considered in this study, representing a series of structural analogues ranging from fully hydrocarbon to fully fluorinated. Fluorine content increases as follows: 10HEDA-MPD < 10HEDA-TFMPD < 10FEDA-MPD < 10FEDA-TFMPD. Color is added to highlight differences in chemical composition.

7.2. Theory

Sorption isotherms for these polymers were analyzed using the NELF model. Unlike the Sanchez-Lacombe model, which describes gas sorption exclusively for polymers in their rubbery state, the NELF model can be applied to glassy polymers by using polymer density as an order parameter.⁴ The relevant parameters and equations for the NELF model, which can be found elsewhere^{15,28}, are included in Table 7.1 for convenience. This table describes a binary gas-polymer system, but the model can also be extended to describe mixed-gas sorption.^{11,29}

Table 7.1. Parameters and Equations for NELF

Parameters for Pure Components		
	Gas Phase (subscript 1)	Polymer Phase (subscript 2)
Characteristic Temperature (K)*	T_1^*	T_2^*
Characteristic Pressure (MPa)*	p_1^*	p_2^*
Characteristic Density (g cm ⁻³)*	ρ_1^*	ρ_2^*
Molecular Weight (g mol ⁻¹)	MW_1	-
Density (g cm ⁻³)	-	ρ_2 (experimentally measured density)
Mass Fraction	ω_1	ω_2
Universal Gas Constant (MPa cm ³ mol ⁻¹ K ⁻¹)	R	
Molar Volume of a Lattice Site of Component	$v_1^* = \frac{RT_1^*}{p_1^*}$	$v_2^* = \frac{RT_2^*}{p_2^*}$
Number of Lattice Sites Occupied by a Molecule	$r_1^0 = \frac{MW_1}{v_1^* \rho_1^*}$	-
Volume Fraction of Species at Close-Packed Conditions	$\Phi_1 = \frac{\frac{\omega_1}{\rho_1^*}}{\frac{\omega_1}{\rho_1^*} + \frac{\omega_2}{\rho_2^*}}$	$\Phi_2 = \frac{\frac{\omega_2}{\rho_2^*}}{\frac{\omega_1}{\rho_1^*} + \frac{\omega_2}{\rho_2^*}}$

Reduced Temperature	$\tilde{T}_1 = \frac{T}{T_1^*}$	$\tilde{T}_2 = \frac{T}{T_2^*}$
Reduced Pressure	$\tilde{p}_1 = \frac{p}{p_1^*}$	$\tilde{p}_2 = \frac{p}{p_2^*}$
Reduced Density	$\tilde{\rho}_1$ (obtained by solving Equation 7.4 using T_1^* , p_1^* , and ρ_1^*)	$\tilde{\rho}_2 = \frac{\rho_2}{\rho_2^*}$
Parameters and Mixing Rules for Binary Mixtures		
Binary Interaction Parameter	k_{12}	
Characteristic Temperature of Mixture (7.1)	$T^* = \frac{p^*}{\frac{\Phi_1 p_1^*}{T_1^*} + \frac{\Phi_2 p_2^*}{T_2^*}}$	
Characteristic Pressure of Mixture (7.2)	$p^* = \Phi_1 p_1^* + \Phi_2 p_2^* - \Phi_1 \Phi_2 (p_1^* + p_2^* - 2(1 - k_{12})\sqrt{p_1^* p_2^*})$	
Characteristic Density of Mixture (7.3)	$\frac{1}{\rho^*} = \frac{\omega_1}{\rho_1^*} + \frac{\omega_2}{\rho_2^*}$	
Molar Volume of a Lattice Site of Mixture	$v^* = \frac{RT^*}{p^*}$	
Number of Lattice Sites Occupied by a Molecule in Mixture	$r_1 = \frac{v_1^* r_1^0}{v^*}$	
Reduced Temperature of Mixture	$\tilde{T} = \frac{T}{T^*}$	
Reduced Pressure of Mixture	$\tilde{p} = \frac{p}{p^*}$	

Reduced Density of Mixture	$\tilde{\rho} = \frac{\omega_2}{\rho_2 \rho^*}$
Model Equations for Binary Mixtures	
Sanchez-Lacombe Equation of State for Pure Penetrant (7.4)	$\tilde{\rho}_1 = 1 - \exp\left(-\frac{\tilde{\rho}_1^2}{\tilde{T}_1} - \frac{\tilde{p}_1}{\tilde{T}_1} - \tilde{\rho}_1\left(1 - \frac{1}{r_1^0}\right)\right)$
Sanchez-Lacombe Chemical Potential of Gas Phase (7.5)	$\frac{\mu_1^0}{RT} = r_1^0 \left(-\frac{\tilde{\rho}_1^2}{\tilde{T}_1} + \frac{\tilde{p}_1}{\tilde{T}_1 \tilde{\rho}_1} + \frac{\ln(\tilde{\rho}_1)}{r_1^0} + \frac{1 - \tilde{\rho}_1}{\tilde{\rho}_1} \ln(1 - \tilde{\rho}_1) \right)$
NELF Chemical Potential of Penetrant in Sorbed Phase (7.6)	$\frac{\mu_1^{ne}}{RT} = \ln(\tilde{\rho} \Phi_1) - \left(r_1^0 + \frac{r_1 - r_1^0}{\tilde{\rho}} \right) \ln(1 - \tilde{\rho}) - r_1 + 1 - \frac{\tilde{\rho} r_1^0 v_1^*}{RT} \left(p_1^* + \Phi_2 \left(p_2^* - (p_1^* + p_2^* - 2(1 - k_{12}) \sqrt{p_1^* p_2^*}) \right) \right)$

*Lattice fluid parameters (LFPs)

To calculate the concentration of a gas (phase 1) sorbed in a polymer (phase 2) at a specific temperature and pressure using the NELF model, the mass fraction of gas sorbed (ω_1) is determined by equating the chemical potentials of the gas in the gas phase and the sorbed phase (*i.e.*, Equations 7.5 and 7.6):

$$\mu_1^0 = \mu_1^{ne} \quad (7.7)$$

As part of Equation 7.5, the reduced density of the gas phase ($\tilde{\rho}_1$) needs to be calculated. This value can be calculated through Equation 7.4 using the appropriate parameters associated with the gas phase. Additionally, the k_{12} parameter describes the deviation from the geometric mixing rule as dictated by Hildebrand's solution theory, where a value of zero represents ideal interactions, positive values represent unfavorable (*i.e.*, less than ideal) interactions, and negative values represent favorable (*i.e.*, greater than ideal) interactions.¹² This parameter, present in Equation 7.2,

is dependent only on the gas–polymer pair and is treated as an adjustable, best-fit parameter between the model and data of a reference sorption isotherm. Assuming no penetrant induced swelling, once the k_{12} parameter is determined for the gas–polymer pair, the value can be reused to obtain isotherms for all other temperatures in a fully predictive manner.¹²

When considering the sorption of highly condensable penetrants, such as CO₂ or hydrocarbons, changes in polymer density can occur due to penetrant–induced swelling. Experimental dilation data can be used to determine the density of the polymer at specific temperatures and pressures. Alternatively, the change in density can be approximated through a linear correlation:¹²

$$\rho_2(p) = \rho_2^0(1 - k_{sw}p) \quad (7.8)$$

where ρ_2^0 (g cm⁻³) is the measured density and k_{sw} is the swelling parameter (MPa⁻¹). In these cases, k_{sw} is treated as an adjustable parameter to fit data points where significant swelling is expected, such as high pressure CO₂. As a result, when penetrant induced swelling is considered, the NELF model requires two fitted parameters, k_{12} and k_{sw} .

The characteristic temperature, pressure, and density of the pure phases (*i.e.*, T_1^* , p_1^* , ρ_1^* , T_2^* , p_2^* , and ρ_2^*) are known as lattice fluid parameters (LFPs). These parameter sets describe certain properties of the phase. Originating from the SL model, the formal definitions of these parameters are⁸:

$$T^* = \frac{\epsilon^*}{k} \quad (7.9)$$

$$p^* = \frac{\epsilon^*}{v^*} \quad (7.10)$$

$$\rho^* = \frac{MW}{rv^*} \quad (7.11)$$

where ϵ^* is the total non-bonded mer-mer interaction energy per mer (*i.e.*, per site), k is the Boltzmann constant, MW is the molecular weight, r is the number of sites a molecule occupies (an r -mer), and v^* is the close-packed mer volume. In terms of developing structure–property relationships for polymer systems, T^* represents interchain interactions such as hydrogen bonding or other secondary interactions, ρ^* represents the close-packed mass density at 0 K and is associated with the polymer density and fractional free volume (FFV), and p^* is defined as the cohesive energy density (CED) and is strictly dependent on T^* and ρ^* .^{8,9,12}

The LFPs for a large database of gases have been previously determined³⁰ and the LFPs for gases tested in this study are shown in Table D.1. Typically, the LFPs for polymers are determined from pVT experiments using a Zoller apparatus^{31,32}, where the data corresponding to the rubbery regime is fit to the SL model to find the best-fit LFPs.¹³ However, the rubbery regime is not accessible for some polymers (*e.g.*, PIM-1, where the polymer backbone degrades before reaching the rubbery state³³) and the experiments are not simple to perform. In these cases, an alternative method to approximate the LFPs has been implemented through the fitting of the experimental infinite dilution sorption coefficient (S_∞) to the equation for S_∞ derived from the NELF model^{15,30}:

$$\ln(S_\infty) = \ln\left(\frac{T_{STP}}{p_{STP}T}\right) + r_1^0 \left[\left(1 + \left(\frac{v_1^*}{v_2^*} - 1\right) \frac{\rho_2^*}{\rho_1^*}\right) \times \ln\left(1 - \frac{\rho_2}{\rho_2^*}\right) + \left(\frac{v_1^*}{v_2^*} - 1\right) + \frac{\rho_2 T_1^*}{\rho_2^* T} \frac{2}{p_1^*} (1 - k_{12}) \sqrt{p_1^* p_2^*} \right] \quad (7.12)$$

where T_{STP} is 273.15 K, p_{STP} is 0.101325 MPa, and the resulting units of S_∞ are $\text{cm}^3(\text{STP}) \text{cm}^{-3} \text{MPa}^{-1}$. A key assumption to the method is $k_{12} = 0$ as a first-order approximation, thereby allowing the LFPs to be treated as fitted parameters using experimental S_∞ values for all isotherms and Equation 7.12.^{12,34} In the limit of infinite dilution, the assumption of $k_{12} = 0$ has been shown to be suitable for penetrants that are non-polar or non-halogenated.^{12,34} A database of LFPs for polymers similar to those shown Figure 7.1 are tabulated in Table D.1.

7.3. Results

7.3.1. Monomer Synthesis and Characterization

The chemical structure of the 10FEDA monomer synthesized for this study was confirmed using ^{19}F NMR and FT-IR spectroscopy. Notably, the ^{19}F peaks for 10FEDP, 10FEDP-COOH, and 10FEDA were previously catalogued by Ando *et al.*³⁵ The ^{19}F NMR for the three molecules are shown in Figure 7.2a with the corresponding peak assignments. All molecules showed a relative peak integration of 1:1:1:2 for peaks 1–3 compared to peak 4, as expected from the structure. In the ^{19}F NMR for 10FEDA, small peaks associated with 10FEDP-COOH with a relative integration of 1:0.05 10FEDA:10FEDA-COOH are present. We suspect that due to the hygroscopic nature of the DMSO- d_6 NMR solvent, the presence of water in the solvent may have caused a small amount of ring-opening to occur during the sample preparation process. However, the FT-IR spectrum for 10FEDA in Figure 7.2b does not show a broad $-\text{OH}$ peak, suggesting full conversion to ring closure was achieved during the dehydration reaction step.

The FT-IR spectra for the three molecules are shown in Figure 7.2b with identifying functional groups highlighted. For 10FEDP, a characteristic nitrile peak was observed at 2250 cm^{-1} . After hydrolysis to 10FEDP-COOH, that peak was replaced with a broad $-\text{OH}$ peak at 3200 cm^{-1} . Lastly, after dehydration to 10FEDA, the $-\text{OH}$ peak was eliminated and characteristic dianhydride peaks at 1780 cm^{-1} and 1870 cm^{-1} were observed, confirming closure of the dianhydride ring.

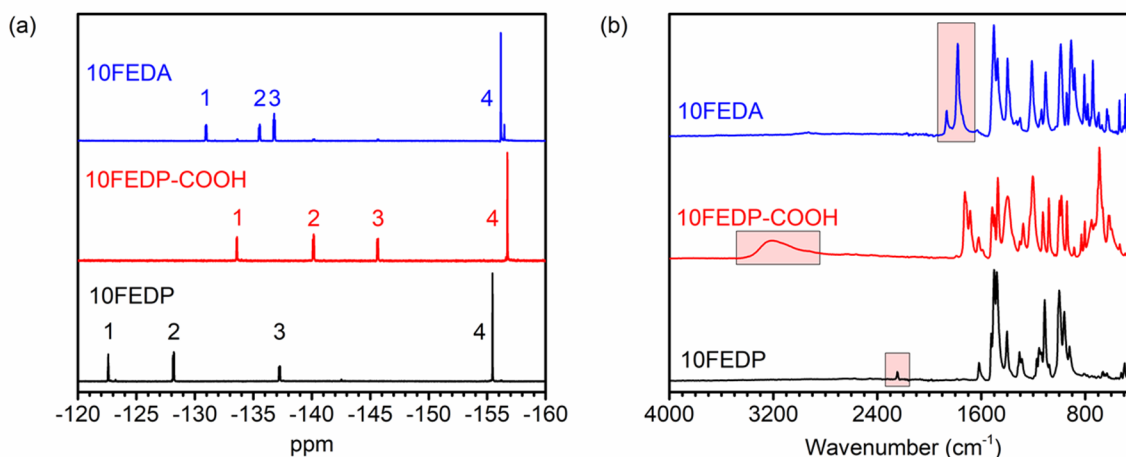
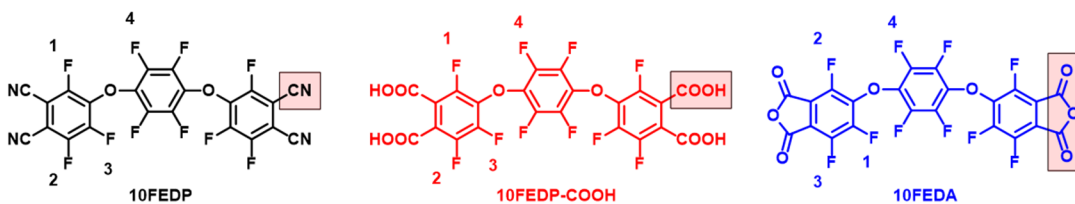


Figure 7.2. Monomer characterization for 10FEDP, 10FEDP-COOH, and 10FEDA using (a) ^{19}F NMR and (b) FT-IR.

7.3.2. Polymer Synthesis and Characterization

Using the synthesized 10FEDA monomer, the four polymers shown in Figure 7.1 were synthesized and cast into films. As noted in previous reports, the as-cast films that were cast at 350 °C are not soluble in common solvents.³⁶ Therefore, the GPC of only the poly(amic acid) precursor solution is reported in Table D.2, showing a limited degree of polymerization prior to the high-temperature cure. The high-temperature cure procedure proposed by Hougham *et al.*, discussed in Section 3.2, suggests that simultaneous end-to-end chain extension and imidization reactions occur for these oligomeric chains, resulting in a film suitable for testing.³⁷ Pictures of the polymer films are shown in Figure 7.3a. The functional groups present in the film can be verified via FT-IR, as shown in Figure 7.3b. Specifically, the peaks at 1780 and 1720 cm^{-1} are associated with imide stretching and the peak at 1380 cm^{-1} is associated with C–N imide stretching, confirming successful

imidization.^{38,39} The lack of amide and carboxylic acid peaks indicate that, at least within the resolution of FT-IR, crosslinking did not occur. Thus, the decreased solubility is attributed to increased aggregation of the polymer chains when curing above their T_g since in the rubbery state, the polymer chains are able to preferentially rearrange prior to cooling below their T_g .³⁶ Additionally, the spectra for 10FEDA-TFMPD matches that in previous reports.³⁶

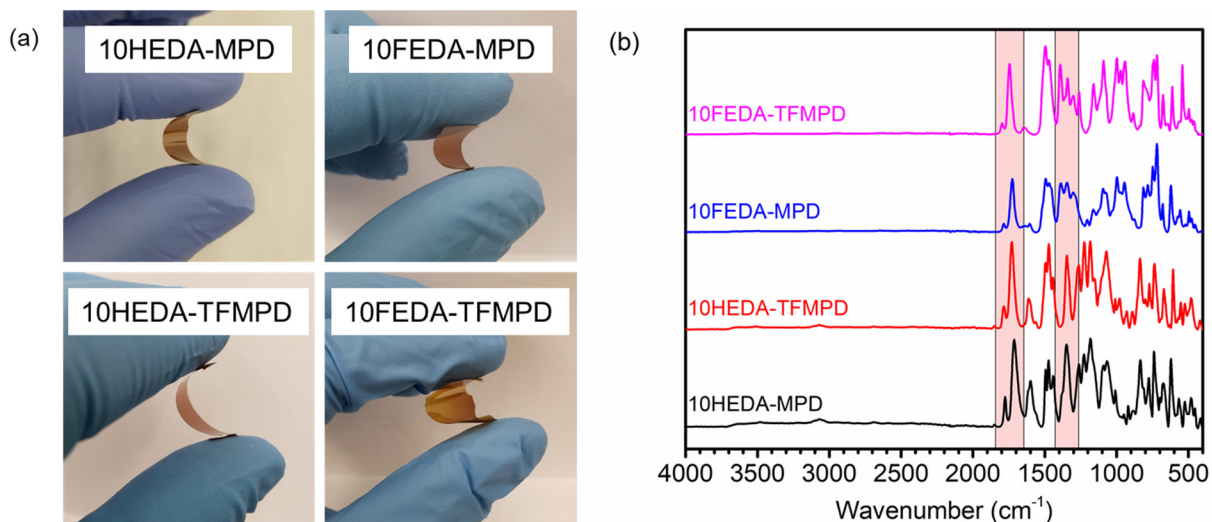


Figure 7.3. (a) Images of the four polymers after casting, resulting in robust films. (b) FTIR spectra for the four polymer films.

DSC, density, and FFV characterization results are summarized in Table 7.2. The DSC traces are shown in Figure D.1. FFV was calculated using the following equation⁴⁰:

$$FFV = \frac{V - V_{oc}}{V} \quad (7.13)$$

where V is the specific volume ($\text{cm}^3 \text{g}^{-1}$) obtained from the experimentally measured density and V_{oc} is the volume occupied by the polymer chains, estimated using our updated group contribution method (see Chapter 8). The volume fraction of fluorine for each polymer was estimated as the

fraction of the total van der Waals volume occupied by fluorine, again estimated using our updated group contribution method.

Of note, when performing DSC measurements at a 10 °C/min ramp rate, a T_g was observed only for 10HEDA-MPD. When increased to 100 °C/min, a T_g was observed for 10HEDA-TFMPD as well, while no noticeable endothermic transitions were observed for 10FEDA-MPD and 10FEDA-TFMPD. This finding indicates a smaller change in the thermal expansion coefficients between the rubbery and glassy states for 10HEDA-TFMPD compared to 10HEDA-MPD and seems to apply for 10FEDA-MPD and 10FEDA-TFMPD as well, thus requiring faster ramp rates to observe a T_g via DSC measurements. In Table 7.2, the T_g for 10HEDA-MPD and 10HEDA-TFMPD corresponds to the third trace of the 100 °C/min ramp rate experiment. Other methods for measuring T_g , such as dynamic mechanical analysis, could prove useful. For example, the T_g for 10FEDA-TFMPD was observed by Ando *et al.* using a thermal mechanical analyzer.³⁶ Nonetheless, the four polymers show a high T_g and are in the glassy state, which will be further elaborated based on the curvature of the sorption isotherms presented later. Additionally, an exothermic peak related to melting was not observed on the DSC trace for all polymers, suggesting the polymers are completely amorphous.

Table 7.2. Summary of polymer film characterization.

	T _g (°C)	Density (g cm ⁻³)	FFV	Volume fraction of fluorine (ϕ_F)
10HEDA-MPD	263	1.48 ± 0.03	0.093	0
10HEDA-TFMPD	289	1.59 ± 0.02	0.105	0.095
10FEDA-MPD	-	1.74 ± 0.03	0.117	0.220
10FEDA-TFMPD	309*	1.79 ± 0.03	0.140	0.292

*From Ando *et al.*³⁶

7.3.3. Estimation of Lattice Fluid Parameters

High-pressure sorption isotherms for O₂, N₂, CH₄, and CO₂ were obtained at 35, 45, 55, and 65 °C for the four polymers. These isotherms were then used to estimate LFPs for each polymer by fitting experimental S_∞ values to Equation 7.12 using the method described in Section 7.2.¹² The S_∞ values for each isotherm are tabulated in the Tables D.3 to D.6.

In many studies^{10,12,14,34}, k_{12} in Equation 7.12 is set equal to zero to estimate LFPs. This approach represents a first-order approximation for non-polar penetrants.³⁴ However, since the highly fluorinated polymers are polar and are expected to display non-ideal mixing behavior, this assumption may not hold for all gas–polymer pairs.²⁰ A previous study on NELF modeling of perfluorinated Teflon[®] AF 2400 and Teflon[®] AF 1600 found that $k_{12} = 0$ fit the data well for O₂ and N₂ and $k_{12} = 0.05$ best described CH₄ interactions.²⁸ In the same study, isotherms using $k_{12} = 0$ were used for CO₂ but did not show a good fit for Teflon[®] AF 2400. Another recent NELF study on perfluorinated poly(PFMD) and poly(PFMMD) found best-fit values of $k_{12} = 0.045$ and 0.07 for CH₄ and $k_{12} = -0.04$ and -0.025 for CO₂ for each polymer, respectively.¹³ Therefore,

as a first-order approximation to estimate the LFPs, k_{12} values of 0, 0, 0.05, and -0.03 were used for the samples with the highest fluorine content (*i.e.*, 10FEDA-MPD and 10FEDA-TFMPD). For 10HEDA-MPD and 10HEDA-TFMPD, a comparison to similar polyimide structures suggested $k_{12} = 0$ was suitable for O_2 , N_2 , and CH_4 , while $k_{12} = -0.03$ was a reasonable estimate for CO_2 .^{12,14}

However, an unconstrained fit of the experimental S_∞ values to Equation 7.12 using T_2^* , p_2^* , and ρ_2^* as fitted parameters resulted in non-physical values. Therefore, an additional constraint was enforced. As noted by Galizia *et al.*⁴¹ and Li *et al.*¹³, a linear correlation exists between FFV as calculated by group contribution theory and FFV as defined by NELF can be used to calculate ρ_2^* :

$$f = \frac{\rho_2 - \rho_2^*}{\rho_2^*} \quad (7.14)$$

thereby allowing for an estimation of ρ_2^* from FFV values calculated through Equation 7.13. This correlation was used in our work and is shown in Figure D.2.

Using expected k_{12} values and calculated ρ_2^* values, an estimate of the LFPs can be obtained using an interior point algorithm in MATLAB using the χ^2 value as the objective function. A parity plot comparing the experimental and calculated S_∞ values for the four polymers is shown in Figure 7.4, showing good agreement. The best-fit values are shown in Table 7.3 and the uncertainty in the LFPs were determined through a single-parameter sensitivity analysis of the χ^2 objective function.⁴² It should be noted that these LFP sets are estimated under our assumptions for k_{12} and ρ_2^* and can be refined further through additional S_∞ data or experimental pVT measurements.

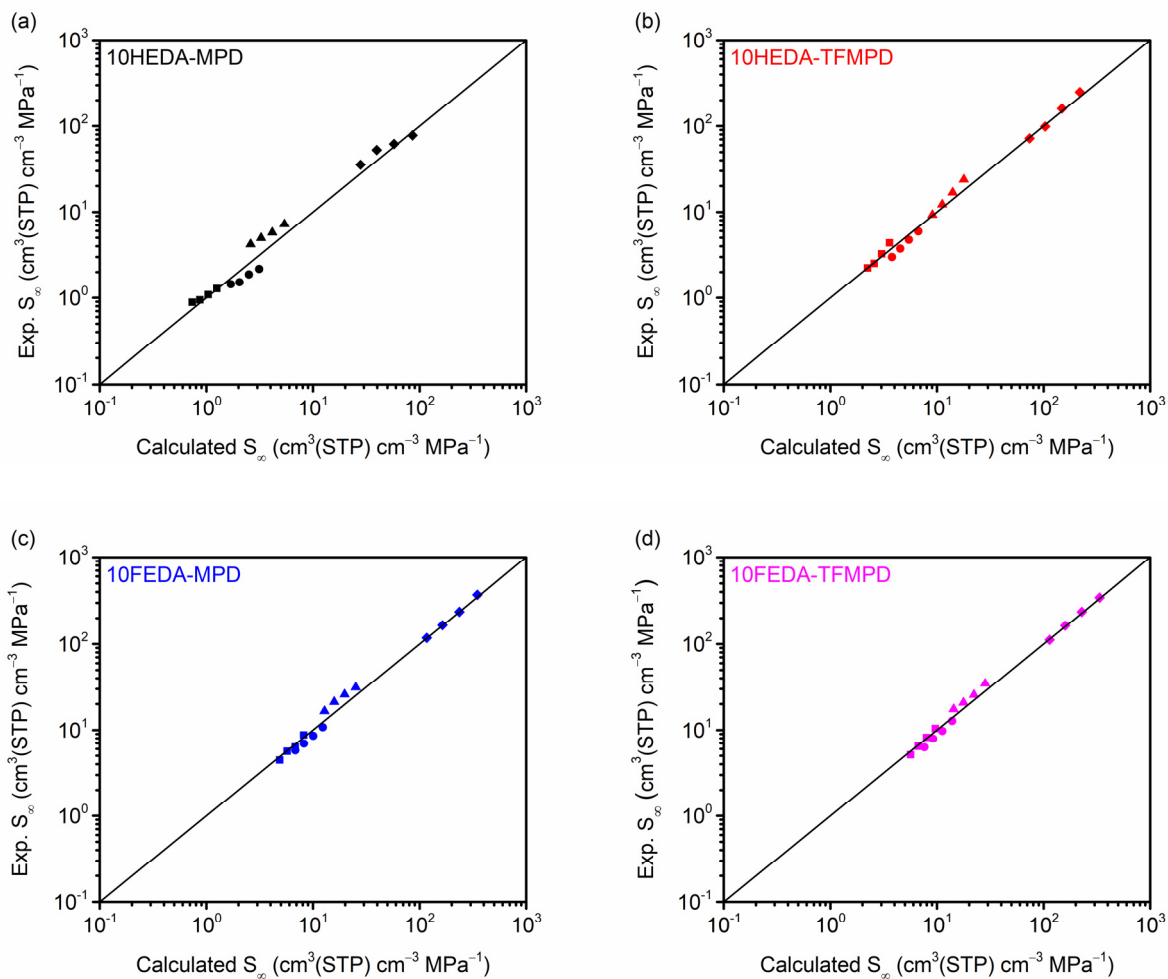


Figure 7.4. Parity plots comparing the experimental and calculated S_{∞} values using the estimated LFPs for (a) 10HEDA-MPD, (b) 10HEDA-TFMPD, (c) 10FEDA-MPD, and (d) 10FEDA-TFMPD for O₂ (squares), N₂ (circles), CH₄ (triangles), and CO₂ (diamonds).

Table 7.3. Estimated LFPs and f for the four polymers.

	T_2^* (K)	p_2^* (MPa)	ρ_2^* (g cm ⁻³)	f
10HEDA-MPD	1030 ± 10	640 ± 20	1.526 ± 0.002	0.030
10HEDA-TFMPD	1130 ± 10	610 ± 20	1.657 ± 0.004	0.040
10FEDA-MPD	1260 ± 10	550 ± 20	1.834 ± 0.005	0.051
10FEDA-TFMPD	1140 ± 10	520 ± 20	1.927 ± 0.002	0.071

In comparison to the LFPs for the other polymers in Table D.1, the best-fit T_2^* and p_2^* values are relatively larger, while the ρ_2^* values follow close agreement. As discussed earlier, T_2^* represents strength of the interchain interactions, suggesting our polymers show significantly stronger secondary interactions than the polymers in Table D.1. This finding could be a result of our casting procedure where the polymer is heated to 350 °C as part of the casting and imidization process. This temperature is near or above the T_g of the polymer, causing the polymer to be in a rubbery or near-rubbery state. Since the polymer slowly cools back down to room temperature over the course of approximately 8 h, the polymer chains are allowed to preferentially rearrange into a packing structure that is denser and closer to equilibrium, thereby resulting in tighter packing and stronger interchain interactions. This description is also in line with the low solvent solubility of the films as well as the low FFV.

We hypothesize that the primary interchain interactions for these polymers are from π - π stacking, similar to other highly aromatic polyimides and poly(ether imide)s.^{39,43,44} The hydrocarbon polymer, 10HEDA-MPD, shows the lowest T_2^* , while higher T_2^* values were calculated for the partially fluorinated polymers, 10HEDA-TFMPD and 10FEDA-MPD. These findings could be

attributed to fluorobenzene-benzene stacking interactions from the distinct aromatic residues in these polymers. In particular, the presence of both fluorobenzene and benzene rings allows for easier π - π stacking based off orientation since the partial charges of the π -orbitals are opposite (*i.e.*, negative for benzene and positive for fluorobenzene).⁴⁵ On the other hand, the higher T_2^* for the perfluorinated 10FEDA-TFMPD compared to 10HEDA-MPD could be a result of polar interactions between partial positively charged fluorobenzene π -orbitals and the partial negatively charged imide linkages. This interaction could also explain the higher T_2^* for 10FEDA-MPD compared to 10HEDA-TFMPD due to the higher molar ratio of aromatic fluorine groups to imide groups. Interestingly, a trend of smaller p_2^* values was observed for these four polymers with increasing fluorine content, consistent with the generally lower CED of perfluoropolymers compared to hydrocarbon polymers observed in Table D.1.

7.3.4. NELF Gas Sorption Modeling and Effect of Fluorine on the Binary Interaction Parameter

With the best-fit LFPs, the isotherms can be modeled using the NELF model once a best-fit k_{12} value is determined for each gas-polymer pair. Here, we used k_{12} as a fitted parameter to the sorption isotherm data at 35 °C using χ^2 as the objective function.⁴² The uncertainty was determined through a single-parameter sensitivity analysis using the χ^2 objective function.⁴² The isotherms for the rest of the temperatures can then be predicted with no other adjustable parameters. For CO₂, the k_{12} parameter was fit to the low-pressure region (*i.e.*, less than 0.3 MPa) and a k_{sw} parameter was fit to the rest of the high-pressure region for each temperature, following recommendations from Galizia *et al.*¹² All fitted parameters are shown in Tables D.7 and D.8. The 10FEDA-TFMPD isotherms and the NELF results up to 2 MPa are shown in in Figure 7.5 and the full isotherms for the all polymers are shown in Figures D.3 to D.6.

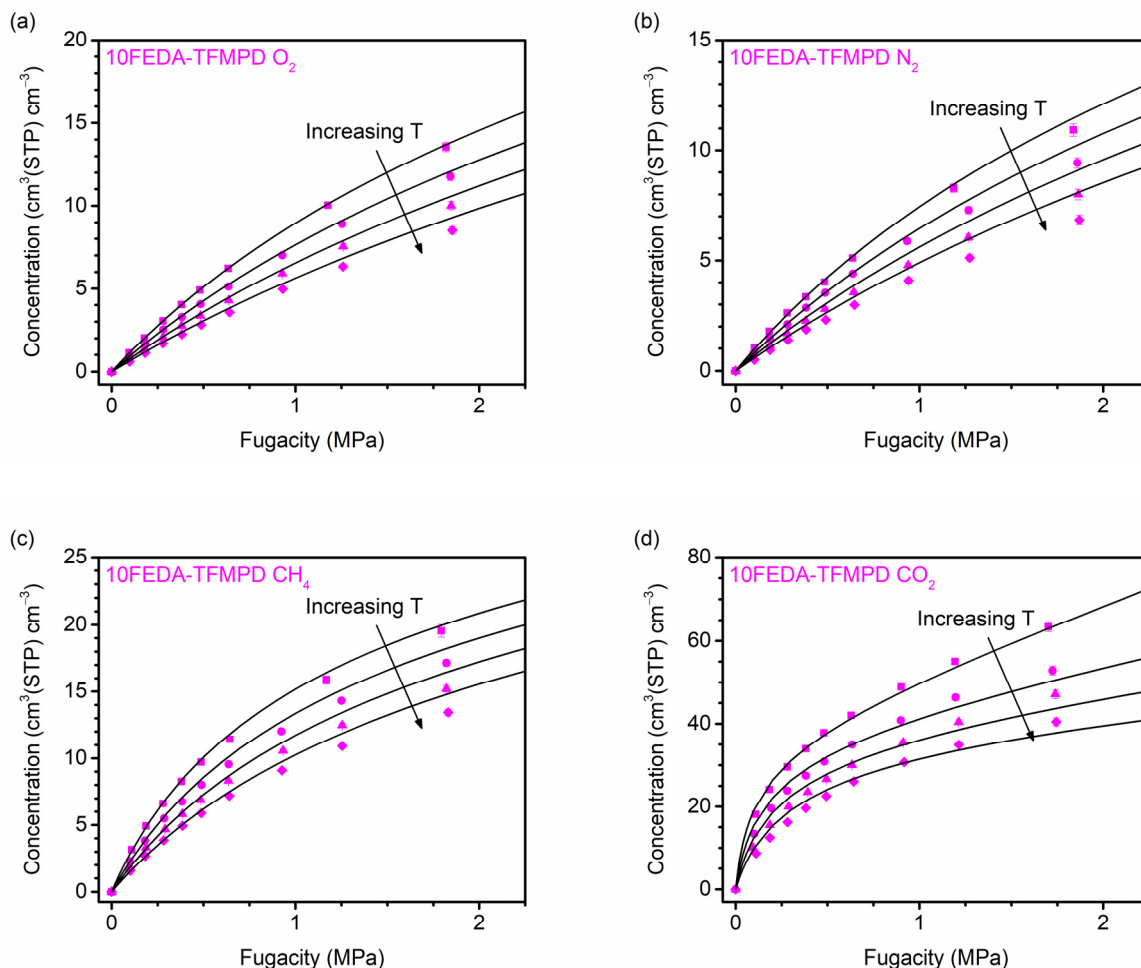


Figure 7.5. Sorption isotherms and NELF modeling of (a) O₂, (b) N₂, (c) CH₄, and (d) CO₂ at 35 °C (squares), 45 °C (circles), 55 °C (triangles), and 65 °C (diamonds) for 10FEDA-TFMPD.

Figure 7.5 shows the lower pressures to highlight the good fit between the model and the data at low pressures, allowing for accurate estimations of S_{∞} for each gas–polymer pair. As is discussed later, S_{∞} describes the sorption behavior in the limit of zero pressure and can be analyzed to determine changes in sorption mechanism as a function of fluorine content.² Because we are interested in obtaining accurate estimations of S_{∞} , we chose the χ^2 parameter as the objective function for the nonlinear optimization of k_{12} as opposed to the sum of squared residuals (SSR). SSR is an unweighted objective function while χ^2 uses the uncertainty in each data point as a

weighing factor, with the smallest uncertainty possessing the largest weight.⁴² Due to the sequential method used to measure sorption and construct the sorption isotherms⁴⁶, the measurement uncertainty for concentration propagates with each step, resulting in progressively larger uncertainty at the higher pressures. Use of the χ^2 parameter takes advantage of the smaller uncertainty at lower pressures to force the fit to match those points over the points with greater uncertainty at higher pressures, which allows for better estimates of S_∞ using the NELF model but can result in inaccuracies at higher pressures. On the other hand, if SSR is used, there are some model fits that are a better fit visually, but provide a worse estimate of S_∞ because the low pressure points are weighted equally to the high pressure points. Examples of the difference in fit between the two objective functions is shown in Figure D.7. In short, we chose the χ^2 objective function to emphasize the fit in the low pressure region of interest. It should be reiterated that k_{12} is only fit at 35 °C and the isotherms and estimates of S_∞ at other temperatures are fully predictive.

Taking the above discussion regarding the strengths and weaknesses of χ^2 versus SSR objective functions, the low pressure region for all gas–polymer pairs are well-described by the NELF model. There is generally good agreement between the data and the model for O₂ for both the low and high pressure regions, although there is some deviation for the isotherm predictions at high pressure for the higher temperatures of 10HEDA-TFMPD. However, we believe that this deviation is acceptable given that the model is completely predictive for temperatures other than 35 °C. For N₂, there are some isotherms that show larger deviation at higher pressure at the reference temperature, such as 10HEDA-TFMPD and 10FEDA-TFMPD. The deviation could either be due to the larger measurement uncertainty at the higher pressures or uncertainty in the LFPs. However, in the low pressure region (*i.e.*, less than 2 MPa), the model and the data match well for all polymers. A similar over-prediction for N₂ at high pressures using the NELF model was also

observed for 6FDA-HAB and TPBO.^{12,14} For CH₄, similar deviations between the model and data were observed for other isotherms at high pressures, such as 10HEDA-MPD and 10FEDA-MPD, while the low pressure region shows good agreement. Again, the relatively poor fit at high pressures at the reference temperature can be attributed to use of the χ^2 parameter. The prediction of the temperature dependence of CH₄ sorption is reasonable but tends to be underestimated, possibly due to uncertainty in the LFPs. Lastly for CO₂, the low pressure region is well-described by the model. Deviations observed at higher pressures are characteristic of using χ^2 instead of SSR as the objective function, showing poor fits at higher pressures. In all cases, the model demonstrates good agreement with the data at low pressures, allowing for analysis into the S_∞ parameter to provide mechanistic insight into the role of fluorination on sorption behavior.

An important parameter to compare across polymers is the binary interaction parameter, k_{12} . The binary interaction parameter originates from the geometric mean mixing rule and is a measure of the deviation from ideal mixing. A positive k_{12} represents less favorable mixing and a negative k_{12} represents more favorable mixing.²⁰ Previously, perfluoropolymers such as Teflon[®] AF 2400 and Teflon[®] AF 1600 have shown systematic deviation towards less favorable mixing for hydrocarbon penetrants in particular, ranging from $k_{12} = 0.05$ for CH₄ to $k_{12} = 0.13$ for *n*-C₄H₁₀.²⁸ In order to relate the sorption behavior of penetrants in hydrocarbon polymers to perfluoropolymers, the best-fit k_{12} values for N₂, O₂, CH₄, and CO₂ were plotted with respect to volume fraction of fluorine in Figure 7.6.

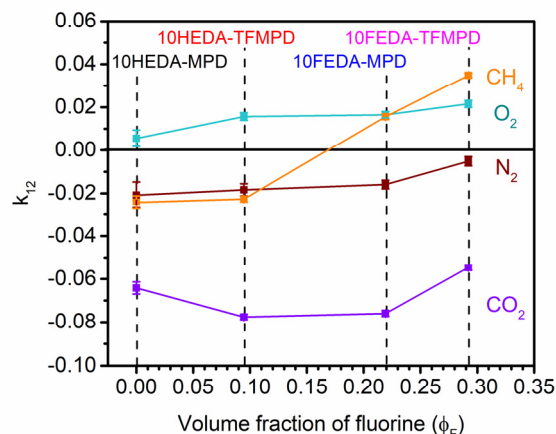


Figure 7.6. The best-fit k_{12} value for each gas plotted as a function of polymer fluorine content.

When comparing the best-fit k_{12} values across fluorine content, a general uptick in k_{12} was observed for all gases, indicating a trend towards increasingly unfavorable deviations from ideal mixing with increasing fluorination. While O₂ showed consistently positive k_{12} values and N₂ and CO₂ showed consistently negative k_{12} values, only CH₄ crossed the threshold from favorable to unfavorable mixing interaction. Additionally, the increase in k_{12} for CH₄ is greater than those for O₂, N₂, and CO₂, potentially indicating a penetrant-specific interaction causing the unfavorable deviation as opposed to an overall governing penetrant property such as penetrant polarity or condensability. This specific unfavorable deviation has been previously observed for hydrocarbon–perfluorocarbon liquids^{47,48}, and for polymers, the magnitude of this deviation appears to be a function of fluorine content. Interestingly, the relationship does not appear to be linear with respect to fluorine content as the lightly fluorinated analogue, 10HEDA-TFMPD, showed a similar k_{12} value for CH₄ as 10HEDA-MPD.

There are a variety of perfluoropolymers with significantly higher fluorine content than those of the polymers considered in this study. Using our approach described earlier in Section 7.3.2,

poly(PFMD)¹³, poly(PFMMD)¹³, Teflon[®] AF 2400²⁸, and Teflon[®] AF 1600²⁸ have $\phi_F = 0.54$, 0.58, 0.59, and 0.62, respectively. Therefore, it is helpful to compare k_{12} values for these polymers and our poly(ether imide)s to determine if an “upper bound” to unfavorable mixing exists with fluorination for CH₄. Interestingly, literature k_{12} values range from 0.045 ± 0.004 to 0.07 ± 0.01 , which are slightly higher than those of 10FEDA-TFMPD^{13,28}. This bound is hypothesized to increase with increasing hydrocarbon molar volume as demonstrated for C₂H₆, C₃H₈, and *n*-C₄H₁₀ in Teflon[®] AF 2400 and Teflon[®] AF 1600.²⁸ Finally, it should be noted that this discussion regarding k_{12} does not describe the relative solubility of gases in the polymer, which is a function of a variety of penetrant and polymer properties, but rather describes the deviation of sorption from ideality.

7.3.5. Effect of Fluorine on Enthalpic and Entropic Contributions to Gas Sorption at Infinite Dilution

The mechanism by which fluorination changes sorption behavior can be probed through an analysis of the S_∞ values.¹² The S_∞ term represents the sorption coefficient in the limit of zero pressure, thereby describing the sorption behavior of the first penetrant in the system and is analogous to the infinite dilution solubility limit of a solute in a solvent.² The NELF equation for S_∞ (Equation 7.12) can be decoupled into enthalpic and entropic contributions:^{12,13,30}

$$\ln(S_\infty) = \ln\left(\frac{T_{STP}}{p_{STP}T}\right) + \phi_H + \phi_S \quad (7.15)$$

$$\phi_H = r_1^0 \left\{ \frac{\rho_2 T_1^*}{\rho_2^* T} \frac{2}{p_1^*} (1 - k_{12}) \sqrt{p_1^* p_2^*} \right\} \quad (7.16)$$

$$\phi_S = r_1^0 \left\{ \left[1 + \left(\frac{v_1^*}{v_2^*} - 1 \right) \frac{\rho_2^*}{\rho_2} \right] \ln \left(1 - \frac{\rho_2}{\rho_2^*} \right) + \left(\frac{v_1^*}{v_2^*} - 1 \right) \right\} \quad (7.17)$$

where the terms have the same meaning as described in Table 7.1. The enthalpic portion (ϕ_H) encompasses penetrant–polymer interactions while the entropic portion (ϕ_S) represents the excess entropy compared to an ideal mixture and is largely associated with the free volume of the polymer membrane. The above two equations can be rewritten in terms of f (see Equation 7.14):¹³

$$\phi_H = r_1^0 \frac{2T_1^*}{p_1^* T} (1 - f)(1 - k_{12}) \sqrt{p_1^* p_2^*} \quad (7.18)$$

$$\phi_S = r_1^0 \left\{ \left[\left(\frac{v_1^*}{v_2^*} - 1 \right) \frac{1}{1 - f} \right] \ln(f) + \left(\frac{v_1^*}{v_2^*} - 1 \right) \right\} \quad (7.19)$$

The enthalpic and entropic contributions to S_∞ were calculated for each gas–polymer–temperature set and are plotted with respect to critical temperature (T_C) normalized by the testing temperature in Figures 7.7a and 7.7b. In this manner, the vertical position of the correlation describes the relative contribution across polymers and the slope of the correlation describes the enthalpic and entropic selectivity. Additionally, ϕ_H has been shown to be directly related to the enthalpy of sorption (*i.e.*, $\phi_H \propto -\Delta H_S$).³⁰ In Figure 7.7a, the magnitude of the enthalpic contribution decreases with fluorine content, indicating that ΔH_S becomes increasingly endothermic (*i.e.*, less negative) with fluorine content for all gases. Mathematically, this result is due to the increase in k_{12} as shown in Figure 7.6, the decrease in p_2^* with fluorine content, and the increase in f as shown in Table 7.2. Greater unfavorable deviation towards mixing would result in an enthalpic penalty, while lower CED could be coupled with higher f and thus reduce the amount of penetrant–polymer interactions.³⁰ As a whole, all three parameter trends are a result of both chemical and structural changes caused by fluorination across the structurally analogous backbones.

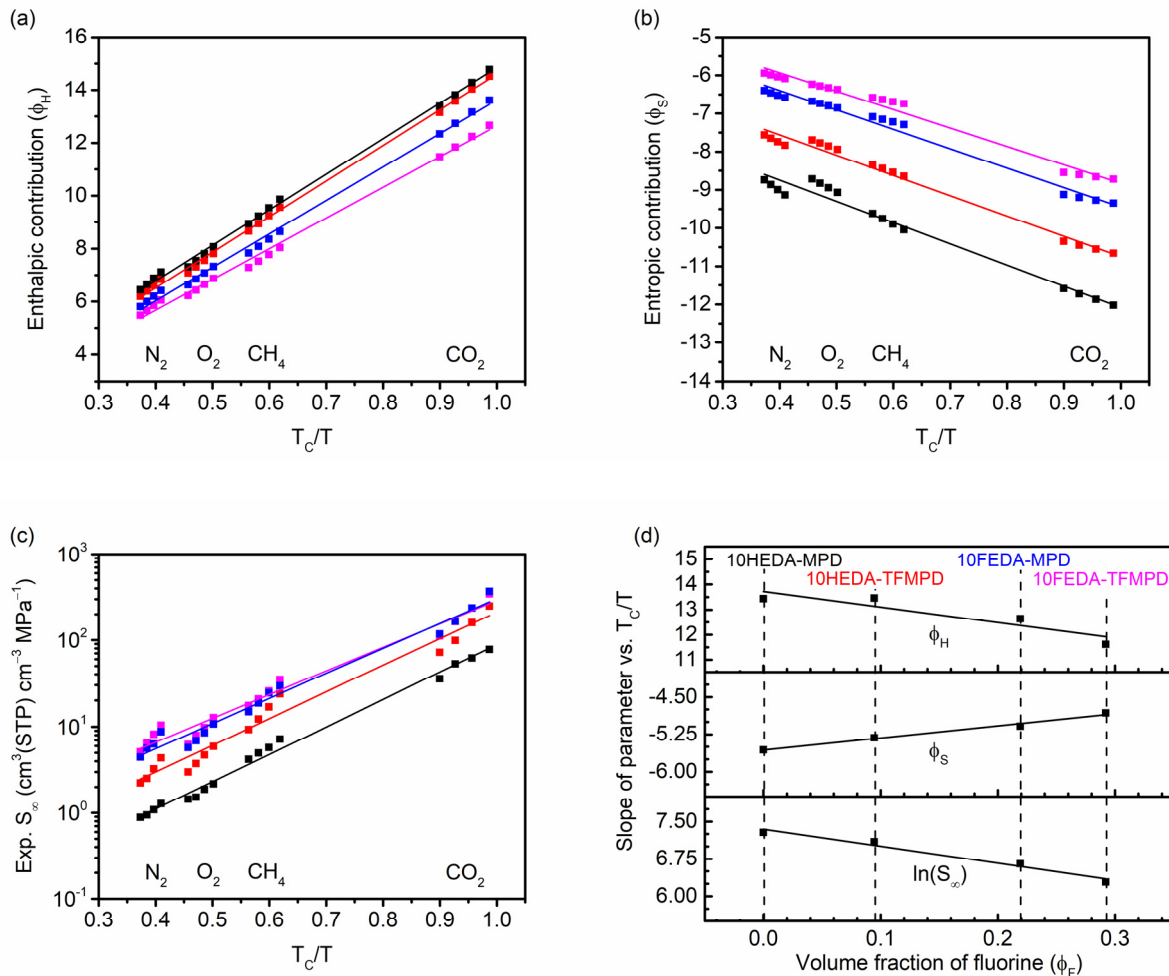


Figure 7.7. Plots for (a) ϕ_H , (b) ϕ_S , and (c) $\ln(S_\infty)$ versus T_c/T for all four polymers. The black points are for 10HEDA-MPD, the red points are for 10HEDA-TFMPD, the blue points are for 10FEDA-MPD, and the magenta points are for 10FEDA-TFMPD. The lines are best-fit lines for each polymer. (d) The slope of the best-fit lines for ϕ_H , ϕ_S , and $\ln(S_\infty)$ for each polymer as a function of fluorine content.

The slope of the ϕ_H correlation for each polymer is plotted in Figure 7.7d, showing a trend of decreasing slope with increasing fluorine content. For this correlation, the decrease in slope can be interpreted as an increase in enthalpic selectivity for gas pairs where the faster permeating gas is also the less strongly sorbing penetrant (*e.g.*, N_2/CH_4). When comparing across penetrants for a

single polymer, the more condensable penetrants will accordingly receive a larger absolute penalty for ϕ_H since condensability scales with the penetrant LFPs and molecular weight. Overall, fluorination results in a lower enthalpic contribution to sorption but a higher enthalpic selectivity.

On the other hand, Figure 7.7b shows the correlations for ϕ_S with respect to T_C/T . Similar to ϕ_H , ϕ_S has been shown to be directly related to the entropy of sorption (*i.e.*, $\phi_S \propto -\Delta S_S$).³⁰ The relative magnitude of the entropic contribution is primarily affected by f and becomes less negative with increasing fluorine content due to the increased packing disrupting caused by the larger size of fluorine compared to hydrogen.³⁹ A statistical interpretation by De Angelis *et al.* suggests that higher free volume provides a higher probability of incorporation of a penetrant into the sorbed phase and therefore a reduced entropic penalty.³⁰ The slopes of the ϕ_S correlation for each polymer are plotted in Figure 7.7d as well, where an increase in slope was observed with increasing fluorination and can be interpreted as a loss in entropic selectivity. The aforementioned statistical interpretation supports this trend, where higher free volume results in more probable incorporation of larger, more condensable penetrants (as quantified by r_1^0 , not molecular diameter).³⁰ Overall, fluorination results in a less negative entropic contribution but lower entropic selectivity through increasing f .

Lastly, Figure 7.7c shows the experimental S_∞ values for each gas–polymer–temperature set plotted with respect to T_C/T . In our earlier study, we observed a continuous linear decrease in the slope of correlations between $\ln(S_\infty)$ and ε/k with respect to fluorine content.² Figure 7.7d shows the slope of the $\ln(S_\infty)$ versus T_C/T correlation with respect to fluorine content, again showing a continuous decrease in slope with increasing fluorination. For this correlation, a decrease in slope is associated with increased sorption selectivity for gas pairs where the faster-permeating gas is also the less-sorbing penetrant. According to Equation 7.15, the behavior of $\ln(S_\infty)$ can be

described using ϕ_H and ϕ_S . When comparing the relative effects of ϕ_H and ϕ_S on $\ln(S_\infty)$, it is clear that ϕ_H dominates over ϕ_S since $\ln(S_\infty)$ and ϕ_H both increase with T_C/T while ϕ_S decreases with T_C/T . However, the increase in ϕ_S is greater than the decrease in ϕ_H with increasing fluorination, resulting in higher $\ln(S_\infty)$ values for the highly fluorinated materials. The change in slope for $\ln(S_\infty)$ across polymers can also be explained through the changes in slope for ϕ_H and ϕ_S . As discussed earlier, ϕ_H shows a decreasing slope and ϕ_S shows an increasing slope with increasing fluorine content, indicating higher enthalpic selectivity and lower entropic selectivity, respectively. Figure 7.7d shows the overall consequence of this enthalpic–entropic tradeoff by the decrease in the slope for $\ln(S_\infty)$ with increasing fluorine content. Previous studies have hypothesized and demonstrated similar changes in $\ln(S_\infty)$, ϕ_H , and ϕ_S for perfluoropolymers.^{13,30} Here, we show a continuous trend for all three parameters across our polymers, demonstrating a gradual change in sorption behavior and its enthalpic and entropic contributions with respect to fluorine content.

7.4. Conclusions

The role of fluorine on the sorption behavior for a series of four structurally analogous poly(ether imide)s ranging from fully hydrocarbon to fully fluorinated was analyzed using the NELF model. A perfluorinated dianhydride monomer, 10FEDA, was synthesized and used to create the highly fluorinated and perfluorinated poly(ether imide) structural analogues. Pure-gas sorption isotherms at 35, 45, 55, and 65 °C were collected for O₂, N₂, CH₄, and CO₂, and LFPs for the polymers were estimated by fitting experimental S_∞ values to the corresponding NELF-derived equation. The sorption isotherms were modeled using the NELF model, obtaining a best-fit k_{12} value to the data at 35 °C. Good agreement between the model and the data was observed, particularly at pressures less than 2 MPa. The change in the best-fit k_{12} for each gas was examined as a function of fluorine

content. Of note, the increase in k_{12} for CH₄ was much more pronounced compared to the other gases, suggesting a penetrant-specific origin for the unfavorable deviation from ideal mixing. Additionally, the magnitude of the deviation for CH₄ appeared to be a nonlinear function of polymer fluorine content. The role of fluorine on total sorption and sorption selectivity was evaluated based on enthalpic and entropic contributions to S_{∞} . In terms of total sorption, the increase in entropic contribution outweighed the decrease in enthalpic contribution, resulting in an increase in S_{∞} with increasing fluorine content. However, in terms of sorption selectivity, the loss in entropic selectivity was less than the increase in enthalpic selectivity, resulting in overall increased sorption selectivity with increasing fluorine content. These findings were correlated with k_{12} , CED, and f . This study connects the sorption behavior of hydrocarbon polymers to perfluoropolymers, providing insight into fluorine-specific structure–property relationships and understanding of the molecular origin behind the exceptional separation performance for this unique class of materials.

7.5. References

- (1) Matteucci, S.; Yampolskii, Y.; Freeman, B. D.; Pinnau, I. Transport of Gases and Vapors in Glassy and Rubbery Polymers. In *Materials Science of Membranes for Gas and Vapor Separation*; 2006; pp 1–47. <https://doi.org/10.1002/047002903X.ch1>.
- (2) Wu, A. X.; Drayton, J. A.; Mizrahi Rodriguez, K.; Benedetti, F. M.; Qian, Q.; Lin, S.; Smith, Z. P. Elucidating the Role of Fluorine Content on Gas Sorption Properties of Fluorinated Polyimides. *Macromolecules* **2021**, *54* (1), 22–34. <https://doi.org/10.1021/acs.macromol.0c01746>.
- (3) Koros, W. J.; Paul, D. R.; Huvard, G. S. Energetics of Gas Sorption in Glassy Polymers. *Polymer* **1979**, *20*, 956–960. [https://doi.org/10.1016/0032-3861\(79\)90192-7](https://doi.org/10.1016/0032-3861(79)90192-7).
- (4) Doghieri, F.; Sarti, G. C. Nonequilibrium Lattice Fluids: A Predictive Model for the Solubility in Glassy Polymers. *Macromolecules* **1996**, *29* (24), 7885–7896. <https://doi.org/10.1021/ma951366c>.
- (5) Minelli, M.; Sarti, G. C. 110th Anniversary: Gas and Vapor Sorption in Glassy Polymeric Membranes - Critical Review of Different Physical and Mathematical Models. *Ind. Eng. Chem. Res.* **2020**, *59* (1), 341–365. <https://doi.org/10.1021/acs.iecr.9b05453>.

- (6) Flory, P. J. Thermodynamics of High Polymer Solutions. *J. Chem. Phys.* **1942**, *10*, 51. <https://doi.org/10.1007/s12045-017-0481-2>.
- (7) Lacombe, R. H.; Sanchez, I. C. Statistical Thermodynamics of Fluid Mixtures. *J. Phys. Chem.* **1976**, *80* (23), 2568–2580. <https://doi.org/10.1021/j100564a009>.
- (8) Sanchez, I. C.; Lacombe, R. H. An Elementary Molecular Theory of Classical Fluids. Pure Fluids. *J. Phys. Chem.* **1976**, *80* (21), 2352–2362. <https://doi.org/10.1021/j100562a008>.
- (9) Sanchez, I. C.; Lacombe, R. H. Statistical Thermodynamics of Polymer Solutions. *Macromolecules* **1978**, *11* (6), 1145–1156. <https://doi.org/10.1021/ma60066a017>.
- (10) Comesaña-Gandara, B.; Ansaloni, L.; Lee, Y. M.; Lozano, A. E.; De Angelis, M. G. Sorption, Diffusion, and Permeability of Humid Gases and Aging of Thermally Rearranged (TR) Polymer Membranes from a Novel Ortho-Hydroxypolyimide. *J. Membr. Sci.* **2017**, *542* (July), 439–455. <https://doi.org/10.1016/j.memsci.2017.08.009>.
- (11) Ricci, E.; Elias, A.; Du, N.; Li, N.; De, M. G.; Guiver, M. D.; Sarti, G. C.; Ricci, E.; Gameda, A. E.; Du, N.; et al. Sorption of CO₂/CH₄ Mixtures in TZ-PIM, PIM-1 and PTMSP: Experimental Data and NELF-Model Analysis of Competitive Sorption and Selectivity in Mixed Gases. *J. Membr. Sci.* **2019**, *585* (May), 136–149. <https://doi.org/10.1016/j.memsci.2019.05.026>.
- (12) Galizia, M.; Stevens, K. A.; Smith, Z. P.; Paul, D. R.; Freeman, B. D. Nonequilibrium Lattice Fluid Modeling of Gas Solubility in HAB-6FDA Polyimide and Its Thermally Rearranged Analogues. *Macromolecules* **2016**, *49* (22), 8768–8779. <https://doi.org/10.1021/acs.macromol.6b01479>.
- (13) Li, Y.; Yavari, M.; Baldanza, A.; Di Maio, E.; Okamoto, Y.; Lin, H.; Galizia, M. Volumetric Properties and Sorption Behavior of Perfluoropolymers with Dioxolane Pendant Rings. *Ind. Eng. Chem. Res.* **2020**, *59* (12), 5276–5286. <https://doi.org/10.1021/acs.iecr.9b03411>.
- (14) Loianno, V.; Zhang, Q.; Luo, S.; Guo, R.; Galizia, M. Modeling Gas and Vapor Sorption and Swelling in Triptycene-Based Polybenzoxazole: Evidence for Entropy-Driven Sorption Behavior. *Macromolecules* **2019**, *52* (11), 4385–4395. <https://doi.org/10.1021/acs.macromol.9b00577>.
- (15) Baschetti, M. G.; Doghieri, F.; Sarti, G. C. Solubility in Glassy Polymers: Correlations through the Nonequilibrium Lattice Fluid Model. *Ind. Eng. Chem. Res.* **2001**, *40* (14), 3027–3037. <https://doi.org/10.1021/ie000834q>.
- (16) Yampolskii, Y.; Belov, N.; Alentiev, A. Perfluorinated Polymers as Materials of Membranes for Gas and Vapor Separation. *J. Membr. Sci.* **2020**, 117779. <https://doi.org/10.1016/j.memsci.2019.117779>.
- (17) Squire, E. N. Optical Fibers Comprising Cores Clad with Amorphous Copolymers of Perfluoro-2,2-Dimethyl-1,3-Dioxole. US Patent 4,530,569, 1985.
- (18) Squire, E. N. Amorphous Copolymers of Perfluoro-2,2-Dimethyl-1,3-Dioxole. US Patent 4,754,009, 1988.
- (19) Colaianna, P.; Brinari, G.; Arcella, V. Amorphous Perfluoropolymers. US Patent

- 5,883,177, 1999.
- (20) Merkel, T. C.; Pinnau, I.; Prabhakar, R. S.; Freeman, B. D. Gas and Vapor Transport Properties of Perfluoropolymers. In *Materials Science of Membranes for Gas and Vapor Separation*; 2006; pp 251–270.
- (21) Merkel, T. C.; Bondar, V.; Nagai, K.; Freeman, B. D.; Yampolskii, Y. P. Gas Sorption, Diffusion, and Permeation in Poly(2,2-Bis(Trifluoromethyl)-4,5-Difluoro-1,3-Dioxole-Co-Tetrafluoroethylene). *Macromolecules* **1999**, *32* (25), 8427–8440. <https://doi.org/10.1021/ma990685r>.
- (22) Pinnau, I.; Toy, L. G. Gas and Vapor Transport Properties of Amorphous Perfluorinated Copolymer Membranes Based on 2,2-Bistrifluoromethyl-4,5-Difluoro-1,3-Dioxole/Tetrafluoroethylene. *J. Membr. Sci.* **1996**, *109* (1), 125–133. [https://doi.org/10.1016/0376-7388\(95\)00193-X](https://doi.org/10.1016/0376-7388(95)00193-X).
- (23) Alentiev, A. Y.; Shantarovich, V. P.; Merkel, T. C.; Bondar, V. I.; Freeman, B. D.; Yampolskii, Y. P. Gas and Vapor Sorption, Permeation, and Diffusion in Glassy Amorphous Teflon AF1600. *Macromolecules* **2002**, *35* (25), 9513–9522. <https://doi.org/10.1021/ma020494f>.
- (24) Macchione, M.; Jansen, J. C.; De Luca, G.; Tocci, E.; Longeri, M.; Drioli, E. Experimental Analysis and Simulation of the Gas Transport in Dense Hyflon® AD60X Membranes: Influence of Residual Solvent. *Polymer* **2007**, *48* (9), 2619–2635. <https://doi.org/10.1016/j.polymer.2007.02.068>.
- (25) Comesaña-Gándara, B.; Chen, J.; Bezzu, C. G.; Carta, M.; Rose, I.; Ferrari, M. C.; Esposito, E.; Fuoco, A.; Jansen, J. C.; McKeown, N. B. Redefining the Robeson Upper Bounds for CO₂/CH₄ and CO₂/N₂ Separations Using a Series of Ultrapermeable Benzotriptycene-Based Polymers of Intrinsic Microporosity. *Energy Environ. Sci.* **2019**, *12* (9), 2733–2740. <https://doi.org/10.1039/c9ee01384a>.
- (26) Qian, Q.; Asinger, P. A.; Lee, M. J.; Han, G.; Mizrahi Rodriguez, K.; Lin, S.; Benedetti, F. M.; Wu, A. X.; Chi, W. S.; Smith, Z. P. MOF-Based Membranes for Gas Separations. *Chem. Rev.* **2020**, *120* (16), 8161–8266. <https://doi.org/10.1021/acs.chemrev.0c00119>.
- (27) Yavari, M.; Fang, M.; Nguyen, H.; Merkel, T. C.; Lin, H.; Okamoto, Y. Dioxolane-Based Perfluoropolymers with Superior Membrane Gas Separation Properties. *Macromolecules* **2018**, *51* (7), 2489–2497. <https://doi.org/10.1021/acs.macromol.8b00273>.
- (28) De Angelis, M. G.; Merkel, T. C.; Bondar, V. I.; Freeman, B. D.; Doghieri, F.; Sarti, G. C. Gas Sorption and Dilation in Poly(2,2-Bistrifluoromethyl-4,5-Difluoro-1,3-Dioxole-Co-Tetrafluoroethylene): Comparison of Experimental Data with Predictions of the Nonequilibrium Lattice Fluid Model. *Macromolecules* **2002**, *35* (4), 1276–1288. <https://doi.org/10.1021/ma0106090>.
- (29) Ricci, E.; Benedetti, F. M.; Dose, M. E.; De Angelis, M. G.; Freeman, B. D.; Paul, D. R. Competitive Sorption in CO₂/CH₄ Separations: The Case of HAB-6FDA Polyimide and Its TR Derivative and a General Analysis of Its Impact on the Selectivity of Glassy Polymers at Multicomponent Conditions. *J. Membr. Sci.* **2020**, *612*, 118374. <https://doi.org/10.1016/j.memsci.2020.118374>.

- (30) De Angelis, M. G.; Sarti, G. C.; Doghieri, F. NELF Model Prediction of the Infinite Dilution Gas Solubility in Glassy Polymers. *J. Membr. Sci.* **2007**, *289* (1–2), 106–122. <https://doi.org/10.1016/j.memsci.2006.11.044>.
- (31) Scherillo, G.; Sanguigno, L.; Galizia, M.; Lavorgna, M.; Musto, P.; Mensitieri, G. Non-Equilibrium Compressible Lattice Theories Accounting for Hydrogen Bonding Interactions: Modelling Water Sorption Thermodynamics in Fluorinated Polyimides. *Fluid Phase Equilib.* **2012**, *334*, 166–188. <https://doi.org/10.1016/j.fluid.2012.06.030>.
- (32) Zoller, P. Pressure–Volume–Temperature Relationships of Solid and Molten Polypropylene and Poly(Butene-1). *J. Appl. Polym. Sci.* **1979**, *23* (4), 1057–1061. <https://doi.org/10.1002/app.1979.070230411>.
- (33) Budd, P. M.; Msayib, K. J.; Tattershall, C. E.; Ghanem, B. S.; Reynolds, K. J.; McKeown, N. B.; Fritsch, D. Gas Separation Membranes from Polymers of Intrinsic Microporosity. *J. Membr. Sci.* **2005**, *251* (1–2), 263–269. <https://doi.org/10.1016/j.memsci.2005.01.009>.
- (34) Galizia, M.; De Angelis, M. G.; Sarti, G. C. Sorption of Hydrocarbons and Alcohols in Addition-Type Poly(Trimethyl Silyl Norbornene) and Other High Free Volume Glassy Polymers. II: NELF Model Predictions. *J. Membr. Sci.* **2012**, *405–406*, 201–211. <https://doi.org/10.1016/j.memsci.2012.03.009>.
- (35) Ando, S.; Matsuura, T. Substituent Shielding Parameters of Fluorine-19 NMR on Polyfluoroaromatic Compounds Dissolved in Dimethyl Sulphoxide-d₆. *Magn. Reson. Chem.* **1995**, *33* (8), 639–645. <https://doi.org/10.1002/mrc.1260330805>.
- (36) Ando, S.; Matsuura, T.; Sasaki, S. Perfluorinated Polyimide Synthesis. *Macromolecules* **1992**, *25* (21), 5858–5860. <https://doi.org/10.1021/ma00047a045>.
- (37) Hougham, G.; Tesoro, G.; Shaw, J. Synthesis and Properties of Highly Fluorinated Polyimides. *Macromolecules* **1994**, *27* (13), 3642–3649. <https://doi.org/10.1021/ma00091a028>.
- (38) Liu, Y.; Wang, R.; Chung, T. S. Chemical Cross-Linking Modification of Polyimide Membranes for Gas Separation. *J. Membr. Sci.* **2001**, *189* (2), 231–239. [https://doi.org/10.1016/S0376-7388\(01\)00415-X](https://doi.org/10.1016/S0376-7388(01)00415-X).
- (39) Wu, A. X.; Drayton, J. A.; Rodriguez, K. M.; Qian, Q.; Lin, S.; Smith, Z. P. Influence of Aliphatic and Aromatic Fluorine Groups on Gas Permeability and Morphology of Fluorinated Polyimide Films. *Macromolecules* **2020**, *53* (13), 5085–5095. <https://doi.org/10.1021/acs.macromol.0c01024>.
- (40) Bondi, A. Van Der Waals Volumes and Radii. *J. Phys. Chem.* **1964**, *68* (3), 441–451. <https://doi.org/10.1021/j100785a001>.
- (41) Galizia, M.; Smith, Z. P.; Sarti, G. C.; Freeman, B. D.; Paul, D. R. Predictive Calculation of Hydrogen and Helium Solubility in Glassy and Rubbery Polymers. *J. Membr. Sci.* **2015**, *475*, 110–121. <https://doi.org/10.1016/j.memsci.2014.10.009>.
- (42) Bevington, P. R.; Robinson, D. K. *Data Reduction and Error Analysis for the Physical Sciences*, 3rd ed.; McGraw-Hill: New York, 2003. <https://doi.org/10.1063/1.4823194>.

- (43) Li, T.; Liu, J.; Zhao, S.; Chen, Z.; Huang, H.; Guo, R.; Chen, Y. Microporous Polyimides Containing Bulky Tetra-*o*-Isopropyl and Naphthalene Groups for Gas Separation Membranes. *J. Membr. Sci.* **2019**, *585* (May), 282–288. <https://doi.org/10.1016/j.memsci.2019.05.003>.
- (44) Zhang, C.; Li, P.; Cao, B. Effects of the Side Groups of the Spirobichroman-Based Diamines on the Chain Packing and Gas Separation Properties of the Polyimides. *J. Membr. Sci.* **2017**, *530* (February), 176–184. <https://doi.org/10.1016/j.memsci.2017.02.030>.
- (45) Martinez, C. R.; Iverson, B. L. Rethinking the Term “Pi-Stacking.” *Chem. Sci.* **2012**, *3* (7), 2191–2201. <https://doi.org/10.1039/c2sc20045g>.
- (46) Lin, H.; Freeman, B. D. Permeation and Diffusion. In *Springer-Handbook of Materials Measurement Methods*; 2006.
- (47) Scott, R. L. The Solubility of Fluorocarbons. *J. Am. Chem. Soc.* **1948**, *70* (12), 4090–4093. <https://doi.org/10.1021/ja01192a036>.
- (48) Scott, R. L. The Anomalous Behavior of Fluorocarbon Solutions. *J. Phys. Chem.* **1958**, *62* (2), 136–145. <https://doi.org/10.1021/j150560a002>.

Chapter 8: Revisiting Group Contribution Theory for Estimating Fractional Free Volume of Microporous Polymer Membranes

Abstract

Fractional free volume (FFV) is a commonly used metric for the development of structure–property relationships for polymer membranes. The most common method to calculate FFV uses Bondi’s group contribution method, first introduced in 1964. While updated in 1997, there has not been a significant compilation of new structural motifs since the advent of linear microporous polymers. In this study, we critically examined the assumptions in Bondi’s original method and provide four recommendations to streamline and improve the accuracy of calculating van der Waals volume (V_W) for any group. Using these recommendations, we created an updated list of V_W values for structural groups commonly present in microporous polymers. The V_W and FFV values were then calculated for a database of 123 microporous and high free volume polymers from the literature, showing an average 7% decrease in V_W and corresponding increase in FFV by a factor of 24% when compared to prior group contribution correlations in the literature. The significant apparent increase in estimated FFV provides a new perspective to understand and interpret the role of free volume on the separation performance of linear microporous polymers. Additionally, standardization of the group contribution method allows for the direct comparison of FFV values across studies.

This chapter has been adapted from: Wu, A. X.; Lin, S.; Mizrahi Rodriguez, K.; Benedetti, F. M.; Joo, T.; Grosz, A. F.; Storme, K. R.; Roy, N.; Syar, D.; Smith, Z. P. Revisiting Group Contribution Theory for Estimating Fractional Free Volume of Microporous Polymer Membranes. *Submitted*.

8.1. Introduction

Fractional free volume (FFV) is widely used to describe the relative “empty space” present in a polymer membrane resulting from inefficient packing of the polymer chains in the solid-state.¹ Historically, this free volume concept has been used in the works of Doolittle²⁻⁴ and Williams, Landel, and Ferry⁵ to develop relationships between inherent viscosity and the glass transition temperature, respectively. Currently, FFV is used in a number of polymer applications, such as low- κ dielectrics⁶, proton-exchange membranes⁷, and gas separation membranes⁸, as a fundamental material property to which changes in the polymer structure and performance could be related. For example, in the context of designing a polymer for gas separations, the incorporation of a bulky group on the polymer backbone could be hypothesized to increase FFV by disrupting chain packing and therefore be expected to result in higher gas permeability.⁹ With such observations, generalized correlations relating gas permeability to FFV can be made. Of note, a larger FFV has been shown to correlate with higher permeability coefficients in an exponential manner for a large database of reported polymeric materials:¹⁰

$$P = A \times \exp\left(-\frac{B}{FFV}\right) \quad (8.1)$$

where A and B are constants for a specific gas. In this way, FFV is a useful tool to understand and develop structure–property relationships to aid in the design of materials for specific applications.

However, determining FFV is empirically challenging. FFV is defined as

$$FFV = \frac{V_f}{V} = \frac{V - V_{oc}}{V} \quad (8.2)$$

where V_f is the free volume ($\text{cm}^3 \text{ g}^{-1}$), V is the specific volume ($\text{cm}^3 \text{ g}^{-1}$), and V_{oc} is the volume occupied by the polymer chains ($\text{cm}^3 \text{ g}^{-1}$).¹⁰ While the specific volume is a measureable quantity

equal to the inverse of the polymer film density, researchers must turn to theoretical or empirical models in order to obtain an estimate of V_{oc} . The most widely used model for V_{oc} calculations in the gas separation membrane field was presented by Lee in 1980¹¹, who proposed a method to obtain V_{oc} using a common correlation with the van der Waals volume (V_W):

$$V_{oc} = 1.3 \times V_W \quad (8.3)$$

where the 1.3 term is commonly interpreted as an inverse packing factor relating V_{oc} (*i.e.*, the molar volume at 0 K) and V_W .¹² A comprehensive review on the origin and validity of this 1.3 factor is discussed at length by Horn¹³ and is briefly discussed in this study as well.

On the other hand, V_W is estimated most commonly using Bondi's group contribution method.¹⁴ In Bondi's seminal paper on this topic¹⁴, the van der Waals (VDW) radii of atoms were compiled from X-ray diffraction measurements and were used to determine the atomistic volume contributions in molecules that are impenetrable to thermal collision, the so-called "van der Waals volume", which became of the basis of group contribution theory. Bondi used a simple geometric method to determine the V_W of two bonded atoms. For example, V_W for a C–H group would be calculated by adding the V_W of the carbon and hydrogen atoms minus the intersection/overlapping volume of the spheres. The intersection volume can be exactly calculated and is a function of the radii of both spheres and the distance between their centers (*i.e.*, the bond length).¹⁵ Therefore, with knowledge of the chemical structure, VDW radii, and bond lengths, one could feasibly construct any polymer by applying this geometric method for all chemical bonds in the polymer repeat unit. Bondi performed these calculations for common groups such as, $-\text{CH}_2-$, $-\text{CH}_3$, and $>\text{C}=\text{O}$, thereby creating a modular approach toward estimating V_W for more complex

structures. Over time, the V_W of larger groups were calculated and tabulated, with those of Park and Paul and van Krevelen being the most cited by membrane researchers.^{12,16}

However, the most recent compilations of Park and Paul and van Krevelen were published in 1997 and 2009, respectively.^{12,16} Since the first report of PIM-1 as a gas separation membrane in 2005¹⁷, significant research has been expended in the synthesis of linear microporous polymers, resulting in hundreds of unique structures containing novel, contorted structural units (*e.g.*, triptycene^{18–20} or Tröger's base^{21,22} motifs) or pendant groups (*e.g.*, amidoxime²³ or methyl tetrazole²⁴).^{25–27} As these new groups were not included in the previous compilations, manual calculation of V_W through atom-by-atom addition using Bondi's method becomes increasingly cumbersome.

The aim of this work is threefold, focusing on the calculation of V_W through group contribution theory and the resulting effect on FFV. First, the method for V_W calculation through Bondi's group contribution method was critically evaluated and an updated method with four recommended changes is presented. Second, using the updated method, V_W was calculated for both groups in previous compilations as well as for new groups and structural motifs commonly observed for modern linear microporous polymers. Lastly, the FFV values were calculated for a literature compilation of 123 microporous and high free volume polymers and various analyses were conducted to investigate the implications of the new FFV values on large-scale transport correlations for microporous polymers as a class of materials.

Recently, researchers have used molecular dynamics simulations to estimate FFV, wherein multiple polymer chains are relaxed within a specified box size and a probe is used to determine the amount of free volume.²⁸ While this approach allows for consideration of potential interchain interactions on the packing structure, these simulations can be computationally expensive especially for increasingly rigid structures and large repeat units.²⁹ Additionally, a previous study

reported similar FFV values estimated via MD simulations and calculated via Bondi's method, suggesting that Bondi's method can provide an acceptable estimate of FFV.²⁸ In this study, we follow Bondi's group contribution theory to estimate FFV, thus avoiding computationally-intensive simulations in lieu of a simpler but still accurate group contribution method with broad appeal.

8.2. Methods

8.2.1. Changes from Bondi's Method

Examining Bondi's group contribution method, we identified the four following underlying assumptions with potential for refinement:

1. The VDW radii reported by Bondi represent values still accepted today.
2. Bond lengths can be fixed by bond type (*e.g.*, a C–H bond is always 1.089 Å).
3. Overlap volume only needs to be considered for directly bonded atoms.
4. For unspecified atom-atom connections (*i.e.*, connections between groups), V_W can be calculated by first assuming that the group is connected to an aliphatic carbon atom and then subtracting the sphere cap of the connecting atom.

The following sections describe our approach to address each assumption, with our primary changes noted in italics. Additionally, we assume hybridization does not have a significant effect on the VDW radius (*i.e.*, sp^2 and sp^3 carbons have the same VDW radius).

Assumption 1: The VDW radii reported by Bondi represent values still accepted today.

Bondi's set of VDW radii is still the most widely used in the literature, but there exists slight differences in the VDW radii reported by Pauling in 1940 as well as Slonimskii *et al.* in 1970.^{30,31}

Notably, in 1996, Rowland and Taylor examined a large database of crystallographic data reported since the 1970s to revisit the accuracy of these originally reported VDW radii.³² They concluded Bondi's values showed a negligible discrepancy for all atoms except for hydrogen and suggested that 1.1 Å is more appropriate than the original value of 1.2 Å. *Following Rowland and Taylor's conclusions, we used a radius of 1.1 Å for hydrogen and Bondi's reported VDW radii for all other atoms.*

Assumption 2: Bond lengths can be fixed by bond type (*e.g.*, a C–H bond is always 1.089 Å).

Bond lengths show some deviation depending on their local steric and electronic environments. For example, a C–C bond in a cyclopropane molecule is 1.526 Å, while a C–C bond in a cyclohexane molecule is 1.540 Å.³³ Since the intersection volume is a function of the bond length, these changes in bond length will affect the V_W calculation. *Thus, we implemented a simple molecular dynamics (MD) geometry optimization step to obtain atom coordinates for each group.* Bond lengths specific to the atom and its environment can then be determined directly from their coordinates.

Assumption 3: Overlap volume only needs to be considered for directly bonded atoms.

Bondi's method only considered subtraction of the intersection volume between directly bonded neighbors and does not account for the spatial orientation of the atoms. While this assumption accounts for the large majority of the intersection volume, the use of increasingly contorted structural groups present in state-of-the-art microporous polymers introduces the possibility of intersecting volumes between atoms that are not directly bonded due to their unusual, forced spatial orientation. Inclusion of the overlapping volumes between atoms that are not directly bonded will

necessarily reduce the estimation of V_W , but likewise improve accuracy. For example, consider when atom 1 is bonded to atom 2, and atom 2 is bonded to atom 3. Through Bondi's method, V_1 and V_2 would first be connected to form a volume V_a , then V_3 would be added but only considering the overlap between atoms 2 and 3:

$$|V_1 \cup V_2| = |V_1| + |V_2| - |V_1 \cap V_2| \equiv |V_a|$$

$$|V_a \cup V_3| = |V_a| + |V_3| - |V_2 \cap V_3| = (|V_1| + |V_2| + |V_3|) - (|V_1 \cap V_2| + |V_2 \cap V_3|)$$

However, the union of three sphere volumes can be exactly described through the inclusion-exclusion principle as follows:¹⁵

$$|V_1 \cup V_2 \cup V_3| = (|V_1| + |V_2| + |V_3|) - (|V_1 \cap V_2| + |V_1 \cap V_3| + |V_2 \cap V_3|) + (|V_1 \cap V_2 \cap V_3|)$$

When taking the difference between the two methods, the Bondi method predicts V_W values that are greater than the exact volume by $|V_1 \cap V_3| - |V_1 \cap V_2 \cap V_3|$. Consequently, this extra volume is over-counted by the Bondi method and will result in an overestimation of the total V_W . To account for these additional terms, *we estimated V_W through a Monte Carlo (MC) method, explained in detail below.* If a large number of points is used, an accurate estimate of V_W can be obtained.

Assumption 4: For unspecified atom-atom connections (*i.e.*, connections between groups), V_W can be calculated by first assuming that the group is connected to an aliphatic carbon atom and then subtracting the sphere cap of the connecting atom.

In Bondi's original work, the reporting of V_W without its corresponding sphere cap (see Appendix E for more details) was likely intended for ease of use such that one could build up a complex structure by only needing to add the V_W of the groups required. However, as stated by Bondi, V_W

was calculated assuming the group is connected to an aliphatic carbon atom. Since the intersection volume of spheres is a function of both the atom VDW radii and bond length, this approach is not necessarily appropriate depending on the structure. *Thus, we have decided to report the V_W of groups with their specified sphere cap at the connecting atoms and provide a list of typical bond types with their corresponding overlapping volumes to subtract when adding groups together.* While this approach makes estimation of V_W slightly more convoluted than simply adding groups, the accuracy is improved and the method is more modular. The effect of this assumption is visible particularly when considering heteroatom bonds, which will be discussed in depth later.

To summarize, we have implemented the following changes from Bondi's method with the aim of improving V_W calculations for any group of interest:

- The VDW radius of hydrogen was changed from 1.2 Å to 1.1 Å.
- MD simulations were used to perform geometry optimizations on structural groups to obtain atom coordinates.
- Given the atom coordinates and atom identity from the MD simulation, an MC simulation was used to estimate V_W .
- The V_W reported here does not assume a connection to an aliphatic carbon and does not exclude the sphere cap.

8.2.2. Procedure for Simulated V_W of Groups

The estimation of V_W through our proposed simulation method is a two-step MD simulation followed by an MC procedure. The group of interest was drawn in Materials Studio 8.0 with dummy methyl or aromatic groups representing a connection to another unspecified group. The dummy groups are used solely in this step for geometry optimization and are ignored in the MC

portion of our procedure. The MD simulation was performed using the Forcite module with the COMPASS II forcefield, chosen for the extensive number of atom types and forcefield terms that are supported.³⁴ A Perl script was then used to extract the geometry-optimized atom coordinates and their corresponding identities. The coordinates and identity of the atoms were then transferred to a MATLAB script for the MC portion (see Appendix E) and the atoms corresponding to the dummy groups were identified. In the MC script, a box was first created around the group and 1,000,000 points with random coordinates were generated within the confines of the box. For each point, the distance between the point and each atom was calculated. If the calculated distance was less than the VDW radius of the atom, the point was considered to be “inside the group” and the script would move to the next point. By running a large number of randomly generated points, an unbiased calculation of V_W and its standard deviation (σ) can be estimated using the ratio of points “inside the group” to the total number of points:¹⁵

$$V_{group} = V_{box} \times \frac{n_{inside}}{n_{total}} \quad (8.4)$$

$$\sigma_{group} = \sqrt{V_{group} \times \frac{(V_{box} - V_{group})}{n_{total}}} \quad (8.5)$$

where V_{group} is the volume of the group (\AA^3), V_{box} is the volume of the simulation box (\AA^3), n_{inside} is the number of points considered to be “inside the group”, and n_{total} is the total number of points tested, equal to 1,000,000 for the simulations presented here. V_{group} can then be converted to the more conventional $\text{cm}^3 \text{mol}^{-1}$ form using Avogadro’s number. The V_W calculated for various groups are tabulated in Tables 8.1 to 8.3.

The overlapping volume of typical bond types (*e.g.*, C–C, C–O, C_{ar}–O, etc.) were determined by drawing the simplest structural unit containing the bond type of interest in Materials Studio 8.0,

then performing the MD simulation as described above. Using the calculated distance between the two atoms of interest, the intersecting volume was calculated with knowledge of the atom identities. A full list of bond types and their corresponding overlapping volumes are tabulated in Table 8.4.

8.3. Results

8.3.1. Simulated V_W Values for Previously Reported and New Structural Groups

Following the procedure outlined in Section 8.2, new V_W values were simulated for the 41 groups originally presented by Park and Paul¹⁶ (Table 8.1) and 32 new groups that are commonly found in microporous and other high-free volume polymers (Table 8.2). Additionally, for convenience, 23 of the most common groups found in microporous polymers (*e.g.*, triptycene) were simulated as well (Table 8.3). These large structural groups can be built from the smaller groups in Tables 8.1 and 8.2, but using the larger groups improves the accuracy when applying this method. Our newly reported groups were chosen such that all polymers featured in recent publications of microporous polymers could be built. In Tables 8.1 to 8.3, the groups of interest are represented by black atoms. However, we also show red atoms that are not included in the V_W values. These atoms represent the structure of neighboring groups, such as aliphatic or aromatic connections. Therefore, the red atoms represent dummy groups used solely for geometry optimization. Additionally, Table 8.4 contains information about the bond lengths and calculated overlap volume for each bond type, and Table 8.5 shows the atoms considered and their respective radii and VDW volumes.

An immediate comparison can be made between the V_W values tabulated by Park and Paul against those presented in Table 8.1 (see groups P1 to P41).¹⁶ The V_W values simulated using the new method appear to be greater than those of Park and Paul by 25% on average, but this increase is

mostly artificial and relates primarily to changes in methodology related to assumption 4. The procedure by Park and Paul reports V_W values for groups without their sphere cap(s). Conversely, our reporting of V_W includes the sphere cap(s), resulting in the higher apparent values. Thus, when separating groups P1 to P41 by valency, the monovalent, divalent, trivalent, and tetravalent groups showed an apparent average V_W increase of 12%, 15%, 37%, and 128%, respectively. Viewed this way, there is a general trend of artificially larger V_W values corresponding to the number of sphere caps added per valency. Of course, group-to-group structural variation, the number of hydrogen atoms, and the presence of heteroatoms at valency points all influence V_W , but those specific factors are concealed by inclusion of sphere caps.

Given this methodology change, the new method requires subtraction of the overlap volume between the atoms that connect groups. When assembling groups into a polymer structure, the red atoms should be representative of the structure of the neighboring connecting group, but only the overlapping volume between the directly bonded atoms needs to be subtracted according to Equation 8.6:

$$V_{W,tot} = \sum_{i=1}^n V_{W,i} - \sum_{j=1}^m V_{overlap,j} \quad (8.6)$$

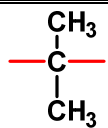
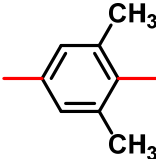
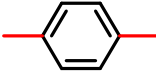
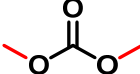
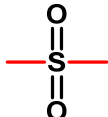
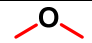
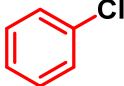

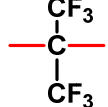

where n is the number of groups, m is the number of connections between groups, $V_{W,i}$ is the van der Waals volume for the groups from Tables 8.1 to 8.3, and $V_{overlap,j}$ is the overlap volume between groups from Table 8.4.

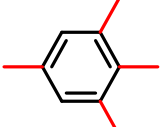
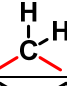
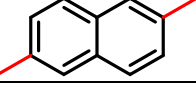
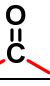
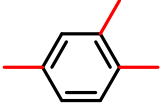
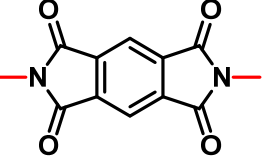

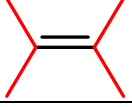
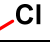
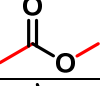
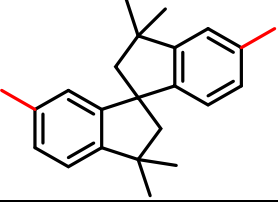
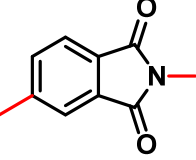
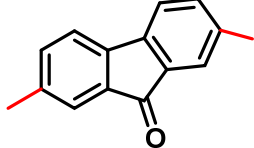
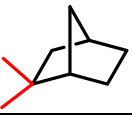

In this way, the V_W for a polymer repeat unit can be calculated. As one example, group P6 has methyl dummy groups, representing single-bonded connections to neighboring groups. The overlap volume between group P6 and its connecting groups is subtracted in the V_W calculation.

In a case where P6 is connected to P3 on both sides (*i.e.*, P3–P6–P3), the overlap volume corresponding to a C_{ar}–O bond (C8) would be subtracted twice. As another example, S2 shows a common spiro center, but the reported V_W can only be used when this spiro center is connected to two aromatic rings on neighboring groups. As in the previous example, the overlap volume between the groups will likewise be subtracted. In a case where S2 is connected to P11 on both sides for a total of four connections (*i.e.*, P11>S2<P11), the overlap volume corresponding to a C–C_{ar} bond (C4) would be subtracted four times. Additionally, it should be noted that we do not strictly enforce implicit hydrogen substitutions on the dummy aliphatic and aromatic groups. Any substitution on the neighboring groups that differs from the implicit hydrogens on the dummy group is assumed to have little effect on the overlap volume.

As an aside, when constructing polymers containing aromatic connections, some groups in Table 8.1 can be treated as roughly equivalent, such as groups P3 and P35 (bivalent, para versus meta connections, 46.249 cm³ mol⁻¹ versus 46.187 cm³ mol⁻¹) or P15 and P36 (trivalent, 1, 2, 4 versus 1, 3, 5 connections, 45.484 cm³ mol⁻¹ versus 45.438 cm³ mol⁻¹). In both cases the simulated V_W values are effectively the same, suggesting a general heuristic that only the number of connections matters for V_W calculations as opposed to the location of the connections for aromatic rings. For example, in the case of an aromatic ring containing ortho connections in the repeat unit, one could use a V_W value of 46.2 cm³ mol⁻¹ as a reasonable estimate for that group. In a similar manner, groups that are identical except for possessing different connection bond types (*e.g.*, P7 and P19 showing aliphatic and aromatic chlorine groups) show effectively the same V_W because any changes in connection bond types are accounted through the use of overlap volume specific to the bond type.

Table 8.1. Reference ID, structure, simulated V_W , and standard deviation in MC simulation for the groups previously considered by Park and Paul.¹⁶ Red bonds directly attached to black atoms represent connections to neighboring groups with the specified geometry. In some cases, extended red structures (*e.g.*, aromatic groups) are shown to more clearly indicate appropriate connecting groups. V_W includes molar volume of the sphere cap(s) at atoms that can connect to other groups.

Updates for groups previously reported by Park and Paul			
Reference ID	Structure	V_W ($\text{cm}^3 \text{mol}^{-1}$)	σ ($\text{cm}^3 \text{mol}^{-1}$)
P1		32.58	0.08
P2		64.5	0.1
P3		46.25	0.08
P4		25.25	0.05
P5		23.14	0.04
P6		8.51	0.02
P7		13.54	0.02
P8		15.97	0.02
P9		51.6	0.1
P10		24.39	0.05

P11		44.67	0.09
P12		13.92	0.03
P13		71.9	0.1
P14		16.24	0.03
P15		45.48	0.08
P16		92.7	0.2
P17		14.63	0.04
P18		19.37	0.03
P19		13.53	0.02
P20		20.63	0.04
P21		159.7	0.4
P22		69.5	0.1
P23		93.5	0.1
P24		58.7	0.1
P25		54.6	0.1

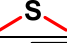
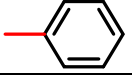

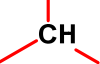
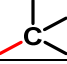
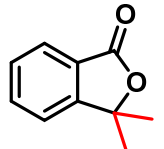
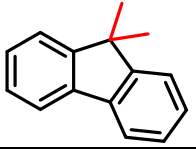
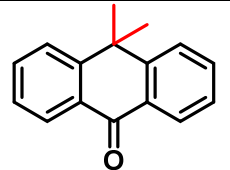
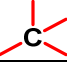
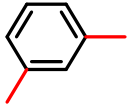
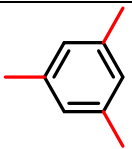
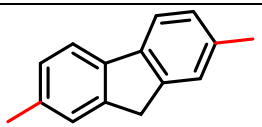
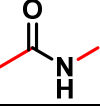


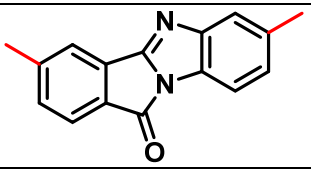
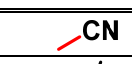
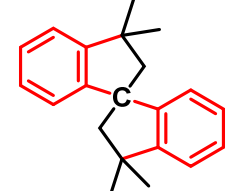
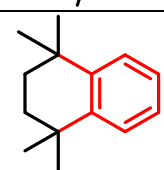
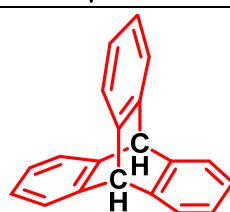
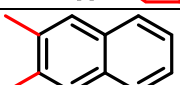
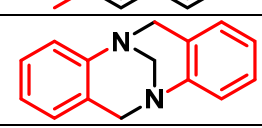
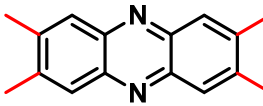
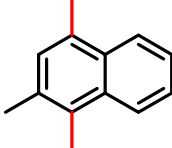
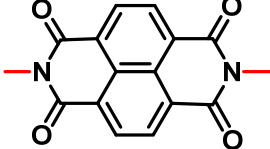
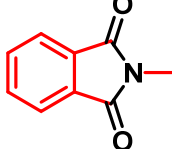
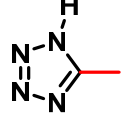
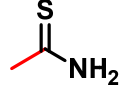

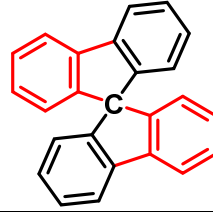
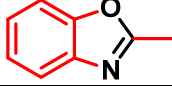
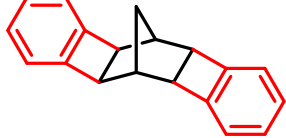
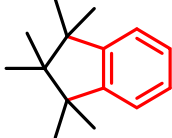
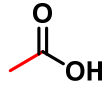

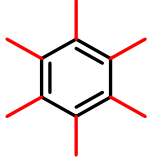
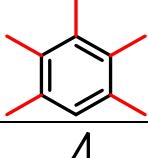
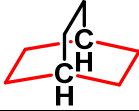

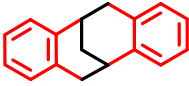
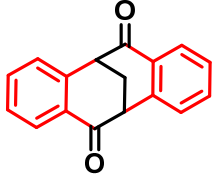
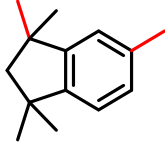
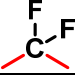
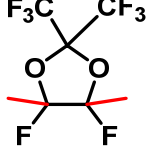
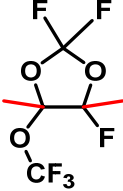
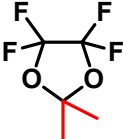
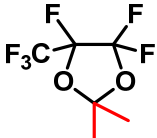
P26		14.73	0.02
P27		47.11	0.09
P28		9.42	0.02
P29		13.15	0.03
P30		42.5	0.1
P31		66.7	0.1
P32		91.5	0.2
P33		102.4	0.2
P34		12.39	0.02
P35		46.19	0.08
P36		45.44	0.08
P37		91.1	0.2
P38		22.05	0.04
P39		11.20	0.03
P40		3.35	0.01
P41		107.9	0.2

Table 8.2. Reference ID, structure, simulated V_W , and standard deviation in MC simulation for the new groups considered in this study. Red bonds directly attached to black atoms represent connections to neighboring groups with the specified geometry. In some cases, extended red structures (*e.g.*, aromatic groups) are shown to more clearly indicate appropriate connecting groups. V_W includes molar volume of the sphere cap(s) at atoms that can connect to other groups.

Small groups (previously unreported)			
Reference ID	Structure	V_W ($\text{cm}^3 \text{mol}^{-1}$)	σ ($\text{cm}^3 \text{mol}^{-1}$)
S1		16.57	0.03
S2		86.8	0.2
S3		78.8	0.2
S4		25.32	0.06
S5		72.2	0.1
S6		44.2	0.1
S7		89.6	0.2

S8		80.8	0.2
S9		118.3	0.2
S10		33.08	0.06
S11		31.52	0.06
S12		29.22	0.06
S13		29.88	0.07
S14		95.6	0.2
S15		21.86	0.04
S16		58.0	0.1
S17		87.6	0.2
S18		21.60	0.04
S19		40.70	0.09

S20		43.10	0.07
S21		43.91	0.08
S22		39.91	0.09
S23		19.64	0.04
S24		48.7	0.1
S25		53.8	0.1
S26		96.0	0.2
S27		20.62	0.04
S28		82.3	0.2
S29		70.9	0.1
S30		50.7	0.1
S31		66.4	0.1

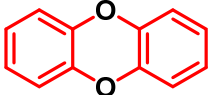
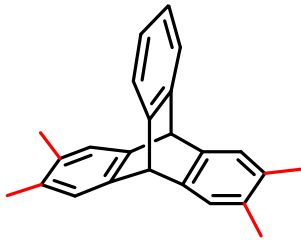
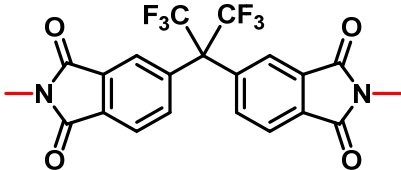
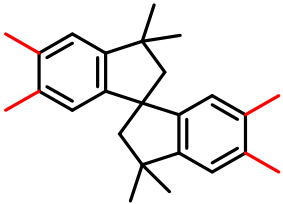
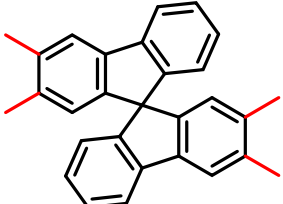
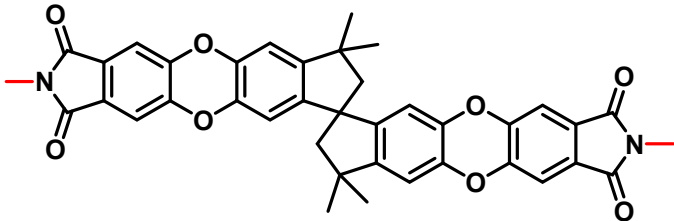
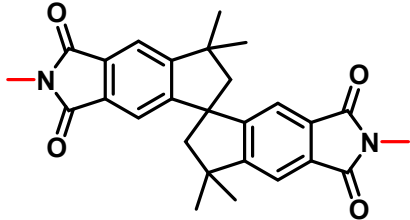
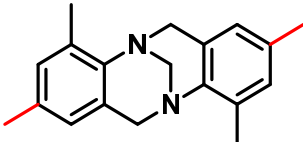
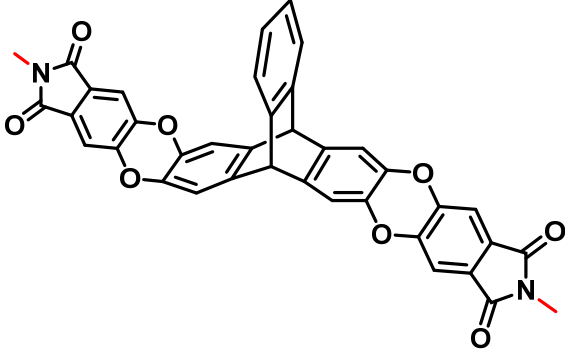
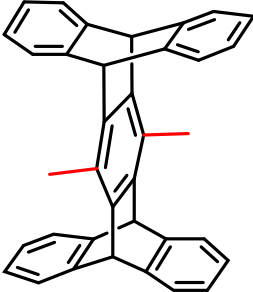
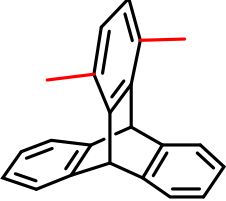
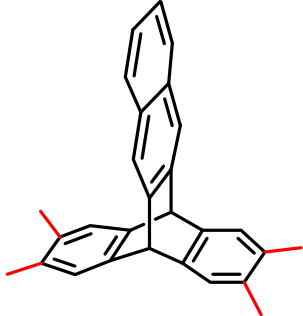
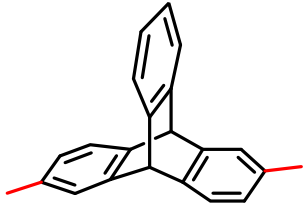
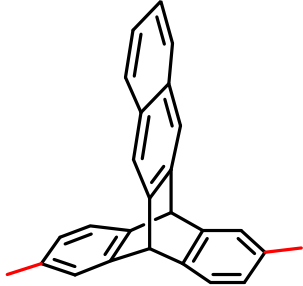
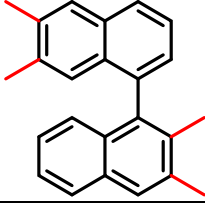
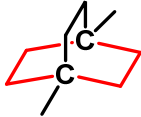
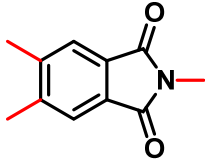
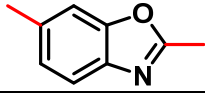
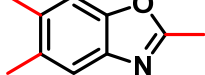
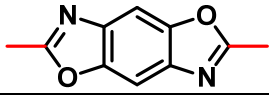
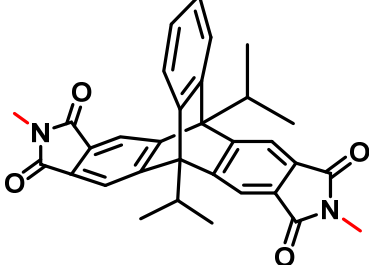
S32	 <chem>c1ccc2c(c1)oc3ccccc3o2</chem>	17.00	0.04
-----	-----------------------------------------------------------------------------------------------------------------------	-------	------

Table 8.3. Reference ID, structure, simulated V_W , and standard deviation in MC simulation for the large groups considered in this study. Red bonds directly attached to black atoms represent connections to neighboring groups with the specified geometry. In some cases, extended red structures (*e.g.*, aromatic groups) are shown to more clearly indicate appropriate connecting groups. V_W includes molar volume of the sphere cap(s) at atoms that can connect to other groups.

Large groups (previously unreported)			
Reference	Structure	V_W ($\text{cm}^3 \text{mol}^{-1}$)	σ ($\text{cm}^3 \text{mol}^{-1}$)
L1		133.5	0.3
L2		180.6	0.4
L3		157.7	0.4
L4		167.2	0.4
L5		297	1

L6		206.1	0.5
L7		135.8	0.3
L8		275.2	0.9
L9		224.0	0.6
L10		135.2	0.3
L11		159.8	0.4

L12		135.5	0.3
L13		161.4	0.4
L14		137.2	0.3
L15		58.5	0.2
L16		68.7	0.1
L17		59.4	0.1
L18		58.5	0.1
L19		72.6	0.1
L20		238.1	0.6

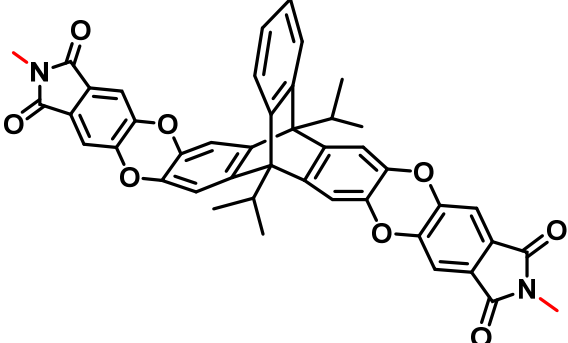
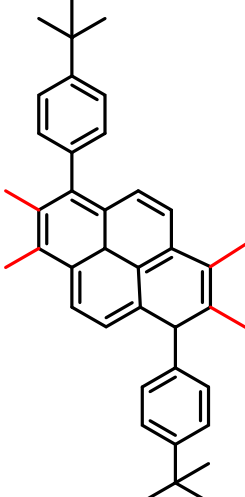
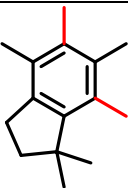
L21		331	1
L22		262.0	0.8
L23		105.8	0.3

Table 8.4. Reference ID, bond type, bond length, and calculated overlap volume for connections considered in this study.

Reference ID	Bond type	Bond length (Å)	Overlap volume (cm ³ mol ⁻¹)
C1	C–H	1.099	2.607
C2	C _{ar} –H	1.099	2.608
C3	C–C	1.525	4.614
C4	C–C _{ar}	1.508	4.688
C5	C _{ar} –C _{ar}	1.437	5.002
C6	C=C	1.337	5.462
C7	C–O	1.416	3.877
C8	C _{ar} –O	1.361	4.091
C9	C=O	1.209	4.694
C10	O–H	0.952	2.418
C11	C–N	1.455	4.018
C12	C _{ar} –N	1.395	4.255
C13	N–H	1.004	2.434
C14	C–S	1.807	3.973
C15	C _{ar} –S	1.777	4.100
C16	S–H	1.321	2.361
C17	C–F	1.380	3.840
C18	C _{ar} –F	1.341	3.988
C19	C–Cl	1.783	3.802
C20	C _{ar} –Cl	1.712	4.099
C21	C–Br	1.939	3.683
C22	C _{ar} –Br	1.920	3.763
C23	C–Si	1.885	5.336
C24	C _{ar} –Si	1.873	5.394
C25	Si–O	1.636	4.970

Table 8.5. Reference ID, Van der Waals radius, and calculated Van der Waals volume for atoms considered in this study.

Reference ID	Atom	VDW Radius (Å)	VDW Volume (cm ³ mol ⁻¹)
A1	H	1.1	3.357
A2	C	1.7	12.393
A3	O	1.5	8.513
A4	N	1.55	9.393
A5	S	1.8	14.711
A6	F	1.47	8.013
A7	Cl	1.75	13.519
A8	Br	1.85	15.971
A9	Si	2.1	23.361

8.3.2. Updated FFV Estimates for Literature Microporous Polymers

New V_W values were calculated for a database of 123 polymer structures that had a reported density. The polymers included in the database are all solution-processable and are either microporous (*i.e.*, have a Brunauer-Emmett-Teller (BET) surface area greater than $30 \text{ m}^2 \text{ g}^{-1}$, a typical value for common glassy polymers)³⁵ or define various upper bounds (*i.e.*, commercial perfluoropolymers).³⁶ The full database is presented in Table E.1. For 7 polymers in the database, the reported FFV was calculated using MD simulations instead of using group contribution methods. These polymers are denoted in Table E.1 with a “*”. Since the FFV values obtained using group contribution and MD simulations are not directly comparable, these polymers were not included in any analysis when comparing reported FFV from group contribution methods.

The reported density was used with the new V_W values to calculate FFV. Example calculations from our group contribution method are included in Appendix E. It should be noted that for the same polymer backbone (*i.e.*, polymers possessing the same V_{oc}), variations in the recalculated FFV may occur due to differences in the reported density. For example, the new FFV for PIM-1 ranges from 0.248 to 0.414. Differences in the reported density can originate from variations in synthesis approach (*e.g.*, low temperature³⁷ versus high temperature³⁸ PIM-1 synthesis), treatment prior to measurement (*e.g.*, methanol treatment, different annealing procedures, etc.) as well as the method used to measure density (*e.g.*, buoyancy in a liquid³⁹, geometrically calculated⁴⁰, etc.). For these reasons, care should be used when comparing FFV values for the same polymer backbone across studies since these differences in treatment and methodology will affect the density measurement.

A plot comparing the reported FFV to the new FFV is shown in Figure 8.1. It should be noted that not all polymers in the database have a reported FFV and would therefore not be represented in

Figure 8.1. In almost every case, with the notable exception of the commercial perfluoropolymers, the new FFV was greater than the reported literature FFV by a factor of 24%, on average. This increase in FFV indicates a decrease in V_W for each polymer resulting from the method changes described in Section 8.2.1. Using the reported FFV values as a basis, changing from the original to the new method resulted in roughly a 7% decrease in V_W .

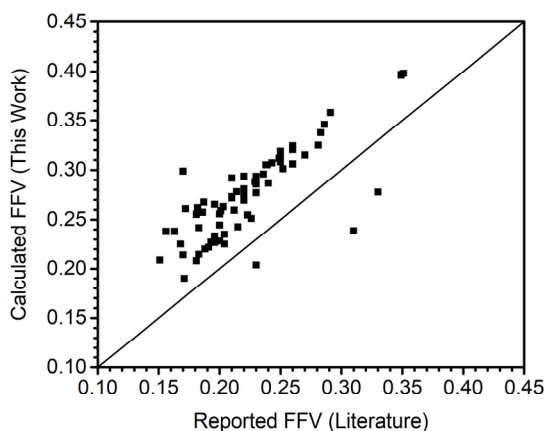


Figure 8.1. Comparison of reported literature FFV values with calculated FFV values using the new method.

In evaluating the effect of each modified assumption on V_W , it was found that the decrease in the hydrogen VDW radius (assumption 1) was a moderate contributor to lower V_W , while variations in bond lengths and consideration of non-adjacent overlap volumes (assumptions 2 and 3, respectively) had a relatively minor effect. Using the spirobisindane (SBI) group as an example (see group L3 from Table 8.3), a V_W of $157.7 \text{ cm}^3 \text{ mol}^{-1}$ was estimated through the new method. When assumption 1 is relaxed (*i.e.*, V_W calculated using a hydrogen VDW radius of 1.2 \AA), the V_W shows a 5% increase up to $166.3 \text{ cm}^3 \text{ mol}^{-1}$. To evaluate the impact of assumption 2, the bond lengths present in the SBI unit were determined from MD simulations and the average length for

each bond type (*i.e.*, C_{ar}–C_{ar}, C_{ar}–C, C_{ar}–H, C–C, and C–H) was determined. When comparing to literature compilations⁴¹, the deviation in average bond length ranged from –0.3% for C_{ar}–C bonds to 1.5% for C_{ar}–H bonds, corresponding to 0.4% and –2.2% changes in the overlap volume, respectively. The impact of assumption 3 can be evaluated by counting the number of points that were located exclusively in the intersection of two non-bonded atoms. In the SBI example, roughly 0.4% of the points satisfied this condition, indicating minimal over-counted overlap volume if the original Bondi method were used. Of note, our use of MD simulations results in assumptions 2 and 3 being coupled because various repulsion terms present in the forcefield minimize overlap of non-bonded VDW volumes. Taken together, assumptions 1 to 3 had a small to moderate impact on V_W values.

On the other hand, changes related to assumption 4 affected V_W values for polymers containing a large number of heteroatom bonds, particularly in the case of the perfluoropolymers. A detailed explanation is provided in Appendix E. Briefly, the assumption that all groups are connected to an aliphatic carbon atom results in a size mismatch at the sphere–sphere cross-sectional interface for heteroatom bonds because of differences in the bond length. For perfluoropolymers, this assumption resulted in a larger V_W , which in turn led to smaller FFV. In contrast with all other polymers considered, the high-free volume commercial perfluoropolymers (Teflon[®] AF 2400, Teflon[®] AF 1600, and Hyflon[®] AD 60) showed a 14% increase for calculated V_W and a corresponding 17% decrease in FFV.

8.3.3. Impact of New FFV Values on Gas Transport Correlations for Microporous Polymers

8.3.3.1. Permeability Correlations with Respect to FFV

Correlations between FFV and general classes of microporous polymers were evaluated using Equation 8.1. These correlations are exclusively based on our newly developed method and 120 microporous polymers in our database. The perfluoropolymers were not included for this analysis since they do not show measurable BET surface areas and are therefore not considered to be microporous.⁴² An example of this analysis is shown in Figure 8.2a for CO₂. Similar plots are shown for all other gases in Figure E.6. Black symbols correspond to the reported literature FFV and red symbols correspond to FFV calculated using our newly developed method. There exist a number of black symbols that deviate significantly from the correlation in Equation 8.1. However, when FFV is calculated using the new method, these original outlier points experience a relatively larger increase in FFV, resulting in an overall improved correlation; for CO₂, the Pearson correlation coefficient changes from -0.48 to -0.66 when comparing the old versus new FFV correlations. Similar changes were observed for all gases. All slopes and Pearson correlation coefficients are tabulated in Table E.2. Interestingly, a large number of these original outlier points are PIM-1 or PIM-1-like polymers. This finding indicates two possibilities. First, the original method may contain limitations in accuracy for estimating FFV. Additionally, the large variations in FFV for identical polymers may result from user error in needing to piece together non-intuitive groups to assemble polymer repeat units. It is likely that both of these possibilities contribute to our findings, emphasizing the great need to modernize and simplify group contribution methods for microporous polymers. Use of our group contribution method for all polymers in the database provides a consistent route for V_W calculation, and thereby acts as a normalization method to facilitate direct comparisons of FFV across multiple studies and research groups.

It should be noted that a moderate amount of scatter about the best-fit line is still observed for these correlations, even after normalizing the calculation method for V_{oc} for all polymers. This scatter can be explained in two ways. The first relates to uncertainties in reported densities, as discussed earlier, which will contribute to scatter in these plots. The second, and likely more important, relates to factors affecting permeability that are not captured by FFV, such as differences in sorption interactions or free volume distribution. For example, a polymer that shows high FFV and low permeability could possess large pockets of free volume but have bottlenecks with limited free volume connectivity, thereby limiting diffusion. Alternatively, a polymer with low FFV could show particularly high sorption affinity to CO₂, thereby resulting in higher permeability. Considered in this way, the presence of scatter demonstrates a weakness of FFV as a correlating variable for permeability from a transport perspective. However, given the significant reduction in scatter from our updated method, there is an advantage to applying this method for the development of improved structure–property–performance correlations.

A significant change was also observed for the best-fit correlation slope, B . Figure 8.2b shows the obtained B values plotted against a measure of penetrant volume (diffusion diameter cubed⁴³) for microporous polymers using both reported literature FFV as well as the FFV calculated from the new method. A linear relationship is observed for both cases, although there is a slight difference in the slope. According to the free volume theory of Cohen and Turnbull and assuming a negligible role of FFV on the sorption coefficient, B corresponds to a minimum critical volume required for diffusion with a γ scaling factor representing an average count of the number of molecules in a free volume element.^{43,44} However, this theory was developed for rubbery polymers, so it is interesting that the linear relationship was preserved for these microporous materials. While further speculation is outside the scope of this work, future studies of this linear trend as well as

interpretations of how γ changes for rubbery, glassy, and emerging microporous polymers would be of interest to elucidate the applicability of transport models across various classes of polymeric materials as free volume increases.

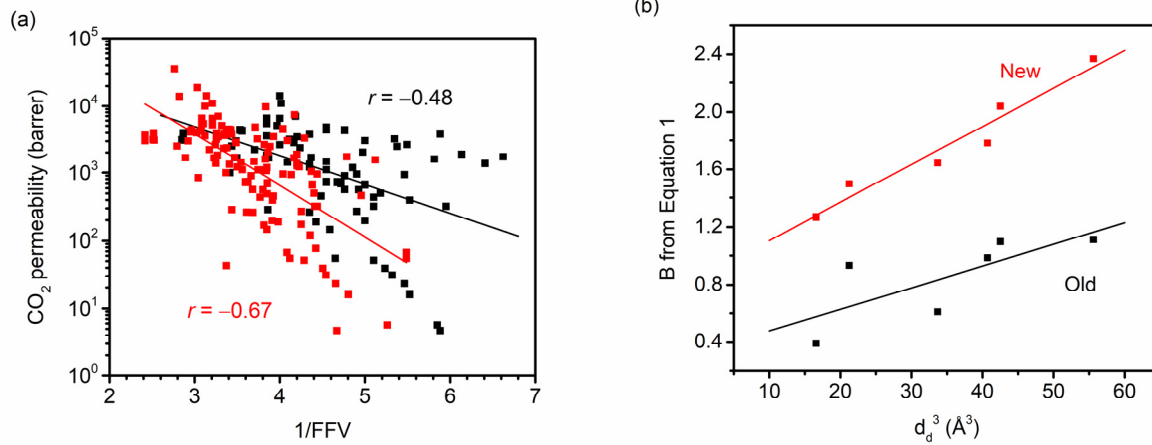


Figure 8.2. (a) Example correlation of $\ln(P)$ vs $1/FFV$ for CO_2 with their respective best-fit lines. (b) Correlation between the best-fit B values from Equation 8.1 and diffusion diameter cubed. For both plots, the black symbols represent values obtained from reported FFV values of microporous polymers and the red symbols represent FFV values calculated using the new method.

8.3.3.2. Revisiting Packing Factor Assumptions

Two useful relationships related to V_W calculations were revisited in the context of microporous polymers. First, we will consider the relationship between specific density and V_W , as discussed by van Krevelen and Park and Paul:^{12,16}

$$V = \beta \sum_{k=1}^K (V_W)_k \quad (8.7)$$

Where $\beta = 1.60$ at 25 °C for conventional glassy polymers (*e.g.*, polysulfone, Matrimid, etc.), effectively acting as a room temperature packing factor to correlate the polymer density to its V_W .¹²

Because glassy polymers are in a non-equilibrium state, β can be interpreted as a rough measure of how close the polymer is to its relaxed equilibrium state, with a larger value indicating a state further from equilibrium. This 1.60 value was obtained using the original Bondi method to calculate V_W .¹² Accounting for the 7% decrease in V_W between the Bondi method and the new method, a β value of 1.72 ± 0.04 can be estimated for conventional glassy polymers. Using the recalculated V_W values for microporous polymers, the average β value was found to be 1.8 ± 0.1 at 25 °C. The marginally higher average value of β for microporous polymers as a class suggests a higher degree of non-equilibrium character compared to typical glassy polymers, consistent with the ultra-rigid nature of the chemical motifs in microporous materials. Moreover, this finding correlates with polymers that have extremely high or undetectable T_g values^{45,46} and accelerated physical aging trends^{47,48}, indicating that other theoretical correlations may exist to connect this work more broadly to phenomena in the polymer physics community.

Second, we will consider the relationship between V_{oc} and V_W (see Equation 8.3), specifically concerning the 1.3 value for the inverse packing factor. As previously mentioned, there has been discussion regarding the origin of this value.¹³ In particular, Horn concluded that absent other information, that 1.3 is a suitable approximation for the packing factor.¹³ Here, the overall permeability versus 1/FFV correlations developed in Section 8.3.3.1 can be used to back-calculate the packing factor for each gas–polymer pair.

$$P = A \times \exp\left(-\frac{B}{1 - \alpha \times \frac{\rho V_W}{MW}}\right) \quad (8.8)$$

Where A and B are the best-fit intercept and slope of the P vs. 1/FFV correlations, α is the packing factor, ρ is the polymer density (g cm^{-3}), V_W is the VDW volume ($\text{cm}^3 \text{ mol}^{-1}$), and MW is the

molecular weight of the repeat unit (g mol^{-1}). Given the best-fit A and B values for each gas discussed in Section 8.3.3.1., an α value can be calculated for each gas–polymer pair. While this is an indirect method of obtaining the packing factor from large-scale transport correlations, this approach provides a valuable means to verify or refine this coefficient, analogous to how upper bound correlations have been used to refine gas diameter sizes.⁴³ Averaging the back-calculated α values for each gas–polymer pair in the database, a value of 1.3 ± 0.1 is obtained for α , in agreement with the typically used value. However, a standard deviation of 0.1 represents a significant variation in FFV. For example, the FFV of a PIM-1 polymer with a density of 1.1 g cm^{-3} would range from 0.245 to 0.353 within the range of $\alpha = 1.4$ to $\alpha = 1.2$. Interestingly, the primary contributor to this uncertainty for all gas–polymer pairs appears only when comparing α values across polymers. When considering the average α value obtained for a single polymer averaged across its gases, a small standard deviation on the order of ± 0.02 is observed, indicating a relatively consistent α value for each polymer. For example, the refined α value for PIM-1 from Chen *et al.*⁴⁹ is 1.28 ± 0.01 . While a value of 1.3 ± 0.1 for α looks to be appropriate for microporous polymers as a whole, there appears to be evidence supporting the existence of an individual α value for each polymer derived from its density and transport properties.

8.4. Conclusions

Estimation of FFV via the group contribution method was reexamined and applied to more recently developed microporous polymers. To calculate V_W , the assumptions and deficiencies present in the original method proposed by Bondi were examined. The following four changes were implemented to improve the accuracy of the V_W calculation and streamline calculations for new groups present in the current membrane literature: (1) The VDW radius of hydrogen was changed from 1.2 Å to 1.1 Å, (2) MD simulations were used to perform a geometry optimization on the

structural group to obtain atom coordinates, (3) MC simulations were used to estimate V_W based on atom coordinates and atom identity from the MD simulations, and (4) V_W was reported with a sphere cap at the end group and without the assumption that the end group is connected to an aliphatic carbon. Using the new method, V_W values were obtained for a total of 96 groups commonly found in microporous and other high-free volume polymers. FFV was recalculated for a database of 123 microporous and high free volume polymers in the membrane literature, resulting in an average 7% decrease in V_W and a corresponding increase in FFV by a factor of 24% when compared to the originally reported literature values. The change in the hydrogen VDW radius accounted for roughly 5% of the change in V_W , the MD and MC simulations accounted for approximately 2% of the change, and assumptions related to the sphere cap accounted for the remainder. Correlations relating gas permeability to 1/FFV were updated using the new FFV values, resulting in a significantly improved correlation compared to the original FFV approach. The updated and modernized method introduced here provides a streamlined process for straightforward and accurate V_W calculations, through which FFV can be calculated using group contribution theory. Additionally, standardization of the V_W calculation established through our method allows for the direct comparison of FFV values across studies. The recalculated FFV values and correlations obtained for microporous polymers provide a more accurate interpretation of the role of free volume on transport properties.

8.5. References

- (1) White, R. P.; Lipson, J. E. G. Polymer Free Volume and Its Connection to the Glass Transition. *Macromolecules* **2016**, *49* (11), 3987–4007. <https://doi.org/10.1021/acs.macromol.6b00215>.
- (2) Doolittle, A. K. Studies in Newtonian Flow. I. The Dependence of the Viscosity of Liquids on Temperature. *J. Appl. Phys.* **1951**, *22* (8), 1031–1035. <https://doi.org/10.1063/1.1700096>.
- (3) Doolittle, A. K. Studies in Newtonian Flow. II. The Dependence of the Viscosity of Liquids

- on Free-Space. *J. Appl. Phys.* **1951**, 22 (12), 1471–1475. <https://doi.org/10.1063/1.1699894>.
- (4) Doolittle, A. K. Studies in Newtonian Flow. III. The Dependence of the Viscosity of Liquids on Molecular Weight and Free Space (in Homologous Series). *J. Appl. Phys.* **1952**, 23 (2), 236–239. <https://doi.org/10.1063/1.1702182>.
 - (5) Williams, M. L.; Landel, R. F.; Ferry, J. D. The Temperature Dependence of Relaxation Mechanisms in Amorphous Polymers and Other Glass-Forming Liquids. *J. Am. Chem. Soc.* **1955**, 77 (14), 3701–3707. <https://doi.org/10.1021/ja01619a008>.
 - (6) Wang, Z.; Zhang, M.; Han, E.; Niu, H.; Wu, D. Structure-Property Relationship of Low Dielectric Constant Polyimide Fibers Containing Fluorine Groups. *Polymer* **2020**, 206, 122884. <https://doi.org/10.1016/j.polymer.2020.122884>.
 - (7) Li, X.; Ma, H.; Wang, P.; Liu, Z.; Peng, J.; Hu, W.; Jiang, Z.; Liu, B.; Guiver, M. D. Highly Conductive and Mechanically Stable Imidazole-Rich Cross-Linked Networks for High-Temperature Proton Exchange Membrane Fuel Cells. *Chem. Mater.* **2020**, 32 (3), 1182–1191. <https://doi.org/10.1021/acs.chemmater.9b04321>.
 - (8) Yavari, M.; Fang, M.; Nguyen, H.; Merkel, T. C.; Lin, H.; Okamoto, Y. Dioxolane-Based Perfluoropolymers with Superior Membrane Gas Separation Properties. *Macromolecules* **2018**, 51 (7), 2489–2497. <https://doi.org/10.1021/acs.macromol.8b00273>.
 - (9) Weidman, J. R.; Guo, R. The Use of Iptycenes in Rational Macromolecular Design for Gas Separation Membrane Applications. *Ind. Eng. Chem. Res.* **2017**, 56 (15), 4220–4236. <https://doi.org/10.1021/acs.iecr.7b00540>.
 - (10) Matteucci, S.; Yampolskii, Y.; Freeman, B. D.; Pinnau, I. Transport of Gases and Vapors in Glassy and Rubbery Polymers. In *Materials Science of Membranes for Gas and Vapor Separation*; 2006; pp 1–47. <https://doi.org/10.1002/047002903X.ch1>.
 - (11) Lee, W. M. Selection of Barrier Materials from Molecular Structure. *Polym. Eng. Sci.* **1980**, 20 (1), 65–69. <https://doi.org/10.1002/pen.760200111>.
 - (12) van Krevelen, D. W.; te Nijenhuis, K. *Properties of Polymers*, 4th ed.; Elsevier: Oxford, 2009. <https://doi.org/10.1017/cbo9780511623097.008>.
 - (13) Horn, N. R. A Critical Review of Free Volume and Occupied Volume Calculation Methods. *J. Membr. Sci.* **2016**, 518, 289–294. <https://doi.org/10.1016/j.memsci.2016.07.014>.
 - (14) Bondi, A. Van Der Waals Volumes and Radii. *J. Phys. Chem.* **1964**, 68 (3), 441–451. <https://doi.org/10.1021/j100785a001>.
 - (15) Petitjean, M. Spheres Unions and Intersections and Some of Their Applications in Molecular Modeling. In *Distance Geometry: Theory, Methods, and Applications*; 2018; pp 61–83. https://doi.org/10.1007/978-1-4614-5128-0_4.
 - (16) Park, J. Y.; Paul, D. R. Correlation and Prediction of Gas Permeability in Glassy Polymer Membrane Materials via a Modified Free Volume Based Group Contribution Method. *J. Membr. Sci.* **1997**, 125 (1), 23–39. [https://doi.org/10.1016/S0376-7388\(96\)00061-0](https://doi.org/10.1016/S0376-7388(96)00061-0).
 - (17) Budd, P. M.; Msayib, K. J.; Tattershall, C. E.; Ghanem, B. S.; Reynolds, K. J.; McKeown,

- N. B.; Fritsch, D. Gas Separation Membranes from Polymers of Intrinsic Microporosity. *J. Membr. Sci.* **2005**, *251* (1–2), 263–269. <https://doi.org/10.1016/j.memsci.2005.01.009>.
- (18) Li, F.; Zhang, C.; Weng, Y. Preparation and Gas Separation Properties of Triptycene-Based Microporous Polyimide. *Macromol. Chem. Phys.* **2019**, *220* (10), 1–7. <https://doi.org/10.1002/macp.201900047>.
- (19) Ghanem, B. S.; Swaidan, R.; Litwiller, E.; Pinnau, I. Ultra-Microporous Triptycene-Based Polyimide Membranes for High-Performance Gas Separation. *Adv. Mater.* **2014**, *26* (22), 3688–3692. <https://doi.org/10.1002/adma.201306229>.
- (20) Carta, M.; Croad, M.; Malpass-Evans, R.; Jansen, J. C.; Bernardo, P.; Clarizia, G.; Friess, K.; Lanč, M.; McKeown, N. B. Triptycene Induced Enhancement of Membrane Gas Selectivity for Microporous Tröger's Base Polymers. *Adv. Mater.* **2014**, *26* (21), 3526–3531. <https://doi.org/10.1002/adma.201305783>.
- (21) Hu, X.; Lee, W. H.; Zhao, J.; Bae, J. Y.; Kim, J. S.; Wang, Z.; Yan, J.; Zhuang, Y.; Lee, Y. M. Tröger's Base (TB)-Containing Polyimide Membranes Derived from Bio-Based Dianhydrides for Gas Separations. *J. Membr. Sci.* **2020**, *610*, 118255. <https://doi.org/10.1016/j.memsci.2020.118255>.
- (22) Carta, M.; Malpass-Evans, R.; Croad, M.; Rogan, Y.; Jansen, J. C.; Bernardo, P.; Bazzarelli, F.; McKeown, N. B. An Efficient Polymer Molecular Sieve for Membrane Gas Separations. *Science* **2013**, *339* (6117), 303–307. <https://doi.org/10.1126/science.1228032>.
- (23) Swaidan, R.; Ghanem, B. S.; Litwiller, E.; Pinnau, I. Pure- and Mixed-Gas CO₂/CH₄ Separation Properties of PIM-1 and an Amidoxime-Functionalized PIM-1. *J. Membr. Sci.* **2014**, *457*, 95–102. <https://doi.org/10.1016/j.memsci.2014.01.055>.
- (24) Du, N.; Robertson, G. P.; Dal-Cin, M. M.; Scoles, L.; Guiver, M. D. Polymers of Intrinsic Microporosity (PIMs) Substituted with Methyl Tetrazole. *Polymer* **2012**, *53* (20), 4367–4372. <https://doi.org/10.1016/j.polymer.2012.07.055>.
- (25) Low, Z. X.; Budd, P. M.; McKeown, N. B.; Patterson, D. A. Gas Permeation Properties, Physical Aging, and Its Mitigation in High Free Volume Glassy Polymers. *Chem. Rev.* **2018**, *118* (12), 5871–5911. <https://doi.org/10.1021/acs.chemrev.7b00629>.
- (26) Wang, Y.; Ma, X.; Ghanem, B. S.; Alghunaimi, F.; Pinnau, I.; Han, Y. Polymers of Intrinsic Microporosity for Energy-Intensive Membrane-Based Gas Separations. *Mater. Today Nano* **2018**, *3* (2018), 69–95. <https://doi.org/10.1016/j.mtnano.2018.11.003>.
- (27) Budd, P. M. Polymers of Intrinsic Microporosity and Their Potential in Process Intensification. In *Sustainable Nanoscale Engineering*; Elsevier, 2020; pp 231–264. <https://doi.org/10.1016/B978-0-12-814681-1.00009-6>.
- (28) Abdulhamid, M. A.; Genduso, G.; Wang, Y.; Ma, X.; Pinnau, I. Plasticization-Resistant Carboxyl-Functionalized 6FDA-Polyimide of Intrinsic Microporosity (PIM-PI) for Membrane-Based Gas Separation. *Ind. Eng. Chem. Res.* **2020**, *59* (12), 5247–5256. <https://doi.org/10.1021/acs.iecr.9b04994>.
- (29) Abbott, L. J.; Hart, K. E.; Colina, C. M. Polymatic: A Generalized Simulated Polymerization Algorithm for Amorphous Polymers. *Theor. Chem. Acc.* **2013**, *132* (3), 1–

19. <https://doi.org/10.1007/s00214-013-1334-z>.
- (30) Pauling, L. *The Nature of the Chemical Bond*, 2nd ed.; Cornell University Press: Ithaca, NY, 1948.
- (31) Slonimskii, G. L.; Askadskii, A. A.; Kitaigorodskii, A. . The Packing of Polymer Molecules. *Polym. Sci. U.S.S.R.* **1970**, *12* (3), 556–577. [https://doi.org/https://doi.org/10.1016/0032-3950\(70\)90345-X](https://doi.org/https://doi.org/10.1016/0032-3950(70)90345-X).
- (32) Rowland, R. S.; Taylor, R. Intermolecular Nonbonded Contact Distances in Organic Crystal Structures: Comparison with Distances Expected from van Der Waals Radii. *J. Phys. Chem.* **1996**, *100* (18), 7384–7391. <https://doi.org/10.1021/jp953141+>.
- (33) Pauling, L.; Brockway, L. O. Carbon—Carbon Bond Distances. The Electron Diffraction Investigation of Ethane, Propane, Isobutane, Neopentane, Cyclopropane, Cyclopentane, Cyclohexane, Allene, Ethylene, Isobutene, Tetramethylethylene, Mesitylene, and Hexamethylbenzene. Revised Values Of. *J. Am. Chem. Soc.* **1937**, *59* (7), 1223–1236. <https://doi.org/10.1021/ja01286a021>.
- (34) Sun, H.; Jin, Z.; Yang, C.; Akkermans, R. L. C.; Robertson, S. H.; Spenley, N. A.; Miller, S.; Todd, S. M. COMPASS II: Extended Coverage for Polymer and Drug-like Molecule Databases. *J. Mol. Model.* **2016**, *22* (2), 1–10. <https://doi.org/10.1007/s00894-016-2909-0>.
- (35) Du, N.; Park, H. B.; Robertson, G. P.; Dal-Cin, M. M.; Visser, T.; Scoles, L.; Guiver, M. D. Polymer Nanosieve Membranes for CO₂-Capture Applications. *Nat. Mater.* **2011**, *10* (5), 372–375. <https://doi.org/10.1038/nmat2989>.
- (36) Robeson, L. M. The Upper Bound Revisited. *J. Membr. Sci.* **2008**, *320* (1–2), 390–400. <https://doi.org/10.1016/j.memsci.2008.04.030>.
- (37) Budd, P. M.; Elabas, E. S.; Ghanem, B. S.; Makhseed, S.; McKeown, N. B.; Msayib, K. J.; Tattershall, C. E.; Wang, D. Solution-Processed, Organophilic Membrane Derived from a Polymer of Intrinsic Microporosity. *Adv. Mater.* **2004**, *16* (5), 456–459. <https://doi.org/10.1002/adma.200306053>.
- (38) Naiying, D.; Jingshe, S.; Robertson, G. P.; Pinnau, I.; Guiver, M. D. Linear High Molecular Weight Ladder Polymer via Fast Polycondensation of 5,5',6,6'-Tetrahydroxy- 3,3,3',3'-Tetramethylspirobisindane with 1,4-Dicyanotetrafluorobenzene. *Macromol. Rapid Commun.* **2008**, *29* (10), 783–788. <https://doi.org/10.1002/marc.200800038>.
- (39) Lai, H. W. H.; Benedetti, F. M.; Jin, Z.; Teo, Y. C.; Wu, A. X.; Angelis, M. G. De; Smith, Z. P.; Xia, Y. Tuning the Molecular Weights, Chain Packing, and Gas-Transport Properties of CANAL Ladder Polymers by Short Alkyl Substitutions. *Macromolecules* **2019**, *52* (16), 6294–6302. <https://doi.org/10.1021/acs.macromol.9b01155>.
- (40) Yerzhankyzy, A.; Ghanem, B. S.; Wang, Y.; Alaslai, N.; Pinnau, I. Gas Separation Performance and Mechanical Properties of Thermally-Rearranged Polybenzoxazoles Derived from an Intrinsically Microporous Dihydroxyl-Functionalized Triptycene Diamine-Based Polyimide. *J. Membr. Sci.* **2020**, *595*, 117512. <https://doi.org/10.1016/j.memsci.2019.117512>.
- (41) Allen, F. H.; Kennard, O.; Watson, D. G.; Brammer, L.; Orpen, A. G.; Taylor, R. Tables of

- Bond Lengths Determined by X-Ray and Neutron Diffraction. Part 1. Bond Lengths in Organic Compounds. *J. Chem. Soc. Perkin Trans. 2* **1987**, No. 12, S1. <https://doi.org/10.1039/p298700000s1>.
- (42) Budd, P. M.; McKeown, N. B.; Fritsch, D. Free Volume and Intrinsic Microporosity in Polymers. *J. Mater. Chem.* **2005**, *15* (20), 1977–1986. <https://doi.org/10.1039/b417402j>.
- (43) Robeson, L. M.; Smith, Z. P.; Freeman, B. D.; Paul, D. R. Contributions of Diffusion and Solubility Selectivity to the Upper Bound Analysis for Glassy Gas Separation Membranes. *J. Membr. Sci.* **2014**, *453*, 71–83. <https://doi.org/10.1016/j.memsci.2013.10.066>.
- (44) Cohen, M. H.; Turnbull, D. Molecular Transport in Liquids and Glasses. *J. Chem. Phys.* **1959**, *31* (5), 1164–1169. <https://doi.org/10.1063/1.1730566>.
- (45) Yin, H.; Chua, Y. Z.; Yang, B.; Schick, C.; Harrison, W. J.; Budd, P. M.; Böhning, M.; Schönhals, A. First Clear-Cut Experimental Evidence of a Glass Transition in a Polymer with Intrinsic Microporosity: PIM-1. *J. Phys. Chem. Lett.* **2018**, *9* (8), 2003–2008. <https://doi.org/10.1021/acs.jpcllett.8b00422>.
- (46) Smith, Z. P.; Sanders, D. F.; Ribeiro, C. P.; Guo, R.; Freeman, B. D.; Paul, D. R.; McGrath, J. E.; Swinnea, S. Gas Sorption and Characterization of Thermally Rearranged Polyimides Based on 3,3'-Dihydroxy-4,4'-Diamino-Biphenyl (HAB) and 2,2'-Bis-(3,4-Dicarboxyphenyl) Hexafluoropropane Dianhydride (6FDA). *J. Membr. Sci.* **2012**, *415–416*, 558–567. <https://doi.org/10.1016/j.memsci.2012.05.050>.
- (47) Tiwari, R. R.; Smith, Z. P.; Lin, H.; Freeman, B. D.; Paul, D. R. Gas Permeation in Thin Films of “High Free-Volume” Glassy Perfluoropolymers: Part I. Physical Aging. *Polymer* **2014**, *55* (22), 5788–5800. <https://doi.org/10.1016/j.polymer.2014.09.022>.
- (48) Struik, L. C. E. Physical Aging in Plastics and Other Glassy Materials. *Polym. Eng. Sci.* **1977**, *17* (3), 165–173. <https://doi.org/10.1002/pen.760170305>.
- (49) Chen, X.; Zhang, Z.; Wu, L.; Liu, X.; Xu, S.; Efome, J. E.; Zhang, X.; Li, N. Polymers of Intrinsic Microporosity Having Bulky Substitutes and Cross-Linking for Gas Separation Membranes. *ACS Appl. Polym. Mater.* **2020**, *2* (2), 987–995. <https://doi.org/10.1021/acsapm.9b01193>.

Chapter 9: Conclusions and Future Directions

Perfluoropolymers are currently in an interesting space as a class of materials, where these polymers as membranes show exceptional property sets in terms of sorption selectivity and separation performance but the underlying theory behind their performance remains underdeveloped. This dissertation has quantified the step-change improvement in separation performance through improved sorption selectivity (Chapter 4), developed fluorine-related structure–property relationships between morphology and diffusion (Chapter 5), and examined changes in sorption behavior with respect to polymer fluorine content using the dual-mode model (Chapter 6) and the non-equilibrium lattice fluid (NELF) model (Chapter 7) to elucidate the underlying mechanism behind the anomalous sorption behavior of perfluoropolymers. This dissertation has also developed a refined and modernized group contribution method for the estimation of fractional free volume in high free volume polymers (Chapter 8). This chapter summarizes these studies, discusses larger implications, and provides recommendations for related future work.

9.1. Conclusions

The exceptional upper bound placement of perfluoropolymers for all helium- and most methane-based gas pairs was previously highlighted by Robeson in 2008¹ and was attributed to exceptional sorption selectivity. Chapter 4 refined Freeman’s upper bound theory² to account for changes in sorption selectivity based off of chemical composition. Theoretical perfluoropolymer upper bounds were established, representing the best combinations of permeability and selectivity for a hypothetical polymer simultaneously exhibiting the best diffusion and sorption selectivity. Interestingly, some perfluoropolymers demonstrate performance at or beyond the theoretical perfluoropolymer upper bounds. Diffusion and sorption selectivity effects on overall separation

performance were decoupled, showcasing the potential step-change in performance resulting from improved sorption selectivity.

Structure–property relationships relating polymer backbone fluorination to permeability and diffusion were the focus of Chapter 5. To investigate the role of aliphatic and aromatic fluorine substitutions on morphology, a two pairs of structurally analogous 6FDA-based polyimides were synthesized, with one pair showing an aliphatic substitution of hydrogen and fluorine (6FDA-6HpDA/6FDA-6FpDA) and the other showing an aromatic substitution (6FDA-OHB/6FDA-OFB). Traditionally, fabrication of robust films for highly fluorinated polyimides is challenging due to the hindered nucleophilicity of fluorinated diamines resulting in a low molecular weight polymer. A high temperature cure to 350 °C allowed for simultaneous chain extension and imidization, allowing for the fabrication of highly fluorinated polymer films. The permeability and diffusion for He, H₂, N₂, O₂, CH₄, and CO₂ were characterized for the four polymers. Aromatic fluorine substitution showed a larger increase in permeability and diffusion and correspondingly a larger decrease in permselectivity and diffusion selectivity compared to the aliphatic substitution. It was found that aliphatic fluorine substitution had minimal effect on chain mobility but increased interchain spacing due to the larger size of fluorine disrupting the packing structure, resulting in a moderate increase in diffusion and decrease in diffusion selectivity. On the other hand, the larger change in transport performance for the aromatic fluorine substitution was tied to lower activation energy of diffusion compared to the other polymers, stemming from increased chain mobility caused by both weakened interchain interactions and larger interchain spacing. This study highlighted the steric and electronic effects associated with incorporation of fluorine on the polymer backbone and its subsequent effect on the overall polymer morphology and transport properties.

Changes in sorption behavior with respect to fluorine content for the same set of 6FDA-based polyimides were examined using the dual-mode sorption model in Chapter 6. High pressure sorption isotherms for the same six light gases were collected at 35, 45, 55, and 65 °C for the four polymers. A new method for the nonlinear fitting of dual-mode parameters involving a linear free energy relationship-inspired constraint allowed for precise best-fit parameters. A continuous increase in sorption selectivity was observed with increasing fluorine content. The increased sorption selectivity was primarily driven by increased Henry sorption selectivity while Langmuir sorption remained relatively invariant. A comparison of the enthalpy of sorption into the two modes showed an increasing endothermic penalty with fluorine content for Henry sorption while that for Langmuir sorption was relatively constant. The increasing endothermic penalty for Henry sorption was associated with increased amounts of unfavorable equilibrium mixing interactions with fluorine content. An analysis of the isosteric heat of sorption showed a slower transition from Langmuir to Henry sorption for the highly fluorinated polymers.

In Chapter 7, changes in sorption behavior with respect to fluorine content were analyzed using the NELF model for a new series of structurally analogous poly(ether imide)s, ranging from fully hydrocarbon to perfluorinated. A perfluorinated dianhydride, 10FEDA, was synthesized in order to complete this series. High pressure sorption isotherms for O₂, N₂, CH₄, and CO₂ were collected at 34, 45, 55, and 65 °C. Lattice fluid parameters for the polymers were determined using the experimental infinite dilution sorption data and the resulting NELF isotherms showed good agreement to the data, especially for pressures less than 2 MPa. The binary interaction parameter, k_{12} , increased with fluorine content, representing increased unfavorable deviations from ideal mixing. The increase for CH₄ was particularly pronounced, potentially suggesting an unfavorable penetrant-specific interaction with fluorine content. An analysis of the enthalpic and entropic

contributions to sorption at infinite dilution revealed continuous trends for enthalpic, entropic, and sorption selectivity with respect to fluorine content. The increase in enthalpic selectivity (caused by higher k_{12} , lower cohesive energy density and higher free volume) was larger than the decrease in entropic selectivity (caused by higher free volume), resulting in overall increased sorption selectivity.

Lastly, the most common method to calculate fractional free volume (FFV) in polymer membranes was refined in Chapter 8. Four assumptions present in Bondi's original method³ were addressed and a modernized and streamlined method to calculate the van der Waals volume (V_W) for any group of interest was developed. The new method was used to calculate and tabulate the V_W for 96 groups commonly found in microporous polymers. FFV was recalculated for a database of 123 microporous and high free volume polymers from the literature, showing an average increase by a factor of 24% when compared to the originally reported literature values. Correlations relating permeability and $1/\text{FFV}$ were also updated using the new FFV values, resulting in overall stronger correlations for all gases.

Overall, from the studies presented in this dissertation, we were able to address the dissertation aims of quantifying the effect of fluorination of separation performance (Chapter 4), develop relevant structure–property relationships related to fluorine (Chapter 5), identify specific mechanisms by which fluorination affects gas sorption (Chapters 6 and 7), and examine and update group contribution theory for fractional free volume calculation (Chapter 8). The refined understanding of fundamental gas–polymer interactions governing gas transport obtained from these works could enable improved design of industrially-relevant polymers for specific applications.

First, we were able to identify that there are certain gas pairs for which perfluoropolymers will not perform as well as hydrocarbon polymers in terms of sorption selectivity, due to the nature of the change in sorption behavior. Namely, gas pairs in which the faster permeating gas is also the more condensable (*e.g.*, CO₂/CH₄, CO₂/N₂, etc.) will theoretically show worse sorption selectivity. We also identified situations where lowered sorption capacity was greater than the improvement in sorption selectivity (*e.g.*, C₃H₆/C₃H₈) and would result in lower performance, so the use of perfluoropolymer membranes is recommended for specific applications such as helium or hydrogen recovery as discussed in Chapter 4.

Additionally, we found that the property sets of hydrocarbon polymers and perfluoropolymers can be connected via partially fluorinated intermediates instead of existing as a step-change in properties, demonstrated in Chapters 6 and 7. This suggests that small amounts of fluorine included on the polymer backbone can introduce incremental beneficial perfluoropolymer sorption behavior to improve sorption selectivity. For example, as shown in Chapter 5, the increase in sorption selectivity brought by –CF₃ groups was able to balance out the decrease in diffusion selectivity caused by larger interchain spacing, thereby resulting in increased permeability with no loss in permselectivity and overcoming the conventional permeability-selectivity trade-off. This example and similar fluorine-related structure–property relationships presented in this dissertation can be used by researchers to inform future syntheses of polymers for targeted applications.

9.2. Recommendations for Future Work

9.2.1. Noble Gases Sorption in Fluorinated Polymers

The sorption isotherms obtained in Chapters 6 and 7 are limited to the six light gases commonly used for transport characterization: He, H₂, O₂, N₂, CH₄, and CO₂. However, these gases have

inherent differences that preclude a well-defined comparison across gas species. For example, He is a point particle, H₂, O₂, and N₂ are diatomic, CH₄ is tetrahedral and is the simplest hydrocarbon, and CO₂ is quadrupolar. While these gases can be sorted by a measure of condensability such as critical temperature, the variability in gas properties that are not accounted for may have an unseen effect on penetrant–polymer interactions and gas sorption. One way to eliminate variability in penetrant properties is through noble gas sorption, such as He, Ne, Ar, Kr, and Xe. For these point particle gases, the only change across gases is penetrant size, which scales with condensability and polarity accordingly. Therefore, changes in sorption behavior across penetrants can be directly attributed to simple properties. For example, noble gas sorption in the poly(ether imide) series presented in Chapter 7 could reveal a trend where increasingly polarizable penetrants show a greater favorable deviation from ideal mixing with increasing fluorine content. Sorption characterization using noble gases would allow for the best comparison across gases for foundational studies.

9.2.2. Sorption of Hydrocarbon, Perfluorocarbon, and Partially Fluorinated Gases in Fluorinated Polymers

An additional set of gases that would be of interest to perform sorption experiments in the poly(ether imide) series are hydrocarbon (*e.g.*, ethane, propane, etc.), perfluorocarbon (*e.g.*, perfluoromethane, perfluoroethane, etc.), and partially fluorinated gases (*e.g.*, trifluoromethane, pentafluoroethane, etc.). Testing these gases would provide variation in fluorine content for the gases as well as the polymers. In particular, a series consisting of methane, fluoromethane, difluoromethane, trifluoromethane, and tetrafluoromethane would stand as a set of structurally analogous gases ranging from fully hydrocarbon to fully fluorinated. The sorption could be

analyzed using the NELF model in a similar manner to Chapter 7, where changes in k_{12} and other sorption parameters could be analyzed as a function of both polymer and gas fluorination.

9.2.3. Development of Structure–Property Relationships Relating Fluorine Content to Plasticization and Physical Aging Resistance

The large focus of the work performed in this dissertation was to determine structure–property relationships relating fluorine content to sorption behavior. However, perfluoropolymers have also demonstrated unusually stable separation performance over time and in the presence of swelling-inducing penetrants, both of which are highly desirable in industrial processes. Similar to sorption behavior, the theory behind the exceptional plasticization and physical aging resistance of perfluoropolymers is not well-developed. In Chapters 6 and 7, we demonstrated that the sorption behavior between hydrocarbon and perfluoropolymers could be unified by an additive model based on fluorine content, suggesting that plasticization and physical aging behavior could be similarly linked. Relationships between fluorine content and fundamental polymer properties, such as isothermal compressibility, could be developed to explain the changes in plasticization and physical aging resistance. These sorts of structure–property relationships would be extremely valuable to fully understand the role of fluorine on performance stability.

9.3. References

- (1) Robeson, L. M. The Upper Bound Revisited. *J. Membr. Sci.* **2008**, *320* (1–2), 390–400. <https://doi.org/10.1016/j.memsci.2008.04.030>.
- (2) Freeman, B. D. Basis of Permeability/Selectivity Tradeoff Relations in Polymeric Gas Separation Membranes. *Macromolecules* **1999**, *32* (2), 375–380. <https://doi.org/10.1021/ma9814548>.
- (3) Bondi, A. Van Der Waals Volumes and Radii. *J. Phys. Chem.* **1964**, *68* (3), 441–451. <https://doi.org/10.1021/j100785a001>.

Appendix A: Supplementary Information for Chapter 4

This chapter has been adapted from the Supplementary Information of: Wu, A. X.; Drayton, J. A.; Smith, Z. P. The Perfluoropolymer Upper Bound. *AIChE J.* **2019**, *65* (12), e16700.

A.1. Diffusion diameters, Lennard-Jones temperatures, and comparison of $\lambda_{A/B}$ values

Table A.1 shows the diffusion diameters and the Lennard-Jones temperatures used in the upper bound analysis. Table A.2 shows a comparison of $\lambda_{A/B}$ values for the non-perfluoropolymer upper bounds obtained following a similar procedure to that used by Robeson in 1991 and 2008. A comparison is also presented for the theoretical $\lambda_{A/B}$ values when considering diffusion and kinetic diameters for the primary gas pairs analyzed in this work.^{1,2}

Table A.1. Diffusion diameters and Lennard-Jones temperatures for each gas considered for the primary analysis of this work.^{3,4}

Gas	Diffusion diameter (Å)	Lennard-Jones temperature (K)
He	2.55	10.2
H ₂	2.77	60
O ₂	3.23	71
CO ₂	3.44	195
N ₂	3.49	107
CH ₄	3.817	149

Table A.2. Tabulated results of $\lambda_{A/B}$ values for the non-perfluoropolymer upper bounds and the theoretical $\lambda_{A/B}$ values when considering diffusion and kinetic diameters.⁵

Gas pair	$\lambda_{A/B}$ for non-perfluoropolymer upper bound	$\lambda_{A/B}$ for diffusion diameters	$\lambda_{A/B}$ for kinetic diameters
He/H ₂	0.217	0.180	0.236
He/CO ₂	0.637	0.820	0.611
He/N ₂	0.983	0.873	0.960
He/CH ₄	1.233	1.241	1.136
N ₂ /CH ₄	0.216	0.196	0.090

A.2. ANOVA test of the Barrer form of the linear free energy relationship

Section 4.3.1 discusses modifications from the previous upper bound analysis, specifically regarding the use of the van Amerongen or Barrer form of the linear free energy relationship (Equations 4.12.1 and 4.13.1).^{6,7} Prabhakar noted that use of the Barrer form, when substituted into the Arrhenius equation for diffusion, resulted in a fixed intercept of b' when plotting $\ln(D)$ vs. $1/T$, regardless of polymer system, while the van Amerongen form did not result in a fixed intercept (Equations 4.12.2 and 4.13.2). The statistical significance of selecting one of these two mathematical forms was determined through the use of a two-factor analysis of variance (ANOVA) without replication on van Amerongen's data.⁶

To perform the two-factor ANOVA, linear regressions of $\ln(D)$ vs. $1/T$ data were calculated for each polymer-gas pair to obtain best-fit intercepts. The best-fit intercepts were analyzed to

determine whether the variance in intercepts could be attributed to a change in the polymer, the gas, both the polymer and the gas, or neither the polymer and the gas. The null hypothesis tested was that the intercept is invariant across all polymer-gas pairings with a significance level of $p = 0.05$. The results of the two-factor ANOVA are shown in Table A.3. It was found that the F -values for both independent variables exceeded the critical F -values for statistical significance and that the p -values for both polymer and gas were lower than the test value of $p = 0.05$. From the F and p -values, it was concluded that the null hypothesis was rejected. In other words, the variance in the best-fit intercepts was found to be statistically significant and vary depending on the polymer/gas pair, thus the van Amerongen form should be used for the primary analysis.

Table A.3. Results of the two-factor ANOVA without replication.

	F -value	Critical F -value	p -value
Polymer	44.73	2.66	7.49×10^{-10}
Gas	51.73	3.16	4.75×10^{-9}

A.3. Sorption coefficient data

Table A.4 shows the sorption data used to determine the M and N solubility parameters in Equation 4.8. All values were measured at or near experimental conditions of 35 °C and 1 atm, and have units of $\text{cm}^3(\text{STP}) \text{cm}^{-3} \text{atm}^{-1}$.

Table A.4. Sorption coefficients used to determine solubility correlation coefficients in Equation 4.8. PTMSP is poly(1-trimethylsilyl-1-propyne), PDMS is polydimethylsiloxane, SBIPC is spirobiindane polycarbonate, 6FDA is 4,4'-(hexafluoroisopropylidene)diphthalic anhydride, HAB

is 3,3'-dihydroxy-4,4'-diamino-biphenyl, mPDA is 1,3-phenylenediamine, PHFP is poly(hexafluoropropylene), and FMVE is perfluoromethylvinyl ether.

Non-perfluorocarbons									
Polymer/Liquid	He	H ₂	N ₂	O ₂	CH ₄	C ₂ H ₆	CO ₂	C ₃ H ₈	Ref.
PTMSP	-	0.45	1	1.2	3	20	7	70	8
n-Heptane	-	0.1	0.2	0.3	0.7	5	2	11	8
PDMS	-	0.05	0.09	0.18	0.4	2.5	1.2	5.5	8
Polyethylene	-	0.012	0.04	0.08	0.2	1.5	0.45	5	8
Nylon 11	0.0045	0.0135	-	-	-	-	0.368	-	9
Polyethylene	0.0065	0.0171	0.0241	-	-	-	0.248	-	9
Polycarbonate	0.19	0.6612	1.3984	2.0976	4.009	-	16.036	-	10
SBIPC	0.5092	1.2996	3.847	5.0008	9.283	-	25.992	-	10
PTMSP	-	-	1.12	1.31	3.6	23.3	6.2	71.3	11
6FDA-HAB	-	0.21	0.44	0.60	1.07	-	4.0	-	12
6FDA-mPDA	-	-	0.7068	0.9044	-	-	12.107	-	13
Perfluorocarbons									
Polymer/Liquid	He	H ₂	N ₂	O ₂	CH ₄	C ₂ H ₆	CO ₂	C ₃ H ₈	Ref.
Teflon [®] AF 2400	-	0.21	0.6	0.85	1.1	3.5	3	7	8
Perfluoroheptane	-	0.13	0.38	-	0.8	2	-	4	8
Hyflon AD 60	-	0.1	0.29	-	0.5	1.5	-	2.3	8
Cytop	-	0.055	0.16	-	0.29	0.8	1.05	2	8
Teflon [®] AF 1600	-	-	0.6	0.71	0.95	3.5	2.76	8.9	11

Teflon [®] AF 2400	-	-	0.64	0.88	1.23	5.06	3.4	15.2	11
PHFP	0.15	0.22	0.66	0.96	1.27	-	4.8	-	14
Copoly-HFP- FMVE	0.09	0.14	0.42	0.7	0.82	-	2.9	-	14

A.4. Calculated f values for various upper bound fronts

Table A.5 shows the calculated f values for the 1991 and non-perfluoropolymer upper bounds.

There were no O₂/CH₄ or N₂/CH₄ upper bounds established in 1991.¹

Table A.5. Calculated f values for 1991 and non-perfluoropolymer upper bounds and the percentage increase between the two values.

Gas pair	f value		Increase in f value
	f for 1991 upper bound (kJ mol ⁻¹)	f for non-perfluoropolymer upper bound (kJ mol ⁻¹)	Increase in f , 1991 f to non-perfluoropolymer f
He/H ₂	81.3	79.9	-1.7%
He/CO ₂	70.6	84.1	19%
He/O ₂	72.4	81.3	12%
He/N ₂	64.0	67.2	5.0%
He/CH ₄	64.8	70.3	8.4%
H ₂ /CO ₂	69.8	90.3	29%
H ₂ /O ₂	73.1	87.8	20%
H ₂ /N ₂	56.9	69.6	22%

H ₂ /CH ₄	63.2	70.9	12%
CO ₂ /CH ₄	18.2	37.5	106%
O ₂ /N ₂	23.3	36.6	57%
O ₂ /CH ₄	-	54.1	-
N ₂ /CH ₄	-	87.0	-

A.5. References

- (1) Robeson, L. M. Correlation of Separation Factor versus Permeability for Polymeric Membranes. *J. Membr. Sci.* **1991**, *62* (2), 165–185. [https://doi.org/10.1016/0376-7388\(91\)80060-J](https://doi.org/10.1016/0376-7388(91)80060-J).
- (2) Robeson, L. M. The Upper Bound Revisited. *J. Membr. Sci.* **2008**, *320* (1–2), 390–400. <https://doi.org/10.1016/j.memsci.2008.04.030>.
- (3) Robeson, L. M.; Smith, Z. P.; Freeman, B. D.; Paul, D. R. Contributions of Diffusion and Solubility Selectivity to the Upper Bound Analysis for Glassy Gas Separation Membranes. *J. Membr. Sci.* **2014**, *453*, 71–83. <https://doi.org/10.1016/j.memsci.2013.10.066>.
- (4) Matteucci, S.; Yampolskii, Y.; Freeman, B. D.; Pinnau, I. Transport of Gases and Vapors in Glassy and Rubbery Polymers. In *Materials Science of Membranes for Gas and Vapor Separation*; 2006; pp 1–47. <https://doi.org/10.1002/047002903X.ch1>.
- (5) Breck, D. W. *Zeolite Molecular Sieves: Structure, Chemistry, and Use*; John Wiley & Sons Ltd.: New York, 1974.
- (6) Van Amerongen, G. J. The Permeability of Different Rubbers to Gases and Its Relation to Diffusivity and Solubility. *J. Appl. Phys.* **1946**, *17* (11), 972–985. <https://doi.org/10.1063/1.1707667>.
- (7) Barrer, R. M.; Skirrow, G. Transport and Equilibrium Phenomena in Gas-Elastomer Systems. I. Kinetic Phenomena. *J. Polym. Sci.* **1948**, *3* (4), 549–563. <https://doi.org/10.5254/1.3542972>.
- (8) Merkel, T. C.; Pinnau, I.; Prabhakar, R. S.; Freeman, B. D. Gas and Vapor Transport Properties of Perfluoropolymers. In *Materials Science of Membranes for Gas and Vapor Separation*; 2006; pp 251–270.
- (9) Ash, R.; Barrer, R. M.; Palmer, D. G. Solubility and Transport of Gases in Nylon and

- Polyethylene. *Polymer* **1970**, *11* (8), 421–435. [https://doi.org/10.1016/0032-3861\(70\)90004-2](https://doi.org/10.1016/0032-3861(70)90004-2).
- (10) Hellums, M. W.; Koros, W. J.; Schmidhauser, J. C. Gas Separation Properties of Spirobiindane Polycarbonate. *J. Membr. Sci.* **1992**, *67* (1), 75–81. [https://doi.org/10.1016/0376-7388\(92\)87041-U](https://doi.org/10.1016/0376-7388(92)87041-U).
- (11) Alentiev, A. Y.; Shantarovich, V. P.; Merkel, T. C.; Bondar, V. I.; Freeman, B. D.; Yampolskii, Y. P. Gas and Vapor Sorption, Permeation, and Diffusion in Glassy Amorphous Teflon AF1600. *Macromolecules* **2002**, *35* (25), 9513–9522. <https://doi.org/10.1021/ma020494f>.
- (12) Smith, Z. P.; Sanders, D. F.; Ribeiro, C. P.; Guo, R.; Freeman, B. D.; Paul, D. R.; McGrath, J. E.; Swinnea, S. Gas Sorption and Characterization of Thermally Rearranged Polyimides Based on 3,3'-Dihydroxy-4,4'-Diamino-Biphenyl (HAB) and 2,2'-Bis-(3,4-Dicarboxyphenyl) Hexafluoropropane Dianhydride (6FDA). *J. Membr. Sci.* **2012**, *415–416*, 558–567. <https://doi.org/10.1016/j.memsci.2012.05.050>.
- (13) Chung, T.; Lin, W.; Vora, R. H. Gas Transport Properties of 6FDA-Durene/1,3-Phenylenediamine (MPDA) Copolyimides. *J. Appl. Phys.* **2001**, *81* (14), 3552–3564.
- (14) Belov, N. A.; Zharov, A. A.; Shashkin, A. V.; Shaikh, M. Q.; Raetzke, K.; Yampolskii, Y. P. Gas Transport and Free Volume in Hexafluoropropylene Polymers. *J. Membr. Sci.* **2011**, *383* (1–2), 70–77. <https://doi.org/10.1016/j.memsci.2011.08.029>.

Appendix B: Supplementary Information for Chapter 5

This chapter has been adapted from the Supplementary Information of: Wu, A. X.; Drayton, J. A.; Rodriguez, K. M.; Qian, Q.; Lin, S.; Smith, Z. P. Influence of Aliphatic and Aromatic Fluorine Groups on Gas Permeability and Morphology of Fluorinated Polyimide Films. *Macromolecules* **2020**, *53* (13), 5085–5095.

Table B.1. GPC results for the four poly(amic acid)s prior to the high temperature cure. The 6FDA-OFB PAA results showed three distinct peaks, representing oligomers of approximately one, two, and three repeat units in size.

Polymer	M _n (Da)	M _w (Da)
6FDA-6HpDA PAA	177,000	347,000
6FDA-6FpDA PAA	110,000	214,000
6FDA-OHB PAA	114,000	186,000
6FDA-OFB PAA	600; 1,700; 3,100	600; 1,700; 3,100
6FDA-OFB film	56,000	138,000

Table B.2. Permeation, diffusion, and sorption results for 6FDA-6HpDA.

Permeability (barrer)						
T (°C)	He	H ₂	O ₂	N ₂	CH ₄	CO ₂
35	65 ± 4	65 ± 4	7.1 ± 0.4	1.44 ± 0.09	0.84 ± 0.05	36 ± 2
45	74 ± 4	73 ± 4	8.0 ± 0.5	1.6 ± 0.1	1.18 ± 0.07	37 ± 2
55	83 ± 5	81 ± 5	9.0 ± 0.5	2.0 ± 0.1	1.39 ± 0.08	38 ± 2
65	92 ± 5	90 ± 5	10.4 ± 0.6	2.9 ± 0.2	2.0 ± 0.1	40 ± 2
Diffusivity × 10 ⁸ (cm ² s ⁻¹)						
T (°C)	He	H ₂	O ₂	N ₂	CH ₄	CO ₂
35	-	-	8.1 ± 0.6	2.4 ± 0.2	0.30 ± 0.02	2.5 ± 0.2
45	-	-	12.0 ± 0.9	3.8 ± 0.3	0.59 ± 0.04	3.5 ± 0.3
55	-	-	18 ± 2	7.9 ± 0.6	1.01 ± 0.07	5.1 ± 0.4
65	-	-	25 ± 3	20 ± 2	1.9 ± 0.1	7.3 ± 0.5
Sorption (cm ³ (STP) cm ⁻³ atm ⁻¹)						
T (°C)	He	H ₂	O ₂	N ₂	CH ₄	CO ₂
35	-	-	0.66 ± 0.06	0.46 ± 0.04	2.1 ± 0.2	11 ± 1
45	-	-	0.51 ± 0.05	0.32 ± 0.03	1.5 ± 0.1	8.1 ± 0.8
55	-	-	0.39 ± 0.04	0.20 ± 0.02	1.0 ± 0.1	5.7 ± 0.5
65	-	-	0.32 ± 0.04	0.11 ± 0.01	0.80 ± 0.07	4.2 ± 0.4

Table B.3. Permeation, diffusion, and sorption results for 6FDA-6FpDA.

Permeability (barrer)						
T (°C)	He	H ₂	O ₂	N ₂	CH ₄	CO ₂
35	114 ± 6	95 ± 5	11.8 ± 0.6	2.5 ± 0.1	1.29 ± 0.07	55 ± 3
45	127 ± 7	106 ± 5	13.0 ± 0.7	2.9 ± 0.1	1.60 ± 0.08	57 ± 3
55	141 ± 7	117 ± 6	14.4 ± 0.7	3.5 ± 0.2	2.0 ± 0.1	58 ± 3
65	156 ± 8	130 ± 7	16.3 ± 0.8	4.5 ± 0.2	2.9 ± 0.1	60 ± 3
Diffusivity × 10 ⁸ (cm ² s ⁻¹)						
T (°C)	He	H ₂	O ₂	N ₂	CH ₄	CO ₂
35	-	-	13 ± 1	4.1 ± 0.3	0.59 ± 0.03	5.3 ± 0.3
45	-	-	18 ± 2	6.4 ± 0.4	0.96 ± 0.06	7.0 ± 0.5
55	-	-	24 ± 3	13 ± 1	2.1 ± 0.1	8.8 ± 0.6
65	-	-	33 ± 5	23 ± 3	8.2 ± 0.6	11.5 ± 0.9
Sorption (cm ³ (STP) cm ⁻³ atm ⁻¹)						
T (°C)	He	H ₂	O ₂	N ₂	CH ₄	CO ₂
35	-	-	0.68 ± 0.07	0.47 ± 0.04	1.7 ± 0.1	7.9 ± 0.6
45	-	-	0.56 ± 0.06	0.34 ± 0.03	1.3 ± 0.1	6.2 ± 0.5
55	-	-	0.46 ± 0.06	0.21 ± 0.02	0.72 ± 0.06	5.0 ± 0.4
65	-	-	0.38 ± 0.06	0.15 ± 0.02	0.26 ± 0.02	4.0 ± 0.4

Table B.4. Permeation, diffusion, and sorption results for 6FDA-OHB.

Permeability (barrer)						
T (°C)	He	H ₂	O ₂	N ₂	CH ₄	CO ₂
35	59 ± 3	58 ± 3	6.4 ± 0.4	1.23 ± 0.07	0.81 ± 0.05	35 ± 2
45	67 ± 4	65 ± 4	7.2 ± 0.4	1.51 ± 0.08	1.13 ± 0.06	36 ± 2
55	75 ± 4	72 ± 4	8.3 ± 0.5	1.9 ± 0.1	1.49 ± 0.08	38 ± 2
65	84 ± 5	81 ± 5	9.8 ± 0.5	2.8 ± 0.2	2.0 ± 0.1	41 ± 2
Diffusivity × 10 ⁸ (cm ² s ⁻¹)						
T (°C)	He	H ₂	O ₂	N ₂	CH ₄	CO ₂
35	-	-	7.4 ± 0.5	1.8 ± 0.1	0.24 ± 0.02	2.3 ± 0.1
45	-	-	9.5 ± 0.7	3.3 ± 0.2	0.38 ± 0.02	3.2 ± 0.2
55	-	-	12 ± 1	6.8 ± 0.5	0.68 ± 0.04	4.4 ± 0.3
65	-	-	23 ± 3	16 ± 1	1.21 ± 0.08	6.6 ± 0.5
Sorption (cm ³ (STP) cm ⁻³ atm ⁻¹)						
T (°C)	He	H ₂	O ₂	N ₂	CH ₄	CO ₂
35	-	-	0.66 ± 0.06	0.52 ± 0.04	2.6 ± 0.2	11 ± 1
45	-	-	0.58 ± 0.05	0.35 ± 0.03	2.2 ± 0.2	8.6 ± 0.7
55	-	-	0.48 ± 0.05	0.22 ± 0.02	1.7 ± 0.1	6.6 ± 0.6
65	-	-	0.32 ± 0.04	0.13 ± 0.01	1.2 ± 0.1	4.7 ± 0.4

Table B.5. Permeation, diffusion, and sorption results for 6FDA-OFB.

Permeability (barrer)						
T (°C)	He	H ₂	O ₂	N ₂	CH ₄	CO ₂
35	220 ± 20	220 ± 20	36 ± 3	9.7 ± 0.7	5.2 ± 0.4	160 ± 10
45	230 ± 20	230 ± 20	38 ± 3	10.1 ± 0.7	5.5 ± 0.4	150 ± 10
55	250 ± 20	240 ± 20	39 ± 3	11.1 ± 0.8	6.2 ± 0.4	150 ± 10
65	270 ± 20	250 ± 20	40 ± 3	12.7 ± 0.9	7.5 ± 0.5	140 ± 10
Diffusivity × 10 ⁸ (cm ² s ⁻¹)						
T (°C)	He	H ₂	O ₂	N ₂	CH ₄	CO ₂
35	-	-	25 ± 3	7.9 ± 0.7	1.6 ± 0.1	8.9 ± 0.8
45	-	-	33 ± 4	11 ± 1	2.0 ± 0.2	11 ± 1
55	-	-	42 ± 6	19 ± 2	3.6 ± 0.3	14 ± 1
65	-	-	60 ± 10	33 ± 4	9.6 ± 0.9	18 ± 2
Sorption (cm ³ (STP) cm ⁻³ atm ⁻¹)						
T (°C)	He	H ₂	O ₂	N ₂	CH ₄	CO ₂
35	-	-	1.1 ± 0.1	0.9 ± 0.1	2.5 ± 0.3	14 ± 2
45	-	-	0.9 ± 0.1	0.67 ± 0.08	2.1 ± 0.2	10 ± 1
55	-	-	0.7 ± 0.1	0.45 ± 0.06	1.3 ± 0.1	8 ± 1
65	-	-	0.5 ± 0.1	0.30 ± 0.04	0.59 ± 0.07	6.1 ± 0.7

Procedure for the Simulation of Conformational Energy Diagrams

The potential energy diagram for each diamine residue was simulated about a dihedral angle using the Conformers module in Materials Studio 2019 by BIOVIA. The structure of the diamine residue and chosen dihedral bond are shown in Figure 5.7. A systematic grid scan was performed about the indicated bond using the COMPASS II forcefield and the conformer energy was calculated after geometry optimization for every step. By applying the same simulation procedure with the entire diamine, as opposed to only its residue, similar results were obtained, but the resolution of the conformational energy diagram was lower. Thus, we only report findings for the diamine residue.

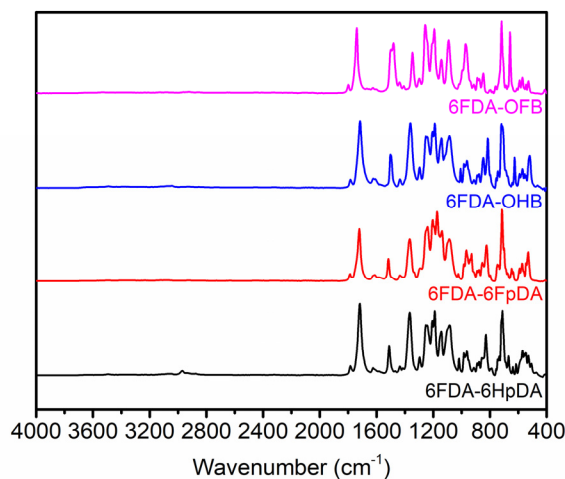


Figure B.1. FTIR spectra for the four polyimide films.

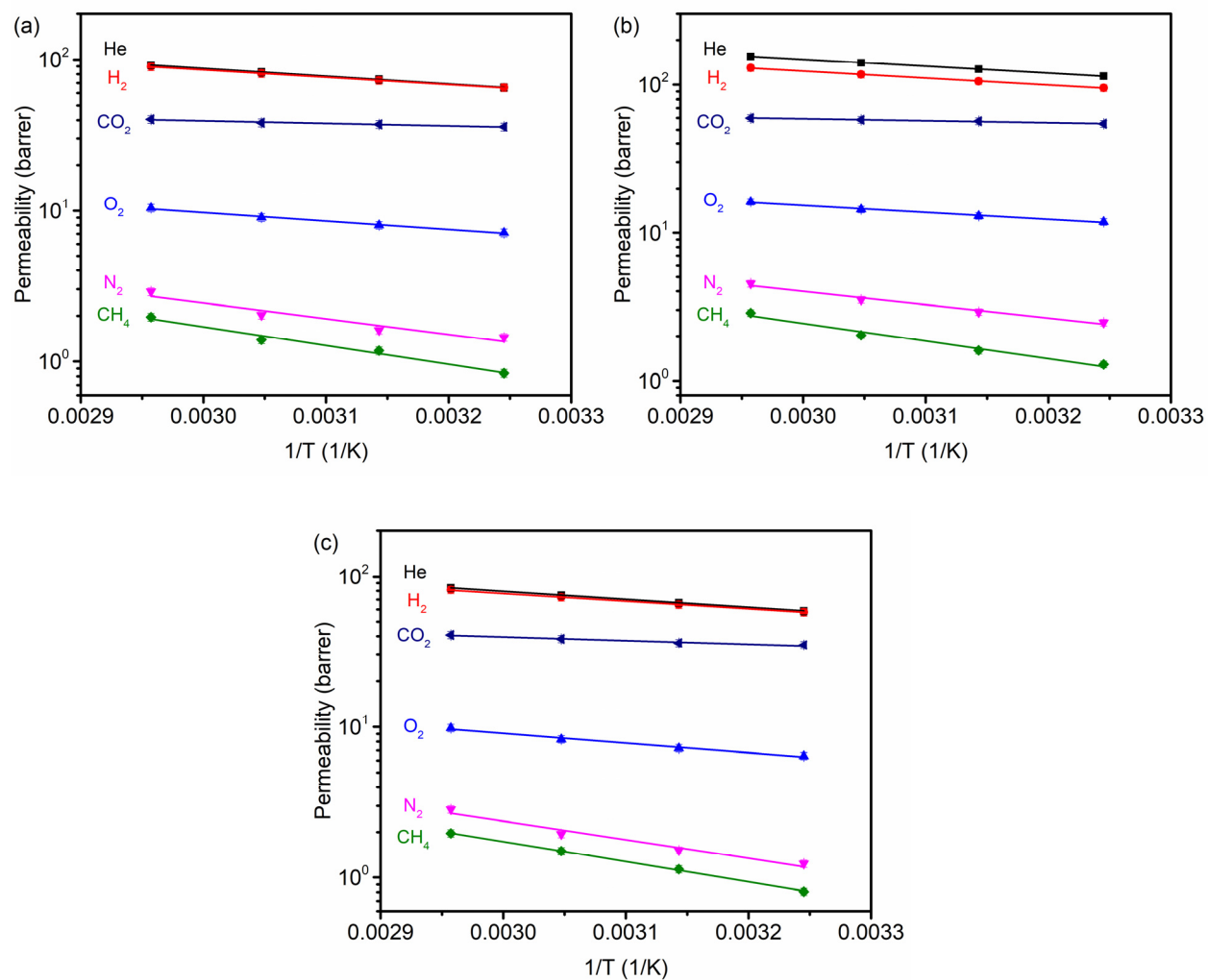


Figure B.2. Arrhenius plots showing the effect of temperature on permeability for (a) 6FDA-6HpDA, (b) 6FDA-6FpDA, and (c) 6FDA-OHB measured at 35, 45, 55, and 65 °C and 15 psi.

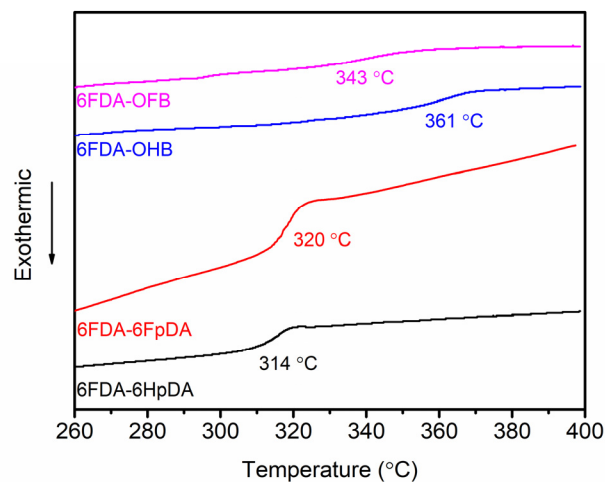


Figure B.3. DSC results for the four polyimide films. The results displayed are the last scan for each polymer.

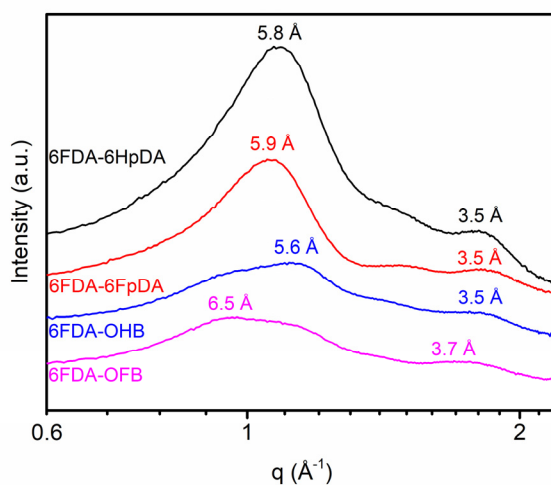


Figure B.4. WAXS results for the four polyimide films.

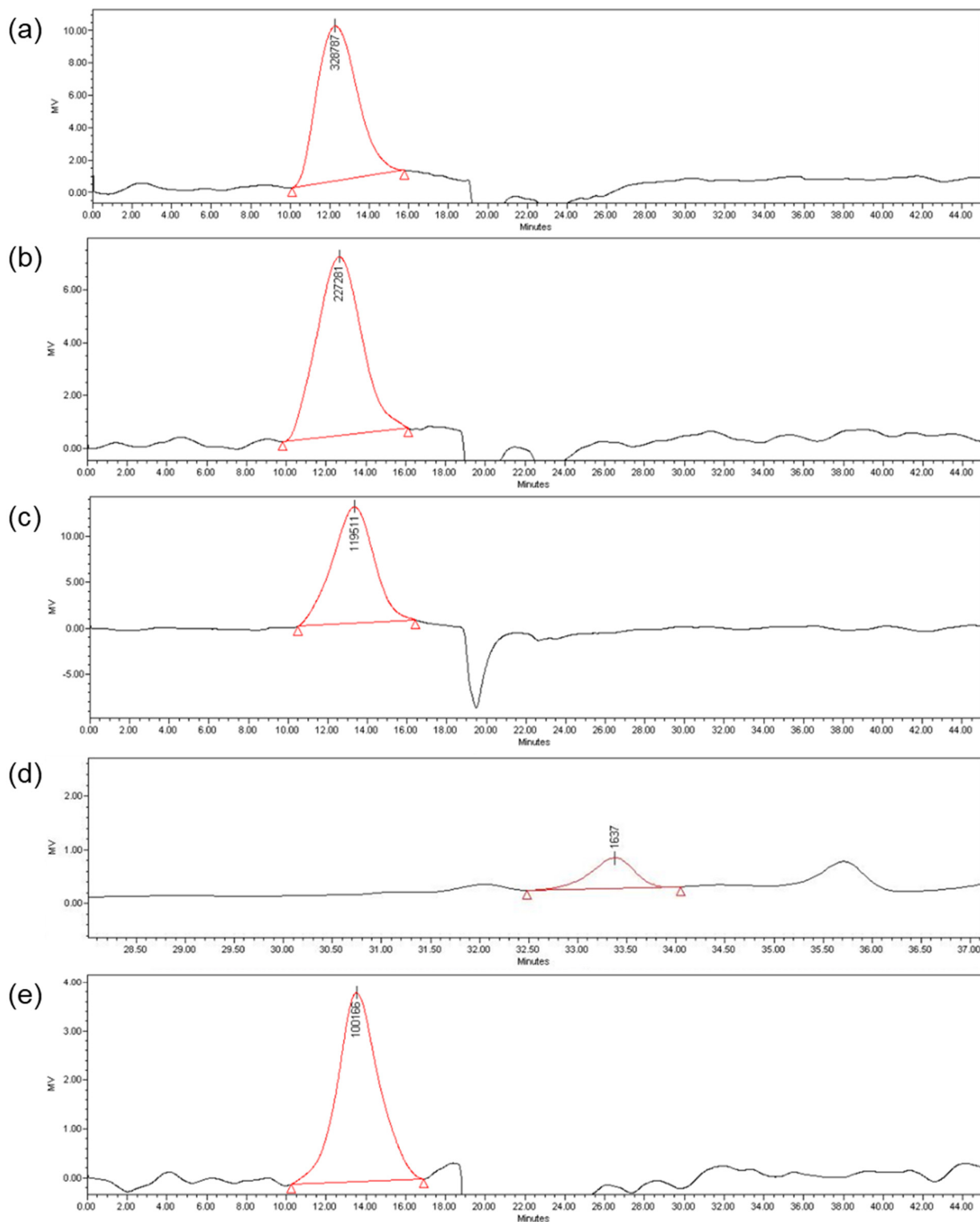


Figure B.5. GPC traces for the (a) 6FDA-6HpDA, (b) 6FDA-6FpDA, (c) 6FDA-OHB, and (d) 6FDA-OFB poly(amic acid), and the (e) 6FDA-OFB film.

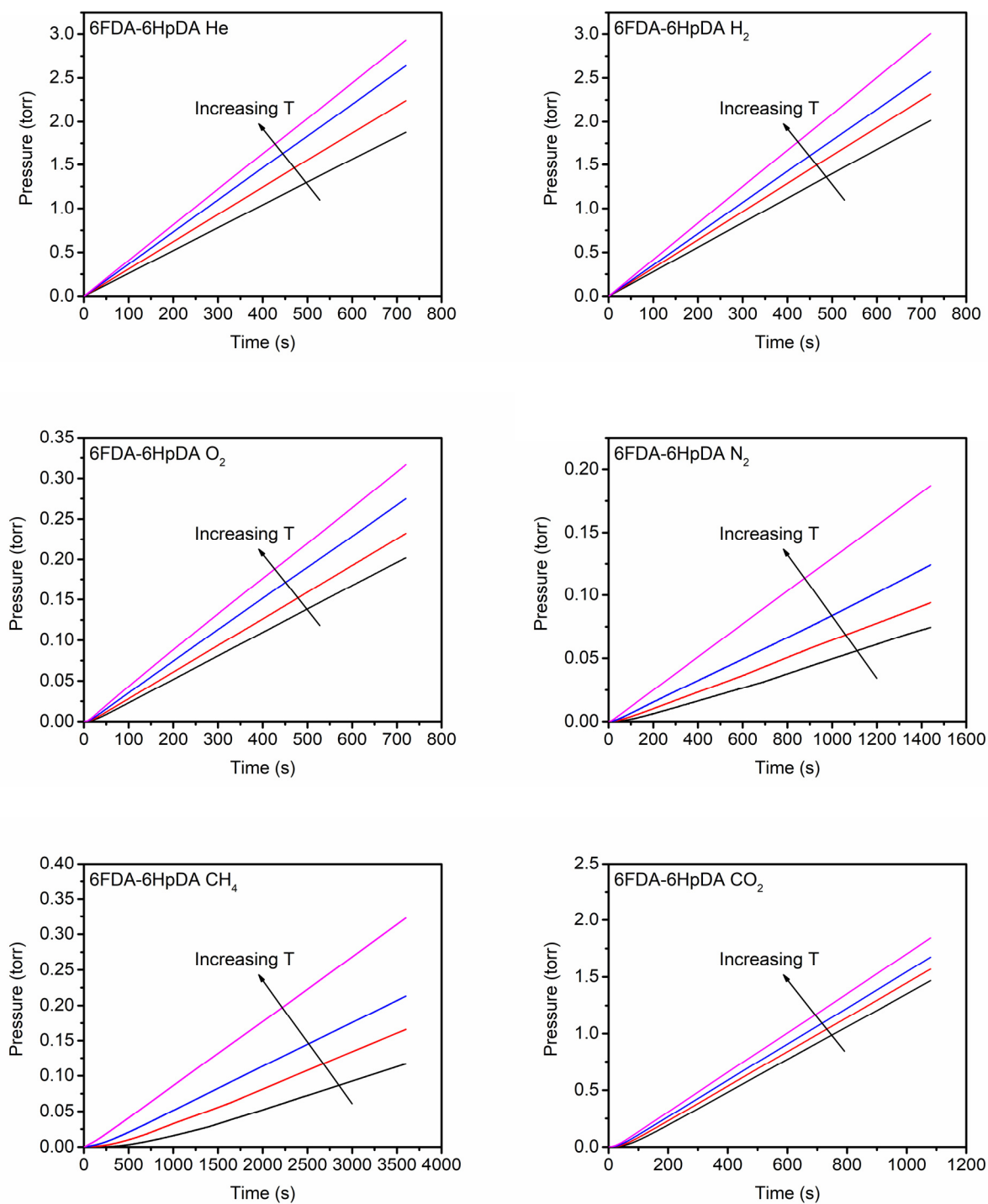


Figure B.6. Normalized pressure versus time plots for 6FDA-6HpDA obtained from permeation experiments. The black, red, blue, and magenta lines are for 35, 45, 55, and 65 °C, respectively.

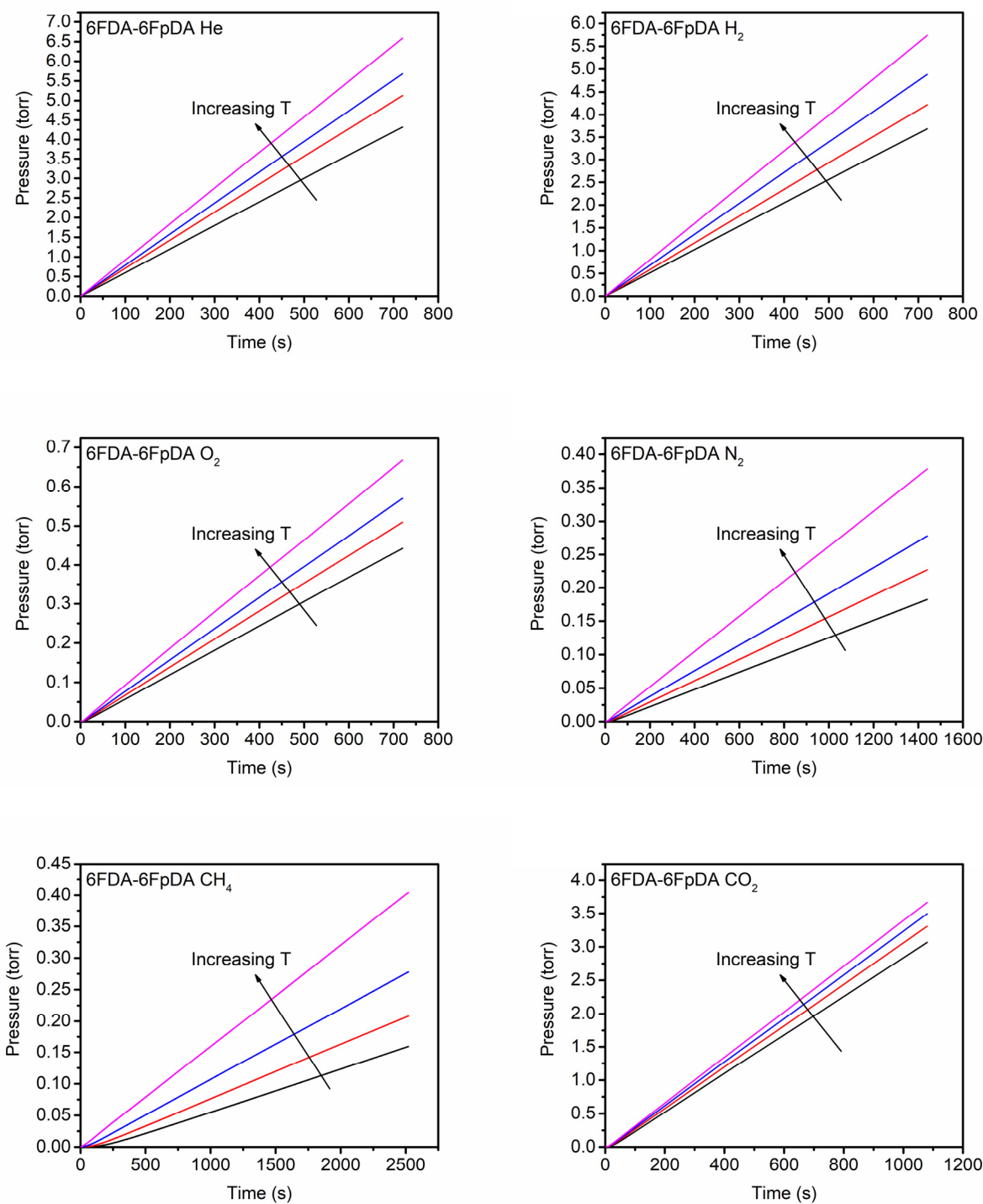


Figure B.7. Normalized pressure versus time plots for 6FDA-6FpDA obtained from permeation experiments. The black, red, blue, and magenta lines are for 35, 45, 55, and 65 °C, respectively.

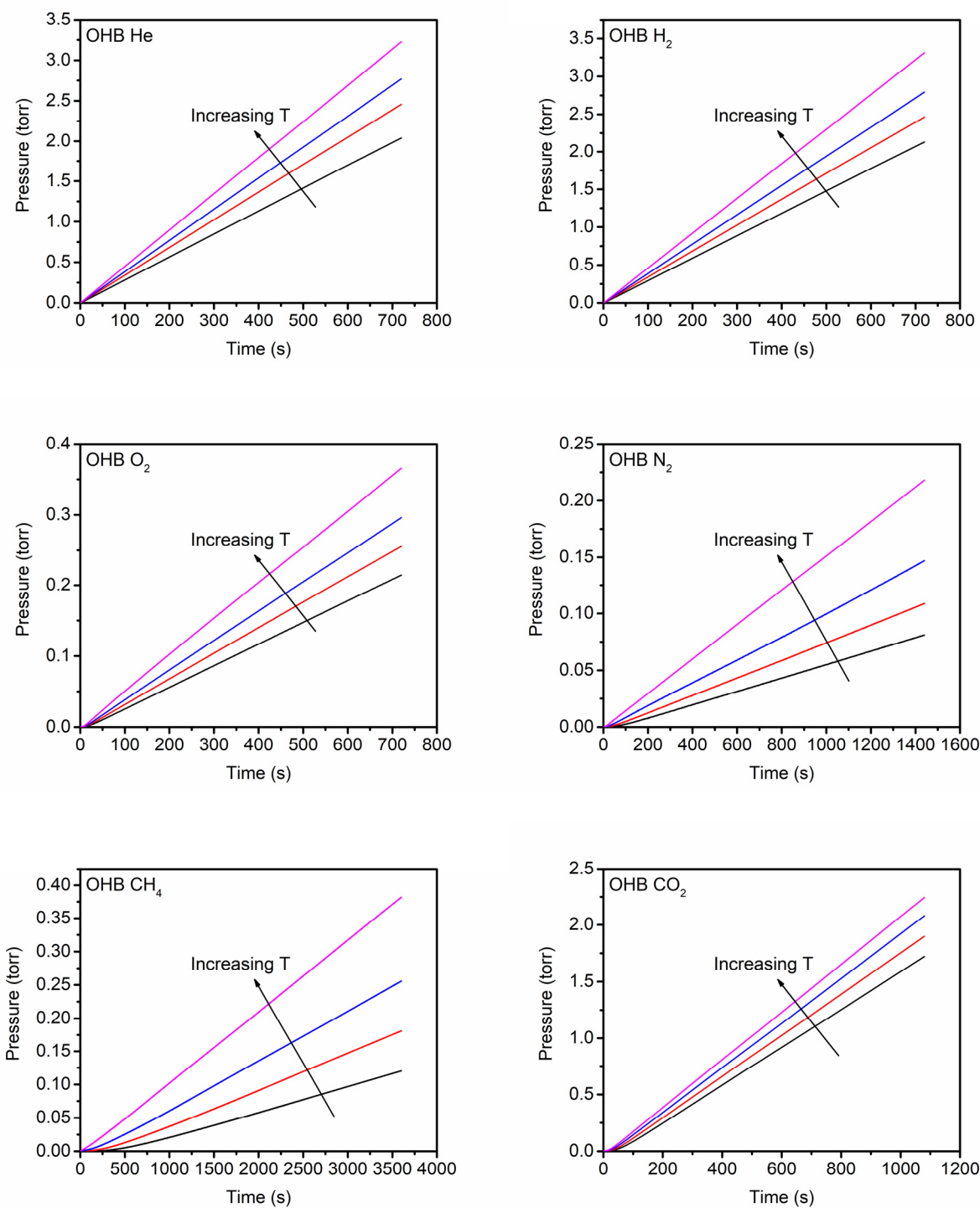


Figure B.8. Normalized pressure versus time plots for 6FDA-OHB obtained from permeation experiments. The black, red, blue, and magenta lines are for 35, 45, 55, and 65 °C, respectively.

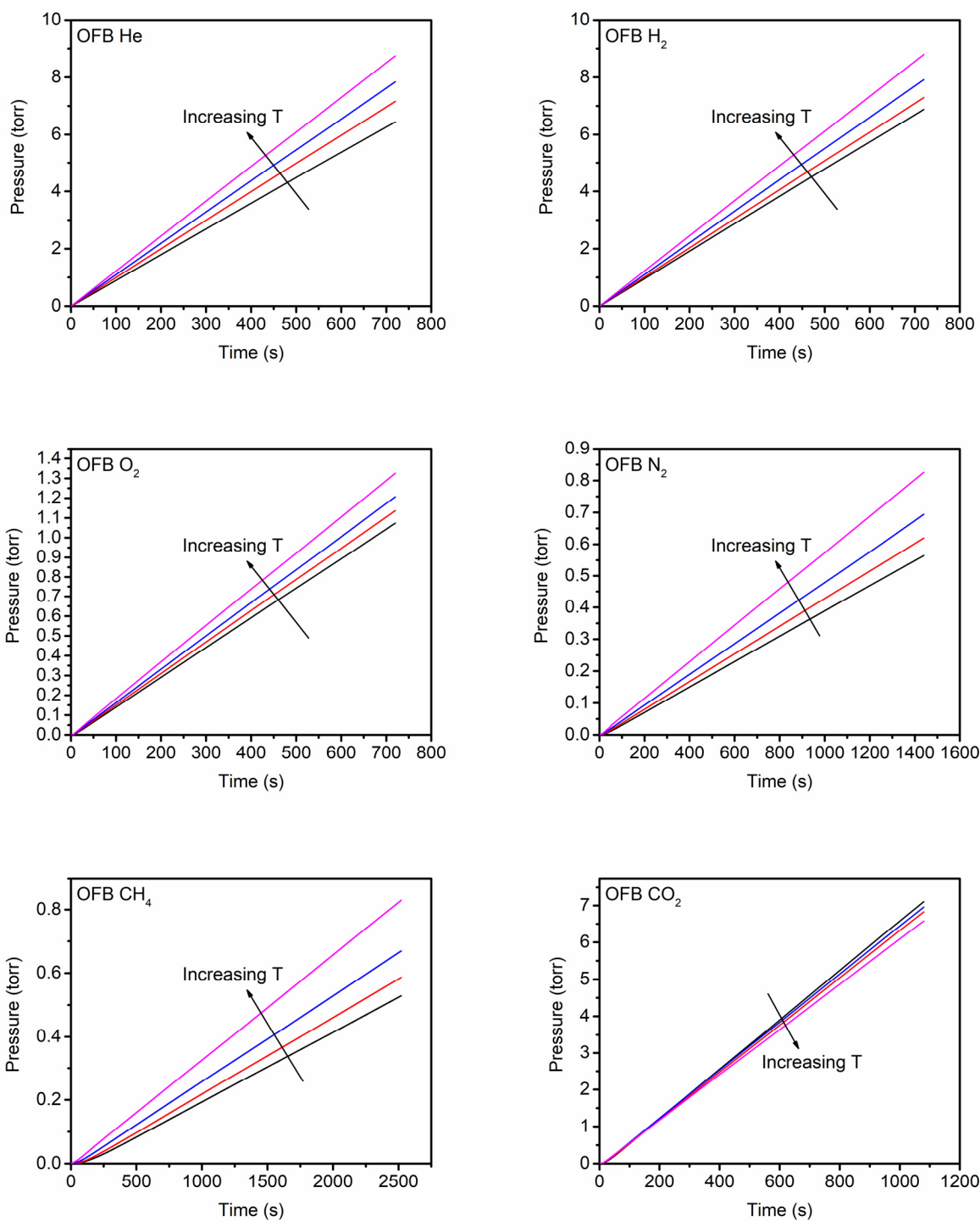


Figure B.9. Normalized pressure versus time plots for 6FDA-OFB obtained from permeation experiments. The black, red, blue, and magenta lines are for 35, 45, 55, and 65 °C, respectively.

Appendix C: Supplementary Information for Chapter 6

This chapter has been adapted from the Supplementary Information of: Wu, A. X.; Drayton, J. A.; Mizrahi Rodriguez, K.; Benedetti, F. M.; Qian, Q.; Lin, S.; Smith, Z. P. Elucidating the Role of Fluorine Content on Gas Sorption Properties of Fluorinated Polyimides. *Macromolecules* **2021**, *54* (1), 22–34.

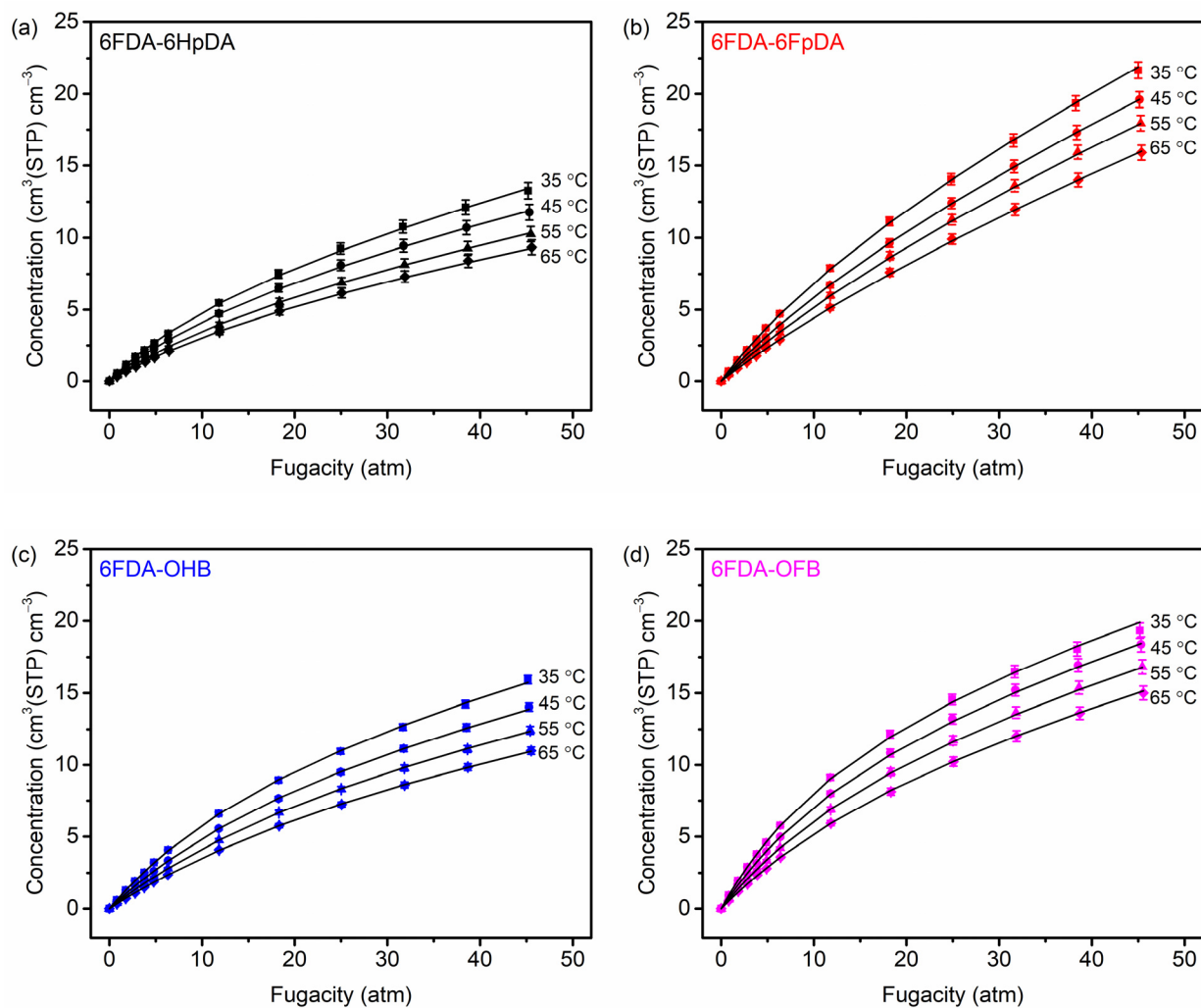


Figure C.1. N₂ isotherms for (a) 6FDA-6HpDA, (b) 6FDA-6FpDA, (c) 6FDA-OHB, and (d) 6FDA-OFB at 35 °C (squares), 45 °C (circles), 55 °C (triangles), and 65 °C (diamonds). Individual points indicate experimental data and lines indicate the dual-mode model fits.

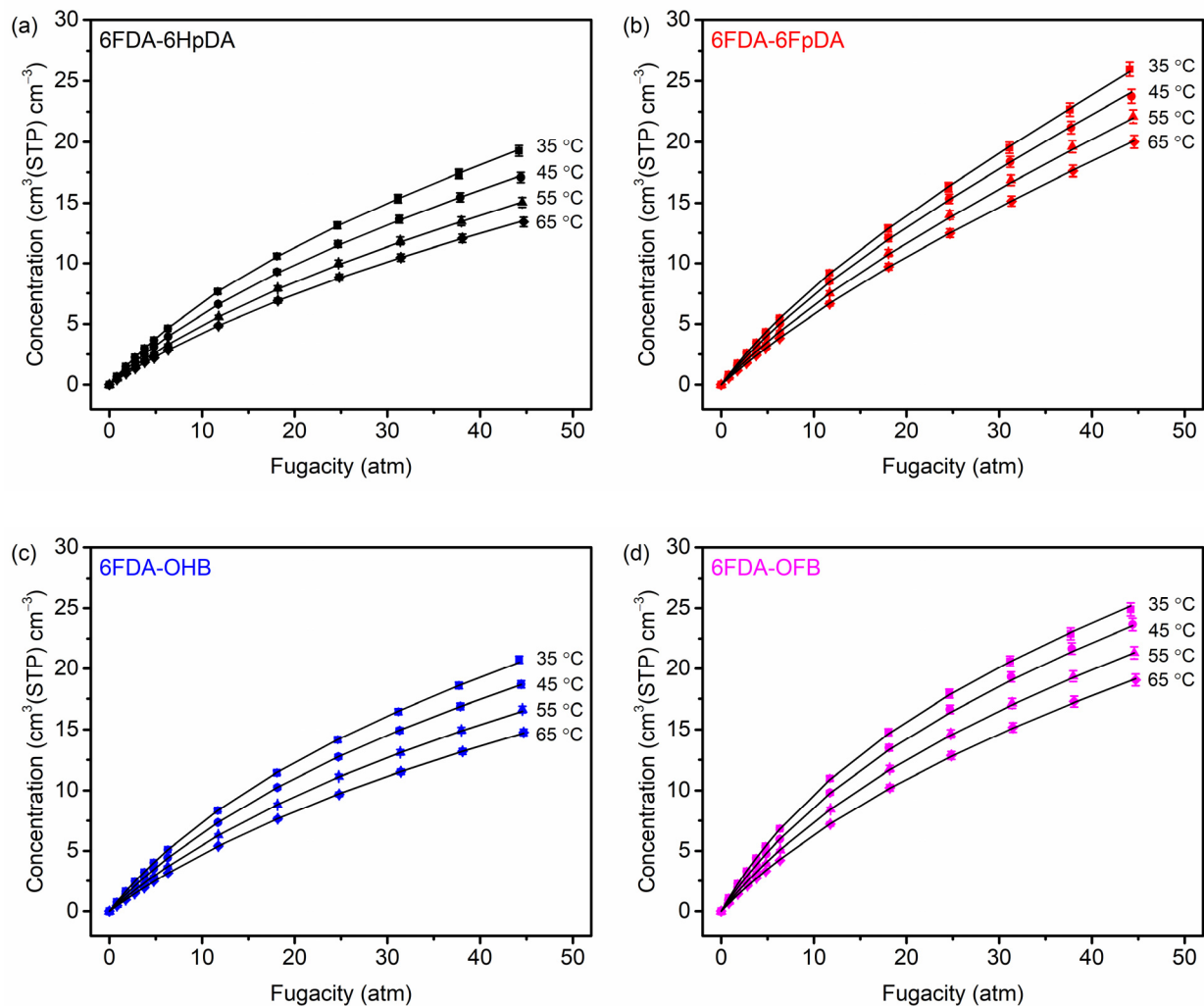


Figure C.2. O₂ isotherms for (a) 6FDA-6HpDA, (b) 6FDA-6FpDA, (c) 6FDA-OHB, and (d) 6FDA-OFB at 35 °C (squares), 45 °C (circles), 55 °C (triangles), and 65 °C (diamonds). Individual points indicate experimental data and lines indicate the dual-mode model fits.

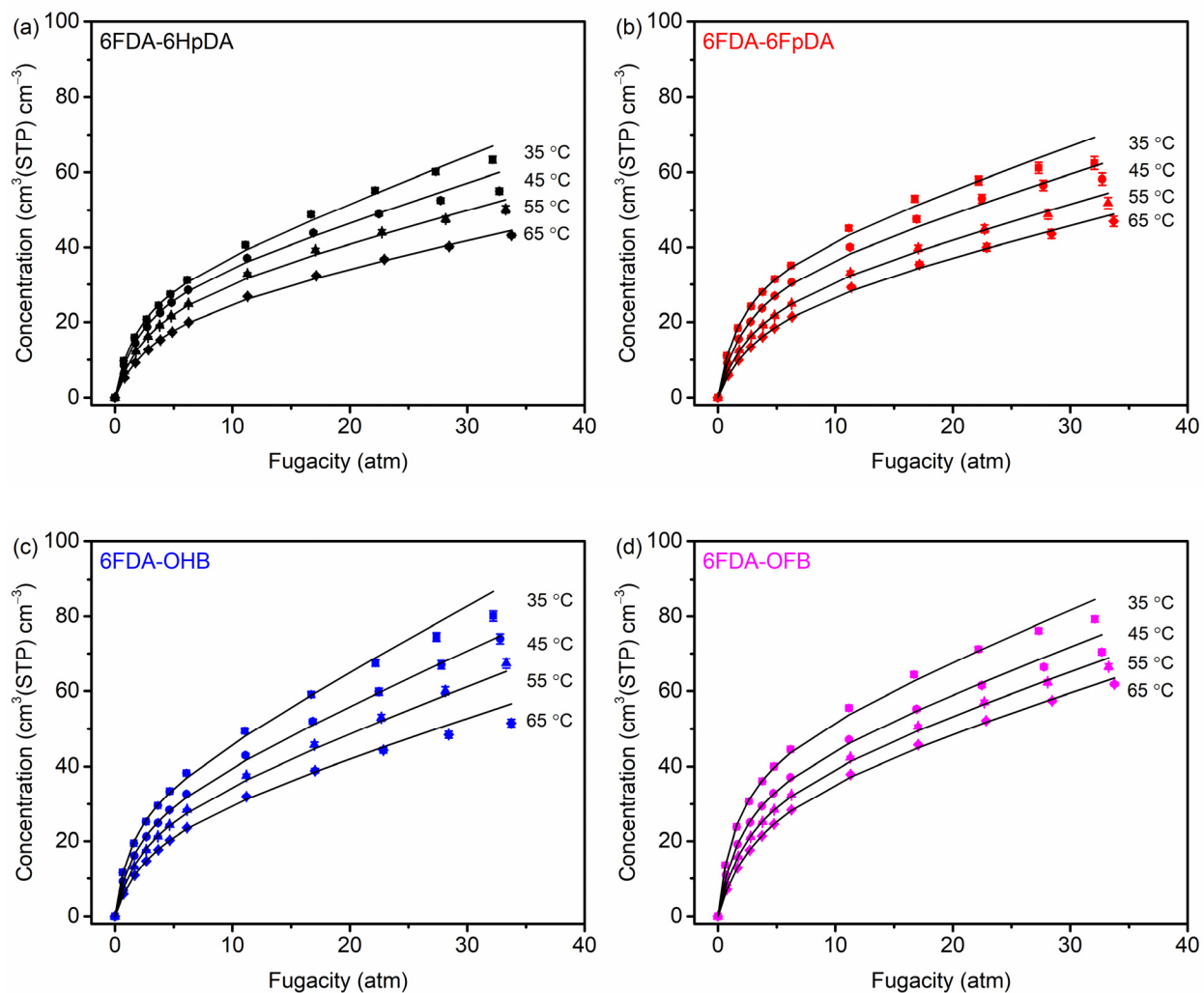


Figure C.3. CO₂ isotherms for (a) 6FDA-6HpDA, (b) 6FDA-6FpDA, (c) 6FDA-OHB, and (d) 6FDA-OFB at 35 °C (squares), 45 °C (circles), 55 °C (triangles), and 65 °C (diamonds). Individual points indicate experimental data and lines indicate the dual-mode model fits.

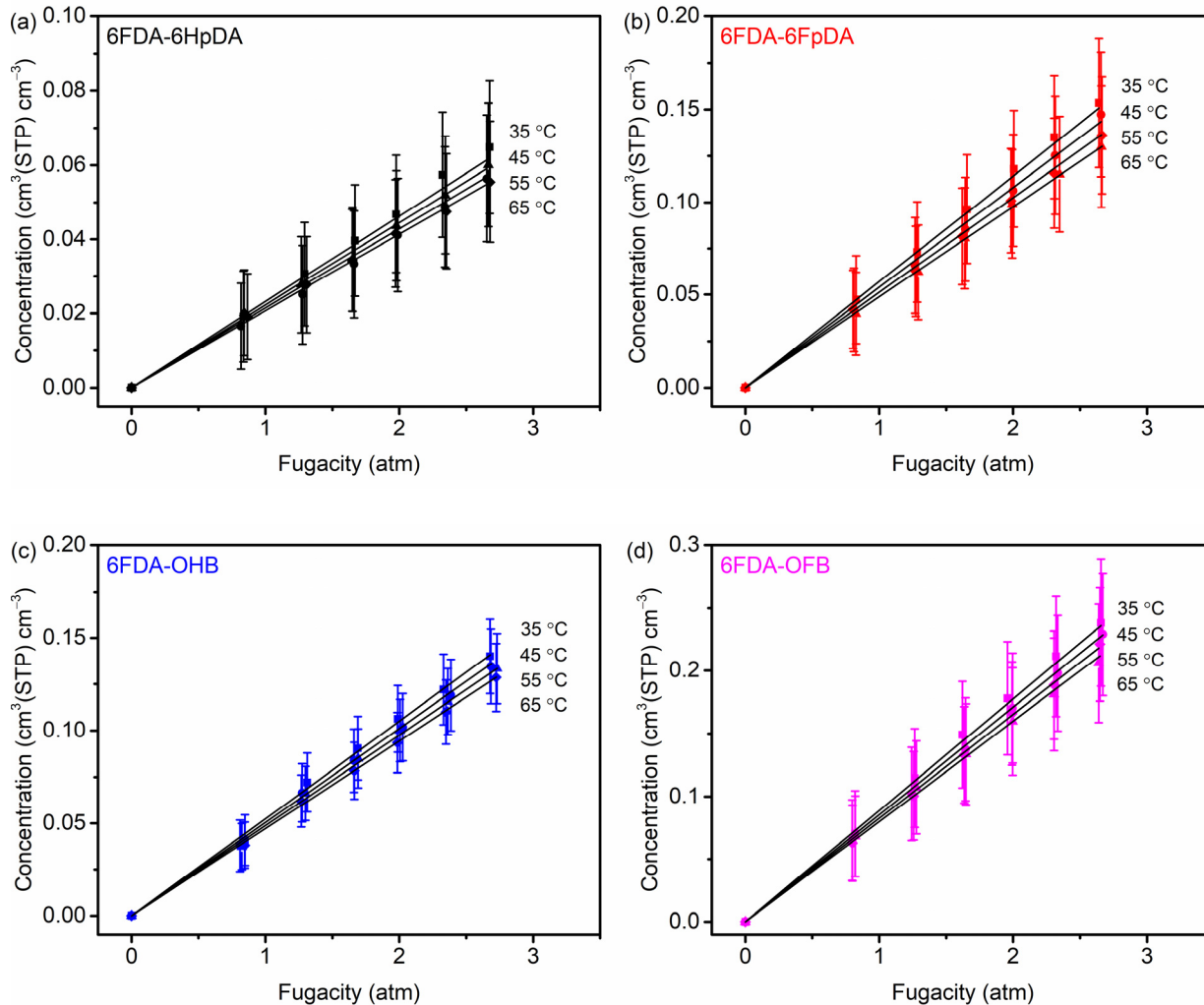


Figure C.4. He isotherms for (a) 6FDA-6HpDA, (b) 6FDA-6FpDA, (c) 6FDA-OHB, (d) 6FDA-OFB at 35 °C (squares), 45 °C (circles), 55 °C (triangles), and 65 °C (diamonds). Individual points indicate experimental data and lines indicate the constrained linear fits.

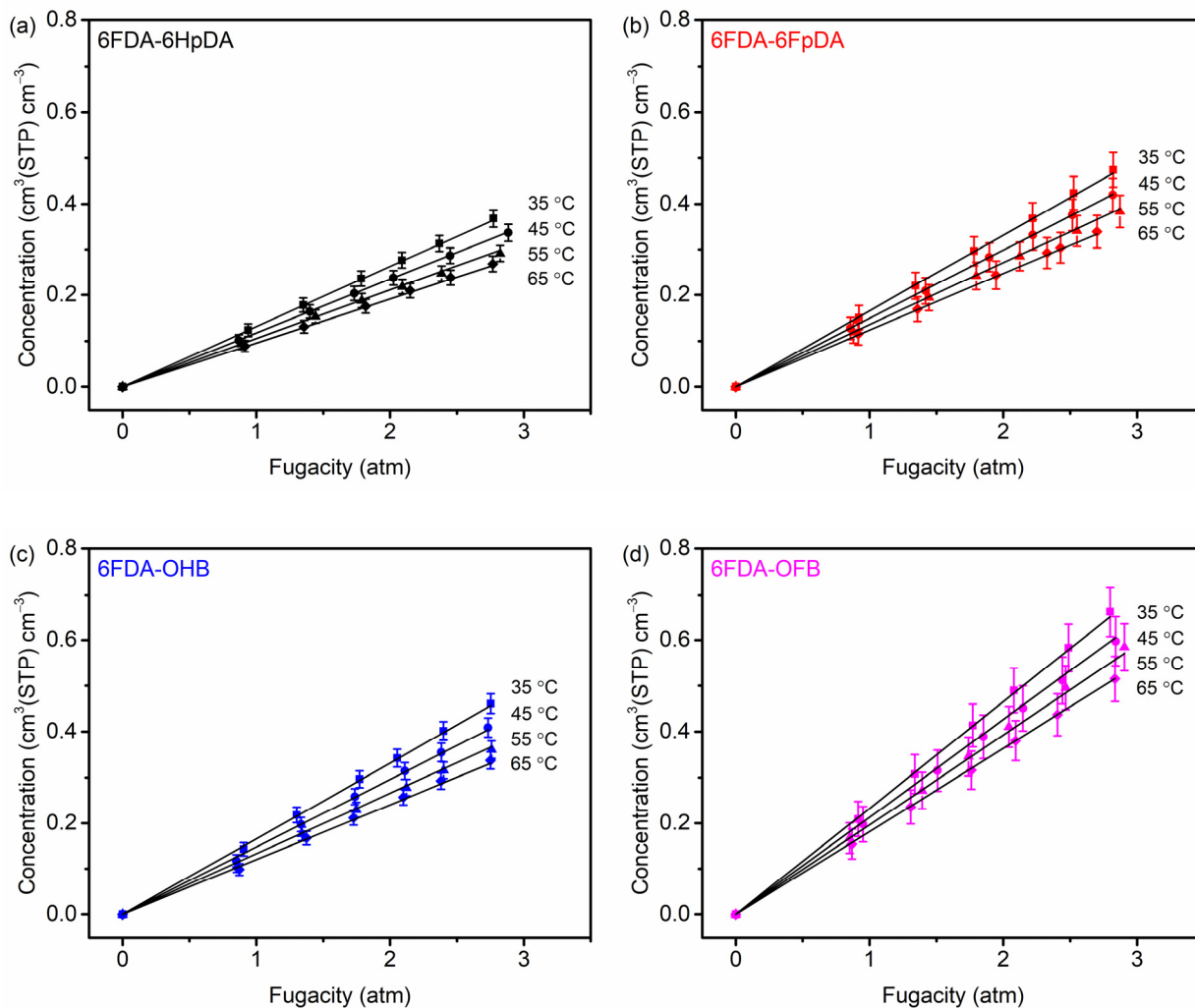


Figure C.5. H₂ isotherms for (a) 6FDA-6HpDA, (b) 6FDA-6FpDA, (c) 6FDA-OHB, (d) 6FDA-OFB at 35 °C (squares), 45 °C (circles), 55 °C (triangles), and 65 °C (diamonds). Individual points indicate experimental data and lines indicate the constrained linear fits.

Table C.1. Summary of nonlinear optimization parameters and their upper and lower bound constraints. It should be noted that C'_H for 35 °C, 45 °C, 55 °C, and 65 °C are each independent parameters, only constrained by relative order of magnitude. An upper bound of 80 for C'_H values was chosen after internal refinement.

Parameter	Constraint [Lower bound, Upper bound]	Initial guess range [Lower bound, upper bound]
$k_{D,0}$ ($\text{cm}^3(\text{STP}) \text{cm}^{-3} \text{atm}^{-1}$)	[0, ∞]	[0.1,1]
ΔH_D (kJ mol^{-1})	[-50,0]	[-10, -20]
b_0 (atm^{-1})	[0, ∞]	[0.001,0.1]
ΔH_b (kJ mol^{-1})	[-50,0]	[-10, -20]
C'_H ($\text{cm}^3(\text{STP}) \text{cm}^{-3}$)	[0,80]	[0,50]

Table C.2. LFER parameters for the four polyimides. See Equations 6.10 and 6.11 for the corresponding units.

6FDA-6HpDA	He	H ₂	N ₂	O ₂	CH ₄	CO ₂
α_D	2.676	2.663	2.592 ± 0.002	2.576 ± 0.001	2.6323±0.0004	2.6406 ± 0.0002
β_D	10.219	5.766	4.98 ± 0.02	3.96 ± 0.01	3.430 ± 0.002	0.0501 ± 0.0008
α_b	-	-	2.632 ± 0.003	2.609 ± 0.002	2.6346±0.0004	2.6734 ± 0.0001
β_b	-	-	7.84 ± 0.03	8.26 ± 0.01	5.486 ± 0.003	2.467 ± 0.001
6FDA-6FpDA	He	H ₂	N ₂	O ₂	CH ₄	CO ₂
α_D	2.678	2.665	2.677 ± 0.004	2.739 ± 0.002	2.5907±0.0008	2.6488 ± 0.0004
β_D	7.875	5.130	3.63 ± 0.02	3.01 ± 0.01	1.692 ± 0.004	0.150 ± 0.001
α_b	-	-	2.65 ± 0.02	2.58 ± 0.01	2.565 ± 0.002	2.6410 ± 0.0002
β_b	-	-	8.79 ± 0.2	7.7 ± 0.1	4.71 ± 0.02	2.373 ± 0.001
6FDA-OHB	He	H ₂	N ₂	O ₂	CH ₄	CO ₂
α_D	2.681	2.666	2.575 ± 0.002	2.564 ± 0.002	2.6272±0.0003	2.6439 ± 0.0005
β_D	8.040	5.169	5.49 ± 0.01	4.45 ± 0.01	2.984 ± 0.002	-0.897 ± 0.003
α_b	-	-	2.570 ± 0.002	2.560 ± 0.002	2.6292±0.0004	2.6469 ± 0.0008
β_b	-	-	8.27 ± 0.02	8.27 ± 0.02	5.112 ± 0.004	1.716 ± 0.007
6FDA-OFB	He	H ₂	N ₂	O ₂	CH ₄	CO ₂
α_D	2.684	2.670	2.539 ± 0.001	2.543 ± 0.001	2.5978±0.0004	2.6454 ± 0.0003
β_D	6.644	4.192	4.747 ± 0.009	3.886 ± 0.008	3.360 ± 0.003	-0.402 ± 0.002
α_b	-	-	2.529 ± 0.002	2.527 ± 0.002	2.5950±0.0006	2.6436 ± 0.0004
β_b	-	-	7.13 ± 0.02	7.47 ± 0.02	5.295 ± 0.005	1.982 ± 0.004

Table C.3. Best-fit parameters for the four polyimides. ΔH_{S_∞} , ΔH_D , and ΔH_b are in units of kJ mol⁻¹ and all C'_H values are in units of cm³(STP) cm⁻³. ΔH_{S_∞} values for He and H₂ were obtained via constrained linear optimization. ΔH_{S_∞} values for the other four gases were obtained using the calculated S_∞ values in Tables C.4–C.7 below.

6FDA-6HpDA	He	H ₂	N ₂	O ₂	CH ₄	CO ₂
ΔH_{S_∞}	-3 ± 4	-9 ± 1	-16.3 ± 0.2	-16.0 ± 0.2	-20.2 ± 0.2	-23.9 ± 0.9
ΔH_D	-	-	-11.9 ± 0.6	-10.8 ± 0.3	-11.2 ± 0.2	-16.91 ± 0.03
ΔH_b	-	-	-11.3 ± 0.5	-11.0 ± 0.2	-16.8 ± 0.2	-18.48 ± 0.05
$C'_{H,35^\circ\text{C}}$	-	-	8.9 ± 0.1	14.5 ± 0.1	15.59 ± 0.07	30.25 ± 0.05
$C'_{H,45^\circ\text{C}}$	-	-	8.4 ± 0.1	13.6 ± 0.2	15.03 ± 0.08	30.25 ± 0.05
$C'_{H,55^\circ\text{C}}$	-	-	7.6 ± 0.2	12.2 ± 0.2	13.99 ± 0.09	28.49 ± 0.08
$C'_{H,65^\circ\text{C}}$	-	-	7.2 ± 0.2	11.5 ± 0.2	13.26 ± 0.09	24.40 ± 0.05
6FDA-6FpDA	He	H ₂	N ₂	O ₂	CH ₄	CO ₂
ΔH_{S_∞}	-5 ± 4	-8 ± 2	-15.7 ± 0.2	-12.2 ± 0.3	-19.2 ± 0.2	-25.6 ± 0.3
ΔH_D	-	-	-7.6 ± 0.8	-6 ± 1	-5.6 ± 0.6	-10.1 ± 0.1
ΔH_b	-	-	-16.6 ± 0.2	-11 ± 1	-14.3 ± 0.5	-16.2 ± 0.1
$C'_{H,35^\circ\text{C}}$	-	-	12.9 ± 0.6	12.0 ± 0.6	14.8 ± 0.3	37.0 ± 0.2
$C'_{H,45^\circ\text{C}}$	-	-	12.1 ± 0.7	12.0 ± 0.6	13.7 ± 0.3	33.6 ± 0.2
$C'_{H,55^\circ\text{C}}$	-	-	11.9 ± 0.8	11.0 ± 0.7	12.3 ± 0.3	28.8 ± 0.2
$C'_{H,65^\circ\text{C}}$	-	-	10.9 ± 0.9	10.1 ± 0.8	10.8 ± 0.3	25.8 ± 0.2

6FDA-OHB	He	H ₂	N ₂	O ₂	CH ₄	CO ₂
$\Delta H_{S_{\infty}}$	-3 ± 2	-9 ± 1	-17.5 ± 0.1	-16.1 ± 0.2	-21.6 ± 0.1	-26.8 ± 0.1
ΔH_D	-	-	-12.3 ± 0.7	-12.5 ± 0.7	-13.1 ± 0.3	-16.43 ± 0.09
ΔH_b	-	-	-15.1 ± 0.5	-14.5 ± 0.4	-19.4 ± 0.2	-21.2 ± 0.2
$C'_{H,35\text{ }^{\circ}\text{C}}$	-	-	15.8 ± 0.2	16.6 ± 0.3	16.7 ± 0.1	32.9 ± 0.2
$C'_{H,45\text{ }^{\circ}\text{C}}$	-	-	15.0 ± 0.3	16.6 ± 0.3	16.1 ± 0.1	30.5 ± 0.2
$C'_{H,55\text{ }^{\circ}\text{C}}$	-	-	14.5 ± 0.3	15.8 ± 0.3	15.5 ± 0.1	28.5 ± 0.2
$C'_{H,65\text{ }^{\circ}\text{C}}$	-	-	13.9 ± 0.3	15.1 ± 0.4	14.8 ± 0.1	26.0 ± 0.2
6FDA-OFB	He	H ₂	N ₂	O ₂	CH ₄	CO ₂
$\Delta H_{S_{\infty}}$	-3 ± 2	-7 ± 1	-16.6 ± 0.2	-15.8 ± 0.3	-21.1 ± 0.7	-27.9 ± 0.4
ΔH_D	-	-	-3.0 ± 0.2	-4.6 ± 0.1	-0.17 ± 0.02	-8.98 ± 0.01
ΔH_b	-	-	-12.3 ± 0.2	-12.5 ± 0.2	-11.71 ± 0.08	-21.59 ± 0.03
$C'_{H,35\text{ }^{\circ}\text{C}}$	-	-	18.1 ± 0.2	23.0 ± 0.2	24.44 ± 0.08	44.94 ± 0.03
$C'_{H,45\text{ }^{\circ}\text{C}}$	-	-	17.2 ± 0.1	22.4 ± 0.2	22.28 ± 0.07	39.43 ± 0.06
$C'_{H,55\text{ }^{\circ}\text{C}}$	-	-	15.8 ± 0.2	20.6 ± 0.2	19.84 ± 0.08	36.65 ± 0.06
$C'_{H,65\text{ }^{\circ}\text{C}}$	-	-	14.2 ± 0.1	18.7 ± 0.2	16.0 ± 0.1	34.49 ± 0.05

Table C.4. Calculated best-fit dual mode model parameters for 6FDA-6HpDA. k_D values are in units of $\text{cm}^3(\text{STP}) \text{cm}^{-3} \text{atm}^{-1}$, b values are in units of atm^{-1} , and S_∞ values are in units of $\text{cm}^3(\text{STP}) \text{cm}^{-3} \text{atm}^{-1}$.

35 °C	He	H ₂	N ₂	O ₂	CH ₄	CO ₂
k_D	-	-	0.154 ± 0.001	0.220 ± 0.001	0.3054 ± 0.0008	1.1943 ± 0.0008
b	-	-	0.0572 ± 0.0008	0.0456 ± 0.0003	0.1494 ± 0.0004	0.5368 ± 0.0006
S_∞	0.023 ± 0.001	0.131 ± 0.002	0.67 ± 0.01	0.883 ± 0.008	2.63 ± 0.01	17.43 ± 0.03
45 °C	He	H ₂	N ₂	O ₂	CH ₄	CO ₂
k_D	-	-	0.133 ± 0.001	0.193 ± 0.001	0.2661 ± 0.0003	0.9706 ± 0.0006
b	-	-	0.0498 ± 0.0006	0.0399 ± 0.0003	0.1215 ± 0.0002	0.4279 ± 0.0003
S_∞	0.0223 ± 0.0003	0.1174 ± 0.0004	0.552 ± 0.009	0.735 ± 0.007	2.09 ± 0.01	13.91 ± 0.03
55 °C	He	H ₂	N ₂	O ₂	CH ₄	CO ₂
k_D	-	-	0.116 ± 0.002	0.174 ± 0.001	0.2339 ± 0.0008	0.7988 ± 0.0005
b	-	-	0.0437 ± 0.0006	0.0351 ± 0.0003	0.1001 ± 0.0003	0.3459 ± 0.0003
S_∞	0.0214 ± 0.0006	0.106 ± 0.001	0.448 ± 0.008	0.600 ± 0.006	1.63 ± 0.01	10.65 ± 0.03
65 °C	He	H ₂	N ₂	O ₂	CH ₄	CO ₂
k_D	-	-	0.102 ± 0.002	0.151 ± 0.002	0.207 ± 0.001	0.665 ± 0.0006
b	-	-	0.0386 ± 0.0007	0.0312 ± 0.0003	0.0834 ± 0.0004	0.2831 ± 0.0003
S_∞	0.021 ± 0.001	0.096 ± 0.002	0.381 ± 0.008	0.51 ± 0.006	1.313 ± 0.01	7.57 ± 0.02

Table C.5. Calculated best-fit dual mode model parameters for 6FDA-6FpDA. k_D values are in units of $\text{cm}^3(\text{STP}) \text{cm}^{-3} \text{atm}^{-1}$, b values are in units of atm^{-1} , and S_∞ values are in units of $\text{cm}^3(\text{STP}) \text{cm}^{-3} \text{atm}^{-1}$.

35 °C	He	H ₂	N ₂	O ₂	CH ₄	CO ₂
k_D	-	-	0.293 ± 0.005	0.39 ± 0.01	0.533 ± 0.002	1.075 ± 0.002
b	-	-	0.044 ± 0.005	0.053 ± 0.003	0.161 ± 0.001	0.4919 ± 0.0007
S_∞	0.057 ± 0.004	0.166 ± 0.004	0.86 ± 0.07	1.03 ± 0.04	2.91 ± 0.05	19.3 ± 0.1
45 °C	He	H ₂	N ₂	O ₂	CH ₄	CO ₂
k_D	-	-	0.267 ± 0.003	0.362 ± 0.006	0.498 ± 0.002	0.9499 ± 0.0008
b	-	-	0.036 ± 0.004	0.046 ± 0.002	0.135 ± 0.001	0.4034 ± 0.0003
S_∞	0.054 ± 0.001	0.1494 ± 0.0007	0.70 ± 0.05	0.91 ± 0.04	2.34 ± 0.04	14.51 ± 0.09
55 °C	He	H ₂	N ₂	O ₂	CH ₄	CO ₂
k_D	-	-	0.244 ± 0.003	0.336 ± 0.002	0.467 ± 0.005	0.846 ± 0.001
b	-	-	0.030 ± 0.003	0.040 ± 0.002	0.114 ± 0.002	0.3349 ± 0.0005
S_∞	0.051 ± 0.001	0.136 ± 0.002	0.60 ± 0.05	0.78 ± 0.04	1.87 ± 0.04	10.49 ± 0.08
65 °C	He	H ₂	N ₂	O ₂	CH ₄	CO ₂
k_D	-	-	0.225 ± 0.004	0.314 ± 0.004	0.439 ± 0.008	0.758 ± 0.002
b	-	-	0.025 ± 0.003	0.036 ± 0.002	0.098 ± 0.002	0.2812 ± 0.0007
S_∞	0.049 ± 0.004	0.124 ± 0.004	0.50 ± 0.04	0.67 ± 0.04	1.50 ± 0.04	8.01 ± 0.07

Table C.6. Calculated best-fit dual mode model parameters for 6FDA-OHB. k_D values are in units of $\text{cm}^3(\text{STP}) \text{cm}^{-3} \text{atm}^{-1}$, b values are in units of atm^{-1} , and S_∞ values are in units of $\text{cm}^3(\text{STP}) \text{cm}^{-3} \text{atm}^{-1}$.

35 °C	He	H ₂	N ₂	O ₂	CH ₄	CO ₂
k_D	-	-	0.1216 ± 0.0009	0.224 ± 0.001	0.365 ± 0.001	1.713 ± 0.003
b	-	-	0.0408 ± 0.0004	0.0449 ± 0.0005	0.1737 ± 0.0005	0.682 ± 0.003
S_∞	0.053 ± 0.002	0.166 ± 0.003	0.77 ± 0.01	0.97 ± 0.01	3.27 ± 0.02	24.2 ± 0.2
45 °C	He	H ₂	N ₂	O ₂	CH ₄	CO ₂
k_D	-	-	0.105 ± 0.001	0.192 ± 0.002	0.3106 ± 0.0004	1.400 ± 0.002
b	-	-	0.0339 ± 0.0004	0.0375 ± 0.0004	0.1369 ± 0.0003	0.526 ± 0.002
S_∞	0.0506 ± 0.0006	0.148 ± 0.002	0.62 ± 0.01	0.81 ± 0.01	2.52 ± 0.01	17.3 ± 0.1
55 °C	He	H ₂	N ₂	O ₂	CH ₄	CO ₂
k_D	-	-	0.092 ± 0.001	0.167 ± 0.002	0.267 ± 0.001	1.159 ± 0.002
b	-	-	0.0285 ± 0.0004	0.0317 ± 0.0004	0.1094 ± 0.0004	0.412 ± 0.002
S_∞	0.0488 ± 0.0008	0.133 ± 0.002	0.51 ± 0.01	0.67 ± 0.01	1.97 ± 0.01	12.9 ± 0.1
65 °C	He	H ₂	N ₂	O ₂	CH ₄	CO ₂
k_D	-	-	0.080 ± 0.002	0.145 ± 0.003	0.232 ± 0.002	0.970 ± 0.003
b	-	-	0.0243 ± 0.0005	0.0271 ± 0.0004	0.0887 ± 0.0005	0.328 ± 0.002
S_∞	0.047 ± 0.002	0.120 ± 0.003	0.42 ± 0.01	0.56 ± 0.01	1.55 ± 0.01	9.50 ± 0.09

Table C.7. Calculated best-fit dual mode model parameters for 6FDA-OFB. k_D values are in units of $\text{cm}^3(\text{STP}) \text{cm}^{-3} \text{atm}^{-1}$, b values are in units of atm^{-1} , and S_∞ values are in units of $\text{cm}^3(\text{STP}) \text{cm}^{-3} \text{atm}^{-1}$.

35 °C	He	H ₂	N ₂	O ₂	CH ₄	CO ₂
k_D	-	-	0.1526 ± 0.0006	0.2141 ± 0.0008	0.2743 ± 0.0003	1.3001 ± 0.0009
b	-	-	0.0561 ± 0.0005	0.0488 ± 0.0005	0.1379 ± 0.0003	0.613 ± 0.001
S_∞	0.089 ± 0.004	0.233 ± 0.005	1.17 ± 0.02	1.34 ± 0.01	3.63 ± 0.01	28.85 ± 0.05
45 °C	He	H ₂	N ₂	O ₂	CH ₄	CO ₂
k_D	-	-	0.1470 ± 0.0007	0.2024 ± 0.0008	0.2743 ± 0.0003	1.1646 ± 0.0008
b	-	-	0.0482 ± 0.0005	0.0419 ± 0.0004	0.1191 ± 0.0003	0.4704 ± 0.0009
S_∞	0.086 ± 0.001	0.213 ± 0.001	0.97 ± 0.01	1.14 ± 0.01	2.92 ± 0.01	19.72 ± 0.04
55 °C	He	H ₂	N ₂	O ₂	CH ₄	CO ₂
k_D	-	-	0.1419 ± 0.0008	0.192 ± 0.001	0.2743 ± 0.0003	1.0501 ± 0.0008
b	-	-	0.0418 ± 0.0005	0.0363 ± 0.0004	0.1039 ± 0.0003	0.3668 ± 0.0007
S_∞	0.083 ± 0.001	0.196 ± 0.002	0.80 ± 0.01	0.94 ± 0.01	2.33 ± 0.01	14.49 ± 0.03
65 °C	He	H ₂	N ₂	O ₂	CH ₄	CO ₂
k_D	-	-	0.137 ± 0.001	0.183 ± 0.001	0.2743 ± 0.0003	0.9528 ± 0.0007
b	-	-	0.0366 ± 0.0005	0.0317 ± 0.0004	0.0913 ± 0.0003	0.2903 ± 0.0006
S_∞	0.080 ± 0.003	0.182 ± 0.005	0.657 ± 0.009	0.777 ± 0.009	1.73 ± 0.01	10.96 ± 0.02

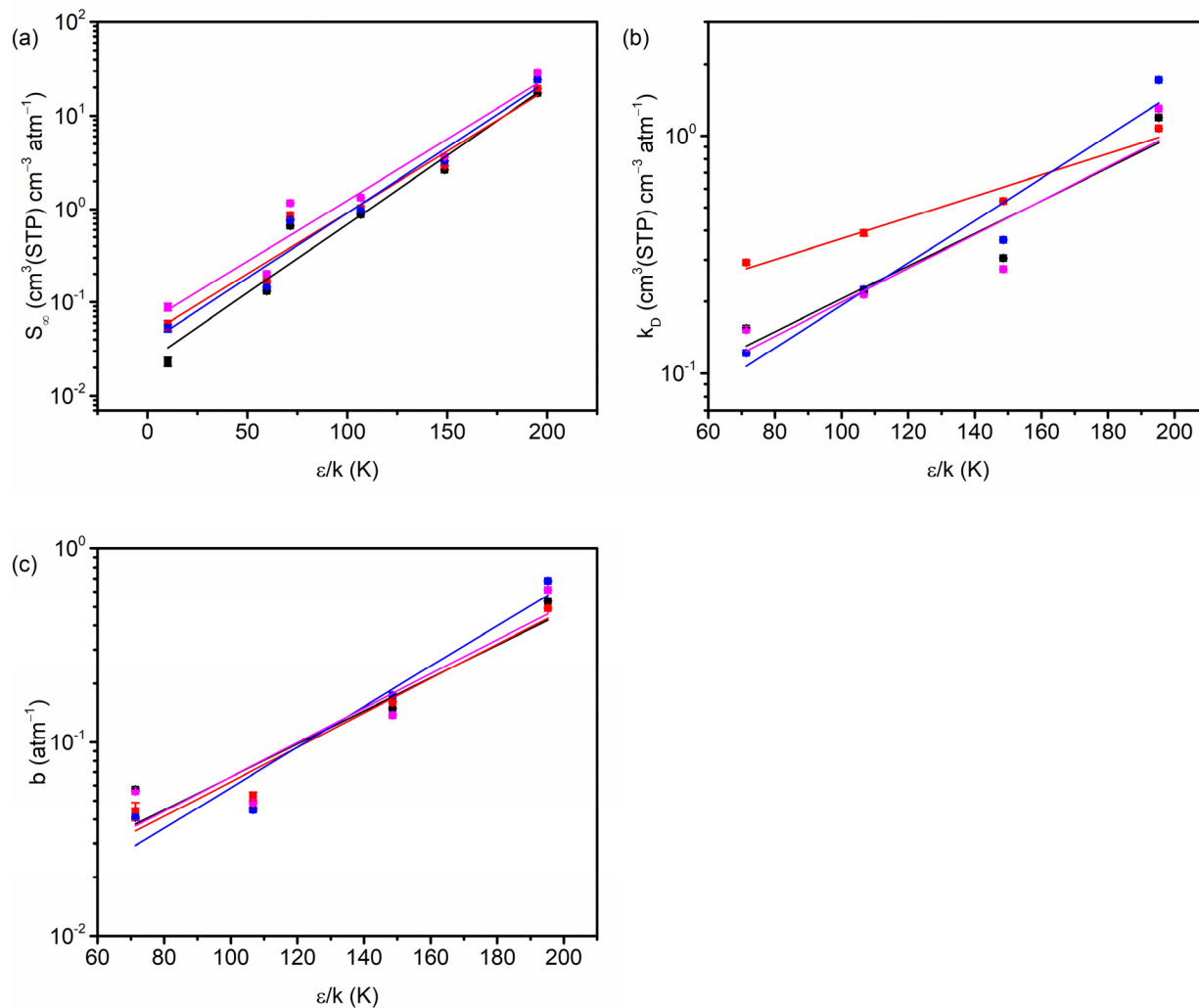


Figure C.6. S_∞ , k_D , and b for each polymer with respect to ϵ/k . The black, red, blue, and pink points represent 6FDA-6HpDA, 6FDA-6FpDA, 6FDA-OHB, and 6FDA-OFB, respectively.

Table C.8. Slopes and intercepts for trends with respect to ε/k (see Equations 6.13–6.15). k_D values are in units of $\text{cm}^3(\text{STP}) \text{cm}^{-3} \text{atm}^{-1}$, b values are in units of atm^{-1} , and S_∞ values are in units of $\text{cm}^3(\text{STP}) \text{cm}^{-3} \text{atm}^{-1}$.

	S_∞		k_D		b	
	$A \times 10^2$	B	$C \times 10^2$	D	$E \times 10^2$	F
6FDA-6HpDA	3.4 ± 0.2	-3.8 ± 0.2	1.6 ± 0.1	-3.2 ± 0.1	2.0 ± 0.2	-4.7 ± 0.3
6FDA-6FpDA	3.0 ± 0.1	-3.1 ± 0.2	1.0 ± 0.1	-2.0 ± 0.1	2.0 ± 0.1	-4.8 ± 0.2
6FDA-OHB	3.3 ± 0.1	-3.3 ± 0.2	2.1 ± 0.1	-3.7 ± 0.1	2.4 ± 0.2	-5.2 ± 0.3
6FDA-OFB	3.0 ± 0.1	-2.8 ± 0.2	1.6 ± 0.1	-3.3 ± 0.1	2.0 ± 0.3	-4.7 ± 0.3

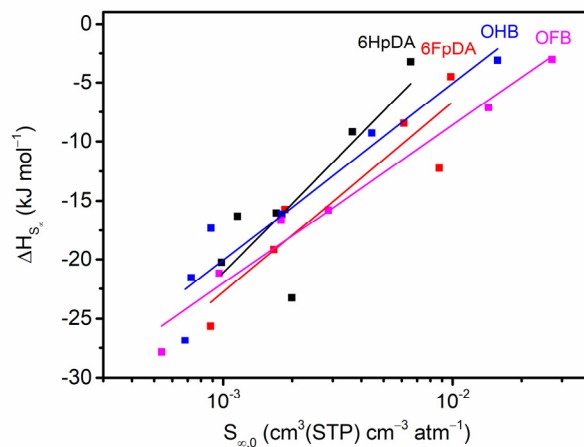


Figure C.7. Experimentally derived LFER for S_∞ for the four polymers. Each data point represents a specific gas–polymer pair.

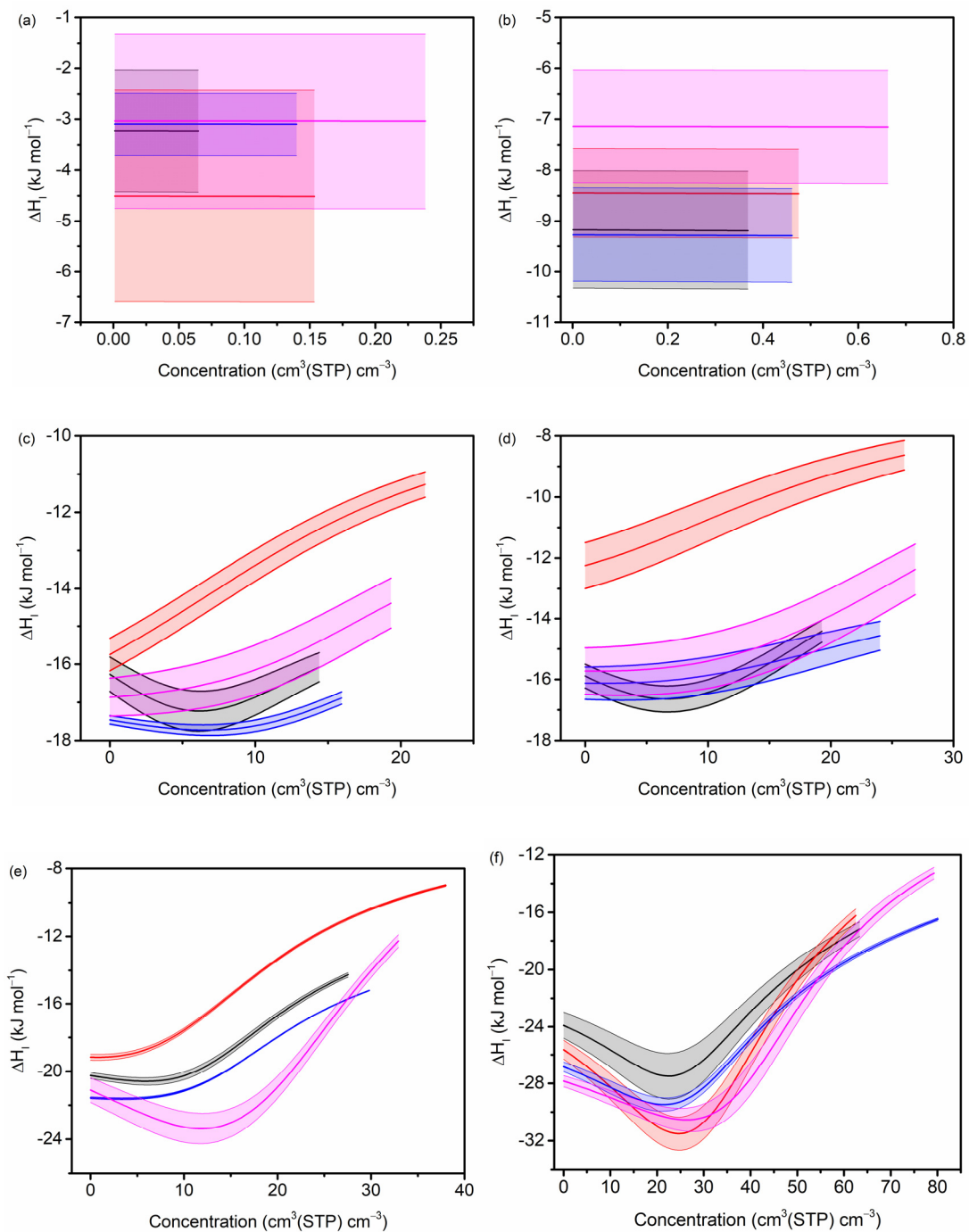


Figure C.8. Isosteric heat of sorption for (a) He, (b) H₂, (c) N₂, (d) O₂, (e) CH₄, and (f) CO₂. The black, red, blue, and pink data sets represent 6FDA-6HpDA, 6FDA-6FpDA, 6FDA-OHB, and 6FDA-OFB, respectively. The shaded areas represent the error in the calculated isosteric heat of sorption for each gas–polymer pair.

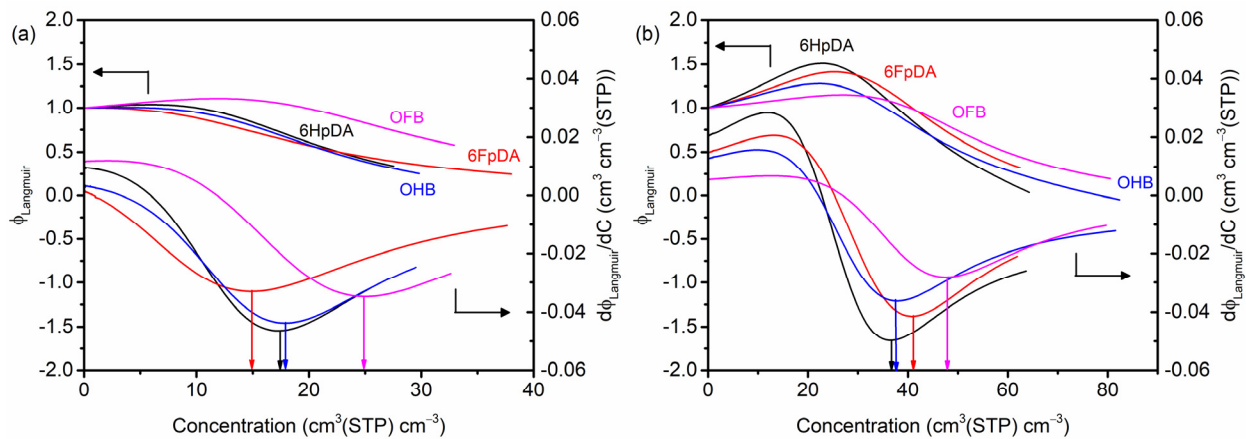


Figure C.9. The $\phi_{Langmuir}$ curves and their derivatives estimated from the calculated isosteric heat of sorption values for (a) CH₄ and (b) CO₂ for all polymers considered. Downward arrows indicate minima.

Appendix D: Supplementary Information for Chapter 7

This chapter has been adapted from the Supplementary Information of: Wu, A. X.; Drayton, J. A.; Ren, X.; Mizrahi Rodriguez, K.; Grosz, A. F.; Lee, J. -W.; Smith, Z. P. Non-Equilibrium Lattice Fluid Modeling of Gas Sorption for Fluorinated Poly(Ether Imide)s. *Submitted*.

Table D.1. LFPs for gases and polymers.

Gases	T^* (K)	p^* (MPa)	ρ^* (g cm ⁻³)	Ref.
N ₂	145	160	0.943	1
O ₂	170	280	1.29	1
CH ₄	215	250	0.5	1
CO ₂	300	630	1.515	1
Polymers	T^* (K)	p^* (MPa)	ρ^* (g cm ⁻³)	Ref.
Poly(PFMD)	640 ± 3.62	300 ± 28	2.184 ± 0.006	2
Poly(PFMMD)	616 ± 18	250 ± 23	2.200 ± 0.010	2
Teflon AF 2400	624	250	2.13	3
Teflon AF 1600	575	280	2.16	3
Hyflon AD 80	550	180	2.150	4
6FDA-ODA	804.2	526.8	1.658	5
6FDA-6FpDA	750.1	476.5	1.806	5
6FDA-HAB	720 ± 41	481 ± 20	1.609 ± 0.039	6
TR450-30min	930.0 ± 23	446.9 ± 7.3	1.528 ± 0.037	6

Table D.2. GPC of poly(amic acid)s.

Polymer	M_n (g mol ⁻¹)	M_w (g mol ⁻¹)	Degree of Polym.
10HEDA-MPD	3,900	4,800	8
10HEDA-TFMPD	5,500	6,500	10
10FEDA-MPD	3,500	4,500	5
10FEDA-TFMPD	5,300	6,200	7

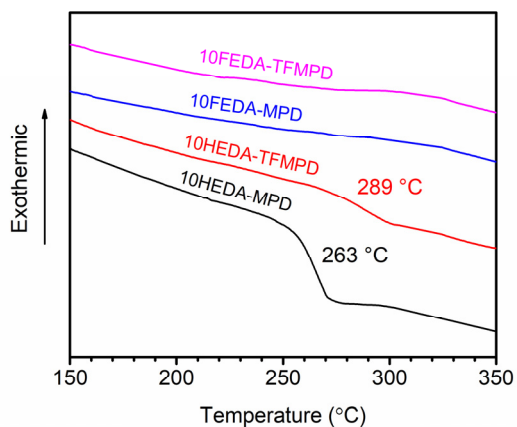


Figure D.1. DSC traces for the four polymers with a 100 °C/min ramp rate. The third trace is shown here. Traces are offset for ease of viewing.

Table D.3. S_{∞} values for 10HEDA-MPD in $\text{cm}^3(\text{STP}) \text{cm}^{-3} \text{atm}^{-1}$.

	O ₂	N ₂	CH ₄	CO ₂
35 °C	0.130 ± 0.007	0.22 ± 0.01	0.73 ± 0.04	7.9 ± 0.2
45 °C	0.111 ± 0.006	0.190 ± 0.009	0.58 ± 0.03	6.3 ± 0.1
55 °C	0.096 ± 0.005	0.154 ± 0.008	0.50 ± 0.03	5.4 ± 0.1
65 °C	0.090 ± 0.005	0.146 ± 0.007	0.43 ± 0.02	3.6 ± 0.1

Table D.4. S_{∞} values for 10HEDA-TFMPD in $\text{cm}^3(\text{STP}) \text{cm}^{-3} \text{atm}^{-1}$.

	O ₂	N ₂	CH ₄	CO ₂
35 °C	0.44 ± 0.02	0.60 ± 0.03	2.4 ± 0.1	25.2 ± 0.5
45 °C	0.33 ± 0.02	0.48 ± 0.02	1.71 ± 0.09	16.2 ± 0.3
55 °C	0.25 ± 0.01	0.38 ± 0.02	1.24 ± 0.06	10.0 ± 0.2
65 °C	0.23 ± 0.01	0.30 ± 0.01	0.94 ± 0.05	7.3 ± 0.2

Table D.5. S_{∞} values for 10FEDA-MPD in $\text{cm}^3(\text{STP}) \text{cm}^{-3} \text{atm}^{-1}$.

	O ₂	N ₂	CH ₄	CO ₂
35 °C	0.89 ± 0.04	1.09 ± 0.05	3.0 ± 0.1	37.4 ± 0.7
45 °C	0.64 ± 0.03	0.87 ± 0.04	2.5 ± 0.1	24.0 ± 0.5
55 °C	0.57 ± 0.03	0.70 ± 0.04	1.9 ± 0.1	16.7 ± 0.3
65 °C	0.45 ± 0.02	0.59 ± 0.03	1.51 ± 0.08	11.9 ± 0.2

Table D.6. S_{∞} values for 10FEDA-TFMPD in $\text{cm}^3(\text{STP}) \text{cm}^{-3} \text{atm}^{-1}$.

	O ₂	N ₂	CH ₄	CO ₂
35 °C	1.06 ± 0.05	1.29 ± 0.06	3.5 ± 0.2	34.9 ± 0.7
45 °C	0.83 ± 0.04	0.99 ± 0.05	2.6 ± 0.1	24.0 ± 0.5
55 °C	0.65 ± 0.03	0.80 ± 0.04	2.1 ± 0.1	16.6 ± 0.3
65 °C	0.52 ± 0.03	0.64 ± 0.03	1.78 ± 0.09	11.3 ± 0.2

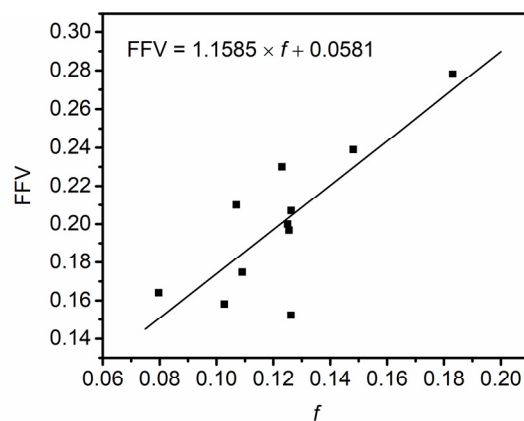


Figure D.2. FFV vs f plot. The polymers included here are Teflon AF 2400³, Teflon AF 1600³, Hyflon AD 80⁴, poly(PFMD)², poly(PFMMD)², 6FDA-HAB⁶, TR-350⁶, TR-400⁶, TR-450⁶, 6FDA-ODA⁵, and 6FDA-6FpDA⁵. FFV for these polymers was calculated using our updated group contribution theory (see Chapter 8).

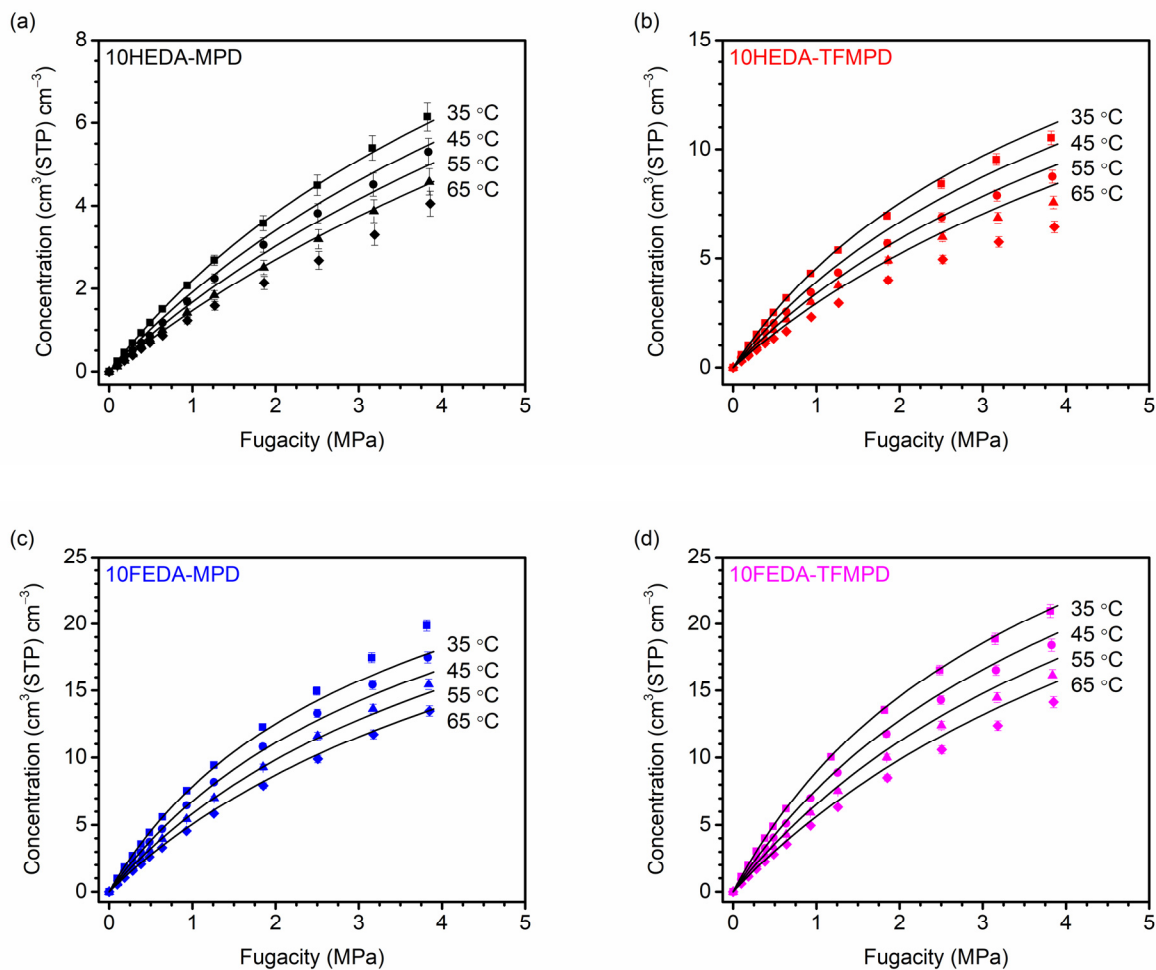


Figure D.3. Isotherms for O₂ for the four polymers at 35 °C (squares), 45 °C (circles), 55 °C (triangles), and 65 °C (diamonds).

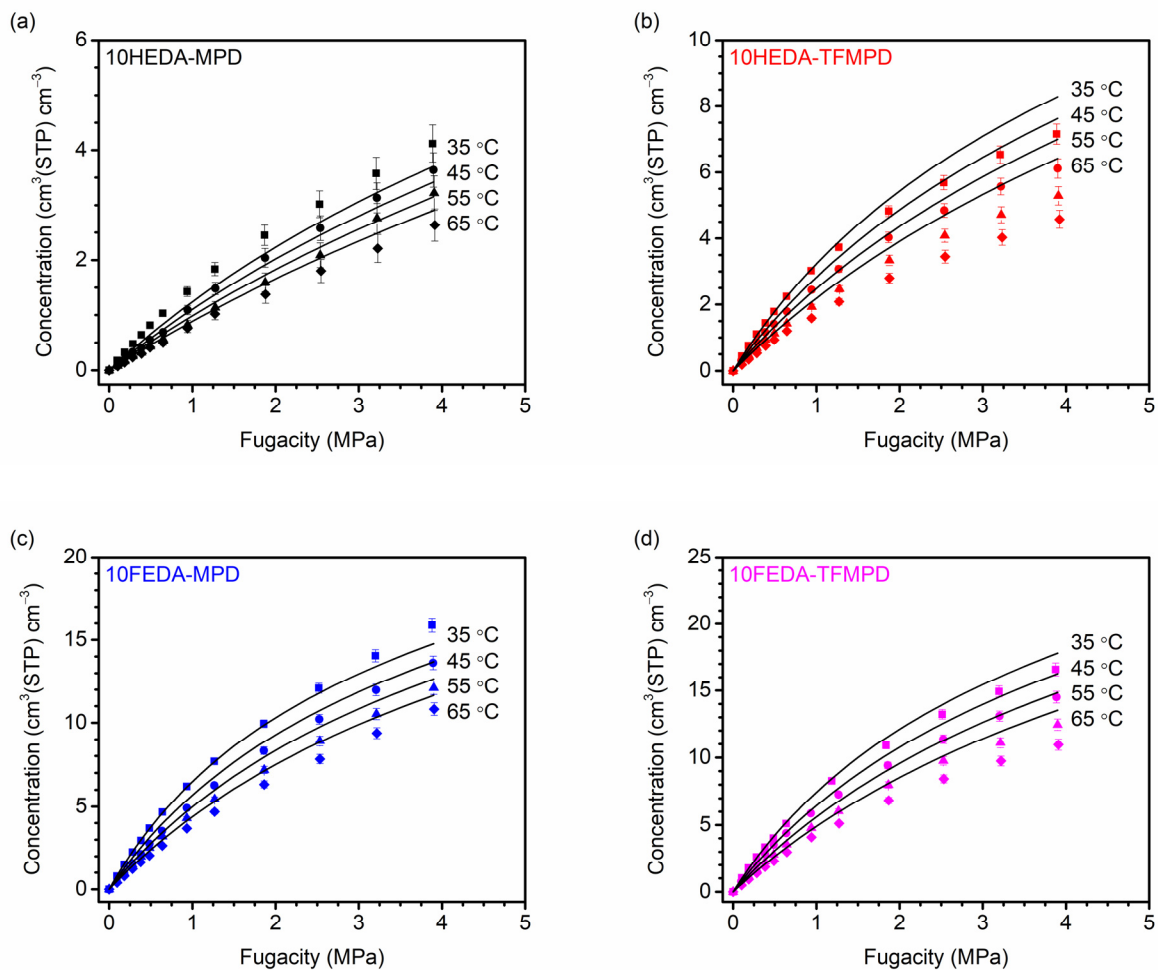


Figure D.4. Isotherms for N₂ for the four polymers at 35 °C (squares), 45 °C (circles), 55 °C (triangles), and 65 °C (diamonds).

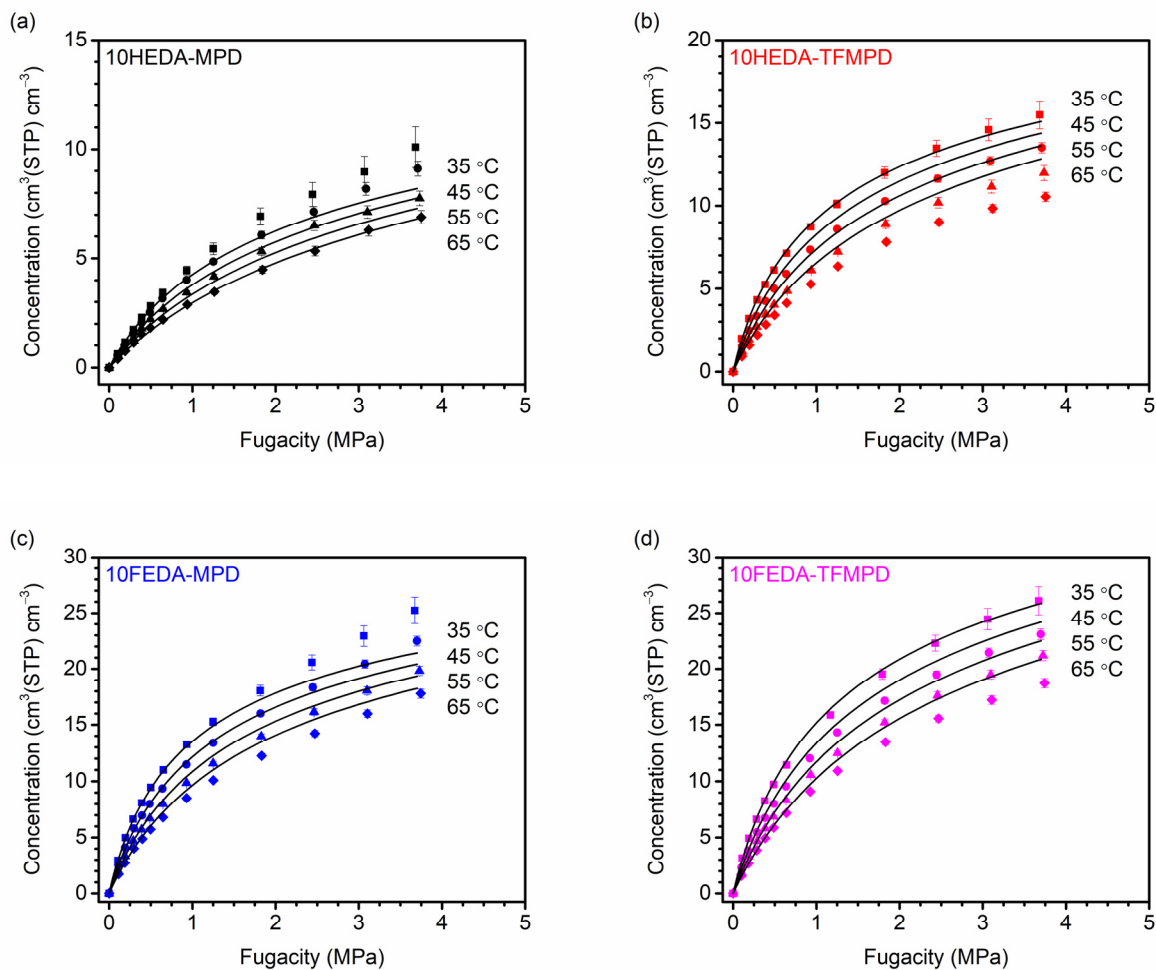


Figure D.5. Isotherms for CH₄ for the four polymers at 35 °C (squares), 45 °C (circles), 55 °C (triangles), and 65 °C (diamonds).

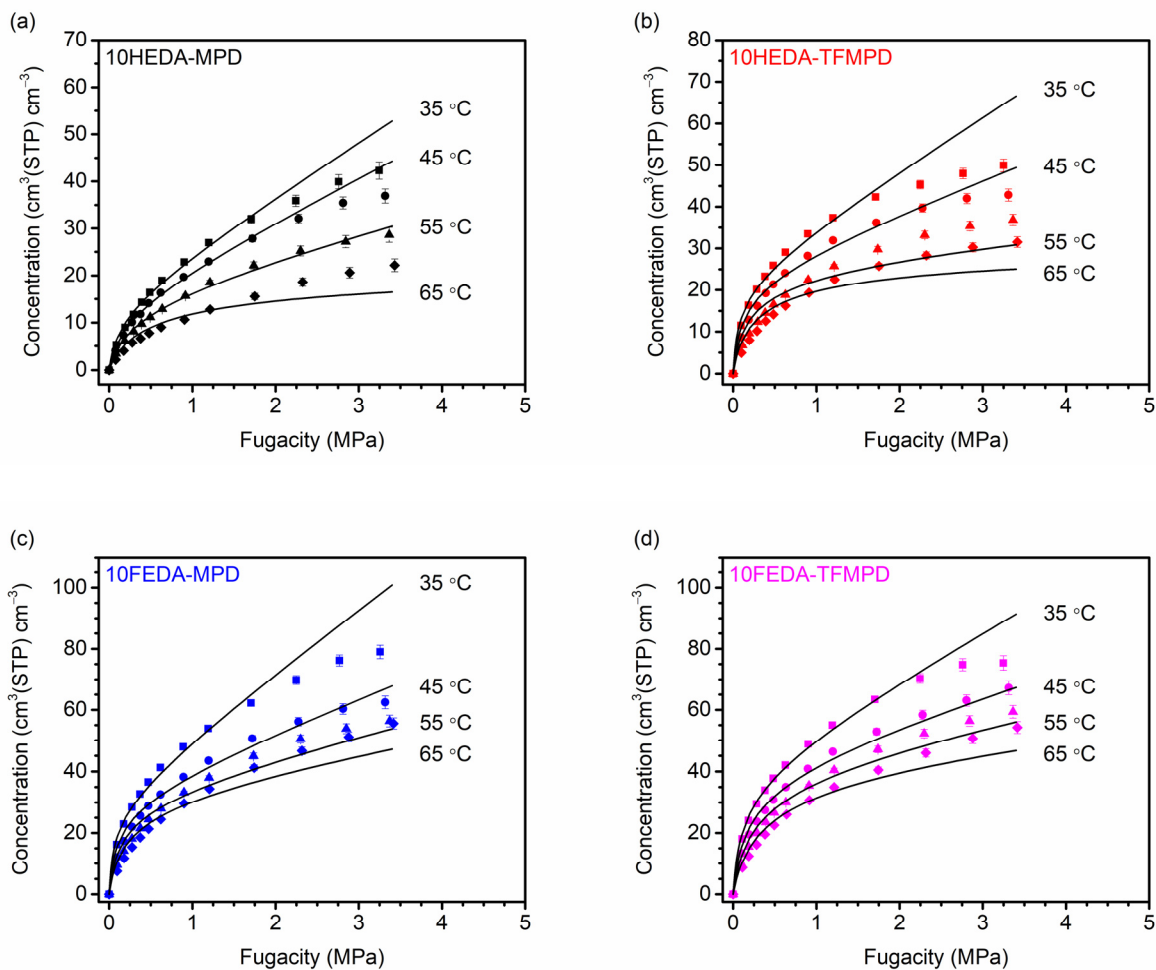


Figure D.6. Isotherms for CO₂ for the four polymers at 35 °C (squares), 45 °C (circles), 55 °C (triangles), and 65 °C (diamonds).

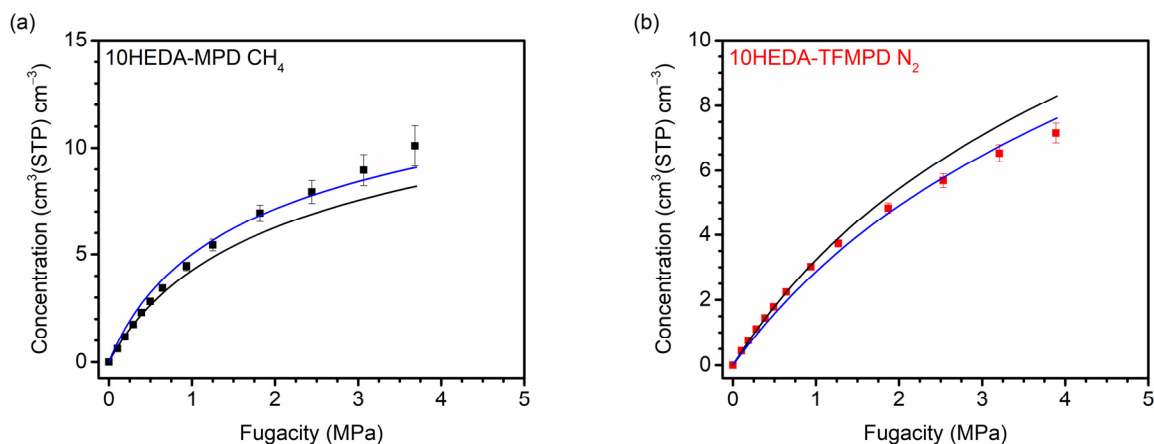


Figure D.7. Comparison of the χ^2 (black lines) and sum of squared residuals (blue lines) objective functions to fit the k_{12} parameter. (a) CH₄ in 10HEDA-MPD at 35 °C. The best-fit k_{12} changes from -0.024 to -0.052 and the fit at the low pressure region is over-predicted while the fit is improved in the high pressure region. (b) N₂ in 10HEDA-TFMPD at 35 °C. The best-fit k_{12} changes from -0.018 to 0.003 and the fit at the low pressure region is under-predicted while the fit is improved in the high pressure region.

Table D.7. Best-fit k_{12} values fit to the sorption isotherm data at 35 °C. For CO₂, this value was fit to points below 0.3 MPa.

	O ₂	N ₂	CH ₄	CO ₂
10HEDA-MPD	0.006 ± 0.004	-0.021 ± 0.006	-0.024 ± 0.003	-0.064 ± 0.003
10HEDA-TFMPD	0.016 ± 0.002	-0.018 ± 0.003	-0.023 ± 0.001	-0.078 ± 0.001
10FEDA-MPD	0.016 ± 0.002	-0.015 ± 0.002	0.016 ± 0.001	-0.076 ± 0.001
10FEDA-TFMPD	0.022 ± 0.002	-0.005 ± 0.002	0.035 ± 0.001	-0.055 ± 0.001

Table D.8. Best-fit k_{sw} values (MPa⁻¹) for CO₂ fit to the sorption data above 0.3 MPa.

	35 °C	45 °C	55 °C	65 °C
10HEDA-MPD	0.018 ± 0.005	0.014 ± 0.005	0.007 ± 0.005	0.000 ± 0.004
10HEDA-TFMPD	0.020 ± 0.005	0.012 ± 0.005	0.003 ± 0.005	0.000 ± 0.002
10FEDA-MPD	0.034 ± 0.001	0.017 ± 0.001	0.011 ± 0.001	0.008 ± 0.001
10FEDA-TFMPD	0.026 ± 0.002	0.014 ± 0.001	0.009 ± 0.002	0.005 ± 0.002

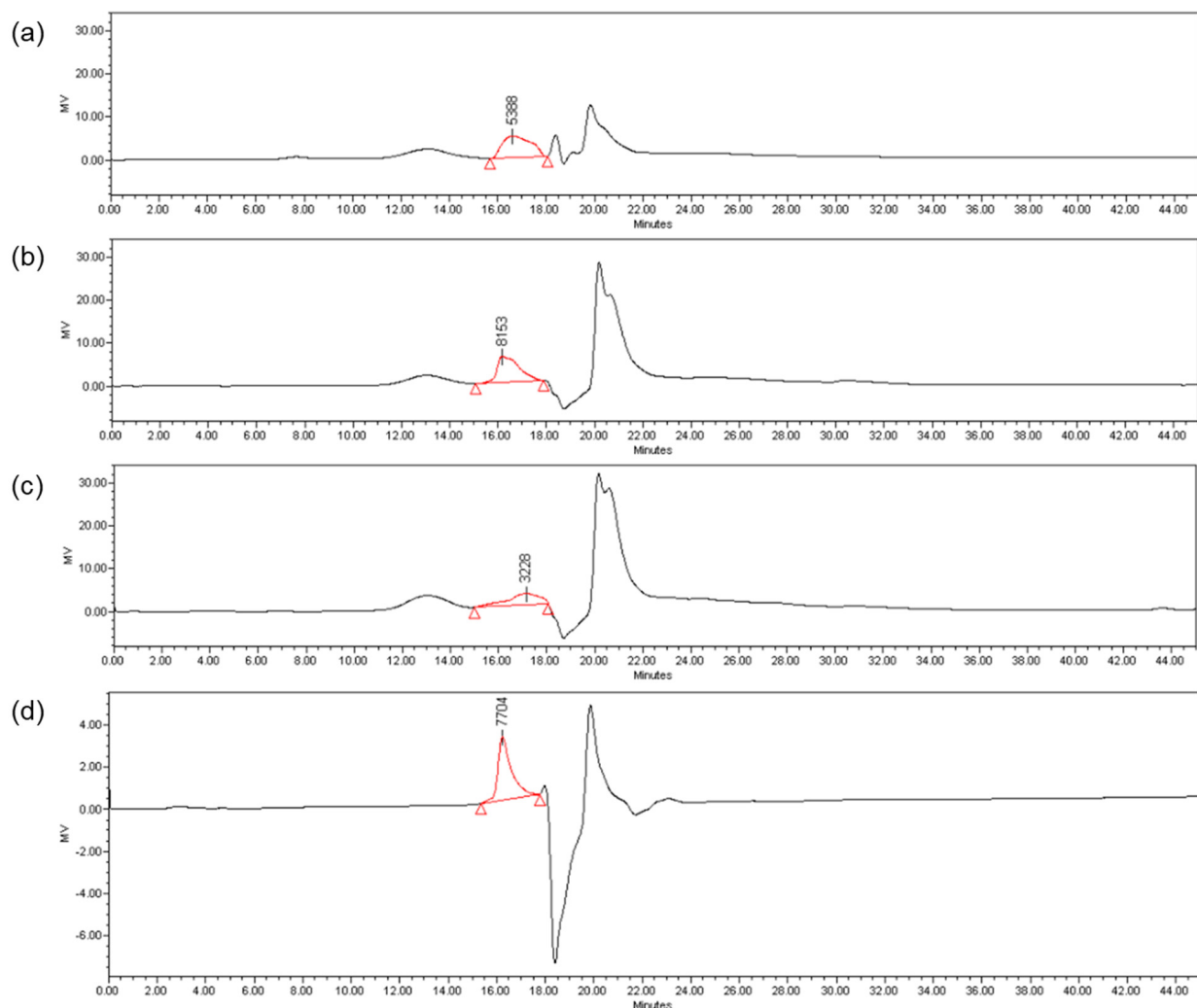


Figure D.8. GPC traces for the (a) 10HEDA-MPD, (b) 10HEDA-TFMPD, (c) 10FEDA-MPD, and (d) 10FEDA-TFMPD poly(amic acid).

References

- (1) De Angelis, M. G.; Sarti, G. C.; Doghieri, F. NELF Model Prediction of the Infinite Dilution Gas Solubility in Glassy Polymers. *J. Membr. Sci.* **2007**, *289* (1–2), 106–122. <https://doi.org/10.1016/j.memsci.2006.11.044>.
- (2) Li, Y.; Yavari, M.; Baldanza, A.; Di Maio, E.; Okamoto, Y.; Lin, H.; Galizia, M. Volumetric Properties and Sorption Behavior of Perfluoropolymers with Dioxolane Pendant Rings. *Ind. Eng. Chem. Res.* **2020**, *59* (12), 5276–5286. <https://doi.org/10.1021/acs.iecr.9b03411>.
- (3) De Angelis, M. G.; Merkel, T. C.; Bondar, V. I.; Freeman, B. D.; Doghieri, F.; Sarti, G. C.

- Gas Sorption and Dilation in Poly(2,2-Bistrifluoromethyl-4,5-Difluoro-1,3-Dioxole-Co-Tetrafluoroethylene): Comparison of Experimental Data with Predictions of the Nonequilibrium Lattice Fluid Model. *Macromolecules* **2002**, *35* (4), 1276–1288. <https://doi.org/10.1021/ma0106090>.
- (4) Minelli, M.; Sarti, G. C. Gas Permeability in Glassy Polymers: A Thermodynamic Approach. *Fluid Phase Equilib.* **2016**, *424*, 44–51. <https://doi.org/10.1016/j.fluid.2015.09.027>.
- (5) Scherillo, G.; Sanguigno, L.; Galizia, M.; Lavorgna, M.; Musto, P.; Mensitieri, G. Non-Equilibrium Compressible Lattice Theories Accounting for Hydrogen Bonding Interactions: Modelling Water Sorption Thermodynamics in Fluorinated Polyimides. *Fluid Phase Equilib.* **2012**, *334*, 166–188. <https://doi.org/10.1016/j.fluid.2012.06.030>.
- (6) Galizia, M.; Stevens, K. A.; Smith, Z. P.; Paul, D. R.; Freeman, B. D. Nonequilibrium Lattice Fluid Modeling of Gas Solubility in HAB-6FDA Polyimide and Its Thermally Rearranged Analogues. *Macromolecules* **2016**, *49* (22), 8768–8779. <https://doi.org/10.1021/acs.macromol.6b01479>.

Appendix E: Supplementary Information for Chapter 8

This chapter has been adapted from the Supplementary Information of: Wu, A. X.; Lin, S.; Mizrahi Rodriguez, K.; Benedetti, F. M.; Joo, T.; Grosz, A. F.; Storme, K. R.; Roy, N.; Syar, D.; Smith, Z. P. Revisiting Group Contribution Theory for Estimating Fractional Free Volume of Microporous Polymer Membranes. *Submitted*.

E.1. Example V_W calculations of PIM-1 and KAUST-PI-1

The PIM-1 repeat unit can be broken into groups as such:

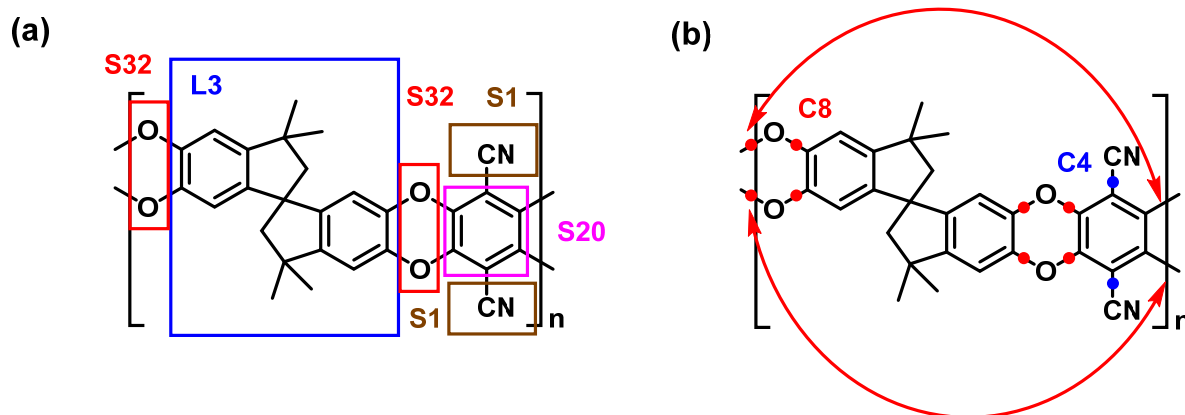


Figure E.1. (a) Segmenting PIM-1 into its various groups. **Note that the largest group possible should be used for best results.** (b) The overlap volumes that should be subtracted in order to connect the groups. Each dot represents a connection between groups, of which the corresponding overlap volume should be subtracted. In this example, the red dots represent a C_{ar}-O connection (C8) and the blue dots represent a C_{ar}-C connection (C4). Care should be taken not to double count repeat unit end groups; the red arrows indicate equivalent connections that should not be double-counted.

To calculate V_W from these groups, the V_W for each group should be added together and the overlap volumes corresponding to the connections between the groups should be subtracted according to Equation 8.6:

$$V_{W,tot} = \sum_{i=1}^n V_{W,i} - \sum_{j=1}^m V_{overlap,j}$$

Where n is the number of groups, m is the number of connections between groups, $V_{W,i}$ is the van der Waals volume for the groups from Tables 8.1 to 8.3, and $V_{overlap,j}$ is the overlap volume from Table 8.4 between groups. Following the example shown in Figure E.1, V_W can be calculated as:

$$V_W = [2 \times S32 + L3 + 2 \times S1 + S20] - [8 \times C8 + 2 \times C4]$$

$$V_W = [2 \times 17.00 + 157.7 + 2 \times 16.57 + 43.10] - [8 \times 4.091 + 2 \times 4.688] = 225.836 \frac{cm^3}{mol}$$

For a typical PIM-1 with a density of 1.05 g cm^{-3} ,⁶ the resulting FFV is:

$$FFV = 1 - 1.3 \frac{\rho}{MW} V_W = 1 - 1.3 \frac{1.05 \frac{g}{cm^3}}{460.63 \frac{g}{mol}} 225.833 \frac{cm^3}{mol} = 0.331$$

Another example calculation for KAUST-PI-1 is shown below

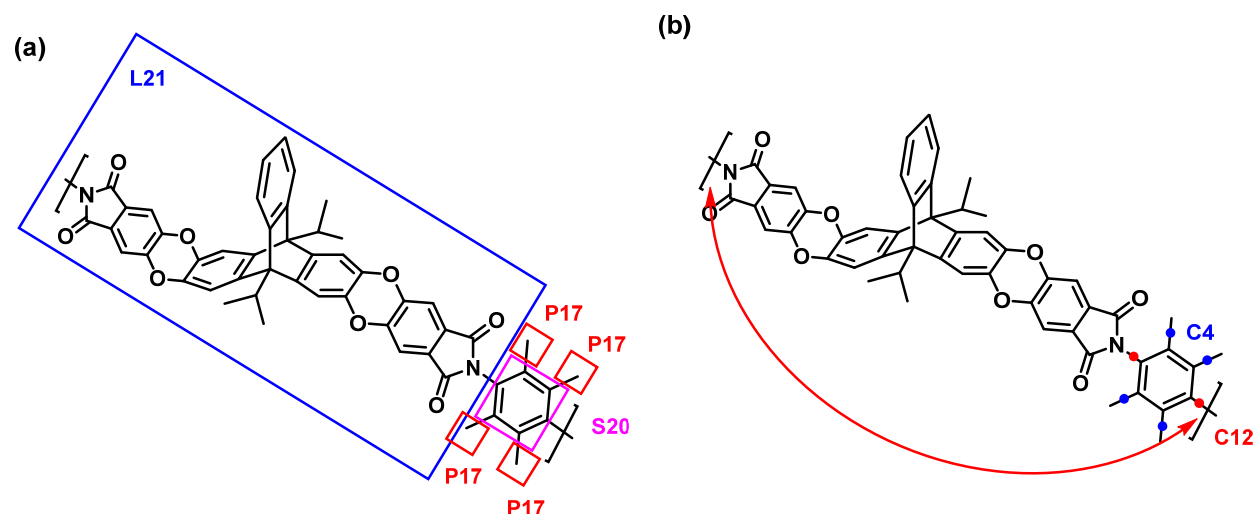


Figure E.2. (a) Segmenting KAUST-PI-1 into its various groups. **Note that the largest group possible should be used for best results.** (b) The overlap volumes that should be subtracted in order to connect the groups. Each dot represents a connection between groups, of which the corresponding overlap volume should be subtracted. In this example, the red dots represent a C_{ar}-N connection (C12) and the blue dots represent a C-C_{ar} connection (C4). Care should be taken not to double count repeat unit end groups; the red arrow indicates equivalent connections that should not be double-counted

Again using Equation 8.6, the V_W can then be calculated as:

$$V_W = [L21 + 4 \times P17 + S20] - [4 \times C4 + 2 \times C12]$$

$$V_W = [331 + 4 \times 14.63 + 43.10] - [4 \times 4.688 + 2 \times 4.255] = 405.358 \frac{cm^3}{mol}$$

For a density of 1.09 g cm^{-3} ,¹⁷ the resulting FFV is:

$$FFV = 1 - 1.3 \frac{\rho}{MW} V_w = 1 - 1.3 \frac{1.09 \frac{g}{cm^3}}{818.95 \frac{g}{mol}} 405.358 \frac{cm^3}{mol} = 0.299$$

The reader may have noted that certain similar groups are present in Tables 8.2 and 8.3. For example, triptycene units are represented in entries S4 and L11, spirobisindane in entries S2 and L3, etc. The groups in Table 8.3 were tabulated for ease-of-use, as they represent the most common forms of the corresponding base unit in Table 8.2. However, there are some structures that do not fully conform with the most common form of the structural unit, especially as new structures are synthesized and characterized. A literature example is for vinylated PIM-1 as synthesized by Halder *et al.*³² The segmented structure is shown below:

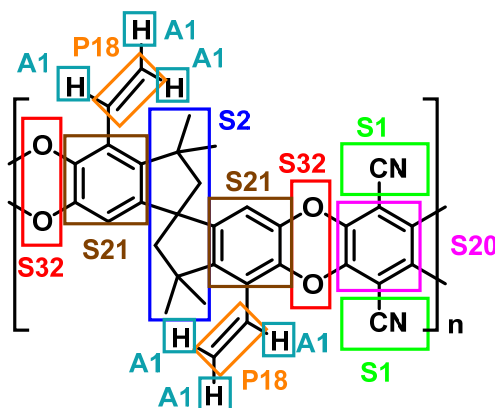


Figure E.3. Segmenting vinylated PIM-1 identified with its various groups.

In this case, use of group L3 to build to spirobisindane group would not be appropriate because group L3 explicitly contains only four connections to other groups on the aromatic rings, while the structure for vinylated PIM-1 requires six total. In this case, use of the base unit S2 along with two S21 groups would be appropriate to build the spirobisindane group for this structure. An alternative approach to build this unit is to start with group L3, subtract the V_W of two hydrogen atoms (A1), then add the overlap volume corresponding to $C_{ar}-H$ (C2). While both approaches are valid, the method shown in Figure E.3 is recommended to minimize the possibility of user error.

E.2. Example calculation comparing reporting methods for perfluoropolymers

As shown in Figure 8.1, the only three polymers that showed a decrease in calculated FFV when comparing the original Bondi method to our updated method were perfluoropolymers. Since these polymers do not contain any hydrogen atoms, the change in the hydrogen VDW radius does not have an effect for these polymers. Assumption 4 states “For unspecified atom-atom connections (i.e., connections between groups), V_W can be calculated by first assuming the group is connected to an aliphatic carbon atom and then subtracting the sphere cap of the connecting atom.” When considering bonds with heteroatoms (e.g., C–O or C–F), this assumption results in a mismatch at the sphere cross-sectional interface as illustrated below. The mismatch at the interface is caused by the difference in bond length between a C–C bond (1.53 Å) and a C–F bond (1.36 Å), and therefore this issue will exist for connections to any bonds with heteroatoms.

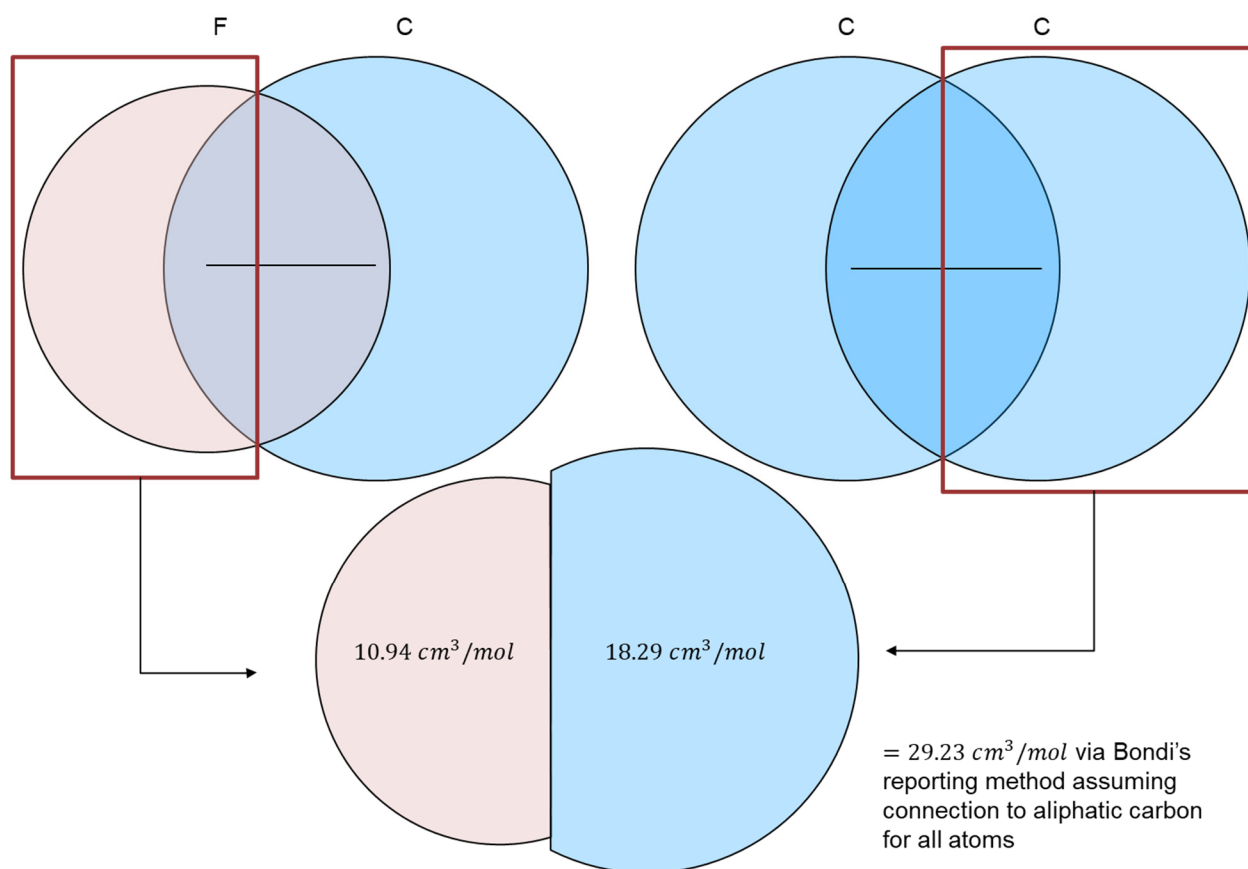


Figure E.4. Schematic showing the effect of assumption 4 when considering bonds to heteroatoms. The circles representing the VDW volumes as well as the lines representing center-to-center bond lengths are drawn to scale. The center-to-center “bond length” of the resulting combination using Bondi’s reporting method is 1.19 Å, considerably shorter than either of the original C–C (1.53 Å) and a C–F (1.36 Å) bond lengths.

On the other hand, the reporting method proposed in this study does not assume any connection and therefore does not prematurely subtract a sphere cap volume, illustrated below.

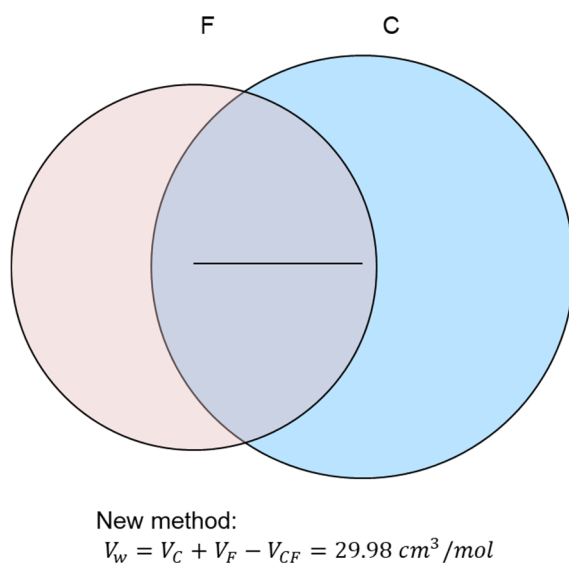


Figure E.5. Schematic showing the proposed reporting method, where the subtracted overlap volume was determined as a function of the two atoms and the bond length.

As shown in Figures E.4 and E.5, the new method results in a larger V_W compared to the old method by $0.75 \text{ cm}^3 \text{ mol}^{-1}$ per C–F bond. When propagated across the 10–12 bonds for Teflon AF 2400, Teflon AF 1600, and Hyflon AD 60 perfluoropolymers, the additional $7.5\text{--}9 \text{ cm}^3 \text{ mol}^{-1}$ resulted in a $\sim 14\%$ increase in the total V_W , which in turn lowered the calculated FFV by $\sim 17\%$.

E.3. Database of literature values

Table E.1. Compiled database of polymers used in this study. Only samples with reported densities were considered. In some cases, the FFV or permeability of certain gases were not reported by the reference. Reported FFV with a “*” designation represents FFV obtained via MD simulation. Polymer names are shown as they appear in their corresponding reference.

Polymer Name	Density (g cm ⁻³)	Reported FFV	New FFV	P_{He} (barrer)	P_{H_2} (barrer)	P_{O_2} (barrer)	P_{CH_4} (barrer)	P_{N_2} (barrer)	P_{CO_2} (barrer)	Ref.
PTMSP	0.78		0.362	6200	16500	8800	17000	6400	35200	1
SBF-PIM	1.056		0.355	2200	6320	2640	1100	786	13900	2
PIM-Trip-TB	1.14		0.261	2500	8039	2718	905	629	9709	3
PIM-1	0.92		0.414					113.9	3027.7	4
PIM-1	1.18		0.248		2254		361.68	222	4521	5
PIM-1	1.05		0.331					283	4011	6
PIM-1	1.05		0.331		1681		497	275		7
PMDA-DAT	1.252	0.196	0.233		71.1	9.4	1.6	1.5	51.4	8
6FDA-DATRI	1.297	0.226	0.251	198	257	39	6.2	8.1	189	9
PIM-6FDA-OH	1.3		0.230		181	23.8	3.4	5.5	119	10
Co-80/20	1.312		0.235		285	32.6	4.1	6.8	173	10
Co-50/50	1.362		0.226		171	16.3	1.45	2.85	77	10
PIM-6FDA-OH	1.245		0.262		228	33.6	5.3	7.15	168	10
Co-80/20	1.25		0.271		380	49.1	6.7	10.2	261	10
Co-50/50	1.329		0.245		155	14.5	1.3	2.5	67	10
PIM-1	1.08	0.25	0.312	1500	3600	1300	430	340	6500	11
PIM-1	1.1	0.17	0.299			728	273	192	3815	12
PIM-1	1.09	0.238	0.305	947.4		585.5	317.7	168.1	3488.7	13
cPIM-1	1.2	0.182	0.262		1619	462.2	208.6	142.9	2654	14
PIM-1	1.112	0.23	0.291				310	228	3799	15
PMDA-TMID	1.158	0.206*	0.260	535		232	76	58	1190	16
KAUST-PI-1	1.09		0.299		4183	827		169		17

PIM-PI-1	1.15		0.266		530	150	77	47	1100	17
PIM-1-00	1.15		0.267			278.2	91.2	72.9	1104.7	18
TPI-PBO-0.25	1.409	0.204	0.225		878	197	34	53	952	19
TPI-PBO-0.50	1.381	0.2	0.228		762	141	25	34	667	19
TPI-PBO-0.75	1.361	0.193	0.227		574	107	18	25	505	19
PIM-1	1.1		0.299			576		178	3657	20
DPt-TMPD	1.1	0.201	0.259	490	1007	348	205	111	2035	21
DPt-MBDAM	1.11	0.183	0.242	285	542	158	86	52	932	21
DPt-BAPFH	1.23	0.168	0.225	177	237	56	21	16	320	21
(PIM-PI) _x -b-(PI) _y (x:y= 1:4)	1.12	0.2868*	0.342				184	176	3011	22
(PIM-PI) _x -b-(PI) _y (x:y= 1:6)	1.18	0.2585*	0.310				104	94	1660	22
(PIM-PI) _x -b-(PI) _y (x:y= 1:8)	1.23	0.2445*	0.282				63	80	1435	22
PIM-Trip-TB	1.02		0.339				310.501		4109.194	23
PIM-1	0.92		0.414					195.4	3694.5	24
TRIP-TR-460-30 (TR-6FDA-DAT1-OH)	1.15		0.329	478	791	170	40.1	50	840	25
6FDA-DAT1-OH	1.24		0.296	90	90	9.36	0.83	1.54	43	25
Bio-TBPI-1	1.093	0.21	0.272	314	669	127	22	27	575	26
Bio-TBPI-2	1.135	0.212	0.260	355	744	165	29	37	702	26
TDAi3-HB	1.07	0.293*	0.297	449	982	188	50	46.1	998	27
6FDA-HB	1.22	0.259*	0.291	271	391	62	10.9	14.2	286	27
6FDA-TrMCA	1.31	0.218*	0.260		193	26.4	3.2	5.52	144	28
CTB1-DMN	1.18		0.240		1295	320	95.7	76.2	1661	29
CTB2-DMN	1.2		0.248		1150	206	40.4	39.9	948	29
SBI-HTB	1.26		0.202		467	75.7	16.3	16.6	466	30
6FDA-HTB	1.46		0.182		167	13.6	0.92	2.26	67	30
6FDA-HTB	1.46		0.182		150	11.6	0.72	1.8	55	30
EAD-DMN	1.17		0.255		2856	655	255	171	3500	31
EA-DMN	1.18		0.233		3291	863	154	171	3321	31
PIM1-CO-100	1.05	0.25	0.319		3710	2180	1525	850	14180	32
PIM1-CO-50	1.07	0.249	0.312		2760	1630	1050	600	10990	32
vinylated PIM-1	1.12	0.187	0.268		1081	410	260	130	3240	32
vinylated PIM-1 CO50	1.15	0.186	0.257		1140	315	185	100	2480	32
thiophenated vinylated PIM-1 CO50	1.18	0.156	0.238		582	180	95	50	1370	32
PIM1-COBr-50	1.19	0.252	0.301		1790	710	370	220	5030	32

thiophenated vinylated PIM-1	1.21	0.151	0.209		775	234	125	70	1735	32
PIM1-COBr-100	1.29	0.243	0.307		1300	480	185	115	3200	32
brominated vinylated PIM-1 CO50	1.32	0.172	0.261		710	225	145	80	1600	32
Brominated vinylated PIM-1	1.58	0.163	0.238		675	305	130	90	1890	32
CANAL-Et	1	0.23	0.293	400	883	310	270	111	1340	33
CANAL-Et-iPr	0.97	0.26	0.306	530	1160	410	350	153	1830	33
CANAL-Me-iPr	0.97	0.27	0.315	730	1510	490	380	193	2210	33
MTTB	0.928	0.351	0.398		5897	864	196	144	3155	34
ITTb	0.93	0.349	0.397		5423	1012	276	187	3901	34
CTTB	0.931	0.349	0.396		5257	791	200	140	3087	34
PIM-M	1.021	0.283	0.337			897	254	230	4370	35
PIM-1	1.059	0.281	0.325			802	258	229	4259	35
PIM-BM-50	1.199	0.236	0.296			450	106	99	2369	35
PIM-BM-70	1.255	0.229	0.288			322	74	70	1689	35
PIM-BM-100	1.339	0.22	0.281			228	43	41	1110	35
CANAL-TB-2	0.945	0.291	0.358		3608	747	205	162	2520	36
CANAL-TB-1	0.983	0.286	0.346		2760	463	121	97	1678	36
PIM-1	1.06	0.26	0.324		3042	1717		629	5366	37
DNPIM-50	1.11	0.25	0.308		1478	522		132	2627	37
TOTPIM-50	1.19	0.22	0.270		2616	1198		413	4756	37
TOTPIM-100	1.28	0.2	0.245		1368	642		190	3056	37
PIM-1	1.09	0.239	0.305		3949	1257	472	337	6957	38
PIM-PMDA-OH	1.18	0.2	0.256		190	30.5	7.7	6.9	198	39
PIM-6FDA-OH	1.22	0.23	0.277		259	45.2	9.1	10.8	263	39
PI-TB-2	1.1876	0.215	0.243	86	134	14	2.1	2.5	55	40
PI-TB-1	1.2592	0.223	0.255	376	607	119	27	31	457	40
TBDA2-SBI-PI	1.13	0.23	0.286	530	1155	240	65	49	1213	41
TBDA1-SBI-PI	1.15	0.21	0.273	398	915	190	45	35	895	41
KAUST-PI-1	1.09		0.299				97.5		2329	42
KAUST-PI-5	1.34		0.195				79.2		1560	42
PIM-1	1.063	0.26	0.322			1133		353	5366	43
TFMPSPIM4	1.089	0.26	0.321			737		217	3616	43
TFMPSPIM3	1.156	0.24	0.287			561		158	2841	43
TFMPSPIM2	1.196	0.22	0.270			308		75	1476	43

TFMPSPI1	1.214	0.22	0.276			156		33	731	43
PIM-1	1.08		0.312		3408	1135	397	356	5135	44
PIM-1	1.06	0.26	0.324			1393	726	472	6538	45
TBPIM25	1.13	0.22	0.294			917	375	262	4441	45
TBPIM33	1.14	0.21	0.292			864	353	240	4353	45
PIM-EA-PI or PIM-PI-12	1.17		0.240	1580	4230	1380	457	369	7340	46
PIM-C1	1.065		0.330	3380	9870	3410	1310	980	18900	47
TPHI	1.339	0.17	0.214		27		0.09	0.19	4.7	48
TPHI-TR-350	1.318	0.181	0.208		61		0.41	0.46	16	48
TPHI-TR-400	1.287	0.196	0.227		520		8.3	16	320	48
TPHI-TR-450	1.273	0.204	0.235		810		4	8.4	270	48
TPHA	1.34	0.171	0.190		27		0.12	0.21	5.7	48
TPHA-TC-300	1.307	0.183	0.215		74		0.82	1.1	23	48
TPHA-TC-350	1.298	0.188	0.220		82		1.3	1.4	31	48
TPHA-TC-400	1.295	0.191	0.222		92		1.7	2.2	39	48
AOPIM-1	1.187		0.260		926	194	42.3	47.3	1073	49
TNTDA-DAT	1.092	0.214	0.278	776		159	24	32	728	50
TNTDA-MMBMA	1.109	0.196	0.265	526		96	16	21	438	50
TNTDA-TBDA1	1.12	0.181	0.255	258		75	12	15	397	50
TNTDA-FDBMA	1.128	0.203	0.263	584		122	22	27	569	50
PIM-1	1.066		0.320		3274	1396	789	483	9896	51
(PIM-PI) _x -(6FDA-durene-PI) _y (1:4)	1.29		0.238				69.4	74.1	1265	52
(PIM-PI) _x -(6FDA-durene-PI) _y (1:6)	1.3		0.237				68.8	73.7	1225	52
(PIM-PI) _x -(6FDA-durene-PI) _y (1:10)	1.32		0.229				60.2	64.4	1047	52
PIM-PI-1	1.16		0.260				37.3	41.1	495	52
PIM-EA(H2)-TB	1.06		0.308				62.6	53.1	1391	53
PIM-EA(H2)-TB	1.06		0.308	606	1630	350	77.6	62.8	1380	53
AZ-PIM-100	1.143		0.287				245		2894	54
AZ-PIM-R50	1.116		0.296				384		4246	54
AZ-PIM-A50	1.099		0.307				331		3879	54
Teflon AF 2400	1.744	0.33	0.278		2090	960	390	480	2200	55
Teflon AF 1600	1.836	0.31	0.239		550	270	80	110	520	55
Hyflon AD 60	1.93	0.23	0.204		210	67	12	24	150	55

E.4. Plots and tables

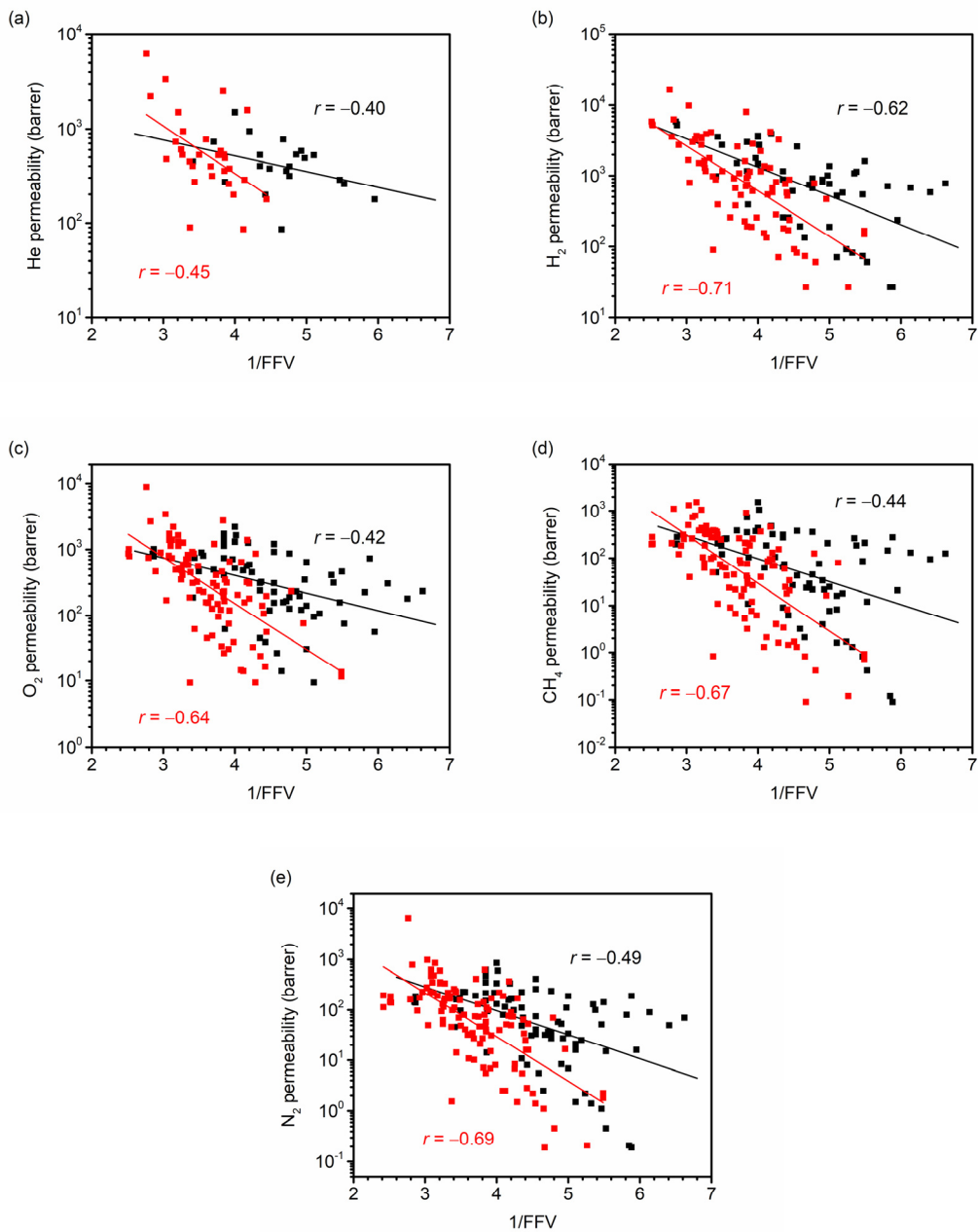


Figure E.6. Plots showing overall correlations for $\ln(P)$ versus $1/FFV$ with their respective best-fit lines and Pearson correlation coefficients for (a) He, (b) H_2 , (c) O_2 , (d) CH_4 , and (e) N_2 . The red symbols represent FFV values calculated using the presented method and the black symbols represent reported FFV values.

Table E.2. Table of the best-fit slopes and Pearson coefficients corresponding to Figure E.6 and Figure 8.2.

Gas	Using new FFV (red symbols)		Using reported FFV (black symbols)	
	Slope	Pearson Coeff.	Slope	Pearson Coeff.
He	-1.268	-0.45	-0.389	-0.40
H ₂	-1.497	-0.71	-0.933	-0.62
O ₂	-1.645	-0.64	-0.610	-0.42
CH ₄	-2.369	-0.67	-1.112	-0.44
N ₂	-2.041	-0.69	-1.098	-0.49
CO ₂	-1.781	-0.67	-0.985	-0.48

E.5. MATLAB code for MC calculation of V_W using group P1 as an example

```
function bondi_mc
%atom identity
grp.a = ["C"
"C"
"C"
"C"
"H"
"H"
"H"
"H"
"H"
"H"
"H"
"H"
"H"
"H"
"H"];

%atom xyz coordinates in angstrom
grp.pos = [-4.344  -0.158  0.666
-3.207  0.631  0.004
-2.344  -0.321  -0.834
-2.34  1.285  1.087
-3.798  1.717  -0.903
-3.951  -0.949  1.326
-4.986  -0.642  -0.088
-4.984  0.499  1.277
-2.939  -0.809  -1.624
-1.903  -1.116  -0.21
-1.516  0.216  -1.324
-1.512  1.861  0.643
-1.899  0.529  1.758
-2.932  1.977  1.709
-4.425  2.419  -0.329
-4.428  1.278  -1.694
-3.005  2.303  -1.395];

%atoms excluded
grp.extra = sort([1
6
7
8
3
9
10
11]);

%removing excluded atoms from set
for i = length(grp.a):-1:1
    if ismember(i,grp.extra)
        grp.a(i) = [];
    end
end
```

```

        grp.pos(i,:) = [];
    end
end

%defining VDW radii and creating structure
vr = [1.1 1.7 1.55 1.5 1.47 2.1 1.8 1.75 1.85]; %H C N O F Si S Cl Br

vdr.H = vr(1);
vdr.C = vr(2);
vdr.N = vr(3);
vdr.O = vr(4);
vdr.F = vr(5);
vdr.Si = vr(6);
vdr.S = vr(7);
vdr.Cl = vr(8);
vdr.Br = vr(9);

%% Monte Carlo
n = 1000000; %number of points
k = 0; %counter

%find box dimensions and generate points
for i = 1:3
    box_dim(i,1) = min(grp.pos(:,i))-max(vr);
    box_dim(i,2) = max(grp.pos(:,i))+max(vr);
    pt_dim(:,i) = box_dim(i,1)+rand(1,n)*(box_dim(i,2)-box_dim(i,1));
end

%MC script; determine if distance between point and atom is less than the
%VDW radius of the atom
for i = 1:n
    pt = pt_dim(i,:);
    for j = 1:size(grp.pos,1)
        sep = dist(pt,grp.pos(j,:));
        if sep < vdr.(grp.a(j))
            k = k+1;
            break
        end
    end
end

%calculate Vw, variance in cm3/mol
box_vol = prod(box_dim(:,2)-box_dim(:,1));
MC_v_w = box_vol*k/n*1e-30*6.022e23*1000000;
MC_v_w_var = MC_v_w*(box_vol-MC_v_w)/n*1e-30*6.022e23*1000000;
end

function d = dist(a,b)
%a,b are xyz coordinates
d = sqrt((a(1)-b(1))^2+(a(2)-b(2))^2+(a(3)-b(3))^2);
end

```

E.6. References

- (1) Srinivasan, R.; Auvil, S. R.; Burban, P. M. Elucidating the Mechanism(s) of Gas Transport in Poly[1-(Trimethylsilyl)-1-Propyne] (PTMSP) Membranes. *J. Membr. Sci.* **1994**, *86* (1–2), 67–86. [https://doi.org/10.1016/0376-7388\(93\)E0128-7](https://doi.org/10.1016/0376-7388(93)E0128-7).
- (2) Bezzu, C. G.; Carta, M.; Tonkins, A.; Jansen, J. C.; Bernardo, P.; Bazzarelli, F.; McKeown, N. B. A Spirobifluorene-Based Polymer of Intrinsic Microporosity with Improved Performance for Gas Separation. *Adv. Mater.* **2012**, *24* (44), 5930–5933. <https://doi.org/10.1002/adma.201202393>.
- (3) Carta, M.; Croad, M.; Malpass-Evans, R.; Jansen, J. C.; Bernardo, P.; Clarizia, G.; Friess, K.; Lanč, M.; McKeown, N. B. Triptycene Induced Enhancement of Membrane Gas Selectivity for Microporous Tröger's Base Polymers. *Adv. Mater.* **2014**, *26* (21), 3526–3531. <https://doi.org/10.1002/adma.201305783>.
- (4) Yu, G.; Zou, X.; Sun, L.; Liu, B.; Wang, Z.; Zhang, P.; Zhu, G. Constructing Connected Paths between UiO-66 and PIM-1 to Improve Membrane CO₂ Separation with Crystal-Like Gas Selectivity. *Adv. Mater.* **2019**, *31* (15), 1–9. <https://doi.org/10.1002/adma.201806853>.
- (5) Wu, X.; Ren, Y.; Sui, G.; Wang, G.; Xu, G.; Yang, L.; Wu, Y.; He, G.; Nasir, N.; Wu, H.; et al. Accelerating CO₂ Capture of Highly Permeable Polymer through Incorporating Highly Selective Hollow Zeolite Imidazolate Framework. *AIChE J.* **2020**, *66* (2), 1–10. <https://doi.org/10.1002/aic.16800>.
- (6) Lau, C. H.; Nguyen, P. T.; Hill, M. R.; Thornton, A. W.; Konstas, K.; Doherty, C. M.; Mulder, R. J.; Bourgeois, L.; Liu, A. C. Y.; Sprouster, D. J.; et al. Ending Aging in Super Glassy Polymer Membranes. *Angew. Chemie Int. Ed.* **2014**, *53* (21), 5322–5326. <https://doi.org/10.1002/anie.201402234>.
- (7) Lau, C. H.; Konstas, K.; Thornton, A. W.; Liu, A. C. Y.; Mudie, S.; Kennedy, D. F.; Howard, S. C.; Hill, A. J.; Hill, M. R. Gas-Separation Membranes Loaded with Porous Aromatic Frameworks That Improve with Age. *Angew. Chemie Int. Ed.* **2015**, *54* (9), 2669–2673. <https://doi.org/10.1002/anie.201410684>.
- (8) Li, F.; Zhang, C.; Weng, Y. Preparation and Gas Separation Properties of Triptycene-Based Microporous Polyimide. *Macromol. Chem. Phys.* **2019**, *220* (10), 1–7. <https://doi.org/10.1002/macp.201900047>.
- (9) Cho, Y. J.; Park, H. B. High Performance Polyimide with High Internal Free Volume Elements. *Macromol. Rapid Commun.* **2011**, *32* (7), 579–586. <https://doi.org/10.1002/marc.201000690>.
- (10) Ma, X.; Mukaddam, M.; Pinnau, I. Bifunctionalized Intrinsically Microporous Polyimides with Simultaneously Enhanced Gas Permeability and Selectivity. *Macromol. Rapid Commun.* **2016**, *37* (11), 900–904. <https://doi.org/10.1002/marc.201600023>.

- (11) Thomas, S.; Pinnau, I.; Du, N.; Guiver, M. D. Pure- and Mixed-Gas Permeation Properties of a Microporous Spirobisindane-Based Ladder Polymer (PIM-1). *J. Membr. Sci.* **2009**, *333*, 125–131. <https://doi.org/10.1016/j.memsci.2009.02.003>.
- (12) Yong, W. F.; Li, F. Y.; Xiao, Y. C.; Li, P.; Pramoda, K. P.; Tong, Y. W.; Chung, T. S. Molecular Engineering of PIM-1/Matrimid Blend Membranes for Gas Separation. *J. Membr. Sci.* **2012**, *407–408*, 47–57. <https://doi.org/10.1016/j.memsci.2012.03.038>.
- (13) Hao, L.; Li, P.; Chung, T. S. PIM-1 as an Organic Filler to Enhance the Gas Separation Performance of Ultem Polyetherimide. *J. Membr. Sci.* **2014**, *453*, 614–623. <https://doi.org/10.1016/j.memsci.2013.11.045>.
- (14) Yong, W. F.; Li, F. Y.; Chung, T. S.; Tong, Y. W. Molecular Interaction, Gas Transport Properties and Plasticization Behavior of CPIM-1/Torlon Blend Membranes. *J. Membr. Sci.* **2014**, *462*, 119–130. <https://doi.org/10.1016/j.memsci.2014.03.046>.
- (15) Mei Wu, X.; Gen Zhang, Q.; Ju Lin, P.; Qu, Y.; Mei Zhu, A.; Lin Liu, Q. Towards Enhanced CO₂ Selectivity of the PIM-1 Membrane by Blending with Polyethylene Glycol. *J. Membr. Sci.* **2015**, *493*, 147–155. <https://doi.org/10.1016/j.memsci.2015.05.077>.
- (16) Álvarez, C.; Lozano, A. E.; de la Campa, J. G. High-Productivity Gas Separation Membranes Derived from Pyromellitic Dianhydride and Nonlinear Diamines. *J. Membr. Sci.* **2016**, *501*, 191–198. <https://doi.org/10.1016/j.memsci.2015.11.039>.
- (17) Chen, Y. R.; Chen, L. H.; Chang, K. S.; Chen, T. H.; Lin, Y. F.; Tung, K. L. Structural Characteristics and Transport Behavior of Triptycene-Based PIMs Membranes: A Combination Study Using Ab Initio Calculation and Molecular Simulations. *J. Membr. Sci.* **2016**, *514*, 114–124. <https://doi.org/10.1016/j.memsci.2016.04.063>.
- (18) Konnertz, N.; Ding, Y.; Harrison, W. J.; Budd, P. M.; Schönhals, A.; Böhning, M. Molecular Mobility and Gas Transport Properties of Nanocomposites Based on PIM-1 and Polyhedral Oligomeric Phenethyl-Silsesquioxanes (POSS). *J. Membr. Sci.* **2017**, *529*, 274–285. <https://doi.org/10.1016/j.memsci.2017.02.007>.
- (19) Luo, S.; Zhang, Q.; Bear, T. K.; Curtis, T. E.; Roeder, R. K.; Doherty, C. M.; Hill, A. J.; Guo, R. Triptycene-Containing Poly(Benzoxazole-Co-Imide) Membranes with Enhanced Mechanical Strength for High-Performance Gas Separation. *J. Membr. Sci.* **2018**, *551*, 305–314. <https://doi.org/10.1016/j.memsci.2018.01.052>.
- (20) Liang, C. Z.; Liu, J. T.; Lai, J. Y.; Chung, T. S. High-Performance Multiple-Layer PIM Composite Hollow Fiber Membranes for Gas Separation. *J. Membr. Sci.* **2018**, *563*, 93–106. <https://doi.org/10.1016/j.memsci.2018.05.045>.
- (21) Sulub-Sulub, R.; Loría-Bastarrachea, M. I.; Vázquez-Torres, H.; Santiago-García, J. L.; Aguilar-Vega, M. Highly Permeable Polyimide Membranes with a Structural Pyrene Containing Tert-Butyl Groups: Synthesis, Characterization and Gas Transport. *J. Membr. Sci.* **2018**, *563*, 134–141. <https://doi.org/10.1016/j.memsci.2018.05.054>.

- (22) Hossain, I.; Nam, S. Y.; Rizzuto, C.; Barbieri, G.; Tocci, E.; Kim, T. H. PIM-Polyimide Multiblock Copolymer-Based Membranes with Enhanced CO₂ Separation Performances. *J. Membr. Sci.* **2019**, *574*, 270–281. <https://doi.org/10.1016/j.memsci.2018.12.084>.
- (23) Genduso, G.; Wang, Y.; Ghanem, B. S.; Pinnau, I. Permeation, Sorption, and Diffusion of CO₂-CH₄ Mixtures in Polymers of Intrinsic Microporosity: The Effect of Intrachain Rigidity on Plasticization Resistance. *J. Membr. Sci.* **2019**, *584*, 100–109. <https://doi.org/10.1016/j.memsci.2019.05.014>.
- (24) Yu, G.; Li, Y.; Wang, Z.; Liu, T. X.; Zhu, G.; Zou, X. Mixed Matrix Membranes Derived from Nanoscale Porous Organic Frameworks for Permeable and Selective CO₂ Separation. *J. Membr. Sci.* **2019**, *591*, 117343. <https://doi.org/10.1016/j.memsci.2019.117343>.
- (25) Yerzhankyzy, A.; Ghanem, B. S.; Wang, Y.; Alaslai, N.; Pinnau, I. Gas Separation Performance and Mechanical Properties of Thermally-Rearranged Polybenzoxazoles Derived from an Intrinsically Microporous Dihydroxyl-Functionalized Triptycene Diamine-Based Polyimide. *J. Membr. Sci.* **2020**, *595*, 117512. <https://doi.org/10.1016/j.memsci.2019.117512>.
- (26) Hu, X.; Lee, W. H.; Zhao, J.; Bae, J. Y.; Kim, J. S.; Wang, Z.; Yan, J.; Zhuang, Y.; Lee, Y. M. Tröger's Base (TB)-Containing Polyimide Membranes Derived from Bio-Based Dianhydrides for Gas Separations. *J. Membr. Sci.* **2020**, *610*, 118255. <https://doi.org/10.1016/j.memsci.2020.118255>.
- (27) Wang, Y.; Ghanem, B. S.; Han, Y.; Pinnau, I. Facile Synthesis and Gas Transport Properties of Hünlich's Base-Derived Intrinsically Microporous Polyimides. *Polymer* **2020**, *201*, 122619. <https://doi.org/10.1016/j.polymer.2020.122619>.
- (28) Abdulhamid, M. A.; Genduso, G.; Wang, Y.; Ma, X.; Pinnau, I. Plasticization-Resistant Carboxyl-Functionalized 6FDA-Polyimide of Intrinsic Microporosity (PIM-PI) for Membrane-Based Gas Separation. *Ind. Eng. Chem. Res.* **2020**, *59* (12), 5247–5256. <https://doi.org/10.1021/acs.iecr.9b04994>.
- (29) Ma, X.; Abdulhamid, M. A.; Pinnau, I. Design and Synthesis of Polyimides Based on Carbocyclic Pseudo-Tröger's Base-Derived Dianhydrides for Membrane Gas Separation Applications. *Macromolecules* **2017**, *50* (15), 5850–5857. <https://doi.org/10.1021/acs.macromol.7b01054>.
- (30) Ma, X.; Abdulhamid, M.; Miao, X.; Pinnau, I. Facile Synthesis of a Hydroxyl-Functionalized Tröger's Base Diamine: A New Building Block for High-Performance Polyimide Gas Separation Membranes. *Macromolecules* **2017**, *50* (24), 9569–9576. <https://doi.org/10.1021/acs.macromol.7b02301>.
- (31) Ma, X.; Pinnau, I. Effect of Film Thickness and Physical Aging on Intrinsic Gas Permeation Properties of Microporous Ethanoanthracene-Based Polyimides. *Macromolecules* **2018**, *51* (3), 1069–1076. <https://doi.org/10.1021/acs.macromol.7b02556>.
- (32) Halder, K.; Neumann, S.; Bengtson, G.; Khan, M. M.; Filiz, V.; Abetz, V. Polymers of Intrinsic Microporosity Postmodified by Vinyl Groups for Membrane Applications. *Macromolecules* **2018**, *51* (18), 7309–7319. <https://doi.org/10.1021/acs.macromol.8b01252>.

- (33) Lai, H. W. H.; Benedetti, F. M.; Jin, Z.; Teo, Y. C.; Wu, A. X.; Angelis, M. G. De; Smith, Z. P.; Xia, Y. Tuning the Molecular Weights, Chain Packing, and Gas-Transport Properties of CANAL Ladder Polymers by Short Alkyl Substitutions. *Macromolecules* **2019**, *52* (16), 6294–6302. <https://doi.org/10.1021/acs.macromol.9b01155>.
- (34) Zhu, Z.; Zhu, J.; Li, J.; Ma, X. Enhanced Gas Separation Properties of Tröger's Base Polymer Membranes Derived from Pure Triptycene Diamine Regioisomers. *Macromolecules* **2020**, *53* (5), 1573–1584. <https://doi.org/10.1021/acs.macromol.9b02328>.
- (35) Chen, X.; Zhang, Z.; Wu, L.; Liu, X.; Xu, S.; Efome, J. E.; Zhang, X.; Li, N. Polymers of Intrinsic Microporosity Having Bulky Substitutes and Cross-Linking for Gas Separation Membranes. *ACS Appl. Polym. Mater.* **2020**, *2* (2), 987–995. <https://doi.org/10.1021/acscpm.9b01193>.
- (36) Ma, X.; Lai, H. W. H.; Wang, Y.; Alhazmi, A.; Xia, Y.; Pinnau, I. Facile Synthesis and Study of Microporous Catalytic Arene-Norbornene Annulation-Tröger's Base Ladder Polymers for Membrane Air Separation. *ACS Macro Lett.* **2020**, *9* (5), 680–685. <https://doi.org/10.1021/acsmacrolett.0c00135>.
- (37) Du, N.; Robertson, G. P.; Pinnau, I.; Guiver, M. D. Polymers of Intrinsic Microporosity with Dinaphthyl and Thianthrene Segments. *Macromolecules* **2010**, *43* (20), 8580–8587. <https://doi.org/10.1021/ma101930x>.
- (38) Li, F. Y.; Xiao, Y.; Chung, T.-S.; Kawi, S. High-Performance Thermally Self-Cross-Linked Polymer of Intrinsic Microporosity (PIM-1) Membranes for Energy Development. *Macromolecules* **2012**, *45* (3), 1427–1437. <https://doi.org/10.1021/ma202667y>.
- (39) Ma, X.; Swaidan, R.; Belmabkhout, Y.; Zhu, Y.; Litwiller, E.; Jouiad, M.; Pinnau, I.; Han, Y. Synthesis and Gas Transport Properties of Hydroxyl-Functionalized Polyimides with Intrinsic Microporosity. *Macromolecules* **2012**, *45* (9), 3841–3849. <https://doi.org/10.1021/ma300549m>.
- (40) Zhuang, Y.; Seong, J. G.; Do, Y. S.; Jo, H. J.; Cui, Z.; Lee, J.; Lee, Y. M.; Guiver, M. D. Intrinsically Microporous Soluble Polyimides Incorporating Tröger's Base for Membrane Gas Separation. *Macromolecules* **2014**, *47* (10), 3254–3262. <https://doi.org/10.1021/ma5007073>.
- (41) Wang, Z.; Wang, D.; Jin, J. Microporous Polyimides with Rationally Designed Chain Structure Achieving High Performance for Gas Separation. *Macromolecules* **2014**, *47* (21), 7477–7483. <https://doi.org/10.1021/ma5017506>.
- (42) Swaidan, R.; Ghanem, B.; Al-Saeedi, M.; Litwiller, E.; Pinnau, I. Role of Intrachain Rigidity in the Plasticization of Intrinsically Microporous Triptycene-Based Polyimide Membranes in Mixed-Gas CO₂/CH₄ Separations. *Macromolecules* **2014**, *47* (21), 7453–7462. <https://doi.org/10.1021/ma501798v>.
- (43) Du, N.; Robertson, G. P.; Song, J.; Pinnau, I.; Thomas, S.; Guiver, M. D. Polymers of Intrinsic Microporosity Containing Trifluoromethyl and Phenylsulfone Groups as Materials for Membrane Gas Separation. *Macromolecules* **2008**, *41* (24), 9656–9662. <https://doi.org/10.1021/ma801858d>.

- (44) Song, Q.; Cao, S.; Pritchard, R. H.; Ghalei, B.; Al-Muhtaseb, S. A.; Terentjev, E. M.; Cheetham, A. K.; Sivaniah, E. Controlled Thermal Oxidative Crosslinking of Polymers of Intrinsic Microporosity towards Tunable Molecular Sieve Membranes. *Nat. Commun.* **2014**, *5*. <https://doi.org/10.1038/ncomms5813>.
- (45) Wang, Z. G.; Liu, X.; Wang, D.; Jin, J. Tröger's Base-Based Copolymers with Intrinsic Microporosity for CO₂ Separation and Effect of Tröger's Base on Separation Performance. *Polym. Chem.* **2014**, *5* (8), 2793–2800. <https://doi.org/10.1039/c3py01608k>.
- (46) Rogan, Y.; Malpass-Evans, R.; Carta, M.; Lee, M.; Jansen, J. C.; Bernardo, P.; Clarizia, G.; Tocci, E.; Friess, K.; Lanč, M.; et al. A Highly Permeable Polyimide with Enhanced Selectivity for Membrane Gas Separations. *J. Mater. Chem. A* **2014**, *2* (14), 4874–4877. <https://doi.org/10.1039/c4ta00564c>.
- (47) Zhang, J.; Kang, H.; Martin, J.; Zhang, S.; Thomas, S.; Merkel, T. C.; Jin, J. The Enhancement of Chain Rigidity and Gas Transport Performance of Polymers of Intrinsic Microporosity: Via Intramolecular Locking of the Spiro-Carbon. *Chem. Commun.* **2016**, *52* (39), 6553–6556. <https://doi.org/10.1039/c6cc02308h>.
- (48) Luo, S.; Liu, J.; Lin, H.; Kazanowska, B. A.; Hunckler, M. D.; Roeder, R. K.; Guo, R. Preparation and Gas Transport Properties of Triptycene-Containing Polybenzoxazole (PBO)-Based Polymers Derived from Thermal Rearrangement (TR) and Thermal Cyclodehydration (TC) Processes. *J. Mater. Chem. A* **2016**, *4* (43), 17050–17062. <https://doi.org/10.1039/c6ta03951k>.
- (49) Wu, J.; Chung, T. S.; Japip, S.; Chung, T. S. Infiltrating Molecular Gatekeepers with Coexisting Molecular Solubility and 3D-Intrinsic Porosity into a Microporous Polymer Scaffold for Gas Separation. *J. Mater. Chem. A* **2020**, *8* (13), 6196–6209. <https://doi.org/10.1039/c9ta12028a>.
- (50) Hu, X.; Mu, H.; Miao, J.; Lu, Y.; Wang, X.; Meng, X.; Wang, Z.; Yan, J. Synthesis and Gas Separation Performance of Intrinsically Microporous Polyimides Derived from Sterically Hindered Binaphthalenetetracarboxylic Dianhydride. *Polym. Chem.* **2020**, *11* (25), 4172–4179. <https://doi.org/10.1039/d0py00594k>.
- (51) Khan, M. M.; Shishatskiy, S.; Filiz, V. Mixed Matrix Membranes of Boron Icosahedron and Polymers of Intrinsic Microporosity (PIM-1) for Gas Separation. *Membranes* **2018**, *8* (1), 1. <https://doi.org/10.3390/membranes8010001>.
- (52) Hossain, I.; Al Munsur, A.; Kim, T.-H. A Facile Synthesis of (PIM-Polyimide)-(6FDA-Durene-Polyimide) Copolymer as Novel Polymer Membranes for CO₂ Separation. *Membranes* **2019**, *9* (9), 113. <https://doi.org/10.3390/membranes9090113>.
- (53) Esposito, E.; Mazzei, I.; Monteleone, M.; Fuoco, A.; Carta, M.; McKeown, N.; Malpass-Evans, R.; Jansen, J. Highly Permeable Matrimid®/PIM-EA(H₂)-TB Blend Membrane for Gas Separation. *Polymers* **2018**, *11* (1), 46. <https://doi.org/10.3390/polym11010046>.
- (54) Neumann, S.; Bengtson, G.; Meis, D.; Filiz, V. Thermal Cross Linking of Novel Azide Modified Polymers of Intrinsic Microporosity—Effect of Distribution and the Gas Separation Performance. *Polymers* **2019**, *11* (8), 1241. <https://doi.org/10.3390/polym11081241>.

(55) Merkel, T. C.; Pinnau, I.; Prabhakar, R. S.; Freeman, B. D. Gas and Vapor Transport Properties of Perfluoropolymers. In *Materials Science of Membranes for Gas and Vapor Separation*; 2006; pp 251–270.